Characterization of *Pseudomonas aeruginosa* mechanosensing through label-free imaging of type IV pili

Lorenzo Anton-Louis TALÀ

Acknowledgements

I am deeply grateful to all the people who contributed in one way or another to the success of my thesis. Without their contributions I would not be where I am today.

First of all, I would like to thank my PhD thesis supervisor Prof. Alexandre Persat for the great confidence he had in me and for believing in me since the day I joined the lab as his first PhD student. He has always been supportive and mentored me during these years in this fantastic adventure. He has been a great tutor throughout these years, both in the scientific and human aspects. I am grateful for his valuable comments during our scientific discussions that shaped my critical thinking as a scientist and brought value to this project. I would also like to thank our collaborator Prof. Joanne Engel for her comments and insights about the Chp system.

Moreover, I would like to thank Prof. Philip Kukura and his lab members Joanna Andrecka, Adam Fineberg and Gavin Young that were so supportive in teaching me how to build an iSCAT in Oxford and then patiently answering all my questions about building the iSCAT in our lab.

I would also like to thank Prof. Suliana Manley, Prof. John McKinney, Prof. Urs Jenal and Prof. Tâm Mignot for their time and for accepting to review my work.

I am grateful for all staff members of the SV workshop that helped with the logistics of building the optic table for iSCAT and the CIME facility at EPFL and especially to Davide Demurtas for his advice on TEM visualization as well as to Sergey Nazarov for his help in learning how to analyze cryo-EM data.

I am so grateful that I spent these years with all the wonderful Persat Lab members! In order of arrival in the lab: Zainebe, Xavier, Tamara, Alice, Jeremy, Sophia, Marco, Alessandra, Pascal, Sourabh, Sofya, Tania and Alix. They all have contributed to create an amazing working atmosphere in the lab and became close friends. A special thank for Zainebe that was always willing to help, Marco with whom I collaborated for the 4th chapter of my thesis and his wise comments and our

Abstract

Bacteria are ubiquitously found in all sorts of environment. They're found in the ocean, soil, or even in our guts or on our skin. Independently of their niche, they can transition from a planktonic state were they freely swim in an aqueous environment to a surface-associated state where they form multicellular communities known as biofilms. It is known that bacteria change their physiology when associated with surfaces. This is many times accompanied with a different transcriptional state compared to planktonic populations. *Pseudomonas aeruginosa* is an opportunistic pathogen often involved in nosocomial infections that can lead to chronic infection in immunocompromised patients. *P. aeruginosa* infections are often associated with a surface-associated biofilm lifestyle. In addition, it uses a host contact-dependent toxin secretion system during pathogenicity. It also possesses a surface-specific motility system known as twitching. These three examples are all physiological adaptation to surface contact. All these are a result of a change in gene expression upon surface contact.

To power twitching motility, *P. aeruginosa* uses long and thin extracellular filaments called type IV pili (TFP). *P. aeruginosa* extends and retracts its TFP to pull itself forward on surfaces. Beyond their function in motility, TFP extension, attachment on a solid substrate and retraction are required for a surface-specific transcriptional response in a process called mechanosensing. A chemotaxis-like two component system called the Chp system also mediates this surface-dependent response. The activated Chp system upregulates transcription of virulence related genes including genes involved in TFP biogenesis. However, little is known about how the Chp system is activated by TFP, and how TFP respond to mechanosensing.

The aim of this thesis is to characterize the mechanisms of mechanosensation in *P. aeruginosa*. In order to achieve this, one must first better characterize the mechanical input signal generated by TFP attachment events. This is an experimental challenge as TFP fibers cannot be imaged with conventional microscopes. In this thesis I present an approach to the investigation of *P. aeruginosa* mechanosensation by leveraging interferometric scattering microscopy (iSCAT) that I optimized for

label-free detection of TFP during live cell imaging. I also show the power of iSCAT microscopy to detect and analyze TFP and their dynamic behavior on surfaces.

By combining iSCAT to fluorescence microscopy, I could then track intracellular regulatory proteins and simultaneous TFP activity. Combining these measurements with single cell motility assays and protein localization, I was able to highlight signaling feedback loops between TFP and the Chp chemotaxis system that are critical to motility and mechanosensing. This feedback system allows for cell-polarization that directs twitching motility, which we term mechanotaxis.

Finally, based on new biophysical and structural evidence, I propose a model for the mechanisms of mechanosensing by TFP and the Chp system. Here, my preliminary data show that the PilA monomers that are disassembled from TFP during retraction interact with the Chp chemosensor PilJ. Due to TFP attachment, the flux of PilA towards PilJ is different in liquid vs surfaces. I propose a mechanism wherein PilJ senses this flux imbalance.

Keywords

Pseudomonas aeruginosa, iSCAT, Mechanosensation, Label-free microscopy, Type IV pili, Chp system, Mechanotaxis

Résumé

Les bactéries sont omniprésentes. On les trouve dans l'océan, dans le sol, ou même dans nos intestins ou sur notre peau. Indépendamment de leur niche, elles peuvent passer d'un état planctonique où elles nagent librement en milieu aqueux à un état sessile où elles forment des communautés multicellulaires appelées biofilms. Sur les surfaces, les bactéries modifient leur physiologie qui s'accompagne souvent d'un état transcriptionnel différent de celui des populations planctoniques. *Pseudomonas aeruginosa* est un pathogène opportuniste souvent impliqué dans les infections nosocomiales qui peuvent conduire à une forme chronique chez les patients immunodéprimés. Les infections à *P. aeruginosa* sont souvent associées à un mode de vie sessile sous forme de biofilm. De plus, pendant la pathogénicité, elles utilisent un système de sécrétion de toxines dépendant du contact avec l'hôte. Elle possède également un mode de motilité spécifique aux surfaces appelé twitching. Ces trois exemples sont tous des adaptations physiologiques liées à une modification de l'expression génique suite au contact d'une surface.

Pour se mouvoir en surfaces, *P. aeruginosa* utilise de fins filaments extracellulaires appelés pili de type IV (TFP) qu'elle étend et rétracte pour se tirer vers l'avant. Outre la motilité, l'extension des TFP, leur attachement et leur rétraction sont nécessaires pour une réponse transcriptionnelle liée aux surfaces appelée mécanosensibilité. Un système à deux composants semblable à la chimiotaxie, appelé système Chp, est également le médiateur de cette réponse. Le système Chp activé régule à la hausse la transcription des gènes liés à la virulence, dont ceux impliqués dans la biogénèse des TFP. Cependant, on sait peu de choses sur la façon dont le système Chp est activé par les TFP, et sur la façon dont les TFP répondent à la mécanosensation.

L'objectif de cette thèse est de caractériser les mécanismes de mécanosensation chez *P. aeruginosa*. Pour y parvenir, il faut caractériser le signal d'activation mécanique généré par l'attachement des TFP. Ceci est un défi expérimental car les fibres TFP ne peuvent pas être imagées par les microscopes conventionnels. Dans cette thèse, je présente une approche de l'étude de la mécanosensation de *P. aeruginosa* en utilisant la microscopie à diffusion interférométrique (iSCAT)

que j'ai optimisée pour la détection in vivo des TFP sans marquage. Je montre aussi la puissance de l'iSCAT pour étudier le comportement dynamique des TFP sur les surfaces.

En combinant iSCAT et microscopie à fluorescence, j'ai suivi simultanément les protéines régulatrices intracellulaires et l'activité des TFP. Ces mesures, combinées avec la motilité individuelle des cellules et la localisation de protéines, ont mis en évidence des boucles de rétroaction entre les TFP et le système Chp qui sont essentielles à la motilité et à la mécanosensibilité. Ce système de rétroaction polarise les cellules et dirige le twitching, ce que nous appelons mécanotaxie.

Enfin, sur la base de nouvelles preuves biophysiques et structurales, je propose un modèle pour la mécanosensibilité par les TFP et le système Chp. Ici, mes données préliminaires montrent que les monomères de PilA qui sont désassemblés des TFP pendant la rétraction, interagissent avec le chimiosenseur de Chp, PilJ. En raison de l'attachement des TFP, le flux de PilA vers PilJ diffère en milieu liquide et en surface. Je propose un mécanisme dans lequel PilJ détecte ce déséquilibre de flux.

Mots-clés

Pseudomonas aeruginosa, iSCAT, Mécanosensation, Microscopie sans marqueurs, Pili de type IV, Système Chp, Mécanotaxie.

Contents

List of Figures

List of Supplementary Figures

List of Tables

List of Equations

To my wonderful daughter Naomi

Chapter 1.   Introduction

1.1 Motivation

Bacteria have evolved to adapt to a variety of environments, developing strategies to find nutrient sources and protect themselves from harmful conditions (*1*). How cells interact with their environment has been studied extensively with a focus on environmental signals that are chemical in nature. However, bacteria colonize a variety of environmental niches that differ widely from one species to another in their physical properties, going from deep waters to streams or even our own digestive tract. One common physical parameter of bacterial life is the transition between the planktonic and sessile lifestyle, as many bacteria explore their fluidic environments and make the decision to stay put.

Pseudomonas aeruginosa is an example of organism that has adapted to live on surfaces. *P. aeruginosa* is an opportunistic pathogen and a frequent agent of nosocomial infections that has developed resistance to most antibiotics (*2*). To enable plantonic to sessile transitions, it has several extracellular structures. This includes the flagellum, that it can rotate in order to swim in aqueous environment. In addition, *P. aeruginosa* can extend and retract another type of extracellular filaments called the type IV pili (TFP) that it uses to crawl on surfaces, in a type of motility called twitching. TFP also enable *P. aeruginosa* to sense surfaces, as they are required to increase the transcription of virulence genes upon surface contact (*3*). However, little is known on the mechanisms that allow TFP to participate into mechanosensing. Answering this important question will allow to target the development of new drug discovery to limit antibiotic resistance selection. In order to address this question, one must first have a clear understanding of how TFP behave on surfaces to better understand the input signal of mechanosensation.

The current limitation in the characterization of TFP as a motility and mechanosensing machinery is the lack of live visualization methods for such small diameters. Due to their small size (6 nm in width), TFP cannot be visualized with typical transmitted-light microscopy techniques and require the need of fluorescent labeling. However, pili labelling is a tedious process and likely damaging the pili

structures thus introducing a bias risk in the measurement of its dynamics. Moreover, recent labeling techniques require to introduce a cysteine mutation in the globular domain of the pilin thus increasing the odds to affect its activity. There is therefore a need to develop new live and label-free imaging techniques to better characterize TFP activity and its role in mechanosensation. To face these challenges and understand the contributions of TFP in *P. aeruginosa* mechanosensing, I managed to: 1) build an interference-based microscope for label-free visualization of TFP, 2) use this setup to characterize TFP dynamics and regulation in a process known as mechanotaxis, and 3) provide new elements that support a mechanism of mechanical activation of virulence in *P. aeruginosa*.

1.2 Background

1.2.1 Bacterial surface filaments

Bacteria have evolved many different cell surface structures in order to explore and colonize their environment. For example, flagella provide the bacteria a means of swimming in fluids. This mode of motility improves the ability of bacteria to find nutrients or to occupy new niches devoid of predators or other stressors. Therefore, swimming motility provides a strong fitness advantage to flagellated species. Many studies have examined the mechanisms of regulation and activity of flagella. Flagella rotate around its longitudinal axis, propelling the cell in medium (*4*). It is composed of membrane bound stators holding the rotor and extracellular components in place. Due to its intrinsic behavior and architecture, flagellum can be observed through fluorescence microscopy by direct labeling, without significant functional defects (*4*), but with limits of imaging frequency.

Other surface filaments include adhesins knowns as fimbriae or pili. This help bacterial cells secure themselves onto surfaces. For example, type 1 pili is short (no more than 3 µm), and promoted colonization of many environments, for example it helps *Escherichia coli* at adhering to biotic and abiotic surfaces (*5*, *6*). Other pili are more active as they not only extend from a cell surface but also retract. These provide bacteria with an alternative motility mode known as twitching (*7*, *8*).

1.2.2 Twitching motility

Twitching has been described as an intermittent and jerky movement on surfaces (*7*) that can occur in both flagellated and unflagellated bacteria. *P. aeruginosa* cells move through extension, attachment and retraction of polar TFP (*8*). Both types of motility seem to occur in a mutually exclusive way, where swimming inhibits twitching and vice versa (*9*). During twitching motility, bacteria can have two different behaviors. They adopt either a walking position where the cells stand on one pole and move randomly over the surface, or they crawl in a more stable direction by lying flat on the surface. Both behaviors depend on the activity of filaments known as type IV pili (TFP) whose activity powers single cell movements (*9*), **(Figure 1.1)**.
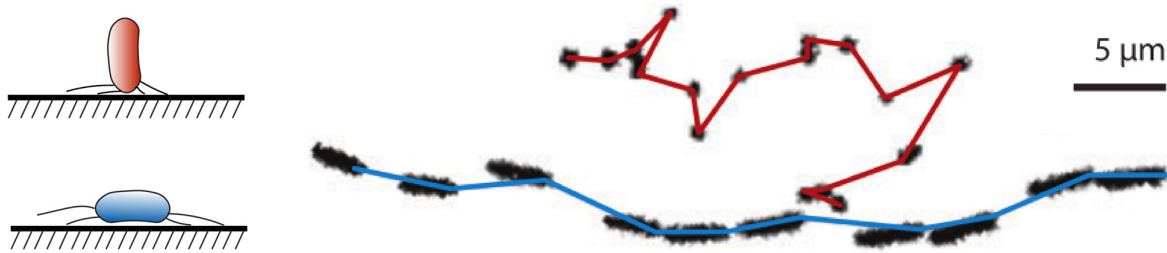
Figure 1.1: Behaviors in twitching motility in *P. aeruginosa*.

Cells can adopt either a walking (red) or crawling (blue) position. Crawling provide a more stable direction of movement while walking is more subject to direction changes and seem to be a random process. Adapted from L. Burrows, *Annual Review of Microbiology* 2012 (*9*)

1.2.3 Type IV pili

TFP are thin filaments no wider than 6 nm that can rapidly extend up to tens of microns outside the cell body before retracting. They are involved in attachment and cell motility on surfaces (*9*) as well as mechanosensing (*3*). TFP consist in a complex machinery, whose main component is the pilin subunit PilA. A platform protein PilC, located in the inner membrane, assembles the subunits. Elongation of the pilus is mediated by the pilin polymerase PilB and retraction is mediated by the pilin depolymerases PilT and PilU. The elongated pilus reaching the outer membrane is secreted in the extracellular space through the secretin PilQ. Stability of the structure is achieved by the protein complex PilMNOP that secure PilQ and PilC to the inner membrane and the peptidoglycan layer (*9*)

(**Figure 1.2**). The model organism that I studied in this project is the Gram-negative opportunistic pathogen *Pseudomonas aeruginosa* PAO1.

P. aeruginosa transitions from a planktonic state, where it freely swims as a single cell, to a surface associated sessile state, where it colonizes solid substrates and eventually creates cell communities in the form of biofilms. The switching between these distinct lifestyles is tightly regulated (*10*). *P. aeruginosa* is the major cause for nosocomial infections and is responsible for chronic infection in immunocompromised patients affected for example by cystic fibrosis. Moreover, *P. aeruginosa* is considered as a serious threat as it has acquired resistance to several antibiotics. This bacterium swims with one flagellum and expresses TFP at the poles in order to progress on surfaces. TFP have been shown to contribute to virulence.

1.2.4 Regulation of TFP activity

The transcriptional regulation and the assembly mechanisms of model piliated species has been vastly investigated and reviewed (*9*, *11–13*). In contrast, little is known about the orchestration of TFP extension and retraction, which take place on a much more rapid timescale of a few seconds. In *P. aeruginosa*, a chemosensory system called Chp has been shown to play a role in twitching motility regulation. Chp mutants have defects in twitching motility, but still have TFP (*11*). The Chp system is homologous to the canonical chemotaxis system regulating flagellar rotation (*14*). Therefore, the current hypothesis is that Chp participate in a chemotactic control of twitching. However, this hypothesis has never been confirmed as no chemical signal has been identified to activate Chp.

The Chp system is composed of a methyl-accepting chemotaxis-like protein PilJ that interacts with a histidine protein kinase ChpA homologous to *E. coli*'s CheA. Activated ChpA then stimulates (potentially by phosphorylation) two response regulators called PilG and PilH that share homology with the Che response regulator CheY. It has been hypothesized that these response regulators activate the extension and retraction motors: PilG may interact with the extension motor PilB and

PilH with the retraction motors PilT and PilU (*11*), (**Figure 1.2**). We will discuss in more detail the roles of PilG and PilH in chapter 4.
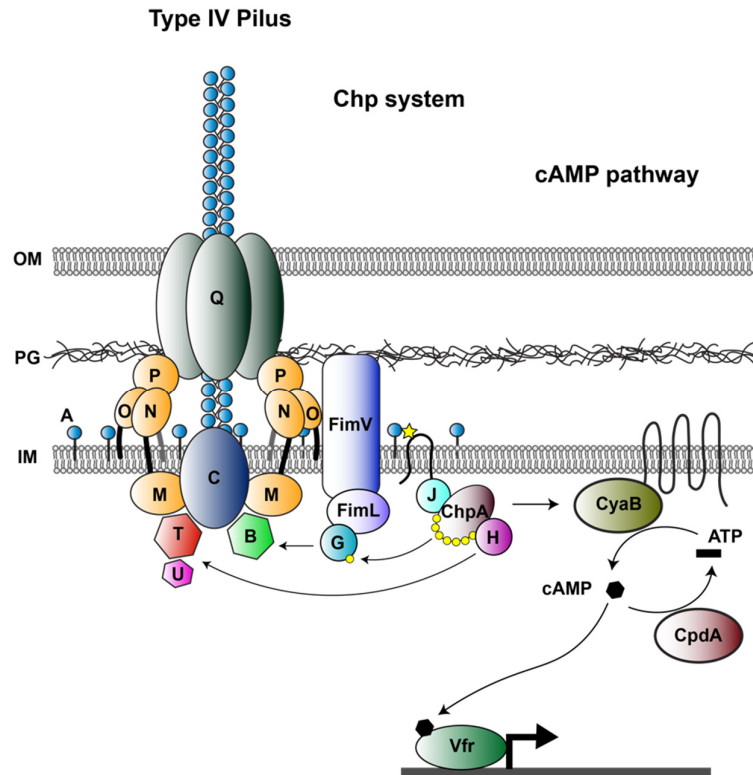
Figure 1.2: Architecture of type IV pili machinery and its interaction with the Chp system (homologous to the the Che system).

The pilin subunit PilA is assembled thanks to the platform protein PilC. PilB and PilTU are the polymerase, depolymerases respectively and are responsible for elongation and retraction of the pilus. The pilus is secreted through the secretin PilQ in the extracellular space. The complex PilMNOP provide stability and anchorage on the inner membrane and the peptidoglycan layer. An interaction between PilA and PilJ in the periplasmic space triggers autophosphorylation of ChpA, which in turns phosphorylate PilG and PilH. PilG interacts with the PilB polymerases and triggers pili extension whereas PilH interacts with PilT/U and triggers retraction. Somehow, the Chp system activates the adenylate cyclase CyaB that triggers the production of cAMP, CpdA acts antagonistically and degrade cAMP. cAMP binds to the Vfr transcription factor and initiate the transcription of many different genes such as virulence related genes.

1.2.5 *P. aeruginosa* transcriptionally respond to surface contact

P. aeruginosa had been hypothesized to sense surface contact. Genome scale transcriptional analysis showed that *P. aeruginosa* responds to surface contact by upregulating many genes (*3*). These include virulence factors under the control of the transcriptional factor Vfr. A transcriptional reporter for one of these genes, the PaQa operon, was used to show that cells respond to surfaces in minutes and in a manner that depends on the stiffness of the solid substrate (*3*) (**Figure 1.3**).

1.2.6 TFP and the Chp system regulate mechanosensation

A high throughput screen has identified the regulators of the PaQa upregulation on surfaces. These regulators include the adenylate cyclase CyaB, which converts ATP into intracellular cyclic AMP (cAMP). cAMP then activates the Vfr transcription factor responsible for the transcription of acute virulence genes and many other (*3*). cAMP levels later decay by increased activity of the phosphodiesterase CpdA which acts antagonistically **(Figure 1.2)**. In addition, this screen identified TFP and the Chp chemotaxis-like system as regulators of surface response. These observations and the fact that PilJ interacts with the PilA pilin subunit (*3*) suggest that a mechanical signal at the TFP level could be transduced directly to the Chp system. Unfortunately, multiple technical limitations are hampering our understanding of the Pil-Chp-dependent mechanosensing system.
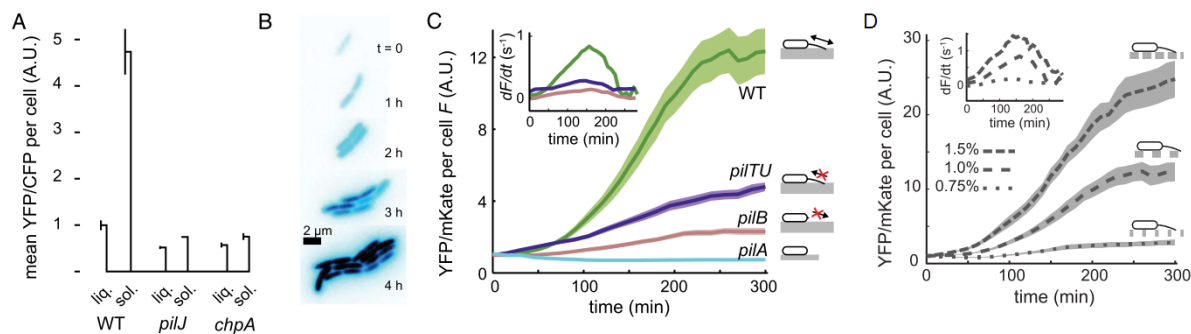
Figure 1.3: Type IV pili enable surface sensing in *P. aeruginosa*.

A) Mean intensity of PaQa-YFP reporter compared to base line (rpoD-mKate) in WT and in Chp system mutants. Chp mutants failed to trigger expression of the reporter. B) Increase in the intensity of the PaQa reporter over time when transitioning form liquid to agarose plate culture. C) Evolution of the intensity of PqQa-YFP reporter over time in WT TFP machinery and mutants (ΔpilA: no pili, ΔpilB: no extension but subunit production, ΔpilTU: no retraction but many surface pili). Compromised TFP function results in decrease cellular response. D) Cellular response quantified by the intensity of PaQa-YFP reporter related to the stiffness of the agarose hydrogel. Cellular response is directly proportional to the stiffness of the gel, confirming the involvement of TFP in mechanosensation. Adapted from Persat et. al, *PNAS* 2015 (3).

1.2.7 Visualization of TFP dynamics

TFP can easily be observed by electron microscopy, which has enabled the resolution of their overall structure (*15*, *16*). Through sensitive techniques such as cryo-electron microscopy (cryoEM), tomograms of the TFP machinery have highlighted structural and assembly characteristic of the

machinery (*16*) (**Figure 1.4**). However, electron microscopy does not allow observation of living cells and therefore prevent the study of the dynamics of these extracellular structures.
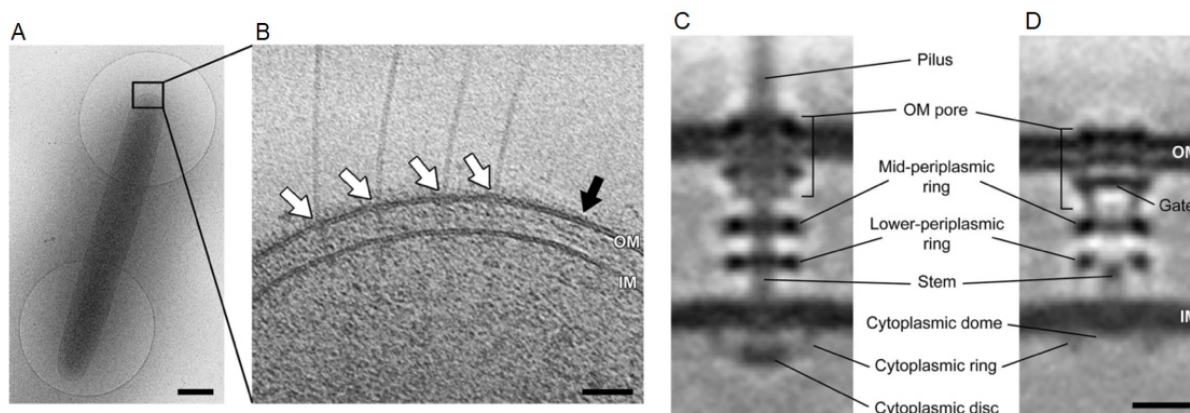
Figure 1.4: CryoEM Tomograms of type IV pili in Myxococcus xanthus.

A) EM view of M. xanthus, B) Zoom on polar region and visualization of 4 extended pili and one empty pilus machinery. C) TFP machinery with pilus. D) Empty TFP machinery. Adapted from Chang Y.W. et *al. Science* 2016 (*16*)

As TFP are too thin (5-6 nm) to be visualized through traditional transmitted light microscopy, live imaging remains quite challenging. Fusions of fluorescent proteins to the pilin subunit is invasive as label might partially interfere with the extension and retraction of the pilus. Non-specific fluorescent staining procedures using an amino-specific Cy3 fluorescent dye have partially solved this issue (*17*) as for the first time, extension and retraction of TFP could be observed in living bacteria (**Figure 1.5**). Labeling with synthetic fluorophores and visualization by TIRF microscopy demonstrated that pili extend and retract at similar speeds (0.5 µm/s). The same study reported the speed of twitching motility by recording the displacement of the cell body to be about 0.3 µm/s (*17*). Recently, Ellison et *al*. developed another technique to fluorescently label TFP of *Caulobacter crescentus* by generating a cysteine mutant in the globular domain of the pilin subunit that allowed subsequent labeling with a thiol-reactive maleimide dye (*18*, *19*). This labelling technique has now been translated to *Vibrio cholerae* (*20*) and *P. aeruginosa* (*21*). Other studies used bright-field microscopy to analyze cell body movements and showed the twitching speed to vary between constant slow speed of 0.3 µm/s and fast and brief (100 ms) events of motion at 1 µm/s (*22*). Theoretical models

attempted to explain how TFP may intervene in what has been called slingshot movements in twitching motility through a release and shift mechanism (*23, 24*). Moreover, biophysical properties of TFP such as retraction forces were indirectly observed through the use of optical tweezers (*25*) or atomic force microscopy (AFM) (*26*).
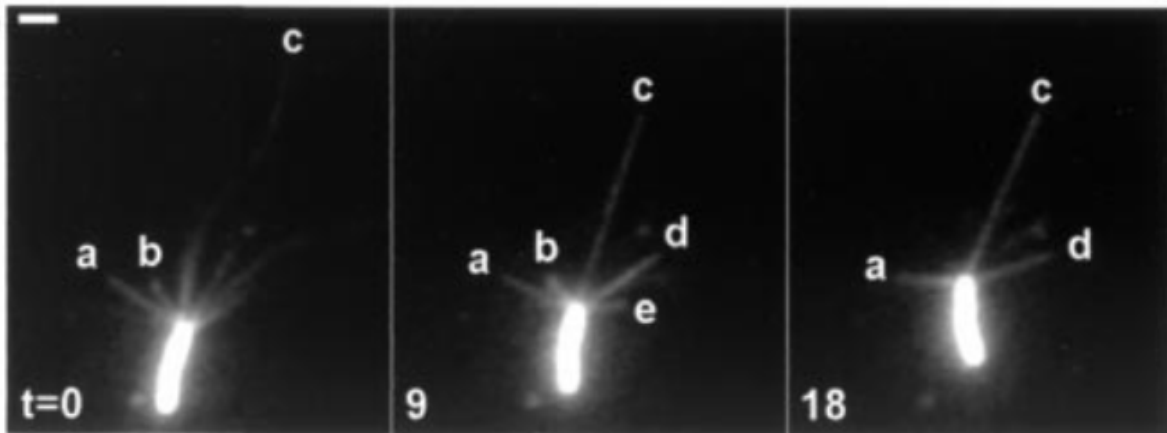
Figure 1.5: Extension and retraction of TFP inducing cell movement of *P. aeruginosa*.

Visualization of stained TFP dynamically extending (TFP e) or retracting (TFP b, c and e). Adapted from Skerker et *al. PNAS* 2001 (*17*)

However, the labelling procedure is tedious and possibly damaging the pili structure or involve to introduce mutations in the pilin structure. Labeling relies on recycling of pilin subunits which turnover and thus renders long dynamic visualizations difficult. In addition, little is known on the effect of the dye on the dynamics of the pili compared to unlabeled pilins and the introduction of a bias cannot be excluded.

To summarize, the state of the art in the visualization techniques for the study of twitching and TFP architecture include electron microscopy (*16*), bright-field (*23*), optical tweezers (*25*), fluorescence (*17*) and atomic force microscopy (*26*). These techniques bring answers to specific questions about pili structures and biophysical properties. However, with the exception of fluorescent labelling, they do not provide a means to study the dynamic of TFP through live imaging and more importantly without interfering with the TFP structure or dynamics.

1.2.8 Interferometric Scattering Microscopy (iSCAT)

To overcome the limitations of the current visualization techniques, and as real time dynamics could not be characterized by the above, there is a need to implement powerful label free imaging methods. Techniques based on scattered light such as dark-field microscopy allow visualization of small objects but only down to a diameter of 20 nm (*27*). As TFP are around 6 nm large, the scattered signal is not strong enough to have a decent contrast. This led us to interference-based microscopy.

1.2.9 Principle of iSCAT

Interferometric Scattering Microscopy (iSCAT) has been first implemented in the group of Vahid Sandoghdar (*28*, *29*) and further optimized by Phillip Kukura and his group in Oxford (*30*, *31*). It has been evolved from the Interference Reflection Microscopy (IRM) developed by Curtis in 1965 (*32*). I illustrate the principle of the technique in **Figure 1.6**.

A monochromatic beam of coherent light is sent through a high numerical aperture oil immersion objective and illuminates a sample in an inverted microscope layout. The reflection of the light caused by the difference of index of refraction at the glass-water interface is sent back through the objective. The transmitted light encounters the sample surface which has a different index of refraction than water resulting in scattering of the beam. The scattered and phase shifted light is harvested through the objective where it interferes with the back reflection of the glass-water interface, resulting in constructive and destructive interferences. **Figure 1.6** shows a schematic of the light interacting with the sample.
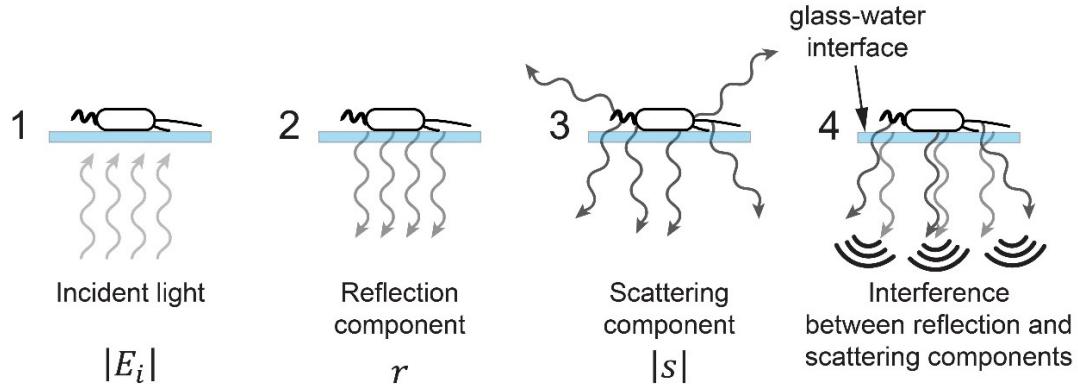
Figure 1.6: Schematic of the principle of iSCAT microscopy.

Reflected Light from the coverslip and scattered light from the sample interfere with each other to generate the iSCAT image.

The intensity of the light reaching the detector I_d can be defined by the following equation (*31*):

$$I_d \propto |E_r + E_s|^2 = E_i^2[r^2 + s^2 + 2r|s|cos\phi] \tag{1}$$

With E_r, E_s and E_i are the reference, scattered and incident electric fields, *r* denotes the amplitude of the reflected light by the glass-water interface, *s* is the complex scattering amplitude and Φ is the phase shift from the scattered light compared to the reflected electric field (*30*). When we observe particles that have a diameter much smaller than the used wavelength, *d << λ,* the scattering cross section σ_s can be defined by the Mie theorem as follows:

$$\sigma_s = |s|^2 \propto \varepsilon_m(\lambda)^2 \frac{\pi}{4} \frac{d^6}{\lambda^4} \left(\frac{\varepsilon_p(\lambda) - \varepsilon_m(\lambda)}{\varepsilon_p(\lambda) + 2\varepsilon_m(\lambda)} \right)^2 \tag{2}$$

with *λ:* illumination wavelength, ε_m and ε_p are the dielectric constant of the medium and the particle, *d:* the diameter of the particle (*31*). As $|s|^2$ becomes negligible for very small diameters, the Intensity equation 1 can be simplified as follows:

$$I_d \propto |E_r + E_s|^2 = E_i^2[r^2 + 2r|s|cos\phi] \tag{3}$$

In contrast with dark-field microscopy where the signal reaching the detector is dominated by the pure scattering term $|s|^2$ and is proportional to d^6, the iSCAT signal relates to the square root of the scattering cross section, which is proportional to d^3. This relation allows a better contrast for small particles compared to purely scattering techniques.

In this case the signal to noise ratio (SNR) is defined as the ratio of the Intensity of the signal over the background fluctuations (*30*):

$$SNR = \frac{I_{signal}}{I_{bkg}} = contrast\sqrt{N}$$

(4)

Where *N* is the number of photons detected by the camera. As all lasers are subject to shot noise, which correspond to the difference in the number of emitted photons at a certain time t compared to t+1, N differs from time to time and affect the SNR. In order to correct for this effect, the beam is scanned in X and Y by acousto-optic deflectors (AODs) at frequencies close to 100 kHz. By setting a difference in the X and Y scanning frequencies, one can scan a square region several times during the exposure time of the camera, thus averaging the number of photons hitting each pixel of the camera during acquisition (**Figure 1.7**).
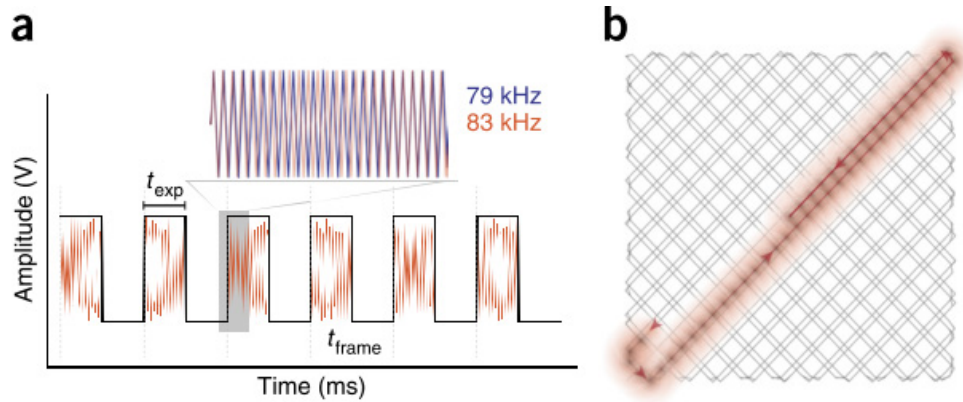
Figure 1.7: Example of synchronization of the AODs and the effect of scanning frequencies difference

Setting a scanning frequency of 79 kHz for X and 83 kHz in Y induces a squared illumination pattern at the objective front focal plane. The pixel of the camera will capture the photon coming from multiple scanning passages, thus averaging the shot noise. Adapted from Ortega Arroyo et *al. Nature Protocols* 2016 (*31*).

Laser scanning has an advantage over widefield illumination because it reduces ring artifacts and speckle patterns generated by the optical elements composing the objective (*27*). If the time of acquisition is short one can simply tune up the intensity of the laser in order to increase the number of photons reaching the camera during the scanning process, justifying the need of high-power lasers.

The separation of the illumination and the imaging path is simply done with a polarizing beam splitter (PBS) and a quarter-wave plate. The illumination beam being s-polarized is reflected by the polarizing beam splitter and get circularly polarized by the quarter wave plate before entering the objective and interacting with the sample. The reflected and scattered light sensed by the objective goes back through the quarter-wave plate resulting in a 90° shift in polarization thus becoming p-polarized. P-polarized light is transmitted by the PBS and sent to the camera (*31*) (**Figure 1.8**).
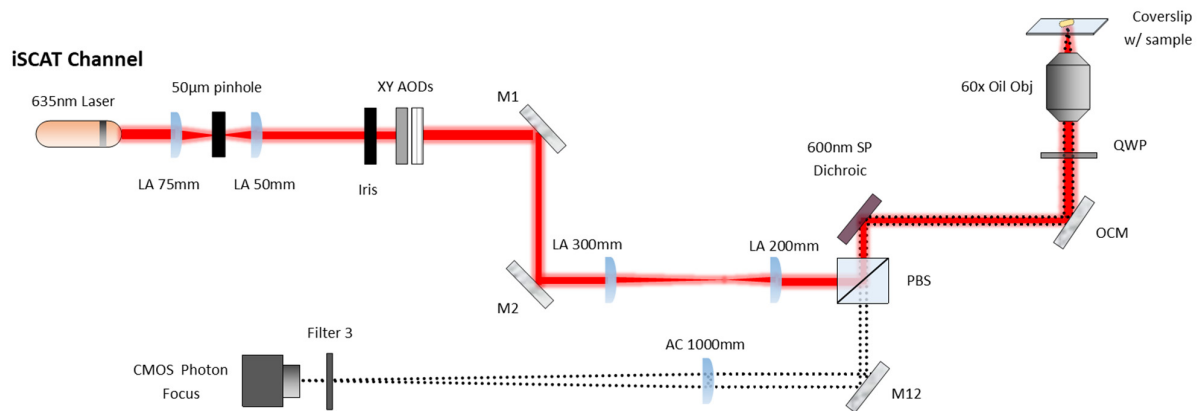
Figure 1.8: Schematic of a typical iSCAT setup as explained by Ortega Arroyo et *al. Nature Protocols* 2016 (*31*)

1.3 iSCAT sensitivity

iSCAT has been developed to detect single particles in vitro down to few nanometers in diameter without the need of labels. To reach such sensitivity, one can play with several parameters that will enhance the contrast between the sample and the background. 1) iSCAT is a shot noise-limited detection, which results in a signal to noise ratio (SNR) for interferometric signals being proportional to $\sqrt{N}$, with *N* being the number of photons detected (*33*). This suggest that increasing the power of

the laser, or increasing the exposure time will result in stronger contrast. 2) Increasing the scattering signal emanating from the particle of interest will also improve the contrast. This can be achieved by carefully choosing an appropriate laser wavelength. In fact, the scattering cross-section of the particle depends on its diameter and the inverse of the wavelength as seen in equation (2) (*27, 31*):

Therefore, choosing a small wavelength will enhance the scattering properties of the particles and therefore the overall quality of the images. This is why most of the latest publications on iSCAT single particle tracking or label-free detection of proteins (*34–36*) use a laser source of 445 nm. However, the Planck equation says that the energy of a photon is inversely proportional to the wavelength

$$E = \frac{hc}{\lambda}$$

(5)

where h is the Planck constant, c is the speed of light in vacuum and λ the light wave length. Therefore, a small wavelength will have a strong scattering property and a higher power.

Because we want to use iSCAT to image living organisms which are subject to phototoxicity, we need to optimize the wavelength to use in the iSCAT channel and also how we image our samples in order to reduce light exposure on the sample. This optimization will be discussed in Chapter 2.

1.3.1 Applications of iSCAT

The technique has been used to study nanoscale protein dynamics such as actin-myosin interactions (*35*), microtubule (*37*) and actin (*33*) assembly, viral particles dynamics (*38*) and lately mass photometry (*34*). These observations show the power of iSCAT for studying biological processes at the nanoscale level (**Figure 1.9**). The technique has been optimized lately to detect mass of purified proteins down to 20kDa (*34*).
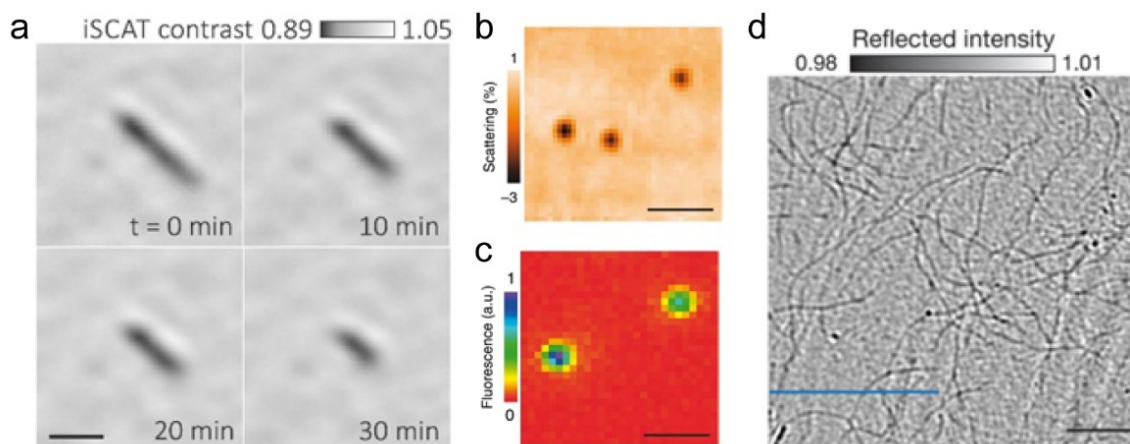
Figure 1.9: Examples of iSCAT images.

a) Evolution of a microtubule degradation Andrecka et *al. Biophysical Journal* 2016 (*37*). b) and c) iSCAT visualization of SV40 viral particles (b) and corresponding fluorescence image (c) Kukura et *al. Nature Methods* 2009 (*38*). c) Actin filaments attaching on the glass coverslip Ortega Arroyo et *al. Nano Letters* 2014 (*39*)

Actin filament, which are approximately 7 nm in diameter and micrometers in length, are similar in size to TFP and can be easily observed through iSCAT (**Figure 1.10**). Therefore, we thought that we could use this visualization technique to image TFP in living bacteria.

1.4 Organization of the thesis

The thesis is organized in 4 main chapters:

In chapter 2, I show how I implemented iSCAT microscopy to visualize TFP without the need of labels. This chapter provides a technical description of iSCAT customization and optimization that ultimately allowed us to perform label-free imaging of TFP in a variety of microbial species.

In chapter 3, I showed how we discovered a new aspect of TFP dynamics that is critical to its function. Using iSCAT microscopy, I demonstrated that TFP dynamics of extension and retraction are highly coordinated events. Namely, I showed that TFP retraction is stimulated by surface attachment.

In chapter 4, I focus on the mechanical regulation of twitching motility. To do this, we investigated the collective regulation of successive TFP extension/retraction events. I demonstrated that

P. aeruginosa actively directs twitching in the direction of mechanical input from TFP, in a process we called mechanotaxis.

In chapter 5, I sought to decipher the mechanisms by which TFP transmit a mechanical signal to the Chp system and how the Chp system transduces this signal into a cellular response. In this part, I explored several hypotheses that could explain how TFP activate the Chp system through its methyl accepting chemotaxis protein PilJ. A first hypothesis consists in a mechanically-induced conformational change that my results disprove. A second hypothesis consists in a TFP-attachment dependent change of intracellular PilA concentration, which is consistent with my results.

In the last chapter I will discuss the implications of the main findings arising from my research and provide insights on future work.

Chapter 2.   Live cell imaging with Interferometric scattering microscopy

Here we present the adaptations we implemented in our iSCAT setup that enabled live-cell imaging with high sensitivity.

2.1 Optimizing iSCAT for live-cell imaging

2.1.1 Compatibility with live cell imaging.

The contrast provided by iSCAT microscopy is based on the principle of interference between the scattered light coming from a sample and the constant back reflection of the glass-water interface of the coverslip (see General Introduction about **the physical principle behind iSCAT**). This intrinsic property allows to image molecules for extended times without the issue of photobleaching due to the fact that iSCAT is completely label-free. Moreover, iSCAT allows the detection of particles far below the diffraction limit (~250 nm) down to a few nanometers. As mentioned above, SNR in iSCAT images depends on $\sqrt{N}$, with N being the number of detected photons. This means that the detection of small particles can be improved if more photons are sensed by the detector. One could theoretically image purified proteins in vitro for an unlimited amount of time and with high laser power but there are physical limitations such as sample or optical damage and dynamic range of the detectors (*27*). This is even more important when observing living cells as exposure to high intensity light for extended periods of time induces phototoxicity which results in cell death. These conditions create a trade-off between detection quality and sample damage.

We discussed previously that a small wavelength will provide higher scattering and higher energy. Thus, a high energy wavelength will potentially generate more cell damage. Therefore, to minimize phototoxicity, we based our optical layout on Ortega Arroyo et *al.* (*31*) and used a red laser (638 nm) for our iSCAT channel.

Further, we aimed at reducing phototoxicity by limiting illumination to the time of data acquisition. This can be achieved by 1) switching the laser on and off, or 2) blocking the laser from reaching the

sample by placing a controllable shutter in the light path. We thoroughly tested each of these methods. First, we measured the mean intensity of iSCAT images when we switched on the laser during acquisition. Switching on the diode laser resulted in a peak in intensity that slowly decreased to reach a stationary value after roughly 300 ms. This intensity peak was detrimental to the quality of the iSCAT images and therefore would need to be avoided by delaying acquisition by at least 300 ms after switching on the laser (**Figure 2.1**). This delay time would therefore contribute to longer exposure at an increased intensity. Second, we setup a shutter in the iSCAT illumination light path by modulating acousto-optic deflectors (AOD) scanning. We measured intensity profiles during shutter opening. When looking at the intensity profile of the blocked beam, we measured an instantaneous increase to the target intensity which remained stable over time. Therefore, we decided to block the iSCAT beam by controlling the output of the AODinstead of modulating the power output of the diode laser. We thus implemented this in the iSCAT microscopy control setup. We designed a computer-controlled actuator to enable the activation of the output of the AODs automatically prior to image acquisition in the LabView acquisition software (*40*).
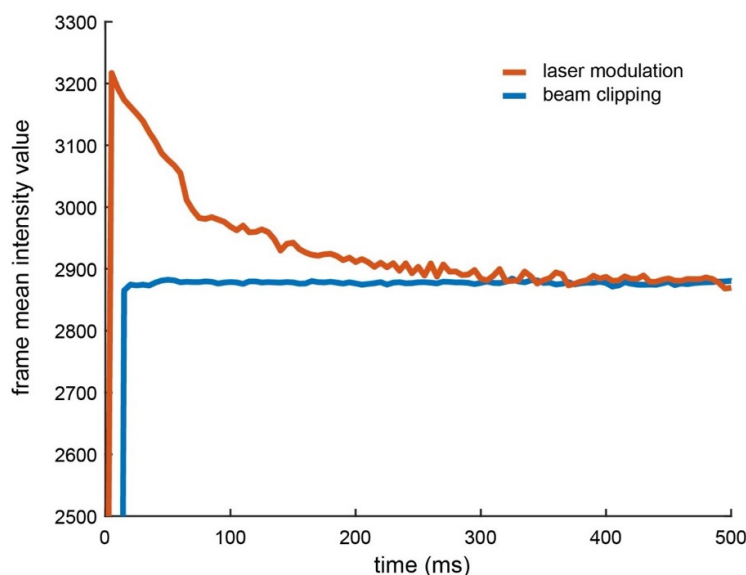
Figure 2.1: Detected laser intensity using different engineering strategies to control the iSCAT illumination path.

Mean pixel value of iSCAT images when switching on the diode laser (red) or opening the shutter (blue). Red: laser modulation resulted in an initial peak intensity that slowly decayed to a stable value after 300 ms. Blue: unblocking the beam by opening a shutter resulted in an instantaneous intensity change to a stable value, indicating that blocking the beam is a better strategy.

2.1.2 Implementation of an optimized autofocus system minimizing cell damage

Another important parameter affecting iSCAT image quality besides laser stability is to suppress mechanical vibrations that will induce noise (*27*, *31*). Mechanical vibrations can cause changes of the sample-objective distance which impacts the light path and therefore the interference intensity. Therefore, to stabilize sample-objective spatial distance we implemented a system that detects any z-drift and corrects for it. When a change in z-position is detected, a compensatory signal is send to a piezo actuator in order to correct for the z-drift and stabilize the z-position to the preset value (*41*). However, in contrast with Ortega Arroyo et *al*. (*31*), that used a 462 nm laser which is too energetic, we used a infra-red laser (850 nm) with minimal power (few hundred microwatts) thus minimizing phototoxicity (*40*).

2.1.3 Final experimental setup

Our experimental setup is described in Talà et *al.* (*41*) and further improvement are presented in Kühn and Talà et *al.* (*40*) (**Figure 2.2**). Briefly, the iSCAT illumination beam was spatially filtered through a 50 µm pinhole and collimated with a 4*f* lens system prior to enter into two perpendicular acousto-optic deflectors (AODs), (AA Opto-Electronic, DTSXY-400-660) the diffraction pattern, with order 1,1, was then imaged into the back focal plane of the objective (Olympus, PLAN APO 60x 1.42) thanks to a 4*f* lens system, a polarizing beam splitter (PBS) (Thorlabs, PBS251) and a quarter-wave plate (QWP) (Thorlabs, AQWP05M-600). The AODs allowed in-plane scanning of the beam on the sample. The objective captured the light scattered by the sample and the reflection of the incident beam at the glass-water interface. QWP and PBS discriminated input illumination from the reflected and scattered light. A 1000 mm focal length achromatic lens imaged the back focal plane of the objective onto a CMOS camera (PhotonFocus, MV1-D1024E-160-CL), yielding a 31.8 nm pixel size. Images were acquired using LabView and a frame grabber (National Instruments, PCIe-1433). We blocked the iSCAT illumination path to prevent unnecessary illumination by modulating the output power of the ADOs through the acquisition software.

We implemented a bright field channel by adding a white LED (Thorlabs, WFA1010) above the stage and imaged the back focal plane of the objective on a CMOS camera (PointGrey, GS3-U3-23S6M) with a 400 mm focal length achromatic lens (pixel size of 43.95 nm) (*41*). The bright field channel allowed to visualize and select cells of interest in a phototoxic free environment prior to acquiring iSCAT movies.

In order to simultaneously visualize fluorescently labelled proteins, we implemented a fluorescence channel by coupling a blue laser with a wavelength of 462 nm (Lasertack, LDM-462-1400-C) to the BF detection path with a 490 nm long pass dichroic mirror (Thorlabs, DMLP490) and to the iSCAT with a 600 nm short-pass dichroic mirror (Edmund optics, 69-204). The laser was focused on the back focal plane of the objective with a plano-convex lens (f = 500 mm, Thorlabs, LA1908-A). The fluorescent signal was then focused onto the same BF camera with the 400 mm focal length achromatic lens and a GFP filter (CWL = 525 nm, Bandwidth = 39 nm, Thorlabs, MF525-39). A computer-controlled shutter was placed in the illumination path of the fluorescence channel in order to prevent unnecessary illumination (*40*).
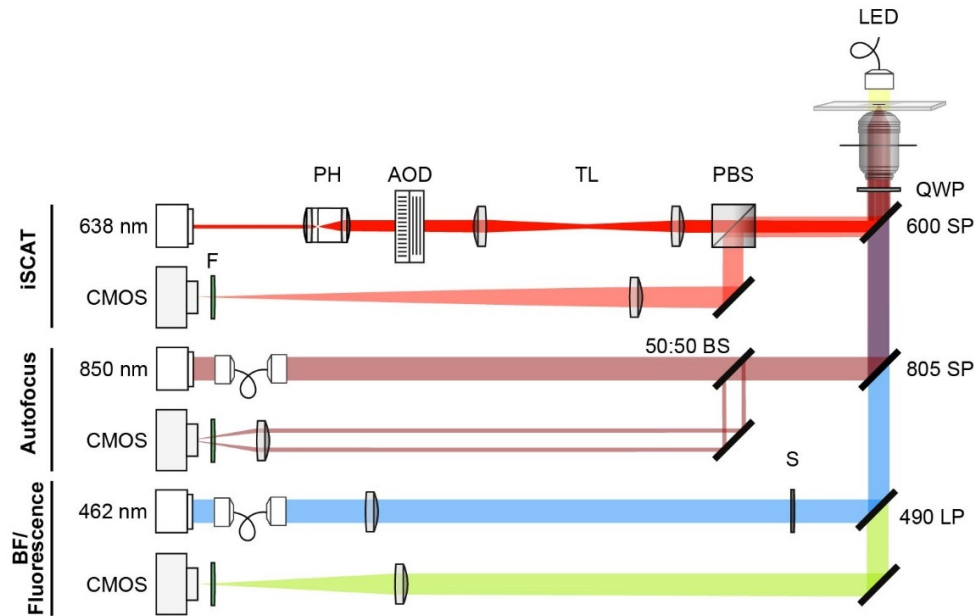
Figure 2.2: iSCAT optical layout developped in our lab.

My iSCAT setup optimized for live cell imaging includes a red laser for the iSCAT channel, an infrared laser for the autofocus system and a brightfield chanel coupled to a green fluorescenc channel. BS: beam splitter, SP: shortpass dichroic mirror, LP: longpass dichroic mirror, F: filters, PBS: polarizing beam splitter, S: shutter, QWP: quarter wave plate. Adapted from Kühn and Talà et *al. PNAS* 2021 (*40*).

2.2   Development of an iSCAT image processing pipeline

The iSCAT signal reaching the detector has two contributions: the strong constant back reflection of the glass-water interface, and the weak interference between reference and the scattered light of the sample (*27*, *30*, *31*). In order to isolate the interference signal, we used several image processing strategies, all aiming at removing the constant back reflection from the raw images.

2.2.1   Temporal median filtering

The back reflection of the glass-water interface remains constant throughout the acquired movie. As a result, it can be isolated by extracting all static features of an acquired movie. We achieved this by generating an image representing the median pixel value for the duration of the movie, providing a temporal median for each pixel. We then divide each movie frame by the temporal median image yielding a median-normalized movie revealing the interference patterns. As a final step, we applied a band pass filter dampening the contributions of small and large structures (smaller than 1 pixel and larger than 13 pixel) with the FFT plugin of ImageJ (*41*, *42*). To further normalize the movie due to some background artefact coming from the FFT, each frame is divided by its mean pixel value (**Figure 2.3A**).

This strategy significantly improves image quality and yields optimal image contrast of extracellular filaments of bacteria. While, this method is best for static or fast-moving cells, it will generate ghost artifacts coming from all features that remained at the same location for more than half of the movie length (**Figure 2.3B**). If a cell stays at the same location, the ghost will not be visible as it will be aligned with the cell body. Similarly, if a cell moves fast enough the median value of the pixel forming its cell body will have a median value matching the background noise. However, the artifact (yellow arrows in **Figure 2.3B**) arises for slow moving cells, or for cells remaining at a specific location for more than half the acquisition time. The same artifact can be observed for static extracellular filaments that would stay at one location of more than half the movie time. This will result in biased images not reflecting the ground truth of extracellular filaments behavior.

In some cases, like the one explained above, we can use other image processing techniques that we developed or adapted from previously published iSCAT protocols (*39*).
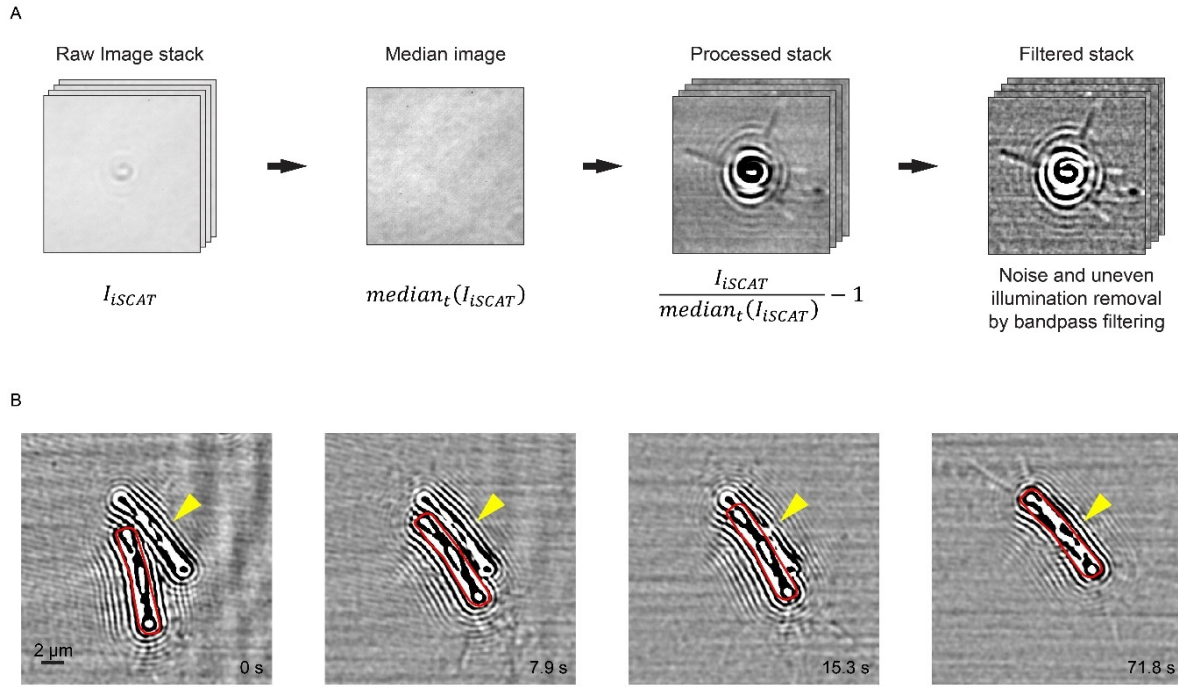
Figure 2.3: Image processing steps in temporal median filtering and remaining artifacts

A) Temporal median filtering allows to effectively isolate interference patterns from iSCAT images. A median image is generated from a movie stack by computing the median value in time of each pixel of a frame, thus isolating the constant feature of the image (back reflection of glass-water interface and background noise). Each movie frame is divided by the median image and further band pass filtering and background intensity normalization yield a high contrasted image of extracellular filaments visible in the raw images. B) Ghost artifact appearing on each frame of the movie (yellow arrow head). The cell (delimited by a red contour) moves from frame 1 to frame 4 until it reaches a stationary position for more than half the movie frames.

2.2.2 Differential filtering

When "ghost" artifacts prevented analysis of a movie, we applied a differential image processing method that consists in computing the difference between frame n and frame n-1 to generate a differential stack. The resulting frames are then composed of only the features that moved between two consecutive frames (*34*) (**Figure 2.4A**). Applying a further band pass filtering as in the previous method, removes unwanted large and small features. The advantage of this method is that ghost artifacts can be removed efficiently, however, static features will be removed as well. This results in extracellular filaments disappearing and reappearing during the movie as they tethered on the glass

surface. Outcomes of applying different processing strategies are depicted in **Figure 2.4B.** An iSCAT image of a cell processed with temporal moving filtering shows many tethered TFP (yellow arrow heads). The same image processed with differential filtering doesn't show tethered TFP but shows the floating one with better contrast instead.

A

B
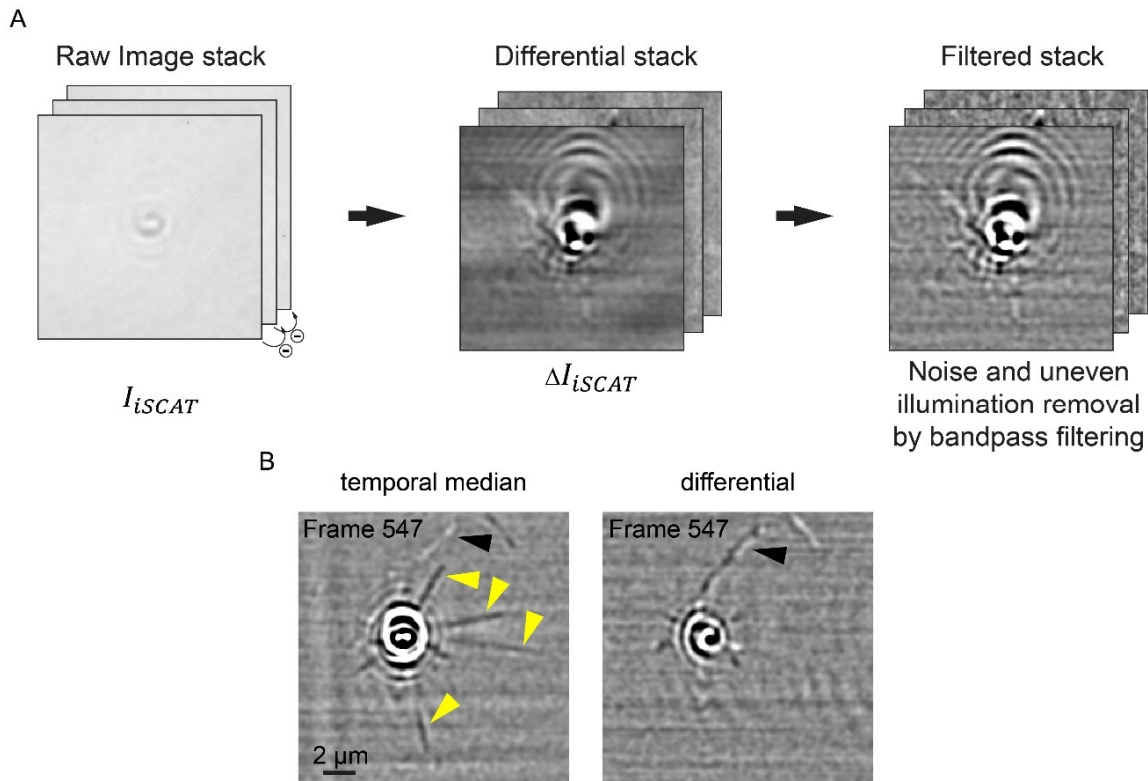
Figure 2.4: Image processing using the differential method and it comparison to the temporal median method

A) Differential stacks are obtained by subtracting each frame by the previous one. Further improvement is achieved by processing the stack by band pass filtering as described in temporal median or differential filtering. B) Comparison of a cell filtered with temporal median filtering (left) and differential filtering (right). The temporal median filtered image (left) shows tethered TFP (yellow arrow heads) and some faint free pilus floating around the cell body (black arrow head). Right: the same cell processed with differential filtering. The tethered TFP could not be observed anymore as it was removed by differential processing. However, the free floating TFP is highlighted with a better contrast (black arrow head). This shows that differential filtering allows detection of objects in motion.

2.2.3 Temporal moving average and moving median filtering

Lastly, the two additional methods that I developed consist in applying the same principle of the temporal median filtering method on substacks from the entire movie. For example, for a movie with 10 frames, a substack can be generated using 3 consecutive frames (N_{-1}, N, N_{+1}), a corresponding reference image (being the median or the average image of the substack) can be computed by which the central frame (N) can then be divided. By repeating this process for all the frames in the movie and doing a mirror padding for the first and last frame we can therefore generate a temporal moving median or averaged stack (**Figure 2.5**). As we use neighboring frames to generate the reference image, optimizing the parameters allows to reduce ghost artifacts. A parameter influencing the quality of the filtered image is the window size used to generate the moving median or average image. Taking a smaller window size will result in differential filtering, thus removing constant features from the image and selecting for moving features. On the other hand, a large window size may result in temporal median filtering by generating ghost artifacts. Fine tuning the window size allows to maximize interference image quality. While these methods provide a great flexibility for filtering raw iSCAT images it increases computing time. For a movie of 3,000 frames, computing time could last 15 min limiting its flexibility. Nonetheless, this approach proved valuable for the analysis of pre-selected movies that yield poor image quality with the other methods.
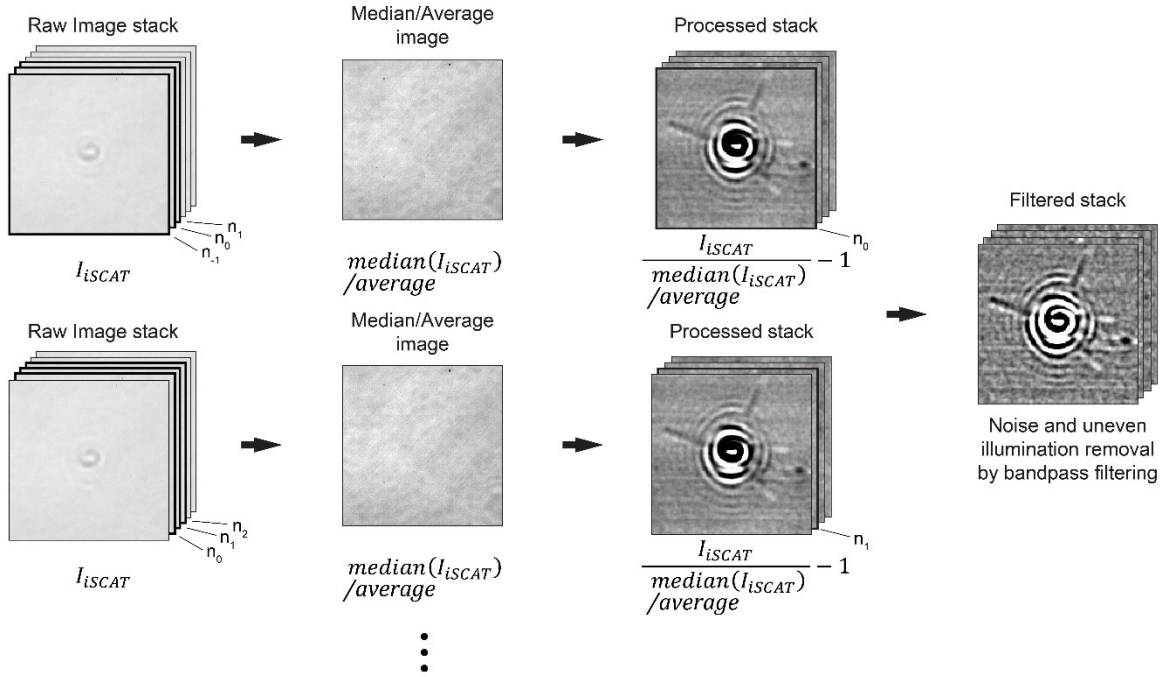
Figure 2.5: Algorithm for temporal moving median and moving average filtering

The algorithm loops over all frames of a movie. A window size defined by the user allows to create iterative substacks centered on the frame of interest. A median or averaged reference image is generated from the substack. The frame of interest is divided by the reference image like in the temporal median filtering method. This process is repeated for all frames of the movie. For the first and last frame of the movie a mirror padding is used to generate the substacks. Finally, we apply a band pass filter and normalize the background as for temporal median filtering.

2.2.4 Summary

I have implemented 4 different ways of extracting the interference signal from iSCAT images. The methods can be used in different situations depending on the motility of the cells and the type of measurement one wants to extract from such images (stationary vs moving features). In most cases the temporal median filtering is sufficient to generate high contrasted images and remained the preferred method for iSCAT images analysis.

2.3   Application of iSCAT in live cell imaging

2.3.1   Imaging extracellular filaments in *P. aeruginosa*

Due to its sensitivity, iSCAT enabled detection of filaments 5 nm in width, such as actin filaments in vitro which could not be resolved in conventional diffraction-limited microscopy without the need for labeling [39]. *P. aeruginosa* uses TFP which extend and retract sequentially to pull themselves along surfaces [17]. TFP are similar in size compared to actin filament (5-6 nm) [15, 43] and thus cannot be resolved in brightfield microscopy. Labeling of TFP with fluorescent dyes allowed to observe some dynamic behaviors. However, fluorescence comes with its limitation such as photobleaching and the need to alter the native structure of filaments to allow labeling [21] which may interfere with their native dynamics. In fact, the cysteine-based labeling methods cannot be easily applied to any bacterial (or even archaeal) species without completely abolishing the ability to make pili. For these reasons, iSCAT has the potential to be a more versatile technique for the visualization of surface filaments in live cells.

P. aeruginosa, like many other bacteria, has another extracellular structure that it uses to swim in aqueous environment called the flagellum. Flagella are approximatively 30 nm in width similar to microtubules. Rotation of the flagellum produces a drag force propelling or pulling the bacterium forward or backward depending on the direction of rotation. It has been extensively studied using both label free techniques such as darkfield microscopy and label-based techniques, such as fluorescence microscopy, in order to study its dynamic properties [44, 45].

We thus used iSCAT to visualize these slender structures. We imaged WT *P. aeruginosa* PAO1 strain that was growing exponentially in liquid culture using simultaneous brightfield and iSCAT imaging. We were able to detect two distinct extracellular filament structures. Long thin and homogenous filaments and patchy structured filaments with alternating black and white intensity along the longitudinal axis. We identified the latter as the flagellum. Due to the helical architecture of the flagellum the interference pattern created by the iSCAT signal will vary from a black image contrast for particles close to the coverslip to white contrast from particles far from the coverslip.

Therefore, we could identify the thin homogenous structure as TFP and the patchy structure as the flagellum (**Figure 2.6**) (*41*).
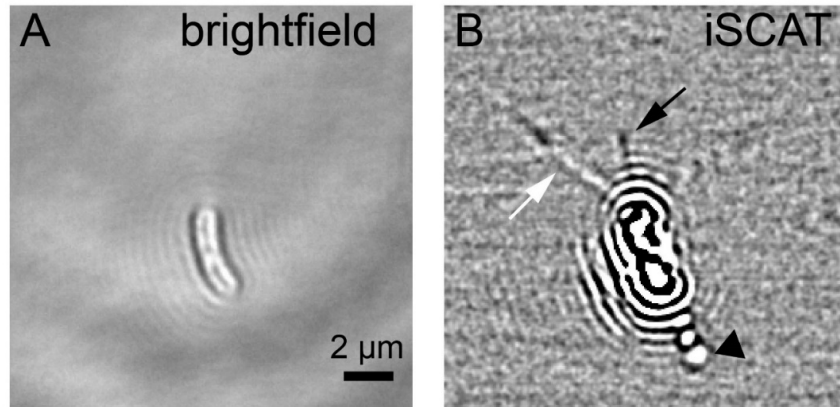
Figure 2.6: Simultaneous visualization of a WT *P. aeruginosa* cell with brightfield microscopy and iSCAT microscopy A) Brightfield view ow a WT *P. aeruginosa* PAO1 cell. No extracellular filament could be observed. B) the same cell visualized with iSCAT microscopy. Tethered TFP are shown with a black arrow, free TFP are shown with a white arrow and the flagellum is shown with the black arrow head. Scale bare in A) is the same for panel B). Adapted from Talà et *al. Nature Microbiology* 2019 (*41*)

The visualization and characterization of TFP by iSCAT microscopy will be addressed in more details in chapter 3. Therefore, in this chapter, we will manly focus on visualization of the flagellum and what type of information we can extract from iSCAT images.

P. aeruginosa has one single flagellum at one pole which it uses to swim in aqueous environment in order to find nutrients or escape from predators. From our images we can clearly distinguish an oscillating contrast along the fiber. We could then extract the handedness of the flagellum. In **Figure 2.7A**, we can see the helical shape of the flagellum where the alternating contrast patterns have inverted angles compared to the longitudinal axis. The white pattern which represent the filament going away from the coverslip has an angle α of -38° from the longitudinal axis whereas the dark pattern representing the filament getting closer to the coverslip has an angle β of +38° from the longitudinal axis. As iSCAT is built in an inverted microscope configuration, this suggest that the cell in **Figure 2.7A** has a left-handed flagellum, which is in line with reported flagellar handedness for *P. aeruginosa* (*46*). From high frame rate movies (300 fps) we could also extract the helical pitch and

the wave front displacement by generating a kymograph along the flagellum axis (**Figure 2.7B**). Our observations show that we could find an helical pitch of 1.4 µm (*41*), similar to reported values for *P. aeruginosa* (*46*), and a wave front propagation speed of approximatively 50 µm/s. These preliminary results show that iSCAT could be used to assess biophysical properties for the flagellum of bacteria without the need for labels.
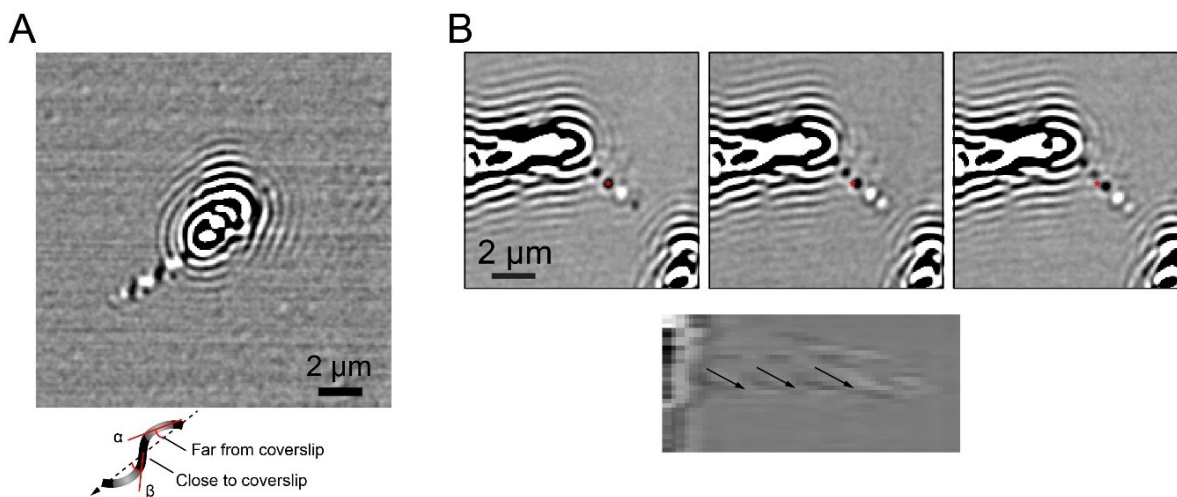
Figure 2.7: Flagella measurements of handedness and wave front speed

A) Image of a left-handed flagellum of *P. aeruginosa* PAO1 cell with helical pitch of 1.41 µm. A schematic drawing of the flagellum shows the different angles α and β (red lines) generated by the helix compared the longitudinal axis (dashed arrow) B) Top row: time-lapse images of a wave front propagation along the flagellum. Red star indicating a reference point. Bottom row: Kymograph along the flagellum seen on the pictures above. Arrows show the direction of the wave front which slope represent the speed of propagation.

2.3.2 Visualization of the archaeon *Haloferax volcanii*

To demonstrate the versatility of iSCAT microscopy. we imaged surface filaments of a variety of microorganisms. Thanks to a collaboration with Sonja-Verena Albers from University of Freiburg we were able to image *Haloferax volcanii*. This archaeon was isolated from the Dead Sea and lives in high salt concentration with temperatures of 42-45 °C. *H. volcanii* possesses an extracellular filament used to swim called the archaellum. However, its biological structure is more closely related to bacterial TFP than bacterial flagella. *H. volcanii* can also form TFP which they can extend out of the cell body.

In order to visualize *H. volcanii* cells we built a heating chamber for the iSCAT as these archaea swim when growing at 42-45°C. Our custom-made heating chamber uses high power resistors as heating modules and monitor the temperature with a temperature sensor. We measured and controlled the current passing through the heating modules with an Arduino. The heating chamber itself was laser cut in transparent acrylic and further insulated using aluminum foil and polystyrene panels (**Figure 2.8**). With this setup, we were able to reach 42°C in the chamber allowing the cells to swim and grow naturally.
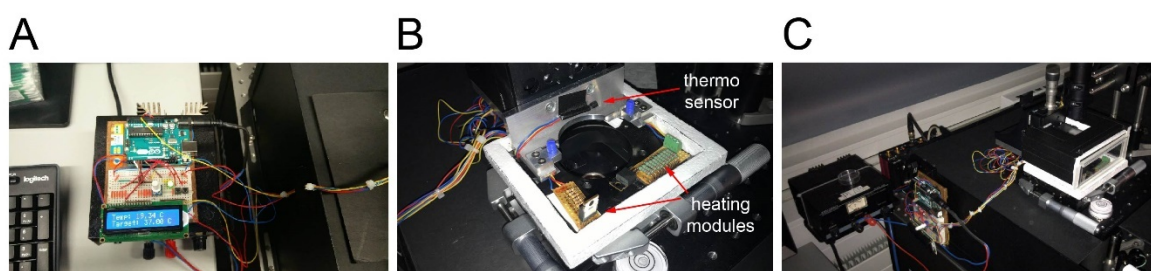
Figure 2.8: Heating chamber made by me for *H. volcanii* visualization with iSCAT microscopy

A) View of the Arduino control panel where the user can set the desired temperature. B) View of the heating modules made with high power resistors and positioning of the thermo sensor for power regulation. C) View of the insulated heating chamber assembled on the iSCAT stage.

iSCAT images revealed two distinct extracellular filament structures as for *P. aeruginosa,* but with slight differences. When TFP from *P. aeruginosa* form long and relatively straight filaments, TFP from *H. volcanii* are more flexible as observed by their stronger curvature. The archaellum appears patchier and more flexible as well (**Figure 2.9***A*). We generated a kymograph from one rotating archaellum and could compute a wave front propagation speed of about 22 µm/s (**Figure 2.9***B*). Furthermore, we could not observe any retraction in the TFP of *H. volcanii* suggesting that *H. volcanii* uses these structures mainly for surface or cell-cell adhesion. Altogether, these visualizations show the power of iSCAT in revealing extracellular filaments in exotic microorganisms that are hard to manipulate genetically and physically, and that environmental control such as high temperature can be implemented on our setup.
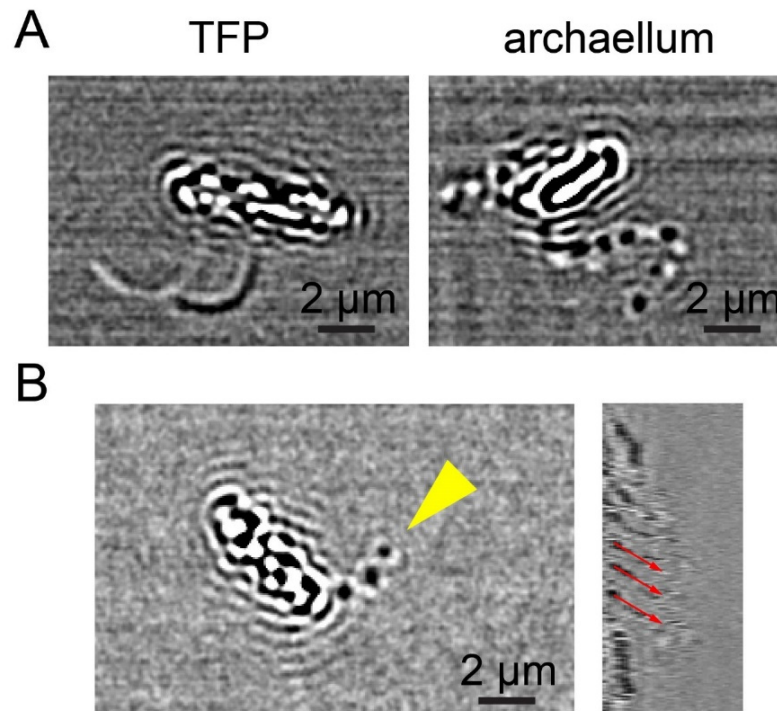
Figure 2.9: Extracellular filaments of *Haloferax volcanii* seen through iSCAT microscopy.

A) TFP of *H. volcanii* bend more easily compared to P. aeruginosa but they cannot retract. The archaellum shows more flexibility as well. In the right picture we see an archaellum forming a tight loop while the tip is attached to the coverslip. B) Picture of a *H. volcanii* cell with a rotative archaellum (yellow arrow head). The corresponding kymograph is shown on the right picture. Red arrows represent various speed measurements of the wave front propagation.

2.3.3 Detecting phage and TFP interaction with live-cell iSCAT microscopy

iSCAT had been previously used to visualize and track viral particles in three dimensions (*38*). The high sensitivity of iSCAT and the label-free method of detection allowed to track the center of mass of a simian virus 40 (SV40) of 45 nm in diameter with high temporal resolution. However, the setup used for viral particle detection included a 532 nm green laser with higher Rayleigh scattering properties than our 638 nm laser. We were therefore curious to see how well our setup could detect viral particles in the scope of phage infection of *P. aeruginosa* during live-cell imaging.

P. aeruginosa can be infected by many phages that use TFP as a receptor. These phages leverage TFP retraction as a means of bacterial entry. To visualize this, we grew WT cells to exponential phase and inoculated them with the lytic phage Luz19 (*47*) of approximately 50 to 60 nm in size that

is known to bind to TFP and infect cells due to TFP retraction. After 1h incubation at 37°C we were able to see a bursting cell and its consequent release of many particles including phages (**Figure 2.10A**). We then looked at phage-TFP interaction by inoculating the DMS3 phage (*48*) that binds to TFP but cannot lyse *P. aeruginosa* PAO1. Thanks to iSCAT microscopy we were able to detect both TFP and floating phages with high contrast. Moreover, we were able to witness a binding event on an extending TFP (**Figure 2.10B**). In the future, we can envision using iSCAT to investigate the dynamics of phage infection at high speed. Also, it has the potential to highlight the details of the mechanism by which TFP assemble by providing a landmark on extending or retracting pili.
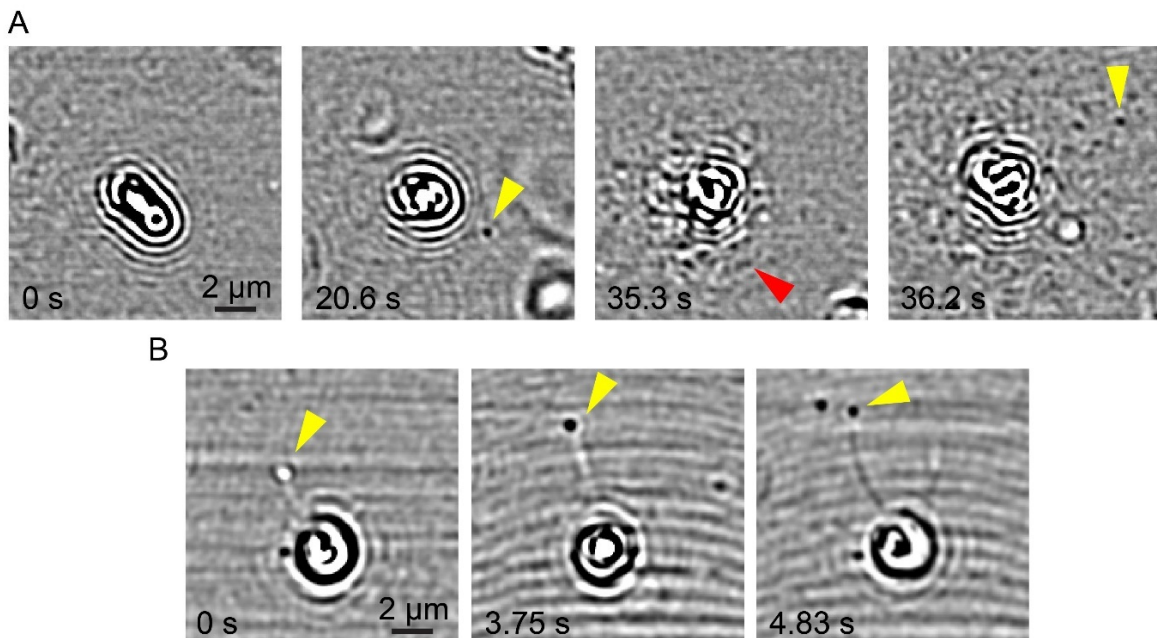
Figure 2.10: Visualization of phage infection in *P. aeruginosa*

A) Time-lapse image of a cell infected with the lytic phage Luz19 after 1h incubation at 37°C. The cell starts to round up before bursting and releasing all its content. A free-floating phage can be seen at 20.6 s (yellow arrow head). Right after burst, a halo of intracellular material (red arrow head) disperse quickly in a radial way. Some phages can be seen among the released material (yellow arrow head at 36.2 s). B) Time-lapse images of a DMS3 phage bound to an extending TFP (yellow arrow head).

2.4 Conclusion and future work

Here we showed an optimization of iSCAT microscopy to study biological processes in living unicellular organisms. The effort in reducing phototoxicity of the iSCAT channel allowed to image cells for minutes without damaging them. We therefore provide a powerful tool to study micro and

nanoscopic interactions of living cells. However, iSCAT still has some limitations in studying live bacteria. As noted in the figures, the cell body scatters a lot of light which interference pattern mask what happens in the close proximity (1 μm) of the cell surface. Therefore, surface proteins or extracellular filaments smaller than 1 μm cannot be resolved.

To further improve our setup and try to reduce the scattering of the cell body we plan on inserting a digital micromirror device (DMD) in the iSCAT illumination path. DMDs have arrays of micromirrors that can be individually switched on and off. When a mirror is "on", it will reflect light into the illumination path, otherwise, light will be focused on a beam stop thus reducing the light exposure at a specific location on the sample. We did a pilot experiment as a proof of concept, consisting in disassembling a digital light processing (DLP) mini projector and introducing its DMD in the illumination path of our iSCAT channel in order to generate a black dot in the center of the field of view of approximatively 3 μm. We then imaged 2 μm polystyrene beads positioned either in the center of the dim area and on the fully illuminated area. We clearly saw a reduction in the intensity of the interference pattern of the bead when it was centered in the dim area (**Figure 2.11**). This suggest that using DMDs to reduce the interference pattern of the cell body could improve the detection of small extracellular filaments and would be worth investigating more on the technique.

A

Raw iSCAT   Filtered iSCAT

B

Raw iSCAT   Filtered iSCAT
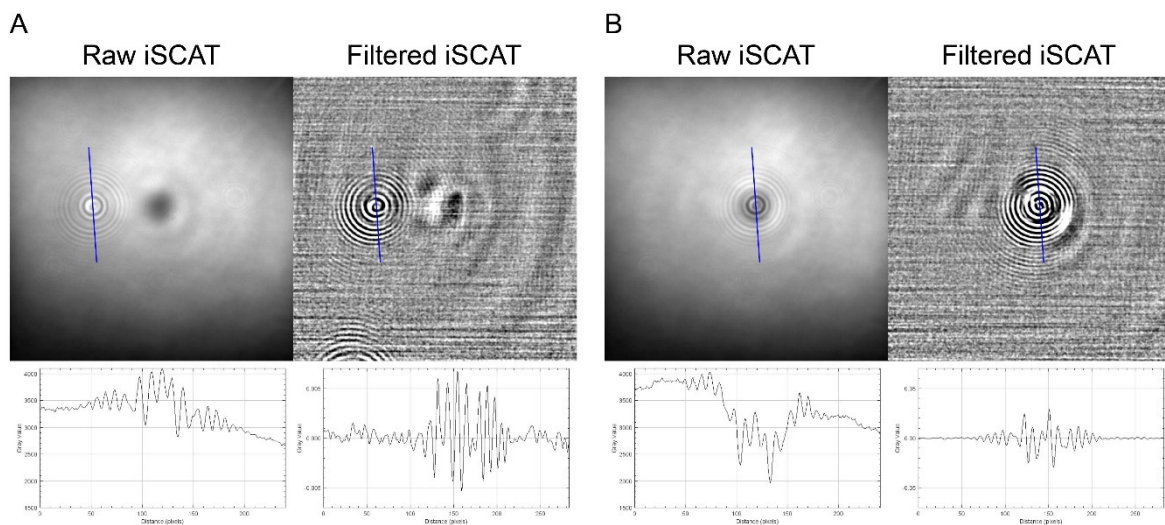
Figure 2.11: Creation of patterns in the illumination path of the iSCAT channel using DMDs

A black dot is generated on the field of view by a DMD placed in the illumination path. A) Intensity profile along the blue line for a 2 μm polystyrene bead placed in the fully illuminated field of view. B) Intensity profile along the blue line for a 2 μm polystyrene bead placed in the shaded area. The interference patter in the Filtered iSCAT is muche smaller in B) compared to A).

Altogether our observations show the versatility of our live-cell iSCAT setup as we can use it to look at thin extracellular filaments in different strains without the need of labeling. Furthermore, our setup is sensitive enough to detect viral particles as well as cellular debris during a burst event. In the next chapter, we will present in more details how we used this powerful technique to measure TFP dynamics during cell surface exploration.

Chapter 3. *Pseudomonas aeruginosa* orchestrates twitching motility by sequential control of type IV pili movements

Authors :

Lorenzo Talà[1], Adam Fineberg[2], Philipp Kukura[2], Alexandre Persat[1]*

Affiliations :

[1]Institute of Bioengineering and Global Health Institute, EPFL, Lausanne, Switzerland

[2]Department of Chemistry, Physical and Theoretical Chemistry Laboratory, University of Oxford, Oxford, United Kingdom.

*Corresponding author: alexandre.persat@epfl.ch

My contributions: Desing of the experiments, building and adapting the iSCAT microscope for live cell imaging, acquire microscopy data and perform data analysis.

3.1 Abstract

Prokaryotes have the ability to walk on surfaces using type IV pili (TFP), a motility mechanism known as twitching [8, 49]. Molecular motors drive TFP extension and retraction, but whether and how these movements are coordinated is unknown [16]. Here, we reveal how the pathogen *Pseudomonas aeruginosa* coordinates motorized activity of TFP to power efficient surface motility. To do this, we dynamically visualized TFP extension, attachment and retraction events at high resolution in four dimensions using label-free interferometric scattering microscopy (iSCAT) [31]. By measuring TFP dynamics, we found that the retraction motor PilT was sufficient to generate tension and power motility in free solution, while the partner ATPase PilU may only improve retraction in high friction environments. By precisely timing successive attachment and retraction, we show that *P. aeruginosa* engages PilT motors very rapidly and almost only after TFP encounter the surface, suggesting contact sensing. Finally, measurements of TFP dwell times on surface show that tension reinforced

the adhesion strength of individual pili to the surface, thereby increasing effective pulling time during retraction. The successive control of TFP extension, attachment, retraction and detachment suggests that sequential control of motility machinery is a conserved strategy for optimized locomotion across domains of life.

3.2 Main

Protein filaments decorate the surface of prokaryotes, allowing single cells to physically interact with their surroundings through motility, adhesion, gene exchange and signaling (*50, 51*). For example, *P. aeruginosa* performs successive rounds of motor-driven TFP extension and retraction to power twitching motility and regulate virulence through mechanosensing (*3, 9, 52*). Pili retraction motors can generate up to 100 pN, but how such large forces end up powering cell body displacements remains unclear (*53, 54*). To answer this question, the distribution of individual pili around single cells have been indirectly inferred from tracking of cell body displacements (*24*). Also, labeling strategies have largely helped in the visualization of extension and retraction events, but also in deciphering the function of TFP in horizontal gene transfer and mechanosensing (*17, 18*). These methods are powerful but remain invasive, and are limited by labeling robustness during high-speed or long-term imaging of TFP. As a result, changes in TFP length, number, and extension-retraction frequencies, which ultimately regulate bacterial interaction with the environment, are difficult to measure during the course of motility. Understanding this connection therefore rests on our ability to visualize and monitor the dynamics of individual TFP on short timescales of extension-retraction (subsecond) and on longer timescales of surface colonization (minutes to hours).

To explore the coordination of their movements, we sought to directly image successive TFP extension-retraction events. iSCAT has previously been used to image single actin filaments *in vitro* without labels (*39*). We reasoned that since actin and TFP are both approximately 5 nm-wide protein polymers, iSCAT may enable TFP visualization. To achieve this, we adapted iSCAT to live cell imaging (**Supplementary Figure 3.1**) (*38*). We reduced phototoxicity by using less energetic iSCAT

and autofocus laser lines, and reduced unnecessary illumination by adding a shutter in the iSCAT illumination path with a brightfield channel for initial bacteria detection (see **3.3 Methods**).

Under brightfield illumination, wild-type (WT) *P. aeruginosa* appeared as rod-shaped without any visible surface structures (**Figure 3.1a**). Simultaneous iSCAT images of the same cell revealed micrometer-long extracellular filaments and shorter structures with alternating intensity extending from the cell body (**Figure 3.1a**). Cells of in-frame deletion mutants in the pilin subunit gene *pilA* displayed no such slender structures (**Figure 3.1b**) suggesting these were TFP. A deletion of the flagellin gene *fliC* removed structures with periodic pattern (**Figure 3.1c, Supplementary Figure 3.2**), suggesting this signal was generated by single helical flagella, which had a periodicity of 1.4 μm ± 0.1 μm (s.e.m., N = 10), consistent with previous measurements for the helical pitch (*55*). Quantification of filaments showed that WT had approximately one pilus per cell, *pilA*⁻ had no TFP, and *fliC*⁻ had about five (**Figure 3.1d**, **Supplementary Figure 3.2** and **3.3 Methods**), and that, as expected, most WT cells had one flagellum and *fliC*⁻ had zero (**Supplementary Figure 3.2**).
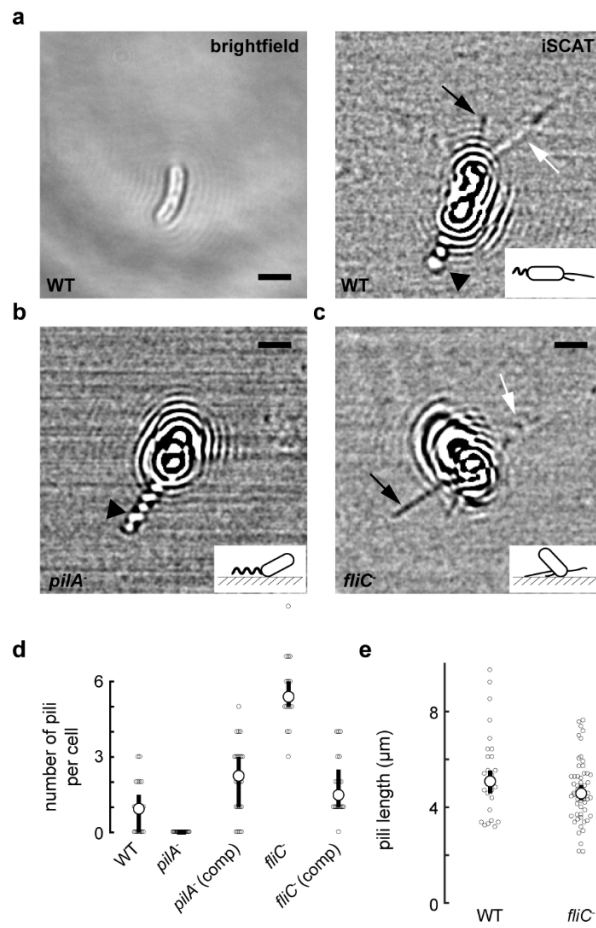
Figure 3.1: iSCAT reveals extracellular bacterial filaments.
(a) Brightfield (left) and iSCAT (right) images of a single WT *P. aeruginosa* cell. The brightfield image only shows the rod-shaped body of the bacterium, while multiple extracellular structures are visible in iSCAT. Flagellum (black arrowhead) and type IV pili with constant (black arrow) or spatially varying contrast (white arrow). (b) A deletion mutant of the pilin gene *pilA* displayed no extracellular slender structures, while (c) a mutant in the flagellin subunit gene *fliC* had no polar filaments with alternating contrast. Inserted illustrations in iSCAT images show the position of cell and filaments relative to the coverslip surface. (d) Quantification of mean TFP per cell with iSCAT. WT has about one pilus per cell in average, (number of cells from the same culture n = 20), *pilA*- has none (n = 19) but WT levels are restored in the complemented strain (n = 22). *fliC*- mutant cells have more TFP than WT (n = 15), which decreases to WT level in the complemented strain (n = 18). We attribute the hyperpiliation of *fliC*- to a selection effect during sample loading (see Materials and Methods). Small circles are individual measurements, large circles are means of bootstrap medians, error bars represent bootstrap 95% confidence interval. (e) Attached TFP length distribution in WT (combined number of pili from cells imaged in at least three biological replicates n = 27) and *fliC*- (n = 54). The flagellum-less mutant has no defect in TFP length. Small circles represent individual measurements, large circles are bootstrap medians and error bars bootstrap 95% confidence interval. (a, b, c) Scale bars: 2 µm.

Live-cell iSCAT can capture multiple successive extension-retraction events while monitoring cell body displacements. For example, **Supplementary Video 3.1** shows a one minute visualization of a WT cell exhibiting multiple rounds of TFP attachment and retraction. Such sequences allow us to quantify attachment-retraction frequencies while monitoring cell body displacement (**Supplementary Figure 3.3**). Since the signal generated from the flagellum was stronger than the one from TFP, and that swimming may interfere with twitching motility, we sought to perform most dynamic visualizations in a *fliC*- background. We tested whether this affected TFP dynamics, and found that there were no distinguishable differences in cell displacement per retraction and in retraction frequencies between WT and the flagellum-less mutant (**Supplementary Figure 3.4, Supplementary Video 3.1 and 3.2**).

We observed three distinct patterns generated by TFP on iSCAT images: straight dark filaments, straight filaments with alternating black and white contrast, or curved filaments with fainter contrast (**Figure 3.2a**). Changes in contrast of a fiber are a manifestation of the shift from constructive to destructive interference with a full phase change corresponding to a spatial shift of $\lambda/2n$, where λ is the illumination wavelength and n the index of refraction of the medium (*30*). Intensity values can thus be used as a proxy for in-depth position of TFP (*56*). For example, TFP having uniform intensity lay flat against the surface (**Figure 3.2a, left panel**). The ones exhibiting successively positive and negative intensity values along their length are at an angle (**Figure 3.2a, center and right panels**). As a result, single iSCAT images provide us with the position and orientation of single TFP in three dimensions, thereby allowing to quantitatively infer spatial position on and away from the attachment surface. We could for example observe differences in TFP positioning of standing *vs* horizontal cells (*49*). TFP of standing cells, which orient vertically on the surface attached by one pole, were in majority (79%) flat against the surface as in **Figure 3.2a**. In contrast, in crawling, horizontal cells, TFP were in most cases (81%) oriented at an angle between the glass surface and the cell pole (**Figure 3.1a**). In summary, iSCAT gives us the ability to probe TFP dynamics at high spatial and temporal resolutions in three dimensions, without obstructing native biological functions.
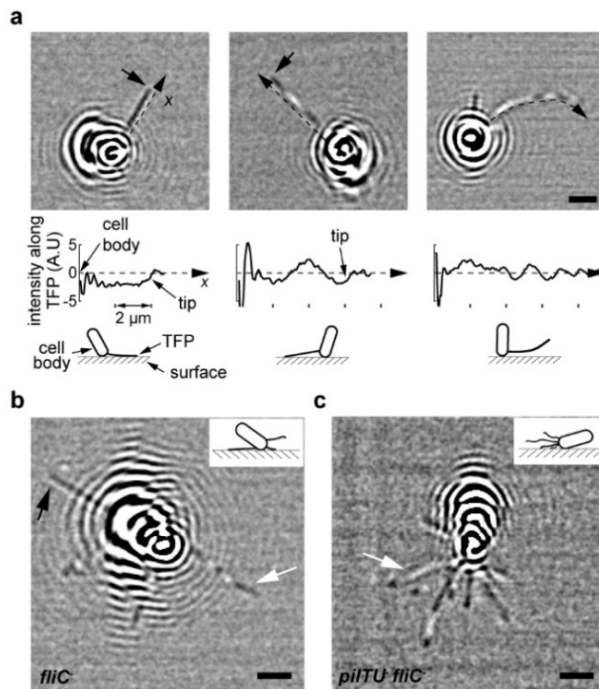
Figure 3.2: Visualization of TFP position and retraction in three dimensions.

(a) Images of three representative TFP positions and orientations visualized by iSCAT, with corresponding iSCAT intensity values along the length of the fiber (below). Changes in iSCAT contrast allows us to infer pilus position in 3D. TFP that have constant contrast are flat on the surface (left panel), the ones with alternating contrast form a finite angle with the coverslip (middle panel), and curved fibers with oscillating and irregular contrast are defined as "floppy" (right panel). Below each image, a plot of the pixel grey value along the pilus allows us to determine if the pili lay flat, at an angle or are fluctuating. The illustration represents the putative 3D orientation of the pilus and the cell body. (b) TFP of fliC- deletion mutant cells exhibit all three morphologies (Supplementary video 3.3). (c) Cells lacking both retraction motor genes pilT and pilU only show floppy TFP, demonstrating retraction and tension force generates straight TFP morphology (Supplementary video 3.4). We encountered these features throughout all our visualizations. Tensed, flat or at an angle, and floppy pili were observed with similar results in all our retractile strains (WT, fliC-, and pilU- fliC-). Whereas only the floppy pili were observed in our pilT- fliC-. (a, b, c) Scale bars: 2 μm.

These images highlight two distinct TFP morphologies and dynamics: straight stationary and curved fluctuating filaments. We verified that the straight conformation was a result of tension generated during retraction. At the molecular level, the extension motor PilB polymerizes PilA subunits to drive TFP growth. The two retraction motors PilT and PilU drive retraction by depolymerizing PilA back into the periplasm, but whether their functions are redundant remains unclear (*9, 11*). *fliC-* cells had both fluctuating curved and stationary straight TFP (**Figure 3.2b**, **Supplementary Video 3.3**). In contrast, a *pilTU- fliC-* mutant had only curved TFP that were fluctuating (**Figure 3.2c**, **Supplementary Video 3.4**). This demonstrates that straight TFP are under tension during retraction.

Given the lack of clear function for two retraction motors in *P. aeruginosa*, we sought to identify functional differences between PilT and PilU by visualizing TFP dynamics in respective mutants. Both *pilT* and *pilU* mutants lose their ability to twitch in typical agar stab assay and have been reported as hyperpiliated (*57*). In *Neisseria gonorrhoeae*, PilU has no apparent role in twitching motility (*58*). In our visualizations, while *pilT- fliC-* could not retract on the timescales of our

visualizations, a *pilU⁻ fliC⁻* deletion mutant could still transition to a tensed state, demonstrating its ability to retract TFP (**Figure 3.3a, Supplementary Videos 3.5-3.6**). In addition, *pilU⁻ fliC⁻* tends to have less, not more, TFP compared to *fliC⁻*, in contrast to *pilT⁻ fliC⁻* (**Figure 3.3b, Supplementary Videos 3.5-3.6**). Thus, cells lacking *pilU* can retract TFP, but still, they do not migrate in typical twitching assays where colonies spread at the interface between a plastic dish and agar (**Supplementary Figure 3.5**) (*11*). We sought to elucidate this paradox by examining TFP dynamic activity. We first found that the length of TFP were identical between *fliC, pilU⁻ fliC⁻* and *pilT⁻ fliC⁻*, demonstrating that extension is not affected (**Figure 3.3c**). Retraction frequency was slightly decreased in *pilU⁻ fliC⁻* compared to *fliC⁻* (**Figure 3.3d**), which however could not explain a full loss of motility observed in twitching assays. Finally, measurements of displacements in free solution on glass shows that each retraction generates approximately a similar displacement in *fliC⁻* and *pilU⁻ fliC⁻* (**Figure 3.3e, Supplementary Videos 3.2 and 3.7**). This demonstrated that TFP of cells lacking *pilU* do not lose their ability to generate displacements.

Since dynamics were not grossly affected by the absence of PilU in free solution, we sought to highlight a potential role of PilU in generating retraction force. We visualized twitching motility at the leading edge of colonies sandwiched between glass and agarose surfaces by phase contrast microscopy (we could not implement iSCAT as the gel scatters strongly). We reasoned that the friction between the cell body and the substrate during locomotion in this configuration is higher than in free solution, thereby requiring larger forces to generate displacements during retraction. *fliC⁻* cells at the leading edge of expanding twitching colonies were highly motile between glass and a 0.5% agarose gel (**Supplementary Video 3.8,** top left). In this same configuration, *pilU⁻* and *pilU⁻ fliC⁻* were barely motile, consistent with twitching assays (**Supplementary Video 3.8,** bottom). We could recapitulate this defect in *fliC⁻* by increasing the friction of the cell body with the surface using higher agarose concentration, which requires a higher retraction force to generate similar displacement (**Supplementary Video 3.8,** top right, **Supplementary Figure 3.6**)**.** Altogether, this suggests that PilU contributes to increasing TFP retraction force in conjunction with PilT, rather than acting as an independent retraction motor. By analogy with the torque-dependent recruitment of flagellar motors,

PilU could be activated when PilT reaches a threshold force (*59*), consistent with the fact that PilU localizes at the leading poles of twitching cells (*60*). Alternatively, PilU could regulate PilT activity, for example through direct interaction or by mediating the function of minor pilins inserted in TFP (*43*). In summary, *P. aeruginosa* uses one motor, PilT, to twitch in low friction environment, but leverages the companion ATPase PilU to power displacements when friction increases.
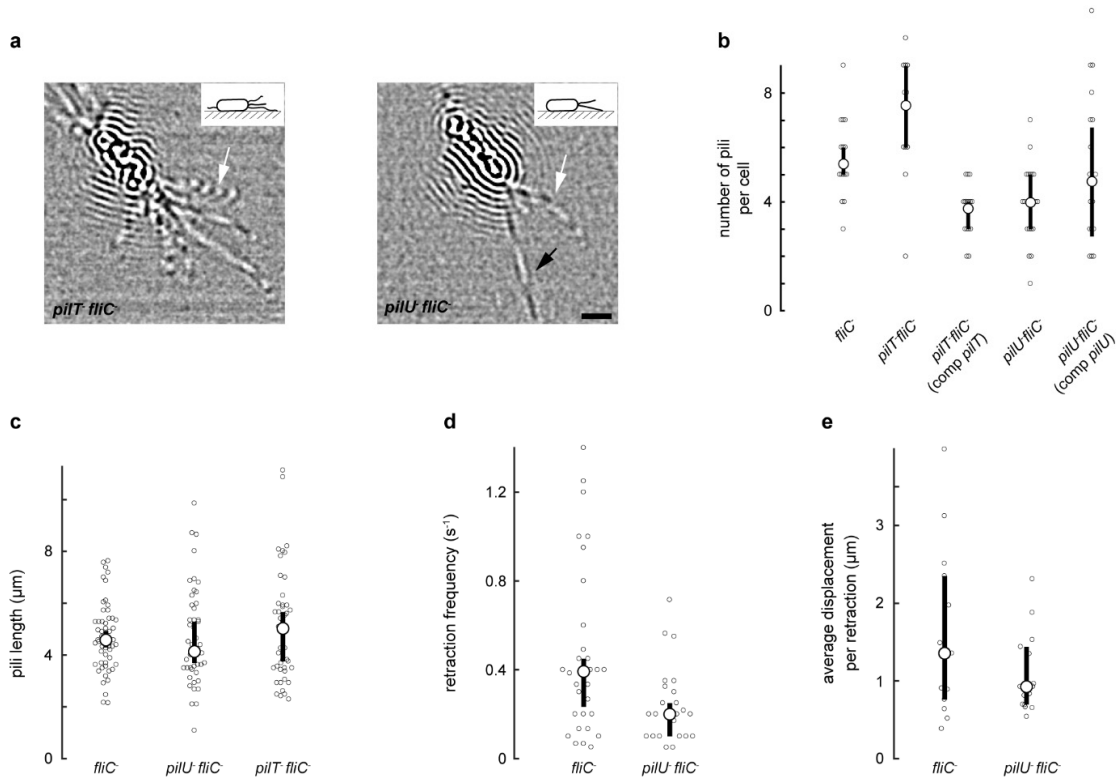
Figure 3.3: PilU does not affect TFP dynamics in free solution.

(a) iSCAT images of pilT⁻ fliC⁻ and pilU⁻ fliC⁻ mutants. pilT⁻ fliC⁻ cells never undergo retraction on the timescale of our movies. The pilU⁻ fliC⁻ mutant picture shows a retraction of one TFP. Scale bar: 2 μm. (b) Number of TFP in motor mutants and their corresponding complementation strains. These have similar numbers of surface pili except pilT⁻ fliC⁻ (number of cells from the same culture n = 11), which had more (fliC⁻ n = 15, pilT⁻ fliC⁻ complemented n = 15, pilU⁻ fliC⁻ n = 18, pilU⁻ fliC⁻ complemented n = 17). Large circles are means of bootstrap medians and error bars bootstrap 95% confidence intervals. Small circles are individual measurements. (c) The average lengths of TFP that attached on the glass surface in fliC⁻ (combined number of pili from cells imaged in at least three biological replicates n = 54), pilU⁻ fliC⁻ (n = 47) and pilT⁻ fliC⁻ (n = 45). (d) Retraction frequencies for pilU⁻ mutant (combined number of pili from cells imaged in at least three biological replicates n = 23,) compared to fliC⁻ (n = 23). The pilU⁻ mutant show a slight decrease in retraction frequencies compared to fliC⁻. (e) Average displacement per retraction for fliC⁻ (number of tracks n = 13) and pilU⁻ fliC⁻ (n = 15). Motility does not strongly differ between these mutants. (c, d, e) Small circles correspond to individual measurements, large circles are medians of bootstrap medians and error bars are bootstrap 95% confidence interval. A difference between two groups is defined as statistically significant when their 95% confidence intervals don't overlap.

A key question arising from these movies of *a priori* random attachment and detachment events is how *P. aeruginosa* orchestrates force generation to drive motility. To optimally generate displacements, cells must coordinate TFP retraction with attachment and detachment (**Figure 3.4a**) (*16*). Is this sequence actively coordinated or do TFP randomly extend and retract? To answer this, we performed visualizations of each step involved in individual TFP cycles (**Figure 3.4b, Supplementary Videos 3.9 and 3.10**). We found that the tip of extended TFP occasionally appeared as a stationary dark spot while the remainder of the fiber fluctuated, indicating initial attachment. The same fiber then transitioned to a straight stationary line indicating retraction and tension, before eventually detaching (**Figure 3.4c, Supplementary Videos 3.9 and 3.10**). We could thus time transitions between attachment, retraction and detachment of single fibers. We first measured the dwell time τ_d defined as the residence time of the pilus on the glass surface from tip attachment to detachment (**Figure 3.4a**). The TFP of the retraction-less mutant *pilT⁻ fliC⁻* could still attach, with median dwell time of 75 ms [65 - 90 ms] (median and 95% bootstrap confidence interval), which is a measurement of the intrinsic residence time of passive fibers on the surface (**Figure 3.4d**). Given that the retraction speed of TFP is about 1 µm.s⁻¹, this would only enable a seemingly short 70 nm displacement per retraction (*17*). Surprisingly, the dwell time in cells capable of retraction was, however, much longer: 2,315 ms [1,710 – 2,635 ms] in WT, 997 ms [590 – 1,795 ms] in *fliC⁻* and 540 ms [405 – 840 ms] in *pilU⁻ fliC⁻* (**Figure 3.4a**). This indicates that tension force during retraction enhances TFP adhesion, increasing surface attachment time, thereby improving effective displacements of the cell body. In analogy with the formation of catch-bonds by the adhesin FimH in *Escherichia coli*, tension force may induces a conformational change in the structure of TFP, thereby increasing the strength of its attachment to the surface (*61, 62*). We also note that dwell times are typically lower than 3 s, thereby allowing TFP release for subsequent extension-retraction cycles, and that *pilU⁻ fliC⁻* had slightly decrease dwell, possibly as a consequence of lower retraction strength.

The short dwell time of relaxed TFP on the surface suggests that retraction must rapidly take place after attachment. To achieve this, retraction must occur at high frequency or systematically after pilus contact with the surface. The first scenario would lead to inefficient conversion of force into displacement, while the second suggests cells sense contact of their TFP. To identify the strategy *P. aeruginosa* uses to coordinate TFP retraction with attachment; we directly measured tension time τ_t defined as the delay between tip attachment and pilus tension (**Figure 3.4a**). We found that TFP became tensed 130 ms [95 - 215 ms] after tip attachment in WT and 135 ms [105 – 198 ms] in *fliC⁻*, which was close to the dwell time of relaxed TFP on the surface of *pilT⁻ fliC⁻*. Also, *pilU⁻ fliC⁻* had a similar reactivity (τ_t = 150 ms [90 - 155 ms]) (**Figure 3.4d**), showing that PilT motors engage rapidly, optimizing retraction efficiency and subsequently increasing the dwell time of TFP on surfaces. This result also hints to the possibility that cells sense tip attachment to rapidly initiate retraction. Measuring the proportion of TFP retraction without attachment further supports this hypothesis: most extended TFP did not retract during the course of visualization unless their tip attached to the surface (**Figure 3.4e, Supplementary Figure 3.7**). This demonstrates that TFP attachment stimulates retraction, and that motors respond to a signal generated by contact of the tip with the surface. Thus, *P. aeruginosa* uses a high-efficiency sensing strategy to deploy and coordinate TFP rather than relying on random motor activation.

Our measurements indicate that *P. aeruginosa* precisely coordinates TFP motorized activity with attachment by successively sensing surface contact, initiating retraction by a first motor, improving surface attachment during retraction through a catch bond, and triggering a second motor to generate displacement under high load (**Figure 3.4f**). In a same manner as animal locomotion, the sequential control of pili movements could be coupled with sensory feedback enabling transformation into cell displacements, thereby increasing the efficiency of conversion of chemical energy into mechanical work. For example, animals use multiple sensory inputs such as mechanosensation and proprioception to control and synchronize limb motion during locomotion (*63, 64*). Here, we suspect that tip contact generates a mechanical signal read out by sensory components that trigger TFP retraction by PilT, and subsequent activation of PilU during twitching under high load. Combining

visualizations of bacterial surface structures dynamics with molecular characterizations will eventually generate a holistic understanding of their functions, ultimately helping us understand how microbes physically interact with their environment and highlighting shared strategies among seemingly distant living organisms (*65*).
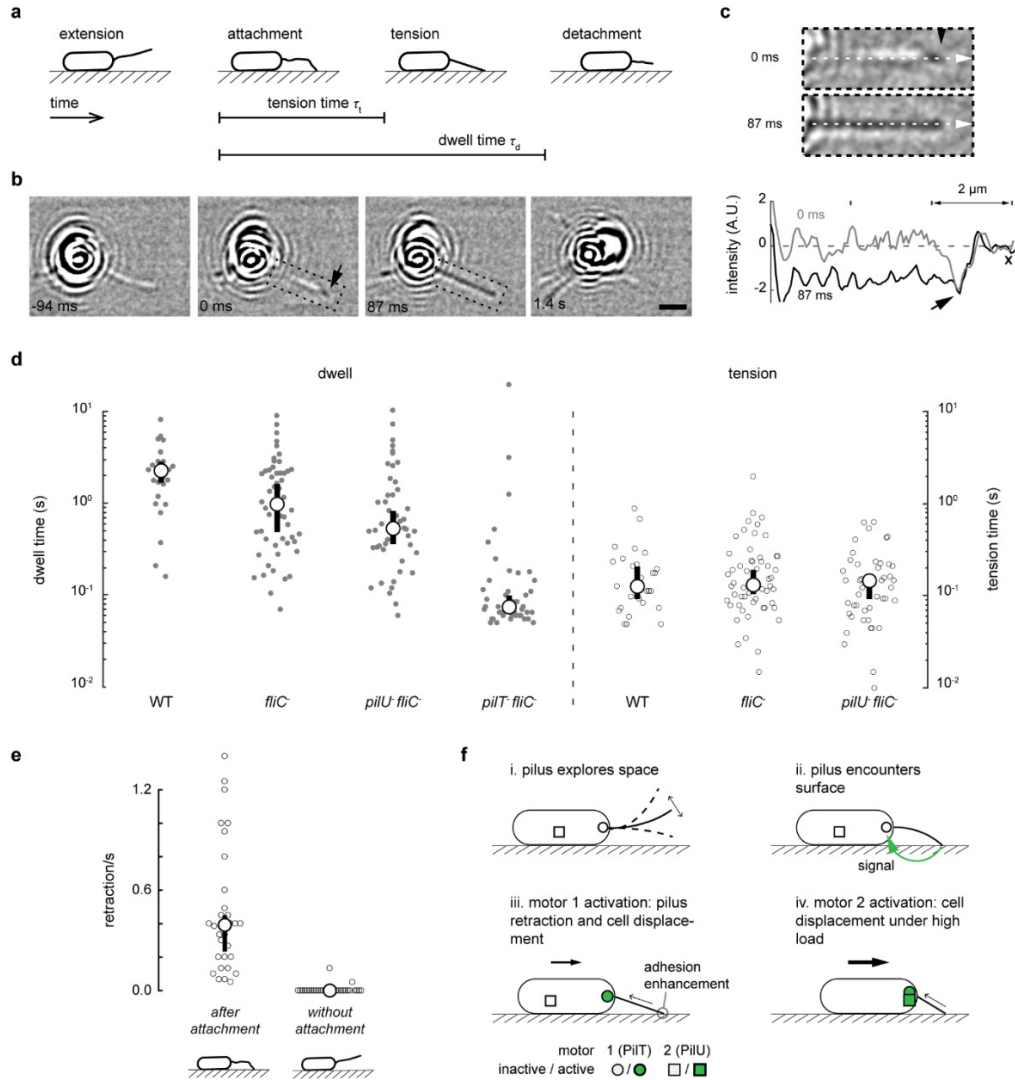
Figure 3.4: Coordination of TFP retraction motors.

(a) Illustration of the optimal sequence of events for TFP function: extension, attachment, tension and release from the surface. (b) Successive events from (a) visualized with iSCAT. Attached pilus tip appears as a stationary dark signal at 0 ms (black arrow). The whole fiber transitions into lower intensity values at τ_t = 87 ms, before detaching at τ_d = 1.4 s. Scale bar: 2 µm (c) Close up view of attachment and tension from (b) with corresponding intensity profile along the pilus. A dip in intensity is observed at the tip at 0 ms (black arrow on image and graph), transitioning to a uniform low value at τ_t. (d) Measurements of dwell and tension times in WT (total number of pili from at least three biological replicates n = 27), *fliC⁻* (n = 54) and *pilU⁻ fliC⁻* (n = 47) and *pilT⁻ fliC⁻* (n = 45). Comparing retraction-capable to retraction-deficient mutants show that TFP tension increases dwell time. The tension times in the retraction-capable cells are close to the dwell time of *pilT⁻ fliC⁻*, showing that motors engage rapidly to initiate retraction. There is no defect in tension time in *pilU⁻ fliC⁻* indicating that PilT is sufficient to initiate this rapid response. (e) TFP retraction frequencies for attached and unattached TFP in *fliC⁻* (number of cells from at least three biological replicates n = 30). TFP retract almost only after their tips touch the surface, indicating attachment stimulates retraction. (d and e) Small circles correspond to individual measurements, large circles to median and error bars to bootstrap 95% confidence intervals. A difference between two groups is defined as statistically significant when their 95% confidence intervals don't overlap. (f) Proposed model for sequential control of TFP motion. During spatial fluctuations (i), attachment of TFP tip to the surface generates a signal activating PilT (ii). This causes pilus retraction and tension, reinforcing attachment and resulting in longer dwell times and cell displacement (iii). PilU engages to power cell displacement under strong loads, for example in environments with increased friction on the cell body (iv).

3.3 Methods

3.3.1 Bacterial strains

Strains and plasmids used in this work were described previously (*11*). Double deletion mutant pilTU-fliC- was generated by conjugation of pilTU- mutants with the plasmid pJB215 using a standard mating protocol (*66*).

3.3.2 Glass coverslip preparation

Glass coverslip (Marienfeld, 22x40 mm No 1.5) were cleaned as described in Young et al. (*34*). Briefly, they were washed sequentially with distilled water, ethanol, distilled water, isopropanol, distilled water, ethanol, distilled water and excess water was dried with a stream of nitrogen. For visualization, we used two platforms. We either plasma-bonded 500 µm wide, 90 µm deep polydimethylsiloxane (PDMS) microchannels fabricated using standard photolithography methods, or we deposited PDMS gaskets on the clean coverslips. PDMS gaskets were obtained using biopsy punches of 3 or 6 mm in diameter.

3.3.3 Sample preparation

Single colonies of the bacterial strains of interest were grown at 37°C in LB medium overnight. The culture was diluted 1:500 and grown to early-exponential phase before visualization. For motility visualization, cells in early-exponential phase were plated on plain LB-agar plates for 4 hours, harvested by gently flushing them with LB medium followed by a dilution to OD 600 < 0.05. The cells were loaded either into a microfluidic chip or in PDMS gaskets. Microfluidic chips were first loaded with plain LB medium. After proper tubing, exhaust tubes were dipped in bacterial culture and cells were loaded by aspiration using a syringe pump (Crpump, ZS100). The gaskets were loaded with 20 µl of bacterial culture at OD 600 < 0.05, washing twice with fresh LB after 5 - 10 min of incubation at RT (if higher OD was used). After loading process was complete, gaskets were sealed with a small coverslip in order to prevent liquid evaporation that generated fluctuations on the iSCAT images.

We found that *fliC* cells had more TFP compared to WT. We attribute this difference to our sample preparation process which first selects for cells that reach and remain on the surface. This loading process induces a selection for more piliated cells that attach more strongly to the coverslip.

3.3.4 Experimental setup

Our experimental setup is adapted from Ortega et al. to allow live cell visualization during long acquisition times (see schematic in **Supplementary Figure 3.1**) [31]. We sought to reduce phototoxicity by using a laser wavelength of 635nm for the iSCAT channel (Lasertack, LDM-638-700-C). The illumination beam was spatially filtered through a 50 µm pinhole and collimated with a 4f lens. The collimated beam was aligned into two perpendicular acousto-optic deflectors (AODs), (AA Opto-Electronic, DTSXY-400-660) and imaged into the back focal plane of the objective (Olympus, PLAN APO 60x 1.42) thanks to a 4f lens system, a polarizing beam splitter (PBS) (Thorlabs, PBS251) and a quarter-wave plate (QWP) (Thorlabs, AQWP05M-600). The AODs allowed in-plane scanning of the beam on the sample. The objective captured the light scattered by the sample and the reflection of the incident beam at the glass-water interface. QWP and PBS discriminated input illumination from the reflected and scattered light. A 1000 mm focal length achromatic lens imaged the back focal plane of the objective onto a CMOS camera (PhotonFocus, MV1-D1024E-160-CL), yielding a 31.8 nm pixel size. Images were acquired using LabView and a frame grabber (National Instruments, PCIe-1433). We added a mechanical shutter into the illumination path to prevent unnecessary illumination. We also implemented a bright field channel by adding a white LED (Thorlabs, WFA1010) above the stage and imaged the back focal plane of the objective on a CMOS camera (PointGrey, CM3-U3-31S4M) with a 400 mm focal length achromatic lens (pixel size of 25.9 nm). This brightfield channel allowed localization of the cells before iSCAT acquisition thus protecting the cells against extended light exposure.

3.3.5 Autofocus system

We ensured the z-position stability of our sample by building a cytocompatible autofocus system with a weak infrared laser (850nm, 3,5mW) (Thorlabs, CPS850). A CMOS camera (Thorlabs,

DCC1545M) detected the infrared light totally reflected by the glass-water interface and a LabView software computed the correction of the drift providing real-time adjustment of the z-position of the stage through a piezo actuator.

3.3.6 Twitching motility assays

Motility assays were performed by stabbing and pipetting a 0.5% agarose LB plate with 2 µl of stationary phase *P. aeruginosa* culture at the gel-plastic interface. These plates were incubated 24 h at 30°C before removing agarose and staining the plastic dish with a 0.1% solution of crystal violet in water. We performed microscopic twitching visualizations (**Supplementary Video 3.8**) by pipetting 0.5 µl of exponentially growing cells (OD = 0.1 at 600 nm) on a 0.5% agarose LB pad. These were then flipped onto a glass bottom dish (Mattek, #1.5 coverslip) and incubate at 30°C for 5 h. The leading edge of the expanding colonies were then visualized for 2 min at 1 fps by phase contrast microscopy on Nikon TiE equipped with a 100x, NA 1.45 objective and a Hamamatsu Orca R2 camera.

3.3.7 Image processing

To reveal the interferometric component of the signal, each frame of a given sequence was divided by a reference. This reference image was generated by computing the median of each pixel value throughout the whole stack of images. To improve visualization, we applied a band pass filter dampening the contributions of small and large structures (smaller than 1 pixel and larger than 13 pixel) with the FFT plugin of ImageJ (*42*). To reduce slight temporal variation in illumination, each frame was divided by its mean pixel grey value.

3.3.8 Image analysis of pili dynamics quantification

In order to extract time delays between attachment and retraction to a tensed state we manually recorded the frame number of the pili tip attachment (appearing of a stationary dark spot at the pili tip) and the frame number of the pili under tension and without fluctuations from the pili were these events were clearly visible and measured with accuracy. Time delays were obtained by multiplying

the frame difference by the acquisition frame time (frame rate: 200 fps). We measured tension times in 20 WT cells (27 retractions), 23 fliC$^-$ cells (54 events) and 30 pilU$^-$ fliC$^-$ cells (47 events) from data acquired from at least 3 different days. Similarly, dwell times were obtained by manually measuring the time difference between attachment and detachment of each pilus from the same cells with the addition of 14 pilT$^-$ fliC$^-$ cells (45 events). Intensity measurements of attachment, tension and detachment were manually extracted by plotting the intensity profile along the pili using the ImageJ "plot profile" built-in tool. We performed intensity peak detections from the recorded profile for tip attachment and tension using MatLab (**Figure 3.2 and 3.4**). Pili lengths were measured from pili tip attachment point to the middle of the first fringe of the cell body diffraction pattern from the same data set. (**Figure 3.1 and 3.3**). Retraction frequencies were computed by counting all the obvious pili retractions within a movie but discarding the pili already tensed in the initial frames. The total number of retractions were then divided by the movie time for 30 fliC$^-$ and 23 pilU$^-$ fliC$^-$ cells (**Figure 3.3**) from at least 3 biological replicates. Pili were counted on 20 WT, 15 fliC$^-$, 18 fliC$^-$ complemented, 19 pilA$^-$, 22 pilA$^-$ complemented, 11 pilT$^-$ fliC$^-$, 15 pilT$^-$ fliC$^-$ complemented, 18 pilU$^-$ fliC$^-$, and 17 pilU$^-$ fliC$^-$ complemented cells (**Figure 3.1 and 3.3**) from the same strain culture. Flagella were counted from 52 WT, 51 fliC$^-$ and 50 fliC$^-$ complemented cells (**Supplementary Figure 3.2**) from at least 3 biological replicates.

3.3.9 Image analysis of cell motility with iSCAT

Cell motility movies were acquired at 10 fps and binned 10 times to obtain a final movie rate of 1 fps. Cell leading pole, defined as the center of the white spot in the middle of the circular fringes of the cell body, was manually tracked along the cell displacement (**Supplementary Figure 3.3**). Only cell displacements were no change in contrast of the leading pole was observed were recorded in order to assess effective influence of pili retraction to displacement and discard Brownian motion effects when the cell was not in contact with the glass surface. We note that some cells appeared to "hover" on the surface by Brownian motion, using TFP to maintain proximity to the surface. We recorded the number of visible retractions along each track. In total 14 tracks were recorded for WT cells, 13 for fliC$^-$ and 15 for pilU$^-$ fliC$^-$ from the same strain culture (**Figure 3.3 and Supplementary Figure 3.4**).

3.3.10   Statistical analysis

As the time delay and tension time data were not normally distributed, we chose the median as an indicator of the central tendency of the distribution. Statistical analysis was performed using the bootstrap method in MatLab to resample our data into 300 different groups and computing the median of the median of each group to obtain a more robust estimate of the population's behavior. We computed the 95% confidence interval by taking the highest and lowest values of the bootstrap median dataset after removing the top and bottom 2.5% of the data points. The same approach has been used to determine retraction frequencies, pili lengths and displacement per retraction. Pili numbers in complementation analysis were analyzed by taking the mean of the bootstrap medians and the bootstrap 95% confidence interval as stated previously. A difference between two groups is defined as statistically significant when their 95% confidence intervals don't overlap.

3.4 Correspondence:

Correspondence and requests for material should be addressed to Alexandre Persat: alexandre.persat@epfl.ch

3.5 Acknowledgements:

3.6 Author contributions:

L.T. and A.P conceptualized the study and performed experiments and data analysis. L.T., A.F., and P.K. implemented and adapted the iSCAT microscope for live cell imaging. L.T., P.K and A.P. wrote the manuscript.

3.7 Competing interests:

Authors declare no competing interests.

3.8 Data availability:

All data are available from the corresponding author upon reasonable request.

3.9 Code availability:

All codes are available from the corresponding author upon reasonable request.

3.10 Supplementary information
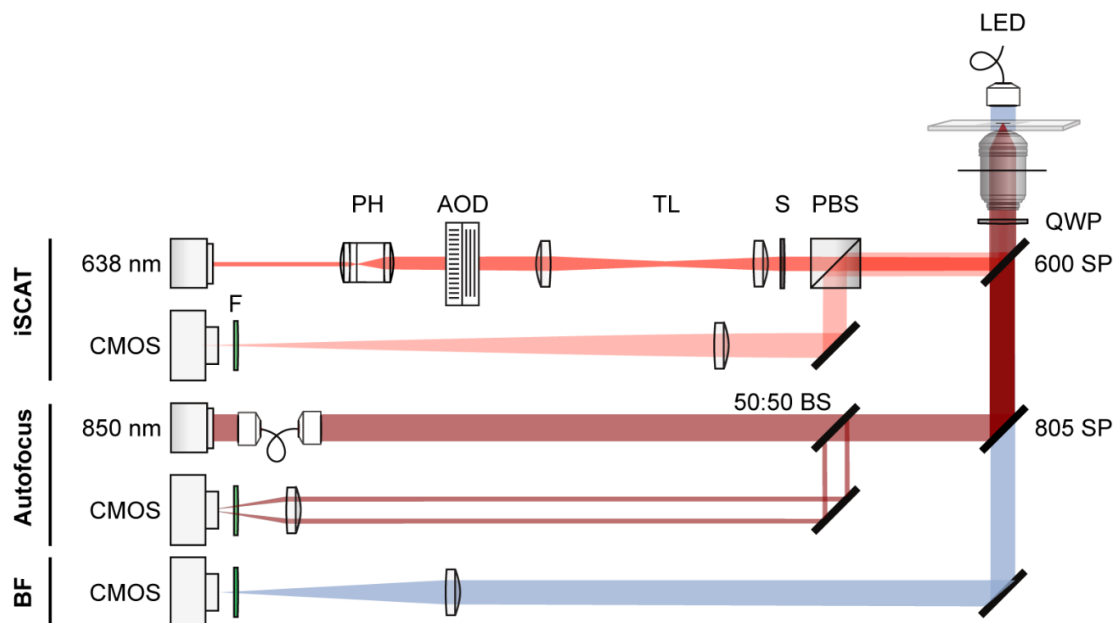
Supplementary Figure 3.1: Optical layout of the microscopy setup.

The setup was composed of 3 channels, iSCAT, Autofocus and Brightfield. For the iSCAT channel, a 638 nm laser source was spatially filtered by a pinhole (PH) and scanned by two acousto-optic deflectors (AOD). The scanned beam was imaged on the back focal plane of the objective by two telecentric lenses (TL). The constant back reflection of the glass-water interface and the light scattered by the sample were captured by the objective and sent to a CMOS camera through a 1000 mm imaging lens. Illumination and imaging light path were separated the by the conjoint effects of the polarizing beam splitter (PBS) and the quarter wave plate (QWP). A shutter (S) allowed clipping of the beam to reduce light exposure on cells. The autofocus channel consisted in an 850 nm infrared laser source spatially filtered through an optic fiber and coupled to the illumination path of the iSCAT channel by an 805 short pass (SP) dichroic. This was made possible by the 25% transmittance of the 600 SP dichroic at 850 nm. The total internal reflection of the beam on the glass-water interface was sent to a CMOS camera by a 50:50 beam splitter (BS). A white LED above the stage, illuminated the sample and the transmitted light was directed to a second CMOS camera with a 400 mm imaging lens, thus creating a brightfield channel. Proper filters (F) were used to prevent unwanted signal reaching the detectors (iSCAT: 635 band pass (BP), Bright field: 525 BP, Autofocus: 850 BP).
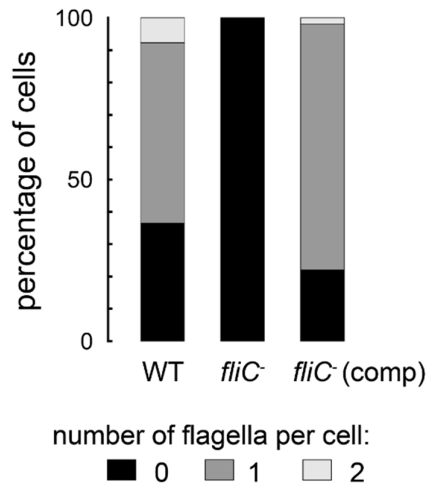
Supplementary Figure 3.2: Quantification of flagella by iSCAT.

We counted structures with periodic patterns in 52 WT, 51 *fliC⁻* and 50 complemented *fliC⁻* cells from at least 3 biological replicates. We found that the structures present in WT were absent in *fliC⁻* mutants and restored to similar levels in the *fliC* complementation strain confirming that they were flagella.
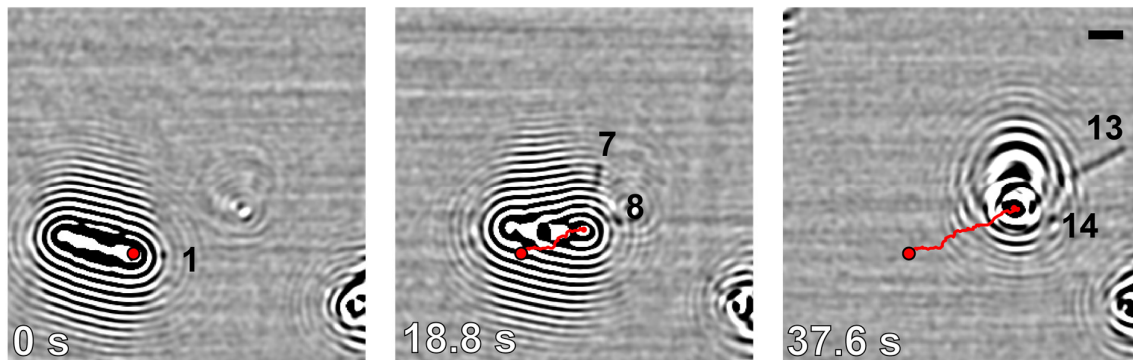
Supplementary Figure 3.3: Simultaneous cell trajectory and TFP activity tracking in single cells by iSCAT.

In this example, a WT cell performs 14 attachment-retraction events during a 54 s visualization. We selected 3 frames where we numbered these events and simultaneously tracked leading pole displacement (red tracks). The red dot corresponds to the initial position of the leading pole. In this example, the cell transition from crawling to standing positions. Similar results were observed in all our motility visualizations in all 3 retractile strains (WT: number of tracks n = 14, *fliC⁻*: n = 13, *pilU⁻ fliC⁻*: n = 15). **Supplementary Video 3.1** is a dynamic visualization of the same data. Scale bar: 2 µm.
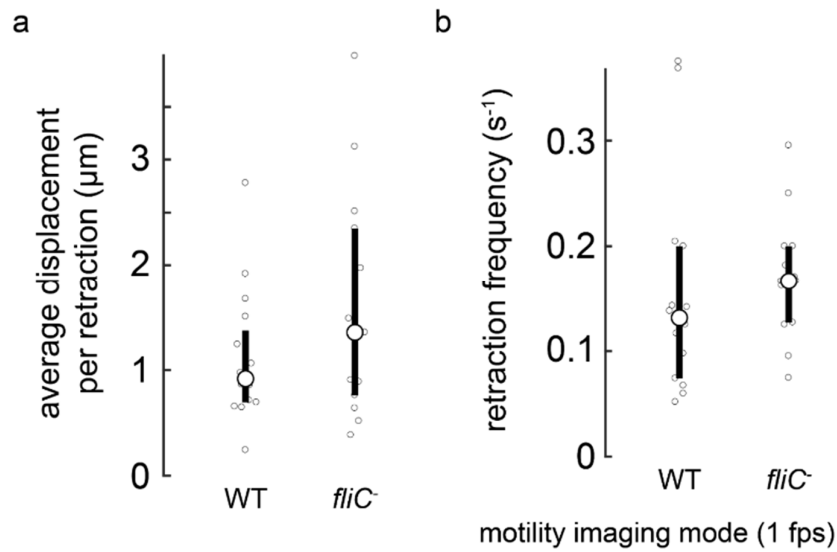
Supplementary Figure 3.4: TFP dynamics in WT and *fliC⁻*.

(a) Average displacement per retraction measured at 1 fps in WT (number of tracks *n* = 14) and *fliC⁻* (*n* = 13) mutant cells. (b) Retraction frequencies measured from the same movies as in (a). Small circles correspond to individual measurements, large circles to medians of bootstrap medians and error bars to bootstrap 95% confidence interval. (a, b) A difference between two groups is defined as statistically significant when their 95% confidence intervals don't overlap.
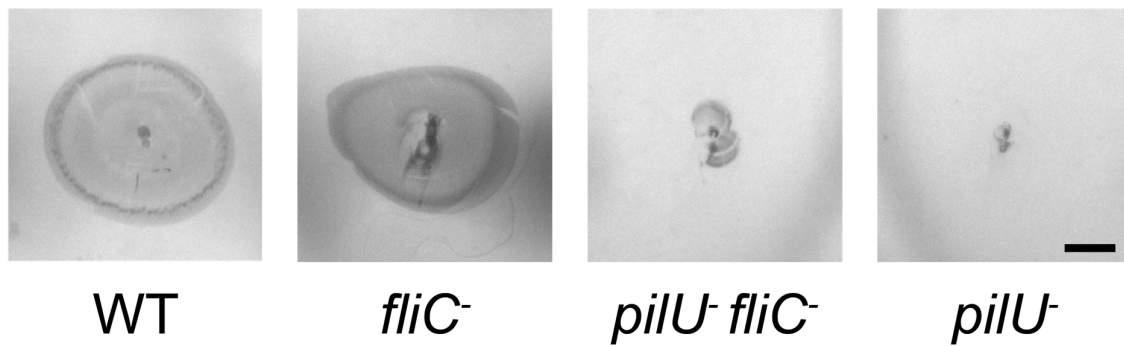
Supplementary Figure 3.5: Twitching assay for WT, *fliC⁻*, *pilU⁻ fliC⁻* and *pilU⁻*.

Traditional twitching stab assays show that *pilU⁻* and *pilU⁻ fliC⁻* mutants have strongly impaired twitching motility compared to WT and *fliC⁻*. Scale bar: 5 mm. Similar result were obtained in 4 replicates.
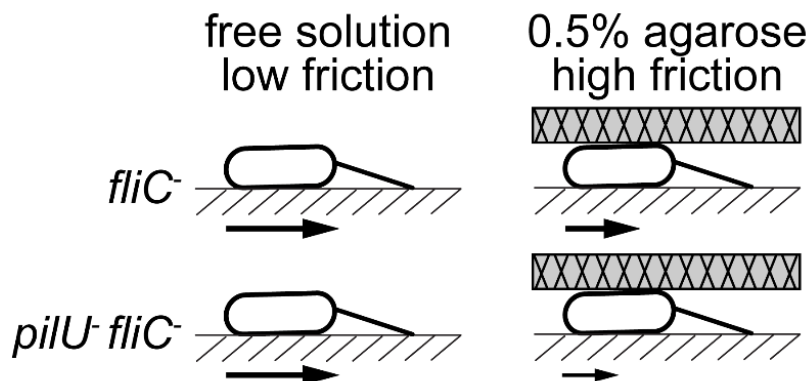
Supplementary Figure 3.6: Illustration summarizing the potential role of PilU in motility adaptation to high friction environments.

Schematic of the different motility behaviors of *fliC*- and *pilU*- *fliC*- mutants in low and high friction environments. Motility on glass in free solution (fluidic bulk) represents a low friction environment for single cell twitching. In contrast, motility between glass and an agarose substrate represents a high friction environment. The force generate by TFP in this high friction environment must overcome this increased friction. **Supplementary Videos 3.7 and 3.8** show that *pilU*- mutants are able to twitch when visualized in plain LB (low friction environment) but are drastically less motile than *fliC*- when visualized under 0.5% agarose (high friction environment). This indicates that PilU may help single cells during motility in environments with increased friction.
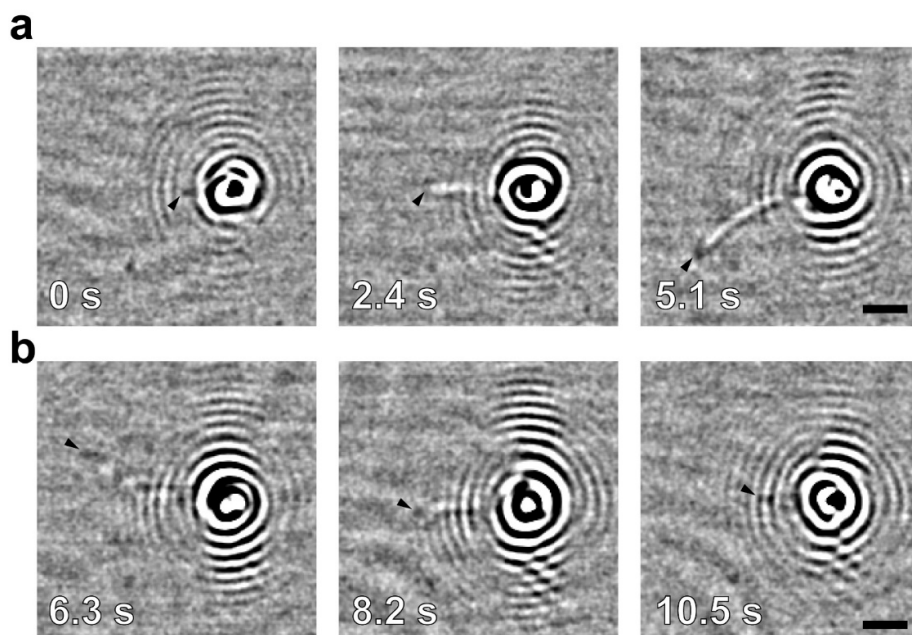
Supplementary Figure 3.7: TFP extension and retraction without attachment.

While retraction events without attachment were rare, some occurrences could be observed (only 3 times in the *fliC*- mutant and 5 times in the *pilU*- *fliC*- mutant). (a) Here, a *pilU*- *fliC*- mutant cell extends a pilus whose tip is indicated by a black arrowhead. Its extension speed is 1.03 μm/s. (b) The same cell retracts the same pilus without attachment of its tip (retraction speed 0.95 μm/s). Scale bar: 2 μm.

Supplementary Video 3.1: iSCAT visualization of a twitching WT cell. (AVI file, 2.26 MB)

Visualization of the WT cell shown in **Supplementary Figure 3.3**. Acquisition rate: 10 fps, temporal binning 4x. The movie is visualized 4 times faster than real speed. The width of the field of view is 20.6 μm. Similar results were observed in all our motility visualizations in WT (number of tracks *n* = 14).

Supplementary Video 3.2: iSCAT visualization of a twitching *fliC* cell. (AVI file, 2.51 MB)

Visualization of a *fliC* cell among the cells included in the data of **Supplementary Figure 3.4**. Acquisition rate: 10 fps, temporal binning 4x. The movie is visualized 4 times faster than real speed. The width of the field of view is 16.3 μm. Similar results were observed in all our motility visualizations in *fliC* (number of tracks *n* = 13).

Supplementary Video 3.3: iSCAT visualization of the *fliC* mutant. (AVI file, 6.91 MB)

Visualization of the *fliC* cell shown in **Figure 3.2b**. *fliC*, like WT, *P. aeruginosa* display a few pili per cell that can extend, attach and retract, thus inducing twitching motility. Acquisition rate: 200 fps. The movie is visualized 5 times slower compared to real speed. The width of the field of view is 16.3 μm. Similar results were observed in all our visualizations (at least 3 biological replicates).

Supplementary Video 3.4: iSCAT visualization of the *pilTU* *fliC* mutant. (AVI file, 9.15 MB)

Visualization of the *pilTU* *fliC* cell shown in **Figure 3.2c**. Complete removal of retraction motors prevent retraction of TFP upon surface attachment as seen in this mutant where the pili length remain unchanged and motion observed is only due to thermal fluctuations of the fiber. Acquisition rate: 200 fps, temporal binning 2x. The movie is visualized 4 times slower compared to real speed. The width of the field of view is 16.3 μm. Similar results were observed in all our visualizations (at least 3 biological replicates).

Supplementary Video 3.5: iSCAT visualization of the retraction motor mutant *pilT* *fliC*. (AVI file, 7.92 MB)

Visualization of the *pilT* *fliC* cell shown in **Figure 3.3a**. This mutant displays many pili per cell that can extend and attach but cannot retract remaining loose and subject to Brownian motion as in the *pilTU* *fliC* mutant of Supplementary video 4. Acquisition rate: 200 fps. The movie is visualized 5 times slower compared to real speed. The width of the field of view is 16.3 μm. Similar results were observed in all our visualizations (at least 3 biological replicates).

Supplementary Video 3.6: iSCAT visualization of the retraction motor mutant *pilU* *fliC*. (AVI file, 8.17 MB)

Visualization of the *pilU* *fliC* cell shown in **Figure 3.3a**. This mutant displays similar pili number per cell than the *fliC* strain that can extend and retract without the need for attachment. Acquisition rate: 200 fps. The movie is visualized 5 times slower compared to real speed. The width of the field of view is 16.3 μm. Similar results were observed in all our visualizations (at least 3 biological replicates).

Supplementary Video 3.7: iSCAT visualization of a twitching *pilU* *fliC* cell. (AVI file, 1.39 MB)

Visualization of a *pilU* *fliC* cell. Acquisition rate 10 fps, temporal binning 4x. The movie is visualized 4 times faster than real speed. The width of the field of view is 20.6 μm. Similar results were observed in all our motility visualizations in *pilU* *fliC* (number of tracks *n* = 15).

Supplementary Video 3.8: Visualization of twitching motility in high friction environment highlights a function for PilU in force generation. (AVI file, 16.0 MB)

Phase contrast videos of *fliC*, *pilU* *fliC* and *pilU* colonies sandwiched between glass and 0.5% agarose gels (top left, bottom right and bottom left respectively). Single *fliC* cells were highly motile at the colony's leading edge, whereas *pilU* *fliC* and *pilU* mutants barely expanded in the same timeframe. This defect is recapitulated by visualizing *fliC* under 1% agarose gel (top right). Acquisition rate: 1 fps. The movie is accelerated 10 times. Experiments were performed in triplicates.

Supplementary Video 3.9: iSCAT visualization of extension, attachment and retraction of a TFP. (AVI file, 1.84 MB)

High frame rate visualization of pili extending, attaching and retracting of the *fliC⁻* cell shown in **Figure 3.4b**. The movie is slowed 30 times to better visualize the time delay between attachment and retraction until the pilus is under tension. Acquisition rate: 300 fps, temporal binning 2x. The width of the field of view is 16.3 µm. Similar results were observed in all our visualizations (at least 3 biological replicates).

Supplementary Video 3.10: iSCAT visualization of extension, attachment and retraction of a TFP. (AVI file, 1.84 MB)

Same as for **Supplementary Video 3.9** but played at real speed.

NB: Supplementary videos are located at the following link: https://www.nature.com/articles/s41564-019-0378-9#Sec14

Chapter 4. Mechanotaxis directs *Pseudomonas aeruginosa* twitching motility

Author

Marco J. Kühn†[,1], Lorenzo Talà†[,1], Yuki Inclan[2], Ramiro Patino[2], Xavier Pierrat[1], Iscia Vos[1,4], Zainebe Al-Mayyah[1],

Henriette MacMillan[2], Jose Negrete[1,4], Joanne N. Engel*[,2,3] and Alexandre Persat*[,1]

Affiliations

[1]Institute of Bioengineering and Global Health Institute, School of Life Sciences, EPFL, Lausanne, Switzerland

[2]Departments of Medicine and of [3]Microbiology and Immunology, University of California, San Francisco, USA

[4]Institute of Physics, School of Basic Sciences, EPFL, Lausanne, Switzerland

†Equally contributed to the work

*Corresponding author: joanne.engel@ucsf.edu and alexandre.persat@epfl.ch

My contributions: Desing of the experiment for iSCAT measurement and static protein localization, coupling a fluorescence channel to the iSCAT microscope, acquire microscopy data and perform data analysis.

4.1 Abstract

The opportunistic pathogen *Pseudomonas aeruginosa* explores surfaces using twitching motility powered by retractile extracellular filaments called type IV pili (T4P). Single cells twitch by sequential T4P extension, attachment and retraction. How single cells coordinate T4P to efficiently navigate surfaces remains unclear. We demonstrate that *P. aeruginosa* actively directs twitching in the direction of mechanical input from T4P, in a process called mechanotaxis. The Chp chemotaxis-like system controls the balance of forward and reverse twitching migration of single cells in response to the mechanical signal. Collisions between twitching cells stimulate reversals, but Chp mutants either always or never reverse. As a result, while wild-type cells colonize surfaces uniformly, collision-blind

Chp mutants jam, demonstrating a function for mechanosensing in regulating group behavior. On surfaces, Chp senses T4P attachment at one pole thereby sensing a spatially-resolved signal. As a result, the Chp response regulators PilG and PilH control the polarization of the extension motor PilB. PilG stimulates polarization favoring forward migration, while PilH inhibits polarization inducing reversal. Subcellular segregation of PilG and PilH efficiently orchestrates their antagonistic functions, ultimately enabling rapid reversals upon perturbations. The distinct localization of response regulators establishes a signaling landscape known as local-excitation, global-inhibition in higher order organisms, identifying a conserved strategy to transduce spatially-resolved signals.

4.2 Significance statement

Single-cells across kingdoms of life explore, prey, escape or congregate using surface-specific motility. Motile eukaryotic cells use chemotaxis to direct migration on surfaces. However, how bacteria control surface motility remains underexplored. *Pseudomonas aeruginosa* twitches on surfaces by successive extension and retraction of extracellular filaments called type IV pili. Here, we show that *P. aeruginosa* directs twitching by sensing mechanical input generated by type IV pili. The Chp sensory system performs spatially-resolved mechanosensing by harnessing two response regulators with antagonistic functions. Our results demonstrate that sensory systems, whose input often remain elusive, can sense mechanical signals to actively steer motility. Furthermore, Chp establishes a signaling principle shared with higher order organisms, identifying a conserved strategy to transduce spatially-resolved signals.

4.3 Introduction

Single-cell organisms have evolved motility machineries to explore their environments. For example, bacteria utilize swimming motility to propel themselves through fluids. In their natural environments, bacteria are however most commonly found associated to surfaces (*10*). Many species use surface-specific motility systems such as twitching, gliding, and swarming to migrate on solid substrates (*67*). However, we still know very little about how cells regulate and control surface motility. In particular,

the role of mechanical signals in regulating the motility of single cells remains vastly underexplored in bacteria, as well as in higher order microorganisms (*68*).

To migrate towards nutrients and light or away from predators and toxins, cells actively steer motility in response to environmental signals. For example, chemotactic systems mediate motility towards specific molecular ligands (*69, 70*). Bacteria have a remarkably diverse set of chemotaxis systems. The canonical Che system, which has been extensively studied as a regulator of *Escherichia coli* swimming, is widely conserved among motile species including non-swimming ones (*71*). However, the signal inputs and the motility outputs of other bacterial chemotaxis-like systems remain incompletely understood in many species (*72*). Finally, chemotaxis-like systems are found with alternative signaling architectures, including additional components compared to the Che system. For example, while Che controls flagella rotation by phosphorylation of a single response regulator, other species can use up to six. The functions of these supplementary elements remain cryptic (*73*).

Pseudomonas aeruginosa is a major opportunistic pathogen well-adapted to growth on surfaces. *P. aeruginosa* colonizes and explores abiotic and host surfaces using twitching motility, which is powered by retractile extracellular filaments called type IV pili (T4P) (*9*). During twitching, single cells pull themselves by successive rounds of T4P extension, attachment and retraction (*9, 52*). T4P extend and retract from the cell surface by respective polymerization and depolymerization of the pilin subunit PilA at the poles (*9, 52*). While an understanding of the assembly mechanisms of individual filaments is beginning to emerge, we still don't know whether and how cells coordinate multiple T4P at their surface to power migration over large distances.

Genetic studies show that a chemotaxis-like system called Chp regulates twitching (*11*). Beyond playing a role in the transcription of T4P genes, the mechanism by which Chp regulates motility remains unknown (*12, 74*). Also unlike Che which possesses a single response regulator, the Chp system possesses two response regulators, PilG and PilH, whose respective functions and mechanism of action are incompletely resolved (*13*) (**Figure 4.1A**). Most Chp mutants twitch aberrantly most often due to downregulation of T4P machinery, making their motility phenotypes

hard to interpret (*11*). In addition, unlike homologs from the well-studied canonical *E. coli* Che system, the Chp methyl-accepting chemotaxis protein called PilJ has no clear chemical ligand (*12, 13*). Several chemical compounds bias collective or single cell twitching migration in a Chp-dependent manner (*75–78*). For example, single *P. aeruginosa* cells twitch up strong gradients of dimethylsulfoxide (*77*). Because most Chp mutants have strong piliation defects, it remains unclear whether chemical gradients passively bias twitching displacements or actively guide motility via chemosignaling.

We previously demonstrated that *P. aeruginosa* upregulates genes coding for virulence factors upon surface contact in a T4P- and Chp-dependent manner (*3, 74*). However how Chp controls motility independently of transcription remains unresolved (*11, 12, 79*). The homology between Chp and Che systems suggests a tactic function for Chp. As a result, we rigorously tested the hypothesis that Chp regulates twitching motility of single cells in response to T4P mechanical input at short timescales.

4.4 Results

The canonical Che system regulates bacterial swimming by transducing an input chemical signal into a motility response via flagellar rotation control (*80*). By analogy, we hypothesized that the chemotaxis-like Chp system regulates the trajectory of single twitching cells (*12*). Chp mutants twitch aberrantly in the traditional stab assay (SI Appendix, **Supplementary Figure 4.1*A* and *B***) (*74, 79*). These mutants also have altered cyclic AMP (cAMP) levels (SI Appendix, **Supplementary Figure 4.1*C***) (*3*). cAMP regulates the transcription of virulence genes upon surface contact, so that Chp mutants have aberrant T4P numbers (SI Appendix, **Supplementary Figure 4.1*D***) (*3*). To overcome a potential cross-talk, we decoupled the Chp-dependent, short timescale motility control from cAMP-dependent transcription by investigating single cell twitching in constitutively low or high cAMP regimes.

We first explored the functions of Chp in directing twitching motility by visualizing individual isolated motile WT (**Figure 4.1*B***, **Movie S4.1**), Δ*cpdA*, Δ*pilH,* and Δ*pilGcpdA* cells, at the interface between a glass coverslip and an agarose pad. For these strains, which all have elevated cAMP levels (SI Appendix, **Supplementary Figure 4.1*C***), we computed the linear displacements of single cells to

visually highlight the balance between persistent forward motion and reversals for single cells (**Figure 4.1*C***). We also computed their mean reversal frequency (**Figure 4.2*A***). WT and Δ*cpdA* cells mostly move persistently forward and only occasionally reversed twitching direction (**Figure 4.1*C* and Figure 4.2*A***). Δ*pilGcpdA* cells reversed so frequently that they appeared to "jiggle", never committing to a single direction of twitching (**Movie S4.2, Figure 4.1*C* and Figure 4.2*A***). They ultimately had very little net migration, consistent with their reduced twitching motility in the stab assay (SI Appendix, **Supplementary Figure 4.1*A***). By contrast, Δ*pilH* moved very persistently in a single direction and reversed very rarely (**Figure 4.1*C* and Figure 4.2*A***). Likewise, Δ*pilHcyaB*, which has reduced cAMP levels compared to Δ*pilH,* had near zero reversal frequency, confirming the Chp-dependent, cAMP-independent control of twitching direction (**Figure 4.2*A***).

WT cells often reversed their twitching direction after a side collision (**Figure 4.2*B* and *C*, Movie S4.3**). Δ*pilGcpdA* reversed almost always after impact, whereas Δ*pilH* almost never did (**Figure 4.2*B* and *C*, Movie S4.3**). This suggest that cell-cell contact may mechanically interrupt Chp signaling at the colliding pole, or that Chp chemically senses the surface of the other cell. To distinguish between these hypotheses, we inspected how cells reversed upon collisions with non-biological material. We produced micrometer-wide glass microfibers that we added to the twitching environment, thereby producing obstacles to the motile bacteria. Upon colliding these microfibers, WT cells often reversed twitching direction (**Figure 4.2*D*, Movie S4.4**). The rate of reversal upon colliding glass was indistinguishable from collisions with other cells (**Figure 4.2*E***). These observations are therefore consistent with a mechanism where cell-cell contact mechanically perturb Chp signaling.
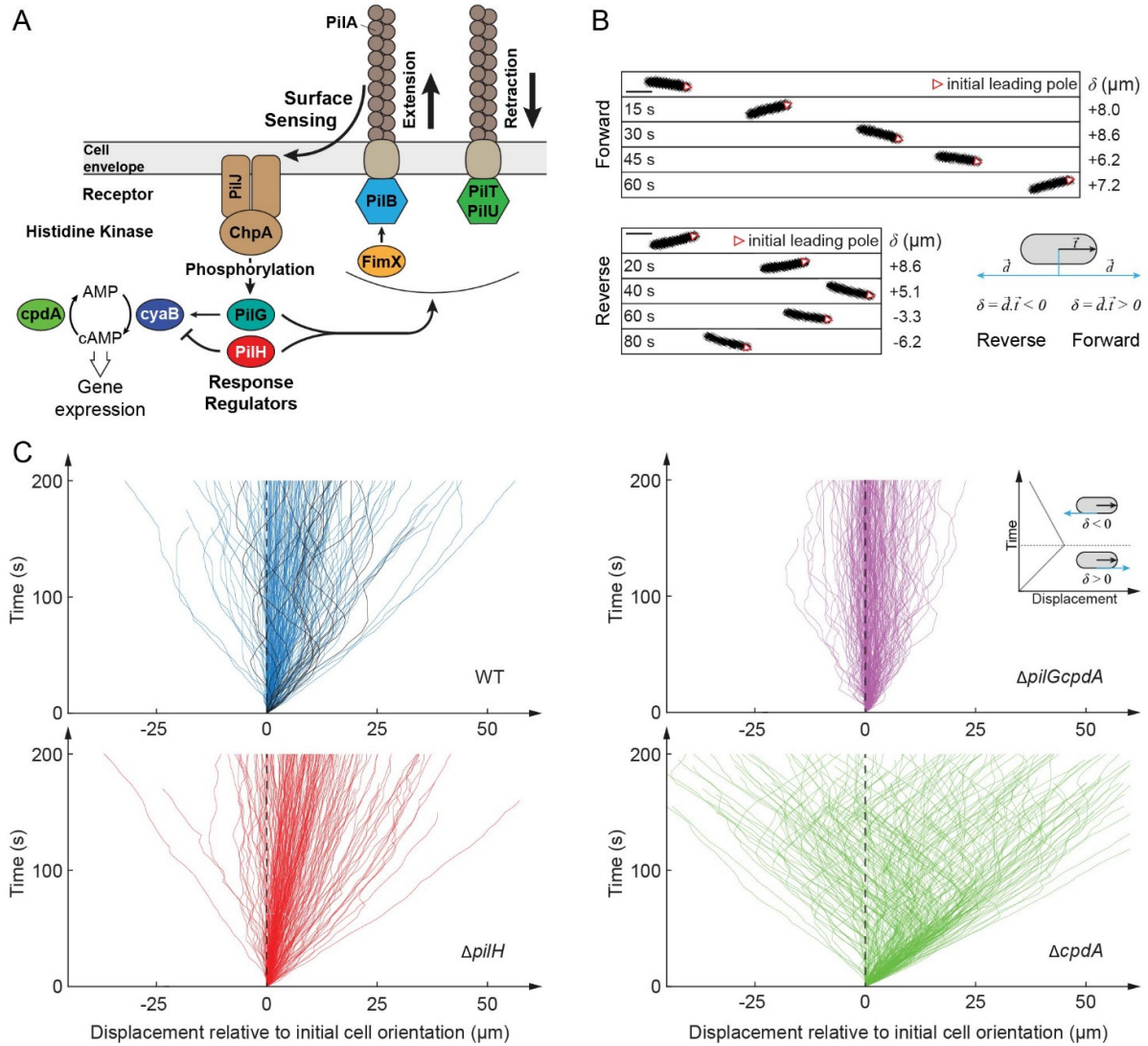
Figure 4.1: The Chp system regulates the twitching trajectories of individual *P. aeruginosa* cells.

(*A*) Schematic representation of the major components of the T4P and Chp system. (*B*) Phase contrast snapshots of forward and reverse migration of twitching cells. $\vec{t}$ is a unit vector oriented along the cell body in the initial direction of motion. $\vec{d}$ is the unit displacement vector. δ is the dot product $\vec{d}.\vec{t}$, which quantifies displacements relative to the initial direction of motility. The red triangle indicates the initial leading pole of the bacterium. Scale bar, 2 µm. (*C*) Graphs of cumulative net displacement as a function of time, highlighting the forward and reverse twitching behavior of Chp mutants. Each curve corresponds to an individual cell trajectory. Tracks of reversing WT cells are highlighted in black. At any given time, a curve oriented toward the top right corresponds to a cell moving forward, while a curve oriented toward top left corresponds to reverse movement (*cf.* inset). Δ*pilGcpdA* constantly reverses twitching direction while Δ*pilH* cells persistently move forward.

The Chp-dependent control of reversal rates is reminiscent of the role of Frz sensory system in controlling motile collective behavior in *Myxococcus xanthus* (*81, 82*). We therefore explored how mutations in Chp influenced group motility. At high cell density, WT cells spread relatively evenly

over the surface (**Figure 4.2*F***). In contrast, collision-blind Δ*pilH* cells jammed head-to-head, forming small groups that inefficiently moved forwards (**Figure 4.2*F*, Movie S4.5**). At much higher cell density, in a WT colony, the bacteria distribute evenly across the field of view and form persistent rafts at the leading edge thereby expanding the colony edge rapidly (SI Appendix, **Supplementary Figure 4.2, Movie S4.6**). Δ*pilH* colonies tend to form clusters of cells jamming into each other, forming swirls and comet-like rafts of migrating cells that quickly disperse, thereby inhibiting persistent collective migration (SI Appendix, **Supplementary Figure 4.2, Movie S4.6**). As a consequence, the leading edge expands more slowly compared to WT, resulting in smaller colony diameter in twitching stab assays (SI Appendix, **Supplementary Figure 4.1A**). These observations could explain the patterns observed at the edge of larger colonies (*13, 83*). In summary, by controlling reversal rates upon collision, Chp-dependent mechanosensing can optimize *P. aeruginosa* collective motility*.

Chp provides single *P. aeruginosa* cells with the ability to migrate persistently in one direction and to rapidly change twitching direction. PilG promotes persistent forward motility, driving migration over long distances. PilH enables directional changes particularly useful upon collisions with other bacteria.

To investigate how PilG and PilH control twitching direction, we focused on the distribution of T4P between the two poles of a cell. We imaged *P. aeruginosa* by interferometric scattering microscopy (iSCAT) to quantify T4P at each cell pole and evaluate their distributions. We found that the T4P of WT and Δ*cpdA* were nearly randomly distributed (SI Appendix, **Supplementary Figure 4.3**). In contrast, T4P of Δ*pilGcpdA* were distributed more symmetrically compared to the random distribution and to WT. While Δ*pilH* had too many T4P for a direct comparison with other mutants, we could quantify symmetry in the less piliated Δ*pilHcyaB* background (SI Appendix, **Supplementary Figure 4.1*D***). The T4P of Δ*pilHcyaB* were markedly more asymmetrically distributed than WT (SI Appendix, **Supplementary Figure 4.3**), consistent with its inability to reverse twitching direction. We conclude that the Chp system polarizes T4P to regulate twitching direction. PilG promotes unipolar T4P

deployment driving persistent forward migration, while PilH promotes T4P deployment at both poles simultaneously, favoring reversals.

T4P extend and retract from the cell surface by respective polymerization and depolymerization of the pilin subunit PilA at the poles. The extension motor PilB assembles PilA monomers to extend T4P, while the retraction motors PilT and PilU disassemble filaments to generate traction forces (**Figure 4.1A**) (*9, 52*). We reasoned that for the Chp system to regulate T4P polarization and set a cell's twitching direction, it must control either extension or retraction at a given pole. To test this hypothesis, we investigated how the localization of extension and retraction motors regulate the deployment of T4P to direct twitching. First, we simultaneously visualized T4P distribution and motor protein subcellular localization within single cells. To this end, we generated chromosomal mNeonGreen (mNG) fluorescent protein fusions at their native loci to the extension motor PilB, to its regulator FimX (*84*), and to the retraction motors PilT and PilU (Figure 4.3*A*). All fusion proteins were functional and exhibited primarily bright fluorescent foci at one or both poles, globally consistent with inducible plasmid-borne fusion proteins, with the exception of PilU which had been reported as asymmetrically localized but under different imaging, expression and growth conditions (*60, 85*). We leveraged correlative iSCAT-fluorescence microscopy for simultaneous imaging of T4P and fluorescent reporter fusions (**Figure 4.3B**) (*31*). In single cells, we identified the pole with brightest fluorescent signal and the pole with most T4P. We then categorized cells into two groups: cells with more T4P at the bright pole versus cells with less T4P at the bright pole. We found that in more than 60% of cells, the poles with more T4P had the brightest PilB-mNG fluorescent signal (**Figure 4.3C**) (*60*). On the other hand, we found no negative correlation between mNG-PilT or mNG-PilU signals and relative numbers of T4P, which would be expected if cells controlled T4P distribution using retraction. We conclude that PilB, but neither PilT nor PilU, control the polarized deployment of T4P.
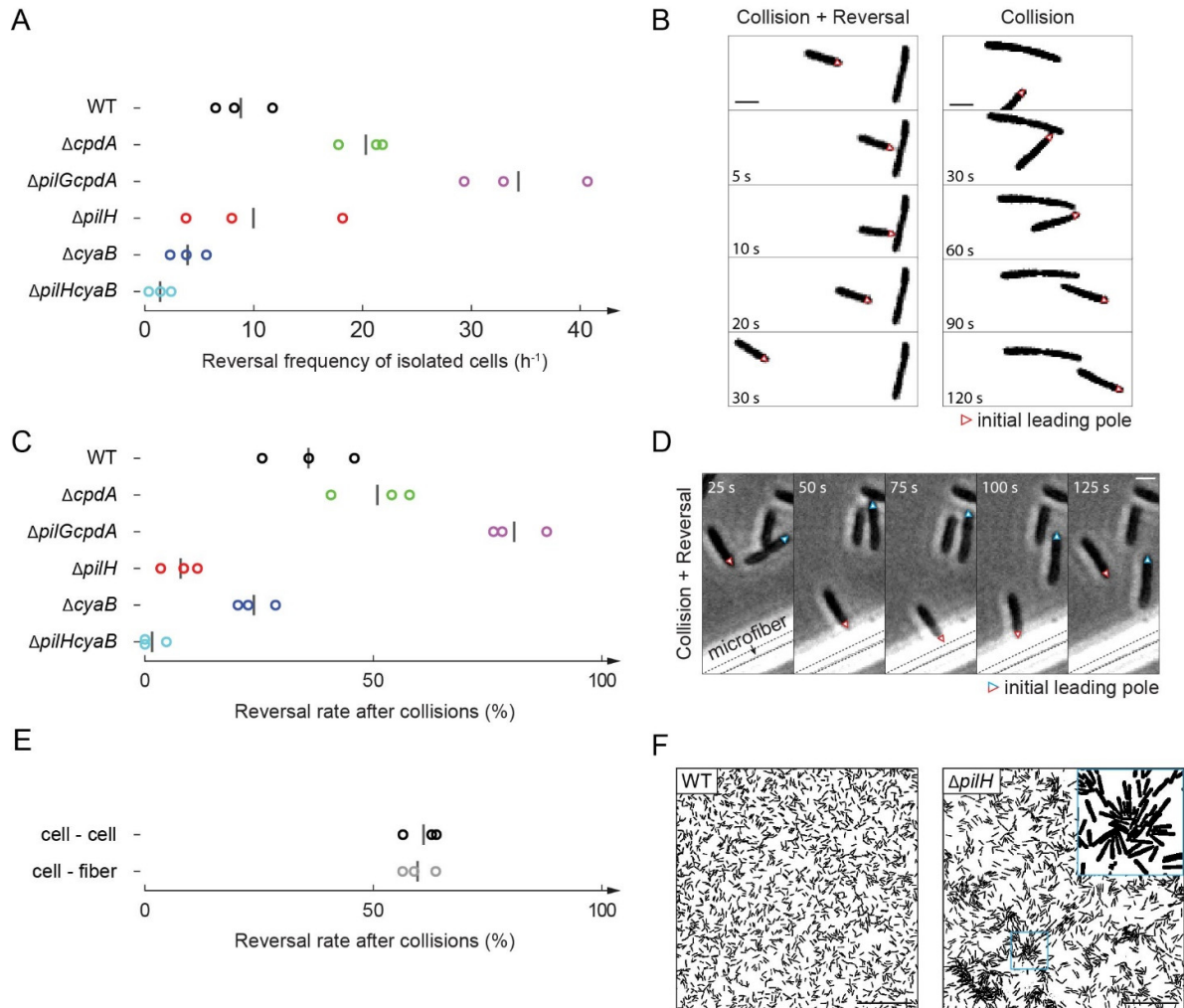
Figure 4.2: The Chp system controls reversals of twitching *P. aeruginosa* cells.

(*A*) Quantification of reversal rates in Chp and cAMP mutants. Δ*pilGcpdA* has highest reversal frequency. Δ*pilH* has a two-fold lower reversal frequency than Δ*cpdA*. Circles correspond to biological replicates, black bars represent their mean. (*B*) Snapshots of WT reversing upon collision with another cell (left). The same sequence for a Δ*pilH* cell, failing to reverse upon collision (right). The red triangle indicates the initial leading pole of the bacterium. Scale bar, 2 μm. (*C*) Fraction of cells reversing upon collision with another cell. About half of WT cells reverse after collision, Δ*pilH* almost never reserves after collision, and Δ*pilGcpdA* almost always reverses. Circles correspond to biological replicates, black bars represent their mean. (*D*) Phase contrast image sequence of WT cells reversing upon collision with glass microfibers and other cells. The dashed lines indicate the position of the fiber. Scale bar, 2 μm. (*E*) Fraction of WT cells reversing upon collision with another cell and with a glass microfiber. 60% of cells reverse after collision irrespective of the type of obstacle. Circles correspond to biological replicates, black bars represent their mean. (*F*) While WT is able to move efficiently at high density, the reduced ability of Δ*pilH* to reverse upon collision leads to cell jamming and clustering. Scale bar, 50 μm. Background strain: PAO1 Δ*fliC*.

Since most, but not all cells had more TFP at the bright PilB pole, we considered whether PilB controls the direction of twitching migration of single *P. aeruginosa* cells. To test this hypothesis, we investigated the dynamic localization of motors in single twitching cells (SI Appendix, **Supplementary Figure 4.4, Movie S4.7**). While mNG-PilT and mNG-PilU fusions were fully functional, PilB-mNG exhibited a partial twitching motility defect (SI Appendix, **Supplementary Figure 4.5**). We therefore systematically validated PilB localization results by visualization of its regulator FimX using mNG-FimX, which was fully functional (SI Appendix, **Supplementary Figure 4.5**). We tracked single cells while measuring the subcellular localization of the fusion proteins. We first categorized cells as moving and non-moving. We then measured the proportion of cells that had asymmetric and symmetric protein localizations based on a threshold of fluorescence ratio between poles. We found that PilB-mNG and mNG-FimX localizations were more asymmetric (*i.e.* polarized) in moving cells compared to non-moving cells (**Figure 4.3D**). In addition, both fusion proteins changed localization and polarity during reversals (SI Appendix, **Supplementary Figure 4.6, Movie S4.8**) (84). In contrast, the localization of mNG-PilT and mNG-PilU was largely symmetric across the population, without marked symmetry differences between non-moving and moving cells. Since PilB and FimX polarize in moving cells, we computed the correlation between the twitching direction and fusion protein polarization (*i.e.* the localization of their brightest polar spot). We found that more than 90% of cells moved in the direction of the bright PilB and FimX pole (**Figure 4.3E**). Thus, PilB polarization correlates more strongly with motility than with T4P number (**Figure 4.3C**). While we measure twitching for minutes, over nearly hundred T4P extension and retraction events (41), correlative iSCAT gives a snapshot of the T4P distribution in a given cell, explaining the discrepancy between conditions. Altogether, our data shows that polarized extension and constitutive retraction controls *P. aeruginosa* twitching direction.
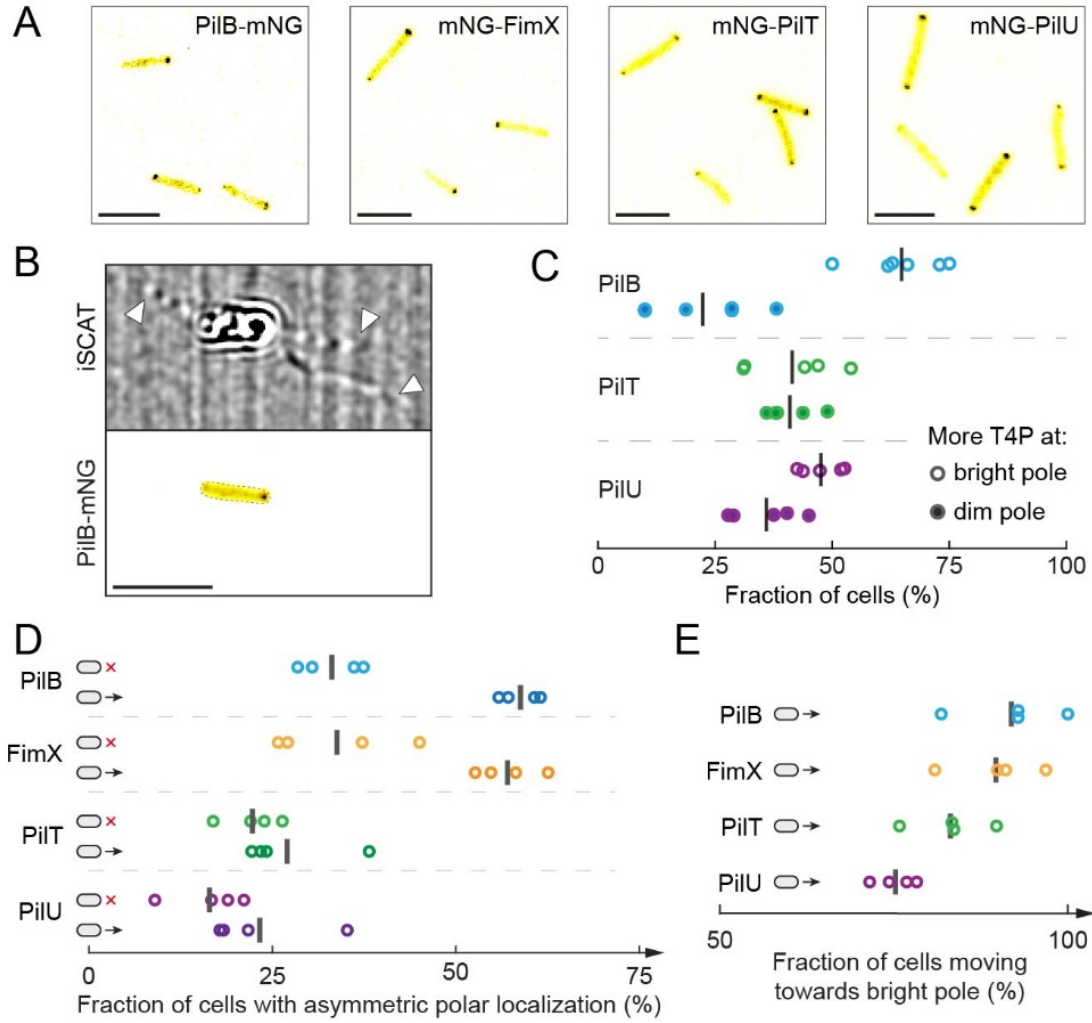
Figure 4.3: The localization of the extension motor PilB sets the direction of twitching and the polarization of T4P activity.

(*A*) Snapshot of chromosomal fluorescent protein fusions to the extension motor PilB, its regulator FimX, and the retraction motors PilT and PilU. Scale bars, 5 µm. (*B*) Simultaneous imaging of PilB-mNG and T4P by correlative iSCAT fluorescence. White arrowheads indicate T4P. Scale bar, 5 µm. (C) Fraction of cells with more T4P at bright *vs* dim fluorescent pole. Most cells have more T4P at the bright PilB-mNG pole. We could not distinguish a T4P depletion at the bright retraction motor poles. Each circle is the mean fraction for one biological replicate. Black bars correspond to their mean across replicates. (*D*) Comparison of the symmetry of polar fluorescence between moving and non-moving cells. PilB and FimX signal is more asymmetric in moving cells, which is not the case for PilT and PilU. (*E*) Fraction of cells twitching in the direction of their brightest pole. Circles correspond the fraction of each biological replicate, black bars represent their mean.

The Chp system regulates T4P distribution, which itself is under the control of the PilB polarization. Since T4P and Chp mediate surface sensing to regulate transcription, we hypothesize that mechanosensing also regulates the subsequent extension of additional T4P (*3*). As a result, we tested whether T4P activity itself regulates PilB polarization. We reasoned that the longer a cell resides on a surface, the more likely it is to experience mechanical stimuli from T4P. We thus compared polarization of cell populations immediately after contact (10 min) with populations that were associated with the surface for longer times (60 min). We focused on the dynamic localization of mNG-FimX. First, we found that in many cells, polar mNG-FimX foci relocated from pole to pole within a short timeframe after surface contact, as if they were oscillating (**Figure 4.4*A*, Movie S4.9**). These observations were reminiscent of oscillations in the twitching and gliding regulators observed in *M. xanthus* (*82, 86, 87*). The proportion of cells exhibiting these oscillations became smaller after prolonged surface contact (**Figure 4.4*B***, SI Appendix, **Supplementary Figure 4.7*A***), suggesting that surface sensing inhibits mNG-FimX oscillations and stabilizes polarization. To test whether mechanosensing with T4P induces polarization of the extension machinery, we visualized mNG-FimX in a Δ*pilA* mutant background, which also displayed oscillations (**Figure 4.4*C*, Movie S4.10**). We found that the fraction of Δ*pilA* cells that showed mNG-FimX oscillations 10 and 60 min after surface contact were equal, near 90% (**Figure 4.4*D***). The distributions of oscillation frequencies between these two states were also indistinguishable (SI Appendix, **Supplementary Figure 4.7*B***). Altogether, our results demonstrate that T4P-mediated mechanosensing at one pole locally recruits and stabilizes extension motors, thereby inducing a positive feedback onto their own activity. While several exogenous molecular compounds bias collective or single cell twitching migration (*75–78*), our data shows chemical gradients are not necessary for active regulation of twitching.
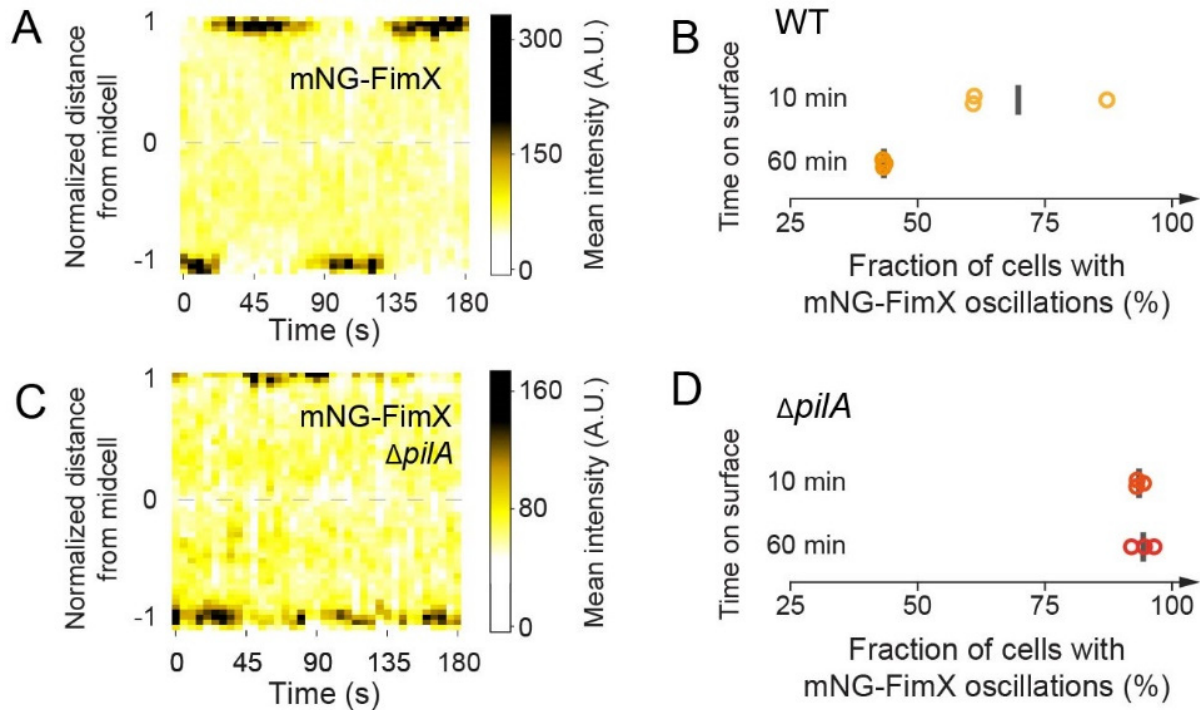
Figure 4.4: Mechanical input signal from T4P controls the polarization of FimX, the activator of the extension motor PilB.

(*A*) Kymograph of mNG-FimX fluorescence in a non-moving cell 10 min after surface contact. The bright fluorescent focus sequentially disappears from one pole to appear at the opposite to establish oscillations. (*B*) Fraction of cells that showed pole to pole oscillations in WT and Δ*pilA*. The proportion of oscillating WT reduces as they remain on the surface, conversely increasing the proportion of stably polarized cells. (*C*) Kymograph of mNG-FimX fluorescence in a Δ*pilA* background 60 min after surface contact. Scale bar, 5 µm. (*D*) Most Δ*pilA* cells maintain oscillatory fluctuations in mNG-FimX polar localization.

PilB polarization sets the twitching direction of single cells, and PilG and PilH regulate T4P polarization to control reversals. We therefore investigated how the Chp system regulates PilB localization to control a cell's direction of motion. We compared the mean localization profiles of PilB-mNG and mNG-FimX in WT, Δ*pilG* and Δ*pilH* backgrounds (**Figure 4.5A and B**, SI Appendix, **Supplementary Figure 4.8A**). Both fusion proteins had greater polar fluorescent signal in Δ*pilH* and lower polar signal in Δ*pilG* compared to WT (**Figure 4.5C and D**). We computed a polar localization index which measures the proportion of the signal localized at the poles relative to the total fluorescence (SI Appendix, **Supplementary Figure 4.8B**). About 50% of the mNG-FimX and PilB-mNG signal is found at the poles for WT, 70% of the signal is polar in Δ*pilH*, and most of the signal is diffuse in Δ*pilG* (**Figure 4.5E and G**). We next computed a symmetry index that quantifies the

extent of signal polarization, that is how bright a pole is compared to the other, with a value of 0.5

being completely symmetric (SI Appendix, **Supplementary Figure 4.8***B*). WT cells grown in liquid

had a mNG-FimX and PilB-mNG symmetry index of about 0.6 (**Figure 4.5***F* **and** *H*). In contrast,

Δ*pilH* cells were more polarized, with a symmetry index close to 0.75. Compared to WT, mNG-FimX

was more symmetric in a Δ*pilG* background (**Figure 4.5***H*). We verified that the increase in

expression levels in the different Chp mutants did not exacerbate PilB and FimX localization and

polarization (SI Appendix, **Supplementary Figure 4.9**). In summary, we showed that PilG promotes

polar recruitment and polarization of PilB and its regulator FimX, which is counteracted by PilH.
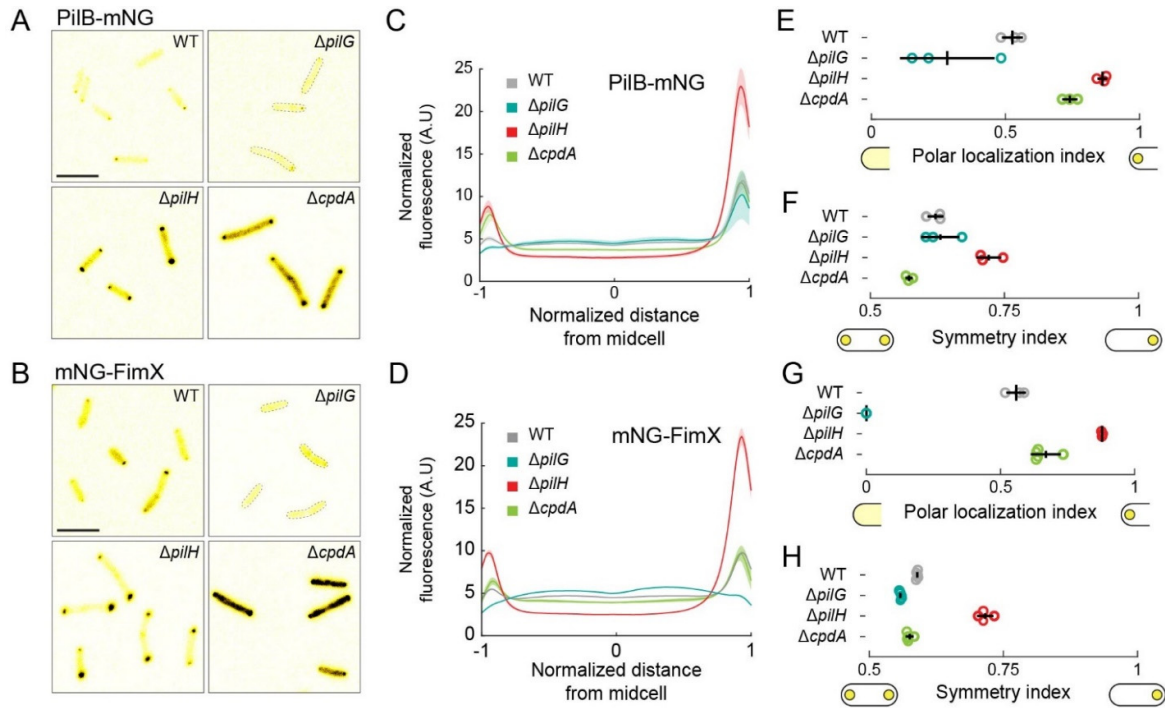
Figure 4.5: PilG and PilH control the polarization of T4P extension machinery

Snapshots of PilB-mNG (*A*) and mNG-FimX (*B*) fluorescence in WT, Δ*pilG*, Δ*pilH* and Δ*cpdA* background. Scale bar, 5 μm. (*C*, *D*) Normalized fluorescence profiles along the major cell axis of the motor protein PilB and its activator FimX (SI Appendix, **Supplementary Figure 4.8***A*). Solid lines: mean normalized fluorescence profiles across biological replicates. Shaded area: standard deviation across biological replicates. (*E*, *G*) Polar localization index of PilB-mNG and mNG-FimX respectively, quantifying the extent of polar signal compared to a diffused configuration (SI Appendix, **Supplementary Figure 4.8***B*). An index of 0 and 1 respectively correspond to completely diffuse and polar signals. Relative to WT and Δ*cpdA*, polar localization is higher in Δ*pilH* and lower in in Δ*pilG*. (*F*, *H*) Symmetry index of PilB-mNG and mNG-FimX respectively, representing the ratio of the brightest pole fluorescence to the total polar fluorescence. 0.5 and 1 respectively correspond to a symmetric bipolar and a unipolar localization. Δ*pilH* has higher symmetry index than WT and Δ*cpdA*. Circles: median of each biological replicate. Black bars: (vertical) mean and (horizontal) standard deviation across biological replicates.

We then wondered how *P. aeruginosa* orchestrates two response regulators with opposing functions. Yeast and amoebae control cell polarization in response to environmental cues using spatially structured positive and negative feedback (*88*). By analogy, we considered a model wherein PilG and PilH segregate to implement positive and negative feedback at distinct subcellular locations (*89*). We therefore investigated the localization of functional mNG-PilG and mNG-PilH integrated at their native chromosomal loci (**Figure 4.6A**). We found that PilG predominantly localizes to the poles (**Figure 4.6B and C**). In contrast, PilH is mainly diffuse in the cytoplasm, with only a small fraction at the poles (**Figure 4.6B and C**). *P. aeruginosa* can therefore ensure the antagonistic functions of PilG and PilH by localizing the former to the poles and the latter to the cytoplasm.

We next analyzed the relationship between a cell's direction of migration with mNG-PilG and mNG-PilH polarization (SI Appendix, **Supplementary Figure 4.10A, Movie S4.11**). We found that 90% of cells moved towards their bright mNG-PilG pole, while only 50% moved towards their bright mNG-PilH, corresponding to a random orientation relative to the direction of migration (**Figure 4.6D**). By comparing the asymmetry of polar foci, we found that mNG-PilG signal was largely asymmetric in motile cells compared to the non-motile population (**Figure 4.6E**). Correlative iSCAT fluorescence highlighted that the brightest mNG-PilG polar spots had more T4P (**Figure 4.6F**). Consistent with this finding, in cells that reversed twitching direction, mNG-PilG localization switched to the new leading pole prior to reversal (SI Appendix, **Supplementary Figure 4.10B, Movie S4.12**). We found that the polar signal of mNG-PilH was mainly symmetric, both in moving and non-moving subpopulations (**Figure 4.6D**). Thus, PilG, but not PilH, actively localizes to the leading pole during twitching, recapitulating the dynamic polarization of PilB and FimX. We confirmed this by imaging the double fluorescent protein fusions mScarlet-I-PilG with mNG-FimX and mScarlet-I-PilG with PilB-mNG (SI Appendix, **Supplementary Figure 4.11 and Supplementary Figure 4.12A**). In both strains, the FimX/PilB and PilG colocalized at the leading pole of twitching cells (SI Appendix, **Supplementary Figure 4.12B**) and changed polarization upon reversals (SI Appendix, **Supplementary Figure 4.12C-F**). We could not however distinguish the order at which FimX and PilG changed polarity during reversals, nor could we measure differences in the delay between

motility reversal and polarity changes in single fusions (SI Appendix, **Supplementary Figure 4.13).**

Therefore, T4P input at the leading pole activates PilG. Polar PilG rapidly drives a local positive

feedback on T4P extension to maintain the direction of twitching. Cytoplasmic PilH stimulate

reversals by inhibiting PilB polarization, permitting reassembly at the opposite pole. In summary, *P.*

aeruginosa controls mechanotactic twitching using a local-excitation, global-inhibition signaling

network architecture akin to chemotactic signaling in amoebae and neutrophils (SI Appendix,

Supplementary Figure 4.14) (*70, 90*).
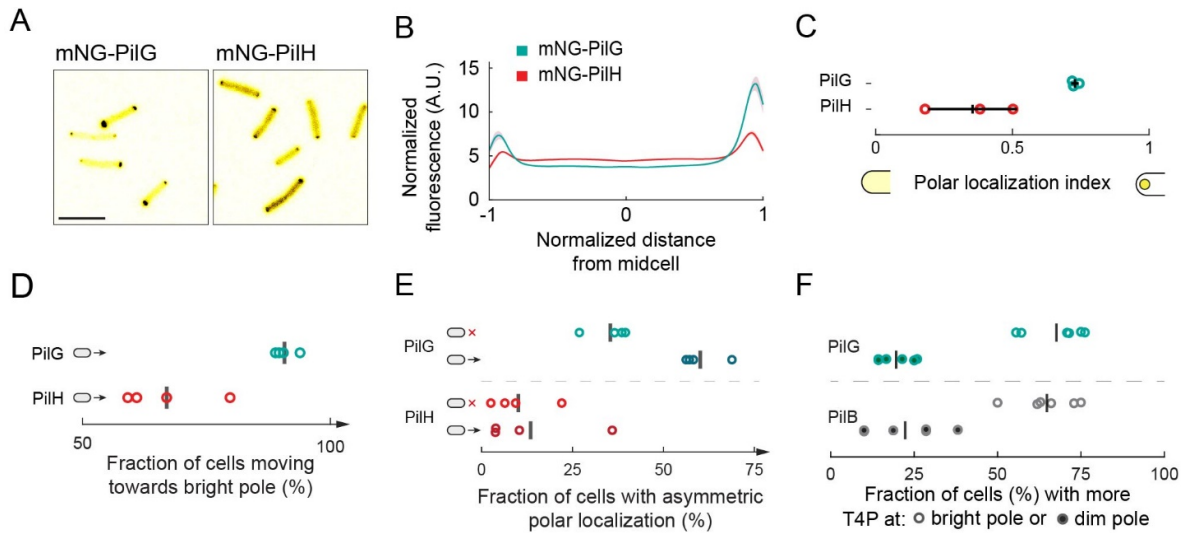
Figure 4.6: PilG and PilH dynamic localization establish a local-excitation, global-inhibition signaling landscape.

(A) Snapshots of mNG-PilG and mNG-PilH fluorescence. Scale bar, 5 μm. (B) Comparison of mNG-PilG and mNG-PilH normalized mean fluorescent profiles. (C) The polar localization index of mNG-PilG is relatively large showing PilG is mostly polar. In contrast, mNG-PilH has a low polar localization index and is thus mostly cytoplasmic. Circles: median of each biological replicate. Black bars: (vertical) mean and (horizontal) standard deviation across biological replicates (D) Protein polarization relative to the twitching direction. Cells predominantly move towards the brighter mNG-PilG pole. The fraction for mNG-PilH is close to 50 %, corresponding to a random polarization relative to the direction of motion. Black bars: mean across biological replicates (E) Comparison of the symmetry of the polar fluorescent foci of moving cells with non-moving cells for mNG-PilG and mNG-PilH fusion proteins. There is an enrichment for mNG-PilG polar asymmetry in moving cells, but no differences in mNG-PilH. Black bars: mean across biological replicates (F) Fraction of cells with more T4P at bright vs dim mNG-PilG fluorescent pole. Most cells have more T4P at the bright mNG-PilG pole, similar to PilB (data from Figure 4.3C in gray as reference). Each circle is the mean fraction for one biological replicate. Black bars correspond to their mean across replicates.

4.5 Discussion

We discovered that *P. aeruginosa* controls the direction of twitching motility in response to mechanical signals through the motility machinery itself. This migration strategy differs from the one employed in chemotactic control of swimming motility. Chemotaxis systems control the rate at which swimming cells switch the direction of rotation of their flagella, generating successive run-and-tumbles [69, 80] or flicks [91] that cause directional changes. However, T4P must disassemble from one pole and reassemble at the opposite in order to reverse cell movement. In essence, this tactic strategy is akin to the one of single eukaryotic cells such as amoebae and neutrophils that locally remodel their cytoskeleton to attach membrane protrusions in the direction of a stimulus [70]. *P. aeruginosa* twitching direction is also biased by chemical gradients, suggesting that Chp also senses chemical stimuli [75–78]. Our results do not disprove that Chp controls twitching chemotactically, but provide a complementary perspective on these observations. In one scenario, a strong chemical gradient could produce a gradient in surface chemistry that causes differential adhesion of T4P between leading and lagging poles, inducing a bias in twitching direction. The relative contributions of chemical and mechanical inputs in activating the Chp system will therefore require further biophysical investigations.

Ultimately, the ability to balance persistent forward migration with reversals optimizes *P. aeruginosa* individual twitching. Reversal may occur spontaneously or upon perturbations, for example when colliding another cell. The Chp system may also promote asymmetric piliation of upright twitching *P. aeruginosa* cells during exploratory motility [49]. We also found that the ability to reverse upon collision prevents jamming of groups of cells, supporting a model wherein the Chp system orchestrates collective migration [12]. More generally, we anticipate that other bacteria, as well as archaeal and eukaryotic species that actively migrate on surfaces leverage mechanosensation to control reversal rates and orchestrate collective motility behaviors [87].

Bacteria use dedicated sensing systems to regulate gene expression and adhesion in response to mechanical signals [18, 68, 92, 93]. Beyond bacteria, eukaryotic cells also transduce mechanical signals into cellular responses, regulating an array of physiological processes including development,

immunity and touch sensation [94]. Eukaryotic cell motility is also sensitive to mechanical cues. For example, adherent mammalian cells migrate up gradients of substrate material stiffness in a process termed durotaxis [95]. We established that single cells can actively sense their mechanical environment to control motility on the timescale of seconds. Our work thus expands our view of signals activating bacterial sensing systems and more generally highlights the role of mechanics in regulating motility, be it in bacteria, archaea or eukaryotes [96].

Altogether, Chp functions as a spatial sensor for mechanical input. Thus, chemotaxis-like systems can sense spatially-resolved mechanical signals, a feat that is still debated when only considering diffusible molecules as input stimuli [97]. Phototactic systems may however be an exception by conferring cyanobacteria the ability to spatially sense gradients of light [98, 99]. Accordingly, the Pix phototactic system of the cyanobacterium *Synechocystis* shares signal transduction architecture with the *P. aeruginosa* Chp system by harboring two CheY-like response regulators, PixG and PixH [98, 99]. There also exists a broad range of chemotaxis-like systems with even higher degrees of architectural complexity [100]. We thus highlight that their subcellular arrangement may play important functions in the mechanism by which they regulate motility.

Finally, we revealed an unexpected commonality between bacteria, and single eukaryotic cells in the way they transduce environmental signals to control polarity [70]. Amoebae and neutrophils harness complex circuitry which combines positive and negative feedback loops to chemotax [88]. Positive regulators activate actin polymerization locally to drive membrane protrusion in the direction of polarization. Negative regulators inhibit actin polymerization throughout the cytoplasm to limit directional changes while also permitting adaptation [88]. Altogether, these cells establish a local activation-global inhibition landscape that balances directional persistence with adaptation [90]. By virtue of PilG and PilH compartmentalization, *P. aeruginosa* replicates the local activation-global inhibition landscape [90]. We have therefore uncovered a signal transduction principle permitting mechanotaxis in response to spatially-resolved signals that is conserved across kingdoms of life.

4.6 Materials and Methods

4.6.1 Bacterial strains and growth conditions

All strains used in this study are listed in **Table 4-1**. The *Pseudomonas aeruginosa* strain used was PAO1 strain ATCC 15692 (American Type Culture Collection). *Escherichia coli* strain DH5α was used for vector construction, *Escherichia coli* strain S17.1 was used for conjugation of vectors into *P. aeruginosa*. All bacterial strains were grown in LB medium (Carl Roth) at 37 °C with 290 rpm shaking. Regular solid LB media were prepared by adding 1.5 % (wt.vol^{-1}) agar (Fisher Bioreagents). Additional information on media and strain construction are given in the SI appendix.

4.6.2 Phase contrast and fluorescence microscopy

Microscopy was performed on an inverted Nikon TiE epifluorescence microscope controlled with NIS-Elements (version AR 5.02.03). Specific experimental procedures are given in the SI appendix. For pure phase-contrast microscopy a 40x Plan APO NA 0.9 phase contrast objective was used. For fluorescence microscopy a 100x Plan APO NA 1.45 phase contrast oil objective and Semrock YFP-2427B or TxRed-A-Basic-NTE filters were used as needed.

4.6.3 Experimental procedures and analysis

An extended description of experimental procedures and analysis methods, including analysis of twitching motility and localization of fluorescent protein fusions, are given in detail in the SI appendix.

4.6.4 Data and code availability

All data are available from the corresponding authors upon request. All ImageJ, Python and MATLAB code is available on Github under the following repository: https://github.com/PersatLab/Mechanotaxis.git

4.7 Acknowledgments

4.8 Author contributions

MJK, LT, JNE and AP conceived and supervised the project. MJK, LT, YI, HM, RP, ZAM conducted the experiments. MJK, LT, IV, JN wrote the tracking code and analyzed the data. MJK, LT, JNE and AP wrote the manuscript.

4.9 Competing interests

Authors declare no competing interests.

4.10 Correspondance

Alexandre Persat (alexandre.persat@epfl.ch)

Joanne Engel (joanne.engel@ucsf.edu)

4.11 SI appendix

4.11.1 Extended Methods

4.11.1.1 Growth conditions and media

For surface association experiments cells were plated on pre-heated solid LB media containing 1 % agarose standard (Carl Roth) and incubated at 37 °C for 3 hours. For twitching motility assays semi-solid tryptone media were prepared by autoclaving (5 g.l^{-1} tryptone (Carl Roth), 2.5 g.l^{-1} NaCl (Fisher Bioreagents), 0.5 % (wt.vol^{-1}) agarose standard (Carl Roth)). For fluorescence visualization under correlative fluorescence and iSCAT cells were washed with PBS (BioConcept AG) and resuspended in M9 medium (VWR) containing 0.2 % of glucose.

4.11.1.2 Strains and vector construction

All strains used in this study are listed in **Table 4-1**. Plasmids and corresponding oligonucleotides are listed in **Table 4-2** and **Table 4-3**, respectively. Gene deletions and gene fusions were constructed by two-step allelic exchange (according to (*66*)) using the suicide vectors pEX18Amp or pEX18Gent. In-frame deletions were generated by combining approximately 500-bp fragments of the up- and downstream regions of the designated gene, leaving only a few codons (usually around six) and verified by colony PCR and sequencing. In-frame insertions were constructed in basically

the same fashion. Insertion fragments with wild-type length (e.g. for complementation) were integrated into the corresponding deletion strain. Fluorophore genes were fused to the N- or C-termini of the desired gene separated by a GGGGG linker and introduced into the wild-type chromosome. Expression and integrity of fluorescent fusions were verified by Western blotting and functionality was tested by twitching motility assays (see corresponding methods). Plasmids were constructed using standard Gibson assembly protocols (*101*) and introduced into *P. aeruginosa* cells by conjugative mating with *E. coli* S17.1 as donor. For selection of *E. coli* the following antibiotic concentrations were used: 100 µg/ml ampicillin, 10 µg.ml^{-1} gentamycin. For selection of *P. aeruginosa* the following antibiotic concentrations were used: 300 µg.ml^{-1} carbenicillin, 60 µg.ml^{-1} gentamycin.

4.11.1.3   Twitching motility stab assay

Square plastic dishes (100x100x20 mm, Sarstedt) were filled with 50 ml of 0.5 % agarose tryptone medium and dried in a flow hood for 30 min. Single colonies grown overnight on LB agar at 37 °C were stabbed with a 10 µl pipette tip through the agarose hydrogel to the bottom of the dish without much force to prevent separation of the hydrogel from the plastic. The plates were incubated at 37 °C overnight in a plastic bag. The hydrogel was then scored around the edges with a 10 µl pipette tip and removed carefully. Twitching motility was quantified by taking two measurements of the twitching zone diameters from two to eight independent stabs. The twitching diameter of wild-type or Δ*fliC* *P. aeruginosa* was used as reference.

4.11.1.4   Western blot

Cells were grown overnight in LB, diluted 1:100 in LB and grown until OD_{600} = 1. One ml of cell suspension was harvested by centrifugation and resuspended in 100 µl of 2x loading bugger (Li-Cor), 100 mM DTT (Sigma) and at least 200 U/ml nuclease (Pierce) until the sample was no longer viscous. 10 µl of each sample was run on a sodium dodecyl sulfate-polyacrylamide gel electrophoresis (SDS-PAGE) at 200 V and transferred onto a nitrocellulose membrane (iblot 2). The membrane was incubated in PBS + 5 % milk powder for 1 h, then in 1:1000 anti-mNeonGreen antibody (Chromotek) in TBST + 5 % milk powder for 1 h, washed 3x with TBST and 1:10,000 Goat anti-Mouse IgG IRDye 800CW (Li-Cor) in TBST + 5 % milk powder for 1 h and washed 3x at room temperature. The blot was visualized with Odyssey CLx (Li-Cor).

4.11.1.5   Fluorescence microscopy image processing

All fluorescent images were background subtracted with ImageJ (version 1.53c). Snapshot images and movies were generated with ImageJ and data were analyzed with custom scripts in Python (version 3.7.6 and 3.8.5) and MATLAB (version R2019b and R2020a), as specified in detail below. Sample sizes for each experiment are listed in **Table 4-4**.

4.11.1.6   Correlative interferometric scattering (iSCAT) fluorescence microscopy setup

Our iSCAT microscope setup was previously described in (*41*). For this study, we added a fluorescent

channel as described in (*31*). Briefly, we implemented a green fluorescence channel by coupling a

blue laser with a wavelength of 462 nm (Lasertack, LDM-462-1400-C) to the iSCAT illumination path

with a 490 nm long pass dichroic mirror (Thorlabs, DMLP490). The laser was focused on the back

focal plane of the objective with a plano-convex lens (f = 500 mm, Thorlabs, LA1908-A). The

fluorescent signal was then focused onto a CMOS camera (PointGrey, GS3-U3-23S6M) with a

400 mm focal length achromatic lens and a GFP filter (CWL = 525 nm, Bandwidth = 39 nm, Thorlabs,

MF525-39). A shutter was placed in the illumination path of the fluorescence channel in order to

prevent unnecessary illumination. The iSCAT illumination was monitored by modulating the acousto-

optic deflectors' output (**Supplementary Figure 4.15**).

4.11.1.7   Glass coverslip and microfluidic chip preparation

Glass coverslips (Marienfeld, 22x40 mm No 1.5) were cleaned as described in (*41*). Briefly, they

were washed sequentially with distilled water, ethanol, distilled water, isopropanol, distilled water,

ethanol, distilled water and excess water was dried with a stream of nitrogen. For visualization, we

either plasma-bonded 500 μm wide, 140 μm deep polydimethylsiloxane (PDMS) microchannels,

fabricated using standard photolithography methods, or we deposited PDMS gaskets on the clean

coverslips. PDMS gaskets were obtained using biopsy punches of 6 mm in diameter.

4.11.1.8   cAMP quantification using PaQa-YFP reporter

The PaQa-YFP reporter system for cAMP measurements including a reference promoter fused to

mKate2 has been previously described in detail (*3*). Single colonies were grown overnight in LB-

carbenicillin, diluted to OD_{600} 0.05 and grown until mid-exponential phase. For surface-association

growth, cells were grown for 3 h at 37 °C on LB 1 % agarose and then harvested in 1 ml LB by gentle

scraping. 1 μl of culture was then loaded on a 1 % agarose-PBS pad and flipped onto a glass bottom

dish (MatTek) prior to visualization. Several images in phase contrast, YFP and mKate2 channels

were acquired. Images were binned 2x2 and fluorescence channels were background subtracted

using a custom macro in ImageJ. Cells were segmented and the cell area and corresponding cell mean fluorescence were extracted using BacStalk (*102*). Median PaQa-YFP to mKate2 fluorescent intensity ratios were computed with a custom Python script for each biological replicate. Each median was then normalized to the mean of the WT biological replicates of liquid cultures.

4.11.1.9 iSCAT-based quantification of type IV pili number

Single colonies were inoculated in LB, grown overnight and diluted 1:500 or 1:1000 followed by a grow period of 2 h to obtain mid exponential phase cultures. 100 µl of the cell suspension were plated on LB 1 % agarose, grown for 3 h at 37 °C and harvested in 500 µl LB by gentle scraping. Cells were diluted to OD_{600} 0.02 prior to visualization. Both liquid and solid grown cells were either loaded on 500 µm x 140 µm PDMS microchannels or in 6 mm PDMS gaskets. Cells sticking to the surface were visualized without flow with iSCAT and movies were recorded at 10 fps for either 2 min, 1 min or 30 s. To reveal the interferometric component of the signal, each frame was processed as described in (*41*). In some cases, we extracted the interferometric signal by differential processing. Briefly, we subtracted each frame at time t-1 to the frame at time t then performed the bandpass filtering and frame normalization as described in (*41*). This technique allowed to drastically decrease strong background signal which revealed hidden floppy pili. However stationary pili disappeared in the process as they became part of the background. Individual movies were manually analyzed by counting the total number of pili in each cell. The residence time of each cell on the coverslip was also recorded. Finally, we computed a bootstrap median of the total pili number for each biological replicate. To compare strains, we then took the mean of the medians for each biological replicate within one strain as well as their standard deviation.

4.11.1.10 Quantification of type IV pili distributions

To quantify pili at both cell poles, we selected flat laying cells (all strains with Δ*fliC* background). Pili from each pole were manually counted and recorded with a custom ImageJ macro. Probabilities were computed and plotted using Python. We focused our analysis on subset populations of cells that had either two, three or four pili and counted the total number of cells in those populations as

well as their corresponding pili distribution combinations (for cells with two pili: (1|1), (2|0) (**Supplementary Figure 4.3A**), for cells with three pili: (2|1), (3|0) (**Supplementary Figure 4.3B**) and for cells with four pili: (2|2), (3|1) and (4|0) (**Supplementary Figure 4.3C**)). We considered a cell to have symmetric pili distribution when they had 0 or 1 pilus difference between poles and we considered asymmetric distributions when cells had 2 and more pili difference between poles. We obtained a probability by dividing the cells in each pili distribution by the total number of cells of the corresponding population. We then compared these percentages with the percentages obtained by a random distribution (**Supplementary Figure 4.3D**).

4.11.1.11   Single cell twitching behavior without fluorescence

Cells from an exponential culture grown in LB were diluted to an OD_{600} of 0.2 in tryptone medium. The agarose pads were prepared by autoclaving tryptone medium 0.5 % agarose, cooling down to 70 °C in the autoclave followed by cooling to 55 °C for 20 min in a water bath, pouring 28 ml into round petri dishes and letting dry for 30 min in a flow hood. Plates were then stored in a plastic bag at 4 °C for 1 day. A round pad was cut out and 1 µl of the diluted cell suspension was pipetted onto the upper side of the agarose pad (i.e. the side that was not in contact with the plastic dish bottom). We note that all of the following conditions were critical in order to reproducibly allow cells to twitch as single, isolated cells: The medium composition (see Media), autoclaving the agarose medium, cooling down and drying as specified above, the initial optical density of the droplet and pipetting on the upper side of the agarose pad. Then, without letting the droplet dry, the pad was flipped onto a microscope glass bottom dish (MatTek) and six droplets of PBS were added to the sides to prevent drying. The cells were incubated at 37 °C and imaged with phase contrast microscopy every hour at 0.2 frames per second for 5 min over 3 h.

The movies were processed with a custom ImageJ macro to ensure compatibility with the downstream analysis. If necessary, drift was also corrected using the *StackReg* plugin (version July 7, 2011; (*103*)) in that step. Cells were then segmented and tracked using BacStalk (version 1.8, (*102*)) to get the cell outline and position of the center of mass (CM) of each isolated bacterium for each frame. Subsequent analyses of the cell tracks were done with custom MATLAB scripts. For

every analysis, cell tracks were categorized into moving and non-moving by using a speed threshold of 1 pixel per frame (here: 32.5 nm s^{-1}). The speed threshold was applied to the speed of each frame (converted from the displacement of the CM between the current and previous frame), setting the speed to 0 if below the threshold. Cells were only considered moving when the speed was unequal to zero for at least three subsequent frames over the tracked time. In **Figure 4.1B**, other cells in the snapshots were cut out for clarity (unmodified images: **Movie S4.1**).

4.11.1.12   Spatiotemporal cumulative displacement maps

In order to analyze twitching displacement relative to the initial cell orientation, we defined a cell orientation unit vector $\vec{t}$ from the CM to the initial leading pole (**cf. Figure 4.1B**). The initial leading pole was determined by comparing the scalar products of the unit vectors from CM to poles A and B (arbitrary classification) to the normalized displacement vector $\vec{d}$ in the first frame with a speed above the speed threshold. The vectors $\vec{t}$ and $\vec{d}$ were then used to determine direction of the cell displacement δ relative to the initial leading pole, giving it a positive sign for forward (i.e. toward initial leading pole) and a negative sign for reverse (i.e. opposite to initial leading pole) movement. The spatiotemporal displacement maps (Fig. 1C) were generated by cumulating the direction-corrected displacement as a function of time, for 200 tracks that were between 31 and 61 frames long.

4.11.1.13   Reversal frequency of isolated cells

To count the reversal frequency of twitching cells, the scalar product between the normalized displacement vector $\vec{d}$ and the cell orientation unit vector $\vec{t}$ was determined (**cf. Figure 4.1B**) and rounded for each frame (starting from the first frame with a speed above the speed threshold). This resulted in a series of numbers that correspond to movement of the cell toward the initial leading pole (1), toward the initial lagging pole (-1) or no movement (0) at that timepoint. Timepoints corresponding to no movement were removed. Cells were considered moving in the same direction (relative to the initial leading pole) as long as the sign remained the same. A reversal was counted when the sign changed, however, only if at least two subsequent frames before and after the reversal had the same sign (this was done to correct for frequent sign changes when a cell was in a non-

moving phase). The reversal frequency (**Figure 4.2*A***) was calculated by dividing the sum of all considered reversals by the total tracked time over all cell tracks for each biological replicate.

4.11.1.14   Reversal frequency after collision with an obstacle (cells and glass microfibers)

Cells were prepared and movies recorded as described above. Reversal rates after collisions with other cells (**Figure 4.2*C***) were determined in the same movies recorded for analyzing spontaneous reversals. To determine the reversal rate after collision with non-biological obstacles, we prepared glass microfibers by vortexing glass microfiber filters (GF/B, ~0.3-3 μm diameter, Whatmann) in 50 ml PBS for 5 min, concentrating the supernatant with sheared off fibers (removing as much liquid as possible), followed by 1 h sonication in a standard sonication bath. This resulted in long microfibers being broken down into lengths between 10 and 200 μm. The fiber suspension was mixed with the cell suspension to an appropriate concentration.

Because only isolated cells were tracked by BacStalk, we counted all collisions and potential subsequent reversals manually. A collision was only considered if the cell was moving for at least three frames in the same direction prior to the collision and the collision lasted for at least two frames (frame interval 5 sec). Furthermore, collisions with angles below 20° (data **Figure 4.2*C***) or 45° (data **Figure 4.2*E***) were not considered. The conditions to consider a collision were adapted for the comparison of cell-cell and cell-fiber collisions (**Figure 4.2*E***) because of the difference in shape of the glass microfibers. Bigger fibers typically lift the agar pad, resulting in accelerating rather than slowing down colliding cells at low collision angles, in contrast to low-angle collision with other cells.

A reversal following a collision was considered only if it occurred within five frames after the collision ended. Freshly divided cells were not considered as they were never found to reverse after a collision, potentially due to the lack of functional pili basal bodies at the new pole. The frequency of reversals following a collision (**Figure 4.2*C, E***) was calculated by dividing the sum of all considered reversals by the sum of all considered collisions for each biological replicate.

In the snapshots of **Figure 4.2*B*** (left), the moving and colliding cell was cut and placed at its original position into frame 10 s for clarity (unmodified images: **Movie S4.3**).

4.11.1.15   Dynamic localization of fluorescent protein fusions in isolated twitching cells

All localization studies in moving cells were performed in Δ*fliC* background to ensure that cells are not moving by means of flagella. Cells and microscope dishes were essentially prepared as described above (*cf*. single cell twitching behavior without fluorescence). The cells were then incubated at 37 °C and imaged with fluorescence microscopy every hour at 0.2 – 0.5 frames per second for 2 min over 3 h. Cells were similarly segmented and tracked with BacStalk, and basic MATLAB analysis was performed as described above, applying a speed threshold (here: 26 - 65 nm s^{-1}) in order to categorize cell tracks into moving and non-moving. Next, the positions of both cell poles were determined using the cell outline obtained from BacStalk. Poles were labeled according to their position in subsequent frames. Average fluorescence intensity was measured in an area around the coordinate of each pole with a radius $r = \frac{cell\ width}{1.8}$.

Cells were then categorized according to their ratio of average fluorescence intensity between the two poles over the whole cell track ($symmetry\ ratio = \frac{intensity\ \dim\ pole}{intensity\ bright\ pole}$). We defined a symmetry ratio threshold (0.69) according to the distribution for PilB-mNG, which showed two subpopulations, that we considered having symmetric and asymmetric subcellular protein localization. Cells were considered symmetric with a ratio below and asymmetric with a ratio above the threshold (**Figure 4.3*D* and 4.6*E***).

In order to measure if cells moved toward the dim or the bright pole (**Figure 4.3*E*, 4.6*D***; including cells which we considered having symmetric protein localization), we defined a unit vector $\vec{e}$ from the dim to the bright pole. We then computed an alignment factor α, which is the scalar product of the normalized displacement vector $\vec{d}$ and the fluorescence polarity vector $\vec{e}$. The alignment factor α represents in which direction the cell is moving relative to the bright pole. An alignment factor $α > 0$ corresponds to movement toward the bright pole, with $α = 1$ corresponding to movement exactly parallel to the cell length axis.

Kymographs were generated with BacStalk (version 1.8; (*102*)) after normalizing the cell length to 50 pixels and resampling the fluorescence intensity data with the *interp1* function in MATLAB. Because the poles were labeled inconsistently by BacStalk, the reference pole was set manually for each frame to represent the initial leading pole.

In order to determine a potential temporal sequence of protein appearance at the new leading pole during reversals, we focused on cells that reversed and showed clear pole switching of the fluorescent foci. Those cells were identified by running a modified version of the MatLab script described above. This script was used to plot fluorescent traces of both poles (as in **Supplementary Figure 4.6***E, F* **or Supplementary Figure 4.10***B*) together with the displacement corrected for the initial leading pole (rounded to 1 and -1). The reversal delay time τ was defined as the time between the last crossover of the fluorescent intensity traces of both poles before the reversal, and the first frame with a displacement with opposite sign (defined as reversal).

4.11.1.16   Colocalization of PilG with PilB and FimX

Double tagged strains were generated as described above using mNeonGreen fusions of FimX and PilB and mScarlet-I fusion of PilG. No spectral crossover could be observed with the corresponding second filters in single tagged strains. Although single tagged fusion proteins were functional (mNG-FimX and mScI-PilG) or partially functional (PilB-mNG) as measured by twitching stab assays (**Supplementary Figure 4.11**), combining both tagged proteins in one strain resulted in significant twitching defects. Nevertheless, single twitching cells could be observed with fluorescence microcopy, however, the fraction of motile cells and cell speed were decreased. Furthermore, the fluorescent signal of some fusions was decreased in the double tagged strain compared to the single tagged strain. Finally, because individual cell speed and twitching direction differed greatly, the offset of the fluorescent foci resulting from the image acquisition delay between fluorescent channels could not be corrected in a uniform and unbiased way. Given those limitation, we decided to determine colocalization during twitching manually. First, we marked cells that twitched smoothly without reversals (but sometimes with short stop-phases). We discarded cells with fluorescent signals below noise level of either tagged protein. Those cells were not considered, because the low fluorescence

is likely a result of the impaired protein function and/or potential protein interaction in the double tagged strains. In the remaining fraction (~85% for mScI-PilG + PilB-mNG and (~75% for mScI-PilG + mNG-FimX), we then determined the bright fluorescent pole for both tagged proteins (always the leading pole, except for a small fraction ~5% of PilB-mNG) and determined if the bright fluorescent foci colocalized.

4.11.1.17   Type IV pili number quantification and motor proteins localization

Overnight cultures grown in LB were diluted 1:500 to 1:1000 and grown for 3 h up to mid-exponential phase then plated for surface-association experiments as described above. Cells were harvested in 500 µl of LB by gentle scraping of the plate and loaded into PDMS gaskets. After 5 min incubation at room temperature (RT) unattached cells were washed with PBS and resuspended in M9 medium to avoid background autofluorescence of LB. Cells were visualized for 4 to 5 s with correlative iSCAT fluorescence microscopy at 100 fps in the iSCAT channel and 5 fps in the fluorescence channel. iSCAT movies were processed as described above. Further image processing and analysis was performed using custom ImageJ macros. Fluorescence images were background subtracted and iSCAT and fluorescence frames were registered using ImageJ's *Align Image by line ROI* function. The scaling factor between fluorescence and iSCAT frames was determined by the difference in effective pixel size of the two cameras. The rotation angle was computed with the two ROI lines used for registration. Pili were manually counted on iSCAT images and total fluorescence at the poles was measured on corresponding fluorescence images. Briefly, cells were selected by the user and cell poles were automatically detected by segmenting the fluorescent cell, extracting its outline, finding its center of mass (CM) and finding the points within the outline with maximum distance from the CM. The total fluorescence at the poles was then computed by measuring the mean fluorescence within a circle at the poles with a diameter corresponding to the cell width and multiplying that mean by the area of the circle. For the statistical analysis we counted how many cells had more pili at the brightest pole and how many had more pili at the dimmest pole in each biological replicate (at least 20 cells per biological replicate). We then divided that number by the total number of cells within the

biological replicate and computed the mean probability across the biological replicates for each strain. Data was plotted using Python.

4.11.1.18   Frequency of bright pole oscillations

Cells and microscope dishes were prepared and microscopy was performed essentially as described above (*cf.* dynamic protein localization). The only difference was that cells were grown and imaged in a heated chamber (37 °C) on the microscope at 0.2 frames per second for 3 min after 10 and 60 min. Earlier timepoints were challenging to record, because of drift and autofocus issues, that usually diminished after a few minutes after preparing the microscope slide.

To count how often the brightest fluorescence signal of a fusion protein switched from one pole to the opposite pole, a similar analysis as for the dynamic protein localization was applied to measure the average fluorescence intensity of both poles over time. Then, a series of numbers (1 or -1) was generated that corresponds to a pole (arbitrary but same over the whole track) being the bright pole (1) or the dim pole (-1) for each frame. Similar to counting reversals, a bright pole switch was counted when the sign changed. Here, no additional filters were applied. The frequency of bright pole switches (**Supplementary Figure 4.7**) was calculated for each cell by dividing the sum of all bright pole switches by the tracked time.

4.11.1.19   Motor protein and response regulator localization in immobilized cells

Cells were grown, visualized and analyzed as described above (*cf.* PaQa-YFP reporter quantification). To characterize the spatial localization of the protein fusions, we segmented each cell in phase contrast and extracted their fluorescence profiles using BacStalk. Fluorescent profiles correspond to the mean pixel value of a transversal section of the cell along the mid-cell axis (**Supplementary Figure 4.8***A*). To compare cells with different expression levels, profiles were normalized by the total fluorescence of the cell (corresponding to the area under the red curve in **Supplementary Figure 4.8***A*) and rescaled by the cell length. We then computed mean profiles and standard deviations for every biological replicate. To quantify the extent of polar localization, we computed a polar localization index. To calculate this index, we integrated the fluorescence intensity at the poles defined by a circle having a diameter of a single cell width (normalized by the cell length,

pink areas a and b in **Supplementary Figure 4.8B**). We corrected this value by subtracting the fluorescence at the poles of the diffused portion of the signal corresponding to the cytoplasmic median fluorescence (hatched areas c and d in **Supplementary Figure 4.8B**). The polar localization index was computed by dividing this value by the sum of the pole areas. A value of 0 correspond to a totally diffused protein whereas a value of 1 correspond to a totally polar protein. Similarly, we computed a symmetry index by taking the ratio between the maximum polar total fluorescence and the sum of the polar total fluorescence. A value of 0.5 corresponds to a perfectly symmetric bipolar localization whereas a value of 1 corresponds to a perfectly unipolar localization. To compare strains, we computed the mean and standard deviation across biological replicates using a custom MatLab script.

4.11.1.20   Localization of the extension motor under arabinose induction

Cells harboring the PilB-mNG expression plasmid were grown overnight in LB gentamycin. Cells were diluted 1:1000 in LB gentamycin and arabinose was added in the following concentrations: 0 %, 0.03 % and 0.1 %. The diluted cultures were grown for 3 h at 37 °C with 290 rpm shaking. Samples were then prepared, visualized and analyzed as described above.

4.11.2   Supplementary Figures
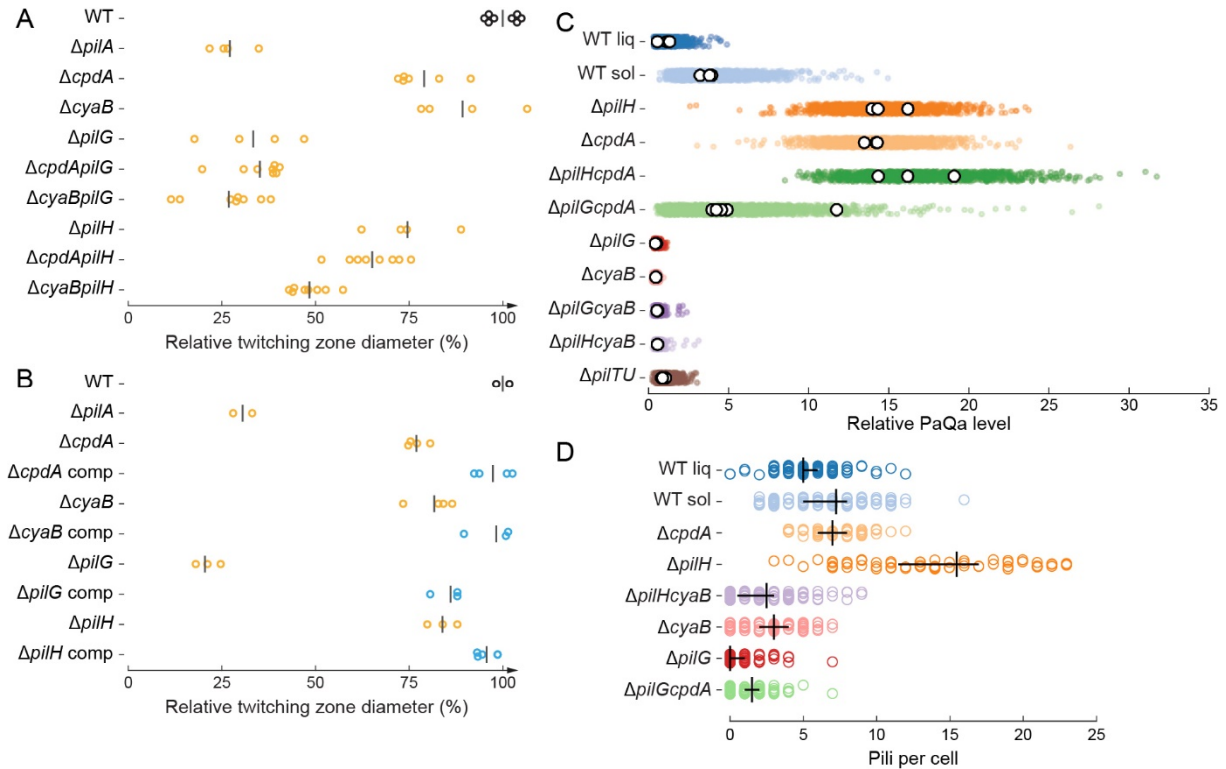
Supplementary Figure 4.1: Quantification of twitching motility by the stab assay, cAMP levels and piliation of Chp mutants.

(A) Twitching motility as measured by the subsurface stab assay of marker-free in-frame deletions of selected Pil and Chp genes. The diameter of the zone for any given mutant is normalized by the mean twitching diameter of WT (background strain PAO1 Δ*fliC*). Each circle corresponds to a single colony. Black bars correspond to the mean of the replicates. (B) Twitching zone diameters of the in-frame deletion mutants and their complemented versions. Yellow circles correspond to the in-frame deletions, blue circles correspond to the complemented mutants. Black bars correspond to the mean diameter of the replicates. Complementation of each of the in-frame deletion mutants restored the twitching zone diameter to WT levels (background strain PAO1). (C) cAMP levels measured by PaQa-YFP reporter fluorescence. Colored circles represent single cells, white circles correspond to median of biological replicates. All levels are normalized by the mean fluorescence intensity of the liquid-grown WT across biological replicates. All strains except WT sol are grown in liquid culture. (D) Quantification of T4P number in Chp and cAMP mutants by iSCAT. Each circle corresponds to the T4P number of an individual cell. Black vertical bars correspond to the boostrap mean of biological replicates, horizontal bars to their bootstrap 95 % confidence interval. All strains except WT sol are grown in liquid culture.
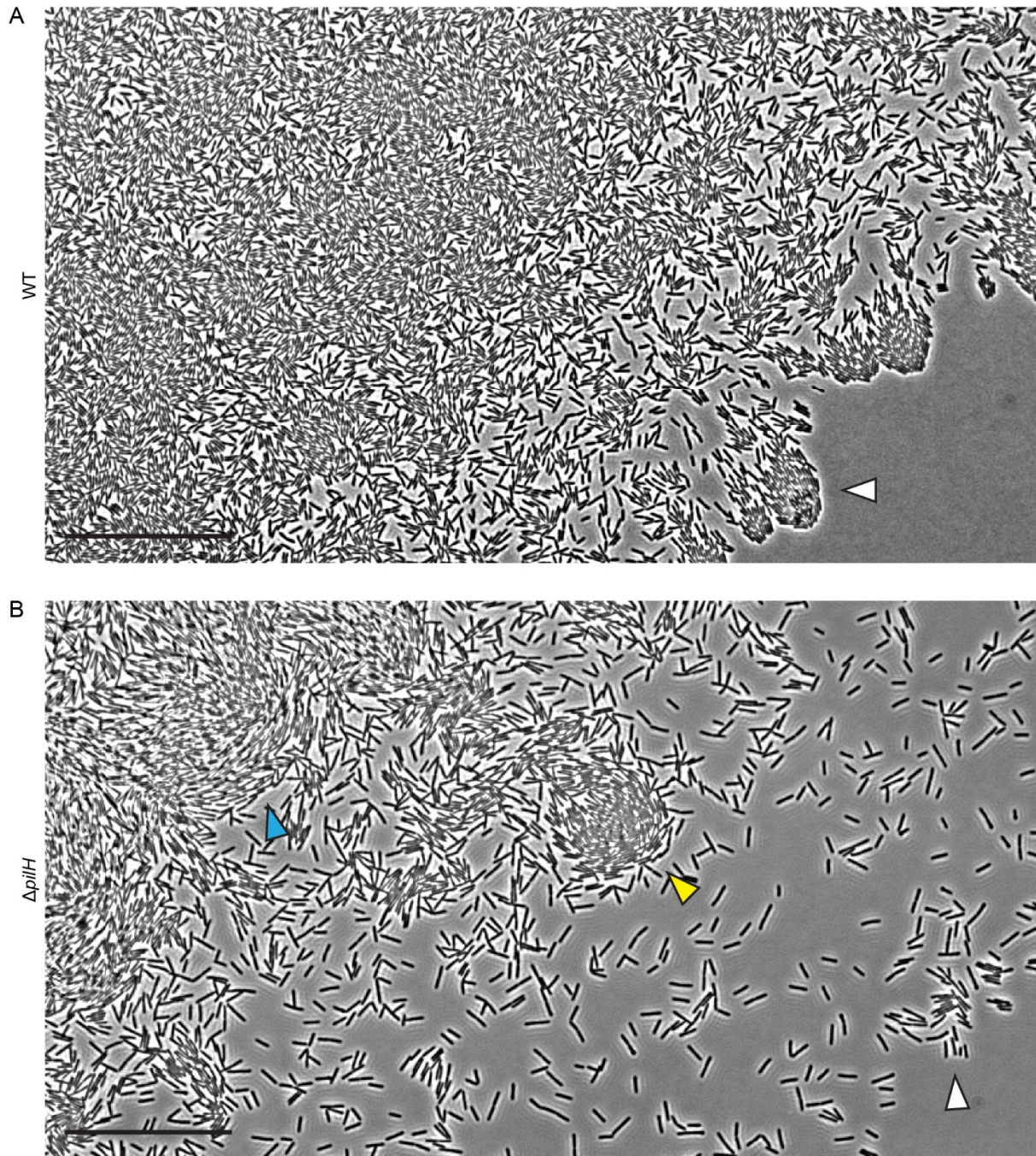
Supplementary Figure 4.2: Colony edge expansion of twitching WT and Δ*pilH* cells.

Both leading edges expand toward the lower right. (A) WT cells spread evenly and form persistent rafts (white triangle) at the leading edge. (B) Δ*pilH* cells form transient comet-shaped rafts (yellow triangle) and swirls (blue triangle) due to their inability to reverse. At the leading edge, rafts don't persist (white triangle), resulting in slower expansion at the macroscopic scale (*cf*. **Supplementary Figure 4.1**). In conditions that only allow cells to move in groups, donut-shaped swirls have been reported for Δ*pilH*, that likely arise from the inability to reverse as well (*13*). Scale bar, 50 μm. Images correspond to Movie S6.
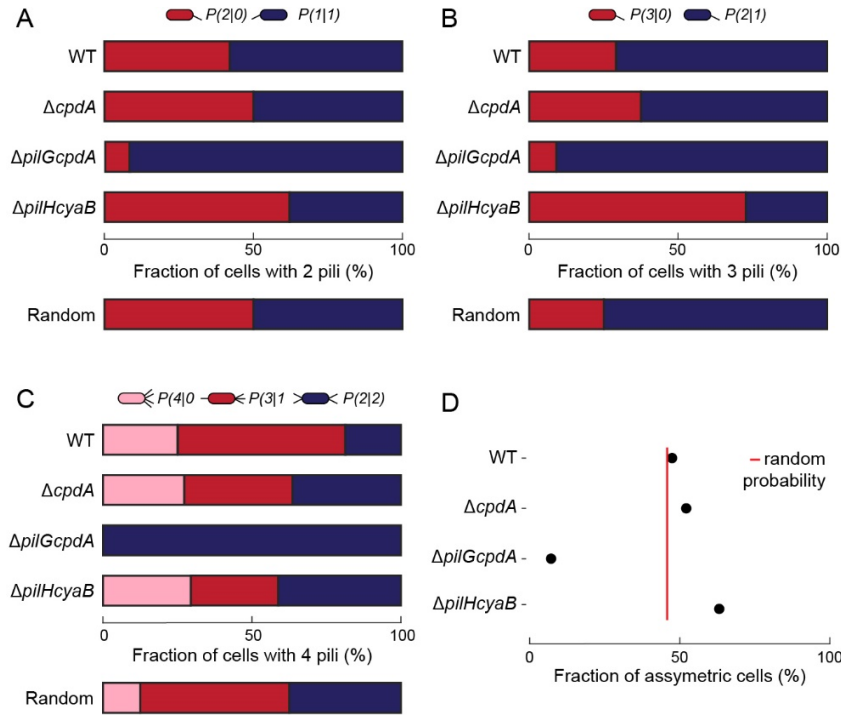
Supplementary Figure 4.3: Chp controls T4P polar distribution in single cells.

We imaged single cells using iSCAT to quantify T4P at each pole. For cells that had two (A), three (B) and four (C) T4P, we calculated the percentage of any given T4P distribution. P(*n*/*m*) corresponds to the fraction of cells that have *n* T4P at one pole and *m* T4P at the opposite pole. For each T4P number, red corresponds to the most asymmetric distribution and blue to the most symmetric as illustrated above the graphs. As a reference, we computed the expected fractions if T4P were to be distributed randomly (shown below the mutants). WT and Δ*cpdA* T4P distributions are close to random. However, the distributions tend to shift toward complete symmetry in Δ*pilGcpdA* and complete asymmetry for Δ*pilHcyaB* and are independent of cAMP levels as these mutants have similar levels. (D) Cumulative fraction of the population with assymetric pili distribution in cells with two, three and four pili. Δ*pilG* mostly have symmetric T4P distribution whereas Δ*pilH* tend to polarize T4P to one pole. All cells are liquid-grown.
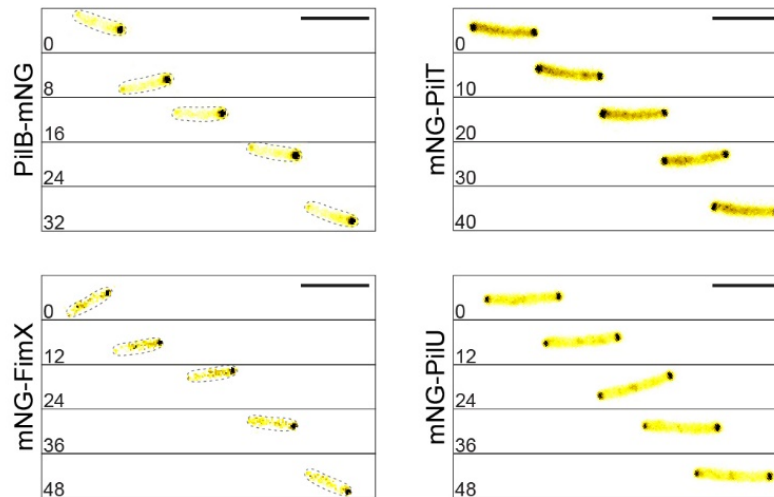
Supplementary Figure 4.4: Timeseries of snapshots of fluorescent fusion proteins in single cells twitching forward.

PilB and FimX localize more prominently to the leading pole, while PilT and PilU tend to localize more symmerically to both poles. Images correspond to **Movie S4.7**. Scale bar, 5 μm.
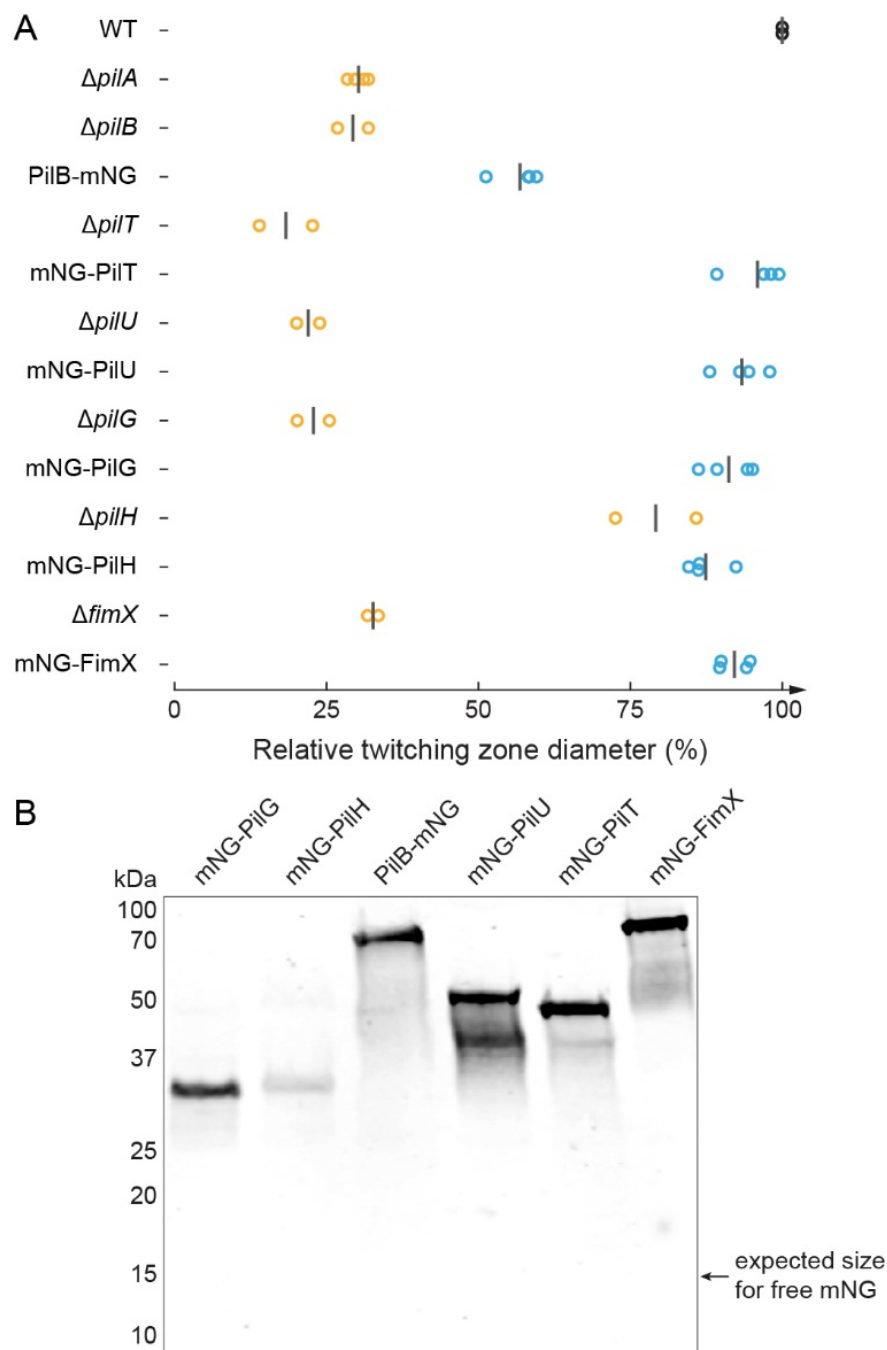
Supplementary Figure 4.5: Functional characterization of fluorescent protein fusions to T4P motors and response regulators.

(B) Twitching diameters (relative to WT) as measured by the subsurface stab assay. Yellow circles correspond to in-frame deletions, blue circles correspond to chromosomally localized fluorescent fusions, black bars correspond to the mean of diameter of twitching zones. (C) Western blot of all mNG fluorescent fusions used in this study to verify expression levels and production of full-length protein fusion. Free mNG was not detected.
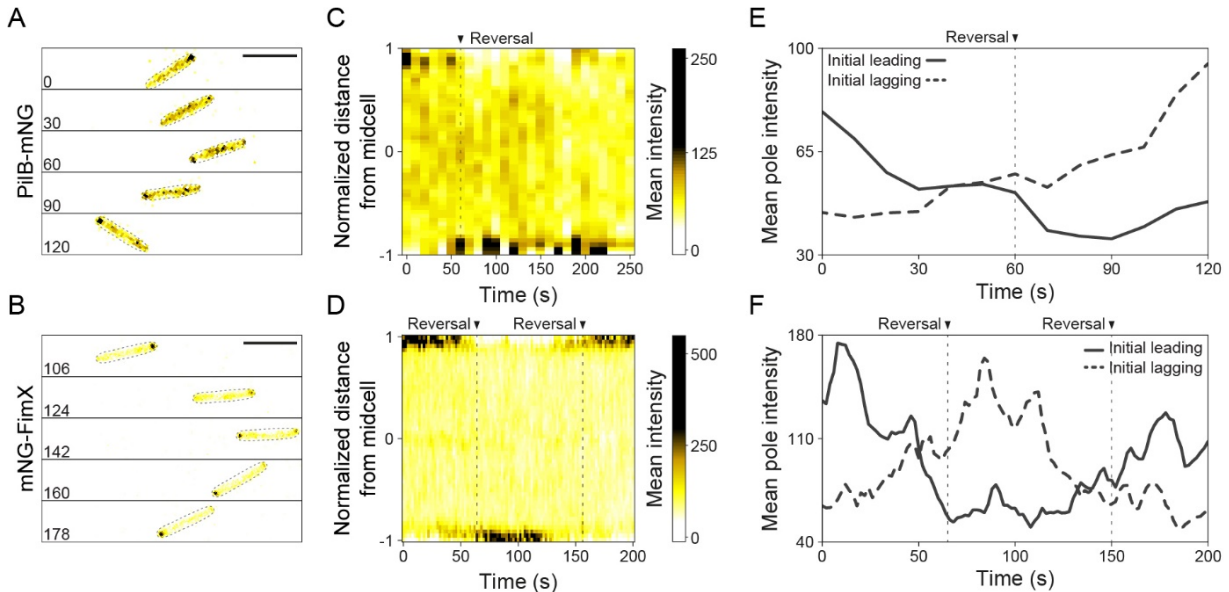
Supplementary Figure 4.6: PilB-mNG and mNG-FimX switch polarization toward the new leading pole during twitching reversals.

Snapshots of fluorescence image sequences of reversing PilB-mNG (A) and mNG-FimX (B) cells (corresponding to **Movie S4.8**). (C and D) Corresponding kymographs during reversal showing relocalization of the fluorescent fusion proteins. (E and F) Fluorescent intensity traces of the leading and lagging poles during the visualization. The dynamic localization behaviour of FimX during reversals is qualitatively similar to the one described previously (*84*). Scale bar, 5 µm.
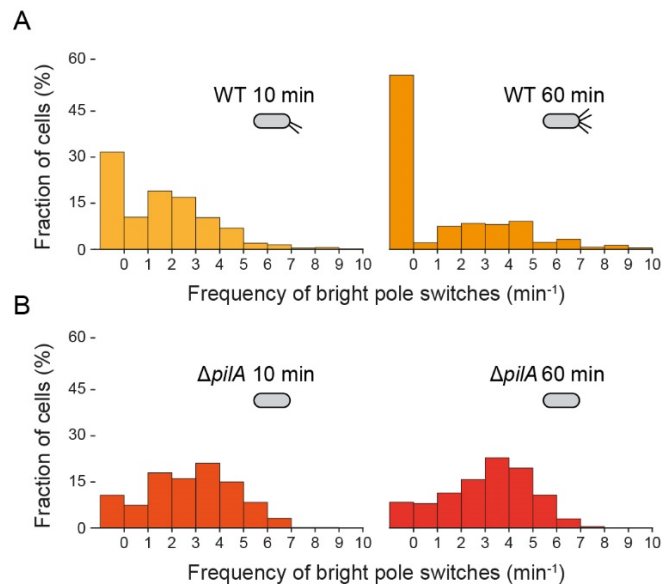
Supplementary Figure 4.7: Frequency distributions of mNG-FimX oscillations upon surface contact is T4P-dependent.

(A) Distributions of bright foci mean switching frequency in WT 10 min (left) and 60 min (right) after surface contact. Right after surface contact, 70% of the population shows pole-to-pole mNG-FimX switches, which goes down to 50% after 1 h on the surface. (B) Distributions of bright focus spot switching frequency in Δ*pilA*. Most cells show pole-to-pole switches. There is no change in the distribution of switching frequencies between cell populations that have been in contact with the surface for 10 min and 60 min.
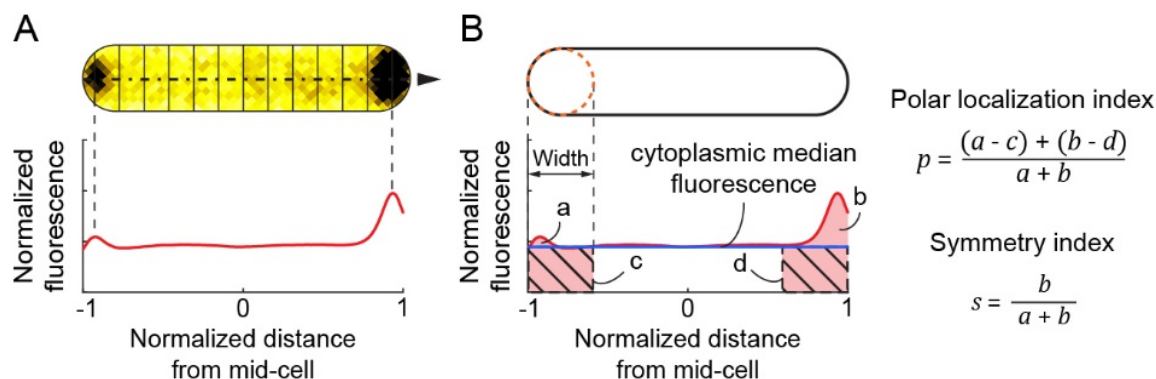
Supplementary Figure 4.8: Computation of fluorescent profile, polar localization and symmetry incides.

(A) Fluorescence profiles were computed with BacStalk by taking the cross-sectional mean pixel value along the cell (dashed line). To correct the profile for differences in expression levels between cells, each was normalized by the total fluorescence intensity of the cell, represented by the area under the red curve. The cell length was also normalized so that the poles are located at -1 and 1 *x*-coordinates. (B) Computation of the polar localization and the symmetry indices. The pole areas (pink areas a and b) were defined by the width of the cell. The hatched areas c and d correspond to the pole areas if the protein-fusion was diffused with fluorescence levels identical to the cytoplasmic median fluorescence of the profile (blue line). To extract the polar localization index for each cell, we subtracted the diffused total fluorescence (c and d) to the actual pole total fluorescence (a and b) and divided this value by the total fluorescence at the poles (a + b). The symetry index for each cell was computed as the total fluorescence of the brightest pole b divided by the sum of the total fluorescence of the two poles a + b.
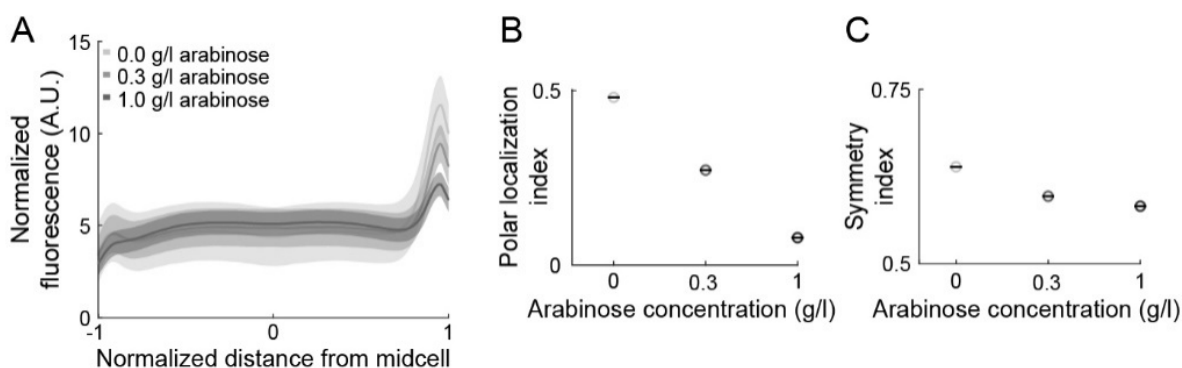
Supplementary Figure 4.9: PilB-mNG polar localization and polarization as a function of expression level.

We induced the expression of PilB-mNG on a low-copy plasmid with arabinose in a Δ*pilB* background. (A) Mean profiles (solid lines) and standard deviation (grey areas) of a population of liquid grown cells in which PilB-mNG was induced for 3 h at three different arabinose concentrations. When normalized, the profiles flatten with increasing inducer concentration. We attribute this to the accumulation of the motor protein in the cytoplasm after T4P machineries are saturated at the poles. (B and C) As a result, the polar localization and symmetry indices of PilB-mNG decrease with increased concentration of inducer.
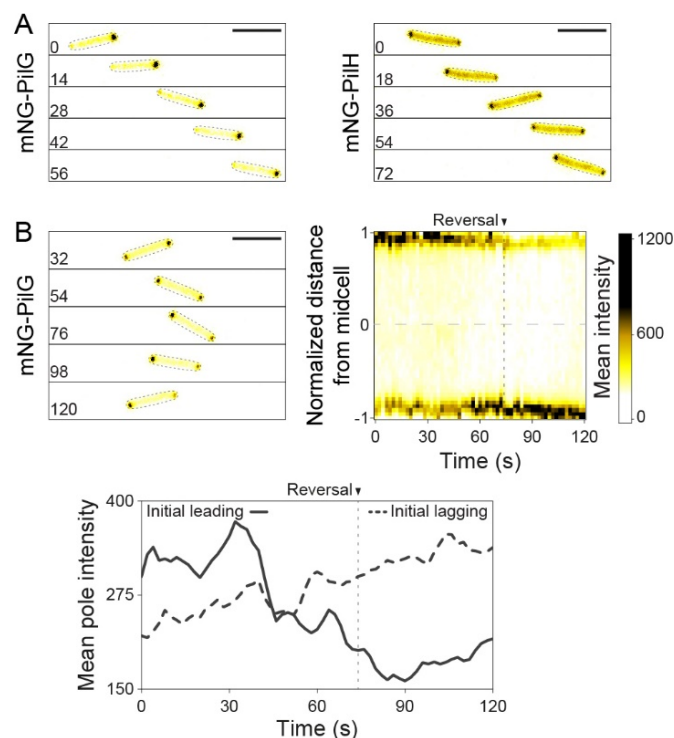
Supplementary Figure 4.10: mNG-PilG and mNG-PilH localization during twitching and reversals.

(A) Snapshots of mNG-PilG and mNG-PilH fluorescent fusions in isolated twitching cells. PilG tends to localize more prominently to the leading pole, while PilH predominantly localizes to the cytoplasm and can be enriched at both poles without marked polarization. Snapshots taken from **Movie S4.11**. (B) Snapshots of a fluorescence image sequence of a reversing cell expressing mNG-PilG at its native locus (taken from **Movie S4.12**), and corresponding kymograph and fluorescent intensity traces.
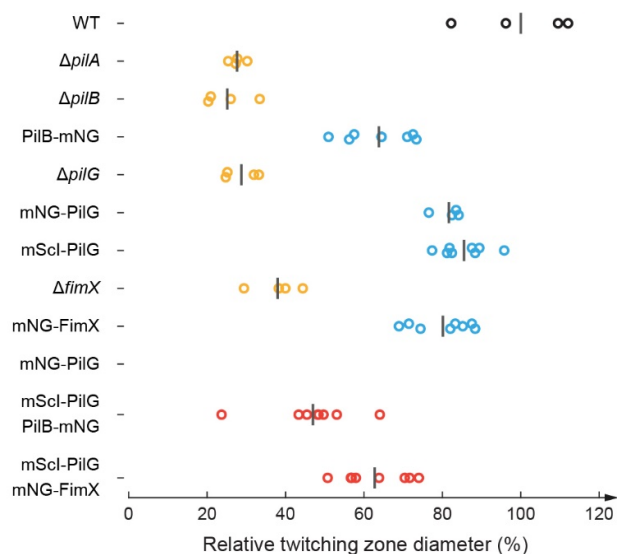
Supplementary Figure 4.11: Functional characterization of double-tagged fluorescent protein fusion strains.

Twitching diameters (relative to WT) as measured by the subsurface stab assay. Yellow circles correspond to in-frame deletions, blue circles correspond to chromosomally localized fluorescent fusions, red circles represent the double-tagged strains, black bars correspond to the mean diameter of twitching zones.
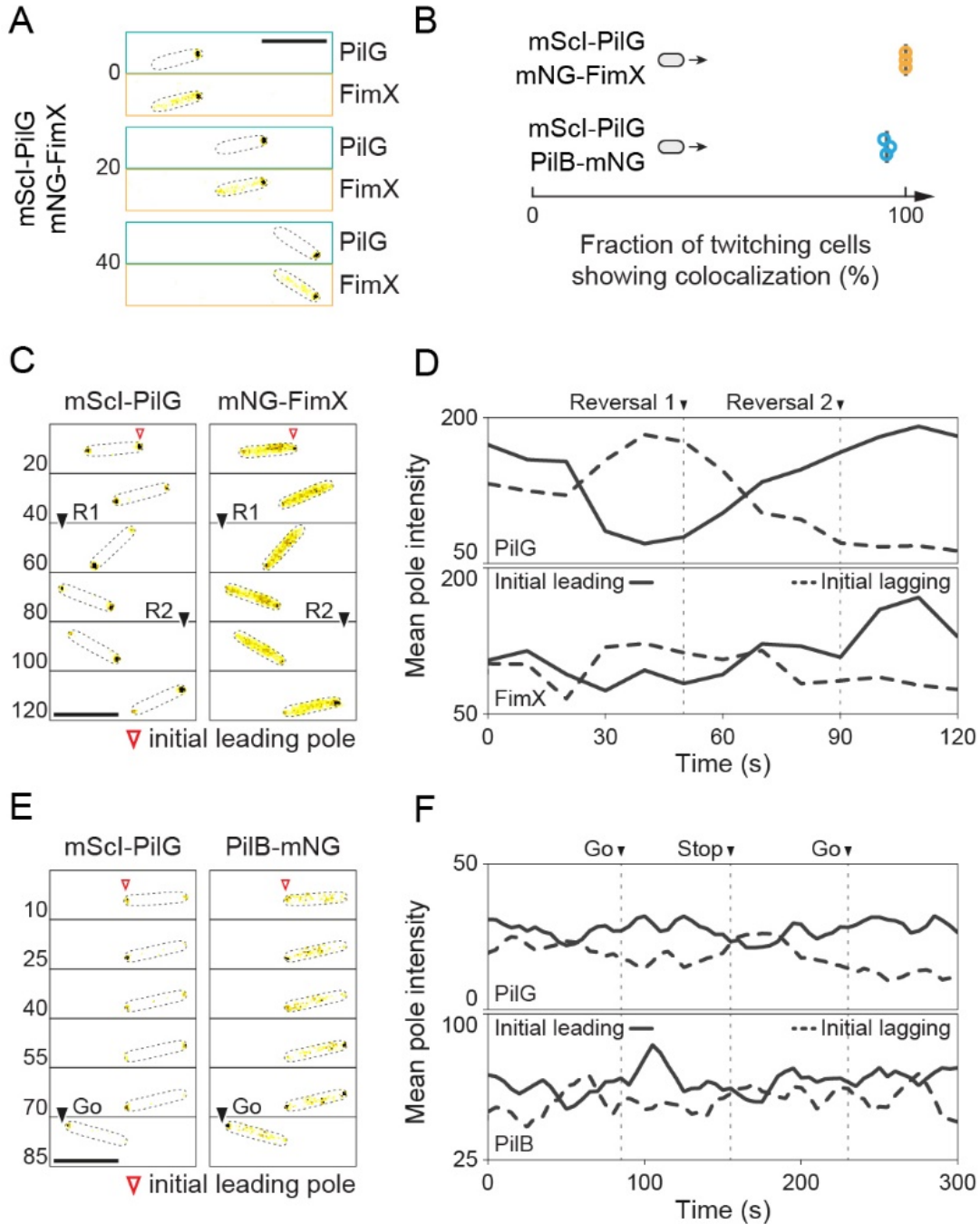
Supplementary Figure 4.12: PilG colocalizes both with FimX and PilB in smooth twitching and reversing cells.

(A) Snapshots of a fluorescence image sequence of a smooth twitching mScl-PilG + mNG-FimX double tagged cell. (B) Fraction of smooth twitching cells showing colocalization of PilG with FimX and PilB at the leading pole. The brighter signal was always located at the leading pole, except for the small fraction of mScl-PilG + PilB-mNG cells showing no colocalization, in which the PilB-mNG signal was located at the lagging pole. Circles correspond to the fraction of each biological replicate, black bars represent their mean. (C and E) Snapshots of fluorescence image sequences of a reversing mScl-PilG + mNG-FimX cell (C) and a mScl-PilG + PilB-mNG cell twitching with intermittent stops (E). (D and F) Corresponding fluorescent intensity traces showing relocalization of both fluorescent fusion proteins at the same time. A three-point moving average was applied to the fluorescent intensities in panel F. Scale bar, 5 μm.
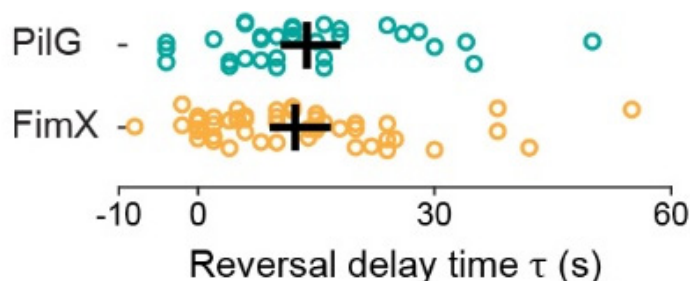
Supplementary Figure 4.13: The delay between protein polarity switch and twitching reversal is indistinguishable between mNG-PilG and mNG-FimX

The reversal delay time τ is the time between the last crossover of the fluorescent intensity traces of both poles (similar to **Supplementary Figure 4.6*E, F* or 4.10*B***) before the reversal and the time point of the reversal. τ was determined in single tagged fluorescent strains.
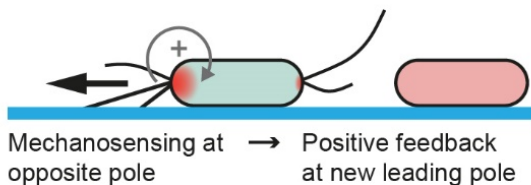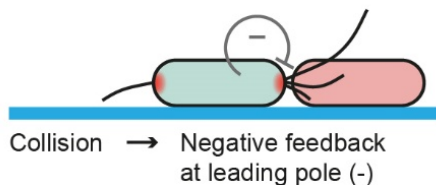
Supplementary Figure 4.14: Mechanotaxis model:

After initial contact a cell explores its surrounding with random T4P distribution at both poles. Upon T4P tip attachment, Chp mechanosensing induces a positive feedback on T4P motors to favor extension at the same pole leading to polarization of the cell and persistent forward motion. After collision (or loss of T4P attachment/retraction) at the leading pole, a negative feedback down regulates T4P activity. T4P at the opposite pole can then attach and generate a positive feedback that reverses cell polarization and lead to persistent reverse twitching.
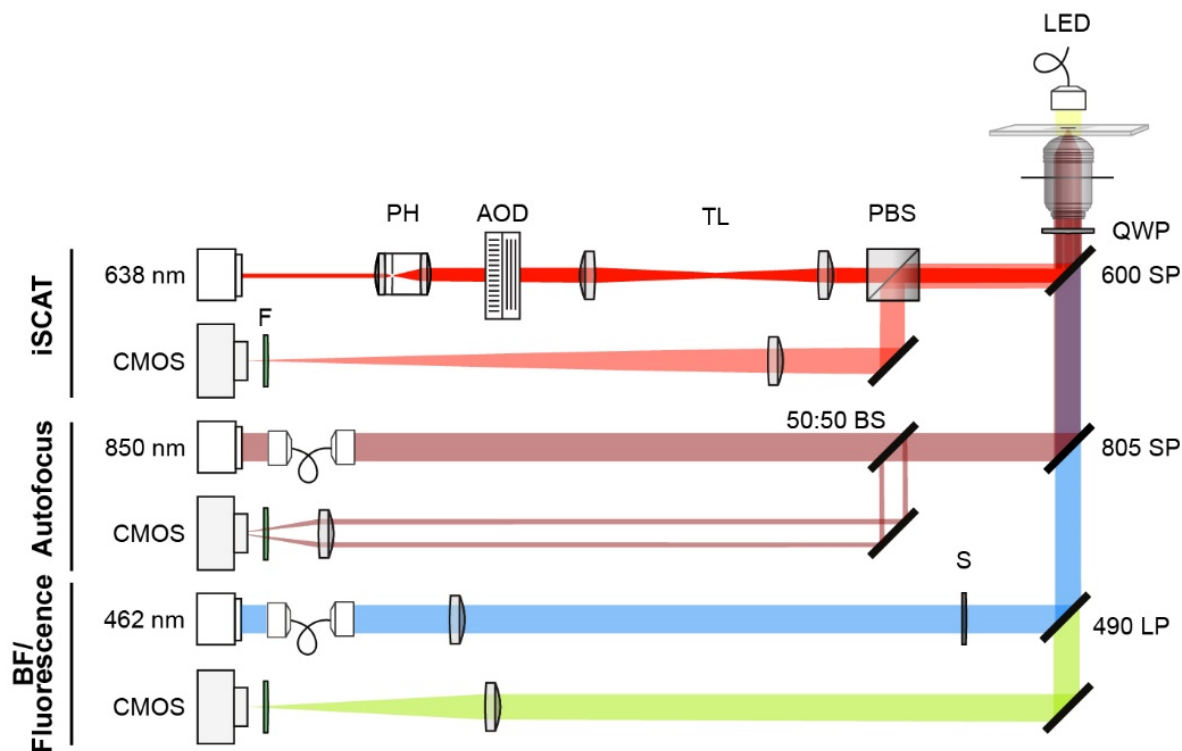
Supplementary Figure 4.15: Optical layout of the correlative iSCAT fluorescence setup.

The setup is a modified version of the one described in (*41*) in which we added a fluorescent channel. Briefly, the fluorescence channel consists in a 462 nm blue laser spatially filtered by an optical fiber and focused to the back focal plane of the objective with a 500 mm lens and a 490 nm long pass dichroic mirror. A shutter (S) allows clipping of the beam to reduce light exposure. The fluorescent signal emitted by the sample is directed to a CMOS camera with a 400 mm imaging lens. Appropriate filters (F) were used to prevent unwanted signal reaching the detectors (iSCAT: 635 band pass (BP), Bright field/fluorescence: 525 BP, Autofocus: 850 BP).

Table 4-1: Strains used in this study.

Name and relevant genotype	Source / Reference	Identifier
Pseudomonas aeruginosa PAO1	(*104*)	ATCC 15692
Escherichia coli DH5α (hsdR rec lacZYA φ80 lacZM15)	Invitrogen	Na
Escherichia coli strain S17.1 (thi pro hsdR recA RP4-2(Tc::Mu)(Km::Tn7))	Stratagene	Na
PAO1 Δ*pilA* (in-frame deletion of PA4525)	(*11*)	81
PAO1 Δ*pilB* (in-frame deletion of PA4526)	(*11*)	172
PAO1 Δ*pilT* (in-frame deletion of PA0395)	(*11*)	89
PAO1 Δ*pilU* (in-frame deletion of PA0396)	(*11*)	87
PAO1 Δ*pilTU*	(*11*)	171
PAO1 Δ*pilG* (in-frame deletion of PA0408)	(*11*)	226
PAO1 Δ*pilH* (in-frame deletion of PA0409)	(*105*)	178
PAO1 Δ*fimX* (in-frame deletion of PA4959)	(*106*)	885
PAO1 Δ*cpdA* (in-frame deletion of PA4969)	(*107*)	180
PAO1 Δ*cyaB* (in-frame deletion of PA3217)	(*107*)	174
PAO1 Δ*cpdA* Δ*pilG*	This study	487
PAO1 Δ*cpdA* Δ*pilH*	This study	488
PAO1 Δ*cyaB* Δ*pilG*	This study	403
PAO1 Δ*cyaB* Δ*pilH*	This study	404
PAO1 Δ*cpdA* complementation (in-frame insertion at native locus)	This study	1110
PAO1 Δ*cyaB* complementation (in-frame insertion at *attB* locus)	(*107*)	1091
PAO1 Δ*pilG* complementation (in-frame insertion at native locus)	(*11*)	1093
PAO1 Δ*pilH* complementation (in-frame insertion at native locus)	(*11*)	1094
PAO1 Δ*fliC* (in-frame deletion of PA1092)	(*11*)	177
PAO1 Δ*fliC* Δ*cpdA*	This study	337
PAO1 Δ*fliC* Δ*cyaB*	This study	326
PAO1 Δ*fliC* Δ*pilH*	This study	232
PAO1 Δ*fliC* Δ*pilG*	This study	330
PAO1 Δ*fliC* Δ*cpdA* Δ*pilG*	This study	459
PAO1 Δ*fliC* Δ*cyaB* Δ*pilH*	This study	436
PAO1 PilB-mNG (C-terminal fluorescent fusion to mNeonGreen, GGGGG linker, native locus)	This study	592
PAO1 PilB-mNG Δ*cpdA*	This study	716
PAO1 PilB-mNG Δ*cyaB* Δ*pilH*	This study	1104
PAO1 PilB-mNG Δ*pilH*	This study	605
PAO1 PilB-mNG Δ*pilG*	This study	590

Name and relevant genotype	Source / Reference	Identifier
PAO1 mNG-PilT (N-terminal fluorescent fusion to mNeonGreen, GGGGG linker, native locus)	This study	591
PAO1 mNG-PilT Δ*pilG*	This study	589
PAO1 mNG-PilT Δ*pilH*	This study	648
PAO1 mNG-PilT Δ*cpdA*	This study	773
PAO1 mNG-PilU (N-terminal fluorescent fusion to mNeonGreen, GGGGG linker, native locus)	This study	448
PAO1 mNG-PilU Δ*pilG*	This study	604
PAO1 mNG-PilU Δ*pilH*	This study	698
PAO1 mNG-PilU Δ*cpdA*	This study	718
PAO1 mNG-PilG (N-terminal fluorescent fusion to mNeonGreen, GGGGG linker, native locus)	This study	512
PAO1 mNG-PilH (N-terminal fluorescent fusion to mNeonGreen, GGGGG linker, native locus)	This study	446
PAO1 mNG-FimX (N-terminal fluorescent fusion to mNeonGreen, GGGGG linker, native locus)	This study	421
PAO1 mNG-FimX Δ*cyaB* Δ*pilH*	This study	1102
PAO1 Δ*fliC* PilB-mNG	This study	316
PAO1 Δ*fliC* PilB-mNG Δ*cpdA* Δ*pilG*	This study	1037
PAO1 Δ*fliC* mNG-PilT	This study	313
PAO1 Δ*fliC* mNG-PilU	This study	314
PAO1 Δ*fliC* mNG-PilG	This study	923
PAO1 Δ*fliC* mNG-PilH	This study	315
PAO1 Δ*fliC* mNG-FimX	This study	463
PAO1 Δ*fliC* mNG-FimX Δ*cpdA*	This study	1022
PAO1 Δ*fliC* mNG-FimX Δ*pilH*	This study	965
PAO1 Δ*fliC* mNG-FimX Δ*pilG*	This study	941
PAO1 ΔfliC mNG-FimX ΔpilG ΔcpdA	This study	1042
PAO1 ΔfliC mScI-PilG (N-terminal fluorescent fusion to mScarlet-I, GGGGG linker, native locus)	This study	954
PAO1 ΔfliC mScI-PilG mNG-FimX	This study	1006
PAO1 ΔfliC mScI-PilG PilB-mNG	This study	1013
PAO1 Δ*fliC* mNG-FimX Δ*pilA*	This study	1044
PAO1 Δ*pilB* + pJN105GM-PilB-mNG (arabinose inducible)	This study	744
PAO1 Δ*fliC* PaQa	This study	764
PAO1 Δ*fliC* Δ*pilH* PaQa	This study	864
PAO1 Δ*fliC* Δ*cpdA* PaQa	This study	867
PAO1 Δ*fliC* Δ*cpdA* Δ*pilH* PaQa	This study	951
PAO1 Δ*fliC* Δ*pilG* PaQa	This study	865

Name and relevant genotype	Source / Reference	Identifier
PAO1 Δ*fliC* Δ*cpdA* Δ*pilG* PaQa	This study	950
PAO1 Δ*fliC* Δ*cyaB* PaQa	This study	866
PAO1 Δ*fliC* Δ*cyaB* Δ*pilH* PaQa	This study	949
PAO1 Δ*fliC* Δ*cyaB* Δ*pilG* PaQa	This study	948
PAO1 Δ*fliC* Δ*pilTU* PaQa	This study	1121

Table 4-2: Plasmids used in this study.

Name and relevant information	Source / Reference	Identifier
pEX100TAP (Suicide vector based on pUC19, Amp^R, ColE1 ori (*E. coli*), *oriT*, *sacB*, *lacZα*)	(*108*)	Na
pEX18AP (Suicide vector based on pUC18, Amp^R, ColE1 ori (*E. coli*), *oriT*, *sacB*, *lacZα*)	(*109*)	Na
pEX18GM (Suicide vector based on pUC18, Gm^R, ColE1 ori (*E. coli*), *oriT*, *sacB*, *lacZα*)	(*109*)	Na
pJN105 (arabinose-inducible plasmid based on pBBR1MCS-5, Gm^R, pBBR1 ori (*E. coli* and *P. aeruginosa*), *araC*-P$_{BAD}$, *lacZα*)	(*110*)	Na
pUCP18 (high-copy plasmid derived from pUC18, Amp^R, ColE1 ori (*E. coli*), R1822-based ori (*P. aeruginosa*))	(*111*)	Na
pEx100TAP-Δ*cpdA* (Suicide vector for marker-free in-frame deletion of PA4969)	(*107*)	pJTW033
pEX18GM-Δ*cpdA* (Suicide vector for marker-free in-frame deletion of PA4969)	This study	pMK019
pEx100TAP-Δ*cyaB* (Suicide vector for marker-free in-frame deletion of PA3217)	(*107*)	pJTW031
pEX18GM-Δ*cyaB* (Suicide vector for marker-free in-frame deletion of PA3217)	This study	pMK018
pEx100TAP-Δ*pilG* (Suicide vector for marker-free in-frame deletion of PA0408)	(*11*)	PJB118
pEx100TAP-Δ*pilH* (Suicide vector for marker-free in-frame deletion of PA0409)	(*11*)	PJB119
pEx100TAP-Δ*fliC* (Suicide vector for marker-free in-frame deletion of PA1092)	(*11*)	pJB215
pEX18amp-Δ*pilA* (Suicide vector for marker-free in-frame deletion of PA4525)	This study	pMK009
pEx100TAP-PilB-mNG (Suicide vector for marker-free in-frame insertion of *pilB* C-terminus fused with mNeonGreen, separated by a GGGGG linker)	This study	pXP121
pEx100TAP-mNG-PilT (Suicide vector for marker-free in-frame insertion of *pilT* N-terminus fused with mNeonGreen, separated by a GGGGG linker)	This study	pXP118
pEx100TAP-mNG-PilU (Suicide vector for marker-free in-frame insertion of *pilU* N-terminus fused with mNeonGreen, separated by a GGGGG linker)	This study	pXP119

pEx100TAP-mNG-PilH (Suicide vector for marker-free in-frame insertion of *pilH* N-terminus fused with mNeonGreen, separated by a GGGGG linker)	This study	pXP125
pEx100TAP-mNG-FimX (Suicide vector for marker-free in-frame insertion of *fimX* N-terminus fused with mNeonGreen, separated by a GGGGG linker)	This study	pXP186
pEX18AMP-mScI-PilG (Suicide vector for marker-free in-frame insertion of *pilG* N-terminus fused with mScarlet-I, separated by a GGGGG linker)	This study	pMK007
pJN105GM-PilB-mNG (arabinose-inducible *p*ilB C-terminally fused with mNeonGreen, separated by a GGGGG linker)	This study	pXP377
pUCP18-PaQa (fluorescent reporter for cAMP level: YFP controlled by *PaQa* promoter (PA1867 and PA1868) and mKate2 controlled by *rpoD* promoter (PA0576) as reference.	(*3*)	pAP02.2

Table 4-3: Oligonucleotides used in this study.

Name and relevant information	Source / Reference	Identifier
mSc_-Strt_F (mutating mScarlet to mScarlet-I; GTG AGC AAG GGC GAG GCA GTG)	This study	oMK019
mSc-T74I_OL_R (mutating mScarlet to mScarlet-I; GGT GCT TGA TGA AGG CCC TGG AG)	This study	oMK020
mSc-T74I_OL_F (mutating mScarlet to mScarlet-I; GGG CCT TCA TCA AGC ACC CCG C)	This study	oMK021
mSc_-Stp_R (mutating mScarlet to mScarlet-I; CTT GTA CAG CTC GTC CAT GCC GCC G)	This study	oMK022
PilG_OL-EcoRI_R (cloning pMK007; GCT ATG ACC ATG ATT ACG CCA TGC TTT CCA GCA TGG GC)	This study	oMK032
PilG_OL-mScI_F (cloning pMK007; ATG GAC GAG CTG TAC AAG GGA GGC GGA GGC GGA GAA CAG CAA TCC GAC GGT TTG)	This study	oMK033
PilG_OL-mScI_R (cloning pMK007; TGC CTC GCC CTT GCT CAC CAT GTT CGC CCT ATA TCG ACT C)	This study	oMK034
PilG_OL-XbaI_F (cloning pMK007; CAT GCC TGC AGG TCG ACT CAT CAG GAT CAC GTC CAG TTC G)	This study	oMK035
Xba1_PilA_F (cloning pMK009; CAT GCC TGC AGG TCG ACT CAC AGA GGG ATG ACC CGG)	This study	oMK039
OL_PilA_KO_R (cloning pMK009; GTT ATC ACA CAT GAA TCT CTC CGT TGA TTA TGT ATA GG)	This study	oMK040
OL_PilA_KO_F (cloning pMK009; AGA TTC ATG TGT GAT AAC TAA GGT GAT CGA AGG)	This study	oMK041
EcoR1_PilA_R (cloning pMK009; GCT ATG ACC ATG ATT ACG CGG TGG AAG TGG AAG TGG)	This study	oMK042
EcoR1_cyaB_F (cloning pMK018; GCT ATG ACC ATG ATT ACG GCC GGT GTT CCT GTA TGT CG)	This study	oMK054
OL_cyaB_KO_R (cloning pMK018; CAT GAA GCC TGT CAT CCT CTA AGT TCG TCG AAC G)	This study	oMK055

Name and relevant information	Source / Reference	Identifier
OL_cyaB_KO_F (cloning pMK018; AGA GGA TGA CAG GCT TCA TGC GCT GGA GAG G)	This study	oMK056
Xba1_cyaB_R (cloning pMK018; CAT GCC TGC AGG TCG ACT TCG CCG AGT TCT ACC CCT ACT ACC)	This study	oMK057
seq fwd del cyaB (check pMK018; TGA TGA CGA GCG TTT CCA CAG T)	This study	oLT021
seq rev del cyaB (check pMK018; GCG TCG ATA CCG AAC TGT TCC AT)	This study	oLT022
XbaI_cpdA_F (cloning pMK019; CAT GCC TGC AGG TCG ACT GAC CTG CGA AGC GAA CTA CG)	This study	oMK058
OL_cpdA_KO_R (cloning pMK019; GTA TCC GGC TGA CAA GGG GCC GTC TCC)	This study	oMK059
OL_cpdA_KO_F (cloning pMK019; CCC TTG TCA GCC GGA TAC TGA CAT GCC CC)	This study	oMK060
EcoRI_cpdA_R (cloning pMK019; GCT ATG ACC ATG ATT ACG CCT GGT AGC GTT CGG GAC G)	This study	oMK061
seq fwd cpda KO (check pMK019; GTC TGG CCG TTG GAA GAT G)	This study	oLT009
seq rev cpda KO (check pMK019; AAA AGT CGG TGT CGC GC)	This study	oLT010
PilB region in PAO1 FWD (1) (cloning pXP121; ACC CTG TTA TCC CTA ACT AGC CTG TGG GGC GAG AAG ATC G)	This study	oXP175
PilB region in PAO1 FWD (2) (cloning pXP121; GTA TGG ATG AAT TGT ATA AAT AAT CCA TGG CGG ACA AAG C)	This study	oXP176
PilB region in PAO1 REV (1) (cloning pXP121; X GAG ACT CCG CCT CCG CCT CCA TCC TTG GTC ACG CGG TTG A)	This study	oXP177
PilB region in PAO1 REV (2) (cloning pXP121; GGA TAA CAG GGT AAT ACT AGT GTA GAC GAT GCC TCC GAA A)	This study	oXP178
G5linker mNeonGreen FWD (cloning pXP121; TCA ACC GCG TGA CCA AGG ATG GAG GCG GAG GCG GAG TCT C)	This study	oXP179
G5linker mNeonGreen REV (cloning pXP121; GCT TTG TCC GCC ATG GAT TAT TTA TAC AAT TCA TCC ATA CCC ATT ACA TCA GTA AAA GC)	This study	oXP180
Seq PilB_mNeonGreen fw (check pXP121; ACG GAG TCG AGC GCA TCG)	This study	oXP226
Seq PilB_mNeonGreen rev (check pXP121; GCG CAA CCT GGC CAA GTA C)	This study	oXP227
PilT PilU region in PAO1 FWD (1) (cloning pXP118; ACC CTG TTA TCC CTA ACT AGT TCG CGC AGG CGG GCG AAC G)	This study	oXP157

Name and relevant information	Source / Reference	Identifier
PilT PilU region in PAO1 FWD (2) (cloning pXP118; ATA AAG GAG GCG GAG GCG GAG ATA TTA CCG AGC TGC TCG CCT T)	This study	oXP158
PilT PilU region in PAO1 REV (1) (cloning pXP118; TCT TCT TCA CCT TTA GAG ACC ATG GGA CTC CCC AAT TAC AAG CAA GCA)	This study	oXP159
PilT PilU region in PAO1 REV (2) (cloning pXP118; GGA TAA CAG GGT AAT ACT AGG TCT TCG CCG CCG AGG TGG T)	This study	oXP160
G5linker mNeonGreen FWD (cloning pXP118; TGT AAT TGG GGA GTC CCA TGG TCT CTA AAG GTG AAG AAG ATA ATA TGG C)	This study	oXP161
G5linker mNeonGreen REV (cloning pXP118; GCG AGC AGC TCG GTA ATA TCT CCG CCT CCG CCT CCT TTA T)	This study	oXP162
Seq mNeonGreen_PilT fw (check pXP118; GAC TGC GAA GGC GCC TTG G)	This study	oXP220
Seq mNeonGreen_PilT rev (check pXP118; CTT CGC CGA TGG CTG CCT C)	This study	oXP221
PilT PilU region in PAO1 FWD (1) (cloning pXP119; ACC CTG TTA TCC CTA ACT AGA CGA ATC GAA GAA GTG CCT G)	This study	oXP163
PilT PilU region in PAO1 FWD (2) (cloning pXP119; ATA AAG GAG GCG GAG GCG GAG AAT TCG AAA AGC TGC TGC GCC)	This study	oXP164
PilT PilU region in PAO1 REV (1) (cloning pXP119; TCT TCT TCA CCT TTA GAG ACC ATG ATG TTC TCG CTC ACT C)	This study	oXP165
PilT PilU region in PAO1 REV (2) (cloning pXP119; GGA TAA CAG GGT AAT ACT AGG CAC CAG TTG CTG GGC GAC G)	This study	oXP166
G5linker mNeonGreen FWD (cloning pXP119; TGT GAG TGA GCG AGA ACA TCA TGG TCT CTA AAG GTG AAG AAG ATA ATA TGG C)	This study	oXP167
G5linker mNeonGreen REV (cloning pXP119; GCG CGC AGC AGC TTT TCG AAT TCT CCG CCT CCG CCT CCT TTA T)	This study	oXP168
Seq mNeonGreen_PilU fw (check pXP119; GCG GCG ATG CTC GAT TAC CTG)	This study	oXP222
Seq mNeonGreen_PilU rev (check pXP119; CCC TTG CGG ATC AGG TCG G)	This study	oXP223
PilG PilH ChpA region in PAO1 FWD (2) (cloning pXP125; ATA AAG GAG GCG GAG GCG GAG CTC GTA TTT TGA TTG TTG ATG ACT CTC GA CC)	This study	oXP232
PilG PilH ChpA region in PAO1 REV (1) (cloning pXP125; TCT TCT TCA CCT TTA GAG ACC ATG GGA TCC CCA TCA CGA A)	This study	oXP232

Name and relevant information	Source / Reference	Identifier
mNeonGreen G5 linker FWD (cloning pXP125; TTC GTG ATG GGG ATC CCA TGG TCT CTA AAG GTG AAG AAG ATA ATA TGG C)	This study	oXP234
mNeonGreen G5 linker REV (cloning pXP125; TCA ACA ATC AAA ATA CGA GCT CCG CCT CCG CCT CCT TTA T)	This study	oXP235
PilG PilH ChpA region in PAO1 FWD (2) (cloning pXP125; ACA AGG GAG GCG GAG GCG GAG CTC GTA TTT TGA TTG TTG ATG ACT CTC CGA CC)	This study	oXP236
PilG PilH ChpA region in PAO1 REV (1) (cloning pXP125; AGC TCC TCG CCC TTG CTC ACC ATG GGA TCC CCA TCA CGA A)	This study	oXP237
Sq pilG ko fwd (check pXP125; CGT GGC GAA GAA CTT CTC G)	This study	oLT042
check_pilGH (check pXP125; TTT ATA CGG CGA CGT CGA GG)	This study	oMK052
FimX region in PAO1 FWD (1) (cloning pXP186; TAT GAC CAT GAT TAC GAA TTC TGC CCA TCG TCA ACC AC)	This study	oXP438
FimX region in PAO1 REV (1) (cloning pXP186; TCT TCA CCT TTA GAG ACC ATG GAA AGG GCT CAG TCC)	This study	oXP439
mNeonGreen G5 linker FWD (cloning pXP186; ACT GAG CCC TTT CCA TGG TCT CTA AAG GTG AAG AAG ATA ATA T)	This study	oXP440
mNeonGreen G5 linker REV (cloning pXP186; CCG CCG CCC GAG CCC CCG CCG CCT TTA TAC AAT TCA TCC ATA CCC ATT A)	This study	oXP441
FimX region in PAO1 FWD (2) (cloning pXP186; CGG GGG CTC GGG CGG CGG GGG CTC GAT GGC CAT CGA AAA GAA AAC CAT C)	This study	oXP442
FimX region in PAO1 REV (2) (cloning pXP186; TGC CTG CAG GTC GAC TCT AGA GGC GCC CTG GTC GCA)	This study	oXP443
seq FimX N' fusion fw (check pXP186; AGG CCC ACG CAC AGG)	This study	oXP456
seq FimX N' fusion rev (check pXP186; GGT GCA AAC CAG TTC GG)	This study	oXP457
EcoRI pilB fwd (cloning pXP377; AAA GAA TTC ATG AAC GAC AGC ATC AAC CTG)	This study	oXP909
mNG in pJN105 (rev) (cloning pXP377; CCG CTC TAG ATC ATT TAT ACA ATT CAT CCA TAC)	This study	oXP616

Table 4-4: Sample sizes and analysis information for all experiments conducted in this study.

Spatiotemporal displacement maps (Figure 4.1*C*)

Analysis script: "save_real_displacement.m" and "graph_real_disp_individual.m"

Analysis data file: "real_displacement_data.mat"

Strain	Replicate	Imaging interval / Time on surface	Number of tracks	Filtered tracks	Displayed tracks
177 ΔfliC	1	5s interval-2h37	1318	138	200
	2	5s interval-2h37	671	223	
	3	5s interval-2h37	346	190	
232 ΔfliC ΔpilH	1	5s interval-2h37	322	165	200
	2	5s interval-2h37	360	182	
	3	5s interval-2h37	668	163	
326 ΔfliC ΔcyaB	1	5s interval-2h37	964	35	200
	2	5s interval-2h37	585	105	
	3	5s interval-2h37	509	169	
436 ΔfliC ΔcyaB ΔpilH	1	5s interval-2h37	578	1	200
	2	5s interval-2h37	1049	131	
	3	5s interval-2h37	660	178	
337 ΔfliC ΔcpdA	1	5s interval-2h37	2268	49	200
	2	5s interval-2h37	1736	48	
	3	5s interval-2h37	1254	103	
459 ΔfliC ΔpilG ΔcpdA	1	5s interval-2h37	597	250	200
	2	5s interval-2h37	1536	542	
	3	5s interval-2h37	2916	892	

Reversal frequency (Figure 4.2*A*)

Analysis script: "save_reversals.m" and "graph_reversals.m"

Analysis data file: "reversals_data.mat"

Strain	Replicate	Imaging interval / Time on surface	Tracks (moving)	Tracked time (h)	
177 ΔfliC	1	5s interval-2h37	1318	26.01	
	2	5s interval-2h37	671	23.51	

Strain	Replicate	Imaging interval / Time on surface		
	3	5s interval-2h37	346	17.09
232 ΔfliC ΔpilH	1	5s interval-2h37	322	15.12
	2	5s interval-2h37	360	16.54
	3	5s interval-2h37	668	19.27
326 ΔfliC ΔcyaB	1	5s interval-2h37	964	14.44
	2	5s interval-2h37	585	14.63
	3	5s interval-2h37	509	18.02
436 ΔfliC ΔcyaB ΔpilH	1	5s interval-2h37	578	5.08
	2	5s interval-2h37	1049	22.48
	3	5s interval-2h37	660	20.14
337 ΔfliC ΔcpdA	1	5s interval-2h37	2268	31.47
	2	5s interval-2h37	1736	22.66
	3	5s interval-2h37	1254	24.23
459 ΔfliC ΔpilG ΔcpdA	1	5s interval-2h37	597	25.12
	2	5s interval-2h37	1536	56.40
	3	5s interval-2h37	2916	97.59

Reversal rate after collision (Figure 4.2*C*)

Analysis plot script: "graph_collisions.m"

Analysis data file: "Count_Collisions.xlsx"

Strain	Replicate	Imaging interval / Time on surface	Counted movies	Counted collisions	
177 ΔfliC	1	5s interval-2h37	4	117	
	2	5s interval-2h37	4	53	
	3	5s interval-2h37	2	48	
232 ΔfliC ΔpilH	1	5s interval-2h37	4	59	
	2	5s interval-2h37	1	61	
	3	5s interval-2h37	4	58	
326 ΔfliC ΔcyaB	1	5s interval-2h37	4	93	
	2	5s interval-2h37	2	59	
	3	5s interval-2h37	2	56	

436 ΔfliC ΔcyaB ΔpilH	1	5s interval-2h37	3	128	
	2	5s interval-2h37	2	65	
	3	5s interval-2h37	2	52	
337 ΔfliC ΔcpdA	1	5s interval-2h37	2	113	
	2	5s interval-2h37	2	50	
	3	5s interval-2h37	2	57	
459 ΔfliC ΔpilG ΔcpdA	1	5s interval-2h37	8	55	
	2	5s interval-2h37	4	58	
	3	5s interval-2h37	2	49	

Reversal rate after collision with fiber (Figure 4.2*E*)

Analysis file: "Count_Collisions_Microfibers.xlsx"

Strain	Replicate	Imaging interval / Time on surface	Counted movies	Counted cell-cell collisions	Counted cell-fiber collisions
177 ΔfliC	1	5s interval-2h37	1	51	33
	2	5s interval-2h37	1	62	56
	3	5s interval-2h37	1	58	39

Pili localization (Figure 4.3*C* and Figure 4.6*F*)

Strain	Replicate	Counted cells			
ΔfliC PilB_mNG	1	56			
	2	35			
	3	20			
	4	48			
	5	21			
	6	20			
ΔfliC mNG_PilT	1	49			
	2	50			
	3	34			
	4	29			

Strain	Replicate	Imaging interval / Time on surface	Tracks (moving)	Tracks (non-moving)	
	5		32		
ΔfliC mNG_PilU	1		57		
	2		54		
	3		32		
	4		38		
	5		40		
ΔfliC mNG_PilG	1		28		
	2		21		
	3		27		
	4		24		
	5		12		
	6		14		

Asymmetry of protein localization during twitching (Figure 4.3*D* and 4.6*E*)

Analysis script: "save_asymmetry.m" and "graph_asymmetry.m"

Analysis data file: "asymmetry_data.mat"

Strain	Replicate	Imaging interval / Time on surface	Tracks (moving)	Tracks (non-moving)	
316 ΔfliC PilB_mNG	1	2s interval-2h37	154	443	
	2	2s interval-2h37	13	211	
	3	2s interval-2h37	28	240	
	4	5s interval-2h37	14	147	
313 ΔfliC mNG_PilT	1	2s interval-2h37	529	592	
	2	2s interval-2h37	205	218	
	3	2s interval-2h37	275	231	
	4	2s interval-2h37	215	325	
314 ΔfliC mNG_PilU	1	2s interval-2h37	483	450	
	2	2s interval-2h37	258	245	
	3	2s interval-2h37	605	383	
	4	2s interval-2h37	636	391	
463 ΔfliC mNG_FimX	1	2s interval-2h37	352	465	

Strain	Replicate	Imaging interval / Time on surface		
	2	2s interval-2h37	144	249
	3	2s interval-2h37	154	225
	4	5s interval-2h37	84	119
923 ΔfliC mNG_PilG	1	2s interval-2h37	526	558
	2	2s interval-2h37	154	118
	3	2s interval-2h37	279	250
	4	5s interval-2h37	211	96
315 ΔfliC mNG_PilH	1	2s interval-2h37	366	274
	2	2s interval-2h37	325	240
	3	2s interval-2h37	95	128
	4	5s interval-2h37	157	111

Alignment factor (Figure 4.3*E* and 4.6*D*)

Analysis script: "save_alignment.m" and "graph_alignment.m"

Analysis data file: "alignment_data.mat"

Strain	Replicate	Imaging interval / Time on surface	Tracks		
316 ΔfliC PilB_mNG	1	2s interval-2h37	154		
	2	2s interval-2h37	13		
	3	2s interval-2h37	28		
	4	5s interval-2h37	14		
313 ΔfliC mNG_PilT	1	2s interval-2h37	529		
	2	2s interval-2h37	205		
	3	2s interval-2h37	275		
	4	2s interval-2h37	215		
314 ΔfliC mNG_PilU	1	2s interval-2h37	483		
	2	2s interval-2h37	258		
	3	2s interval-2h37	605		
	4	2s interval-2h37	636		
463 ΔfliC mNG_FimX	1	2s interval-2h37	366		
	2	2s interval-2h37	325		

	3	2s interval-2h37	95		
	4	5s interval-2h37	157		
923 ΔfliC mNG_PilG	1	2s interval-2h37	352		
	2	2s interval-2h37	144		
	3	2s interval-2h37	154		
	4	5s interval-2h37	84		
315 ΔfliC mNG_PilH	1	2s interval-2h37	526		
	2	2s interval-2h37	154		
	3	2s interval-2h37	279		
	4	5s interval-2h37	211		

Oscillations of polar fluorescent signal of FimX (Figure 4.4*B, D* and Supplementary Figure 4.7)

Analysis script: "graph_pole2pole_oscillations.m"

Strain	Replicates	Imaging interval / Time on surface	Tracks (moving)	Tracks (non-moving)	Tracks (moving + non-moving)
463 ΔfliC mNG_FimX	1	5s interval-10min	378	231	609
	1	5s interval-60min	1045	541	1586
	2	5s interval-10min	469	457	926
	2	5s interval-60min	1225	621	1846
	3	5s interval-10min	489	391	880
	3	5s interval-60min	903	557	1460
1044 ΔfliC mNG_FimX ΔpilA	1	5s interval-10min	0	304	304
	1	5s interval-60min	0	502	502
	2	5s interval-10min	0	334	334
	2	5s interval-60min	0	361	361
	3	5s interval-10min	0	408	408
	3	5s interval-60min	0	478	478

Protein localization (Figure 4.5, Figure 4.6*C, D* and Supplementary Figure 9)

Strain	Replicate	Analyzed cells			
PilB_mNG	1	622			

116

	2	534			
	3	1020			
PilB_mNG ΔpilH	1	162			
	2	245			
	3	164			
PilB_mNG ΔpilG	1	302			
	2	513			
	3	666			
PilB_mNG ΔcpdA	1	287			
	2	247			
	3	301			
ΔfliC mNG_fimX	1	637			
	2	531			
	3	371			
ΔfliC mNG_fimX ΔpilH	1	518			
	2	489			
	3	512			
ΔfliC mNG_fimX ΔpilG	1	626			
	2	556			
	3	642			
ΔfliC mNG_fimX ΔcpdA	1	179			
	2	337			
	3	369			
ΔfliC mNG_PilG	1	462			
	2	546			
	3	840			
ΔfliC mNG_PilH	1	532			
	2	1038			
	3	670			
ΔpilB PilB_mNG not induced	1	298			
ΔpilB PilB_mNG 0.01% ara	1	476			

ΔpilB PilB_mNG 0.03% ara	1	528			

PaQa levels (Supplementary Figure 4.1*C*)

Strain	Growth	Replicate	Analyzed cells		
ΔcpdA ΔfliC	Liquid	1	173		
	Liquid	2	459		
	Liquid	3	687		
ΔcyaB ΔfliC	Liquid	1	253		
	Liquid	2	500		
	Liquid	3	544		
ΔfliC	Liquid	1	282		
	Liquid	2	391		
	Liquid	3	529		
	Solid	1	562		
	Solid	2	503		
	Solid	3	357		
ΔpilG ΔcpdA ΔfliC	Liquid	1	88		
	Liquid	2	556		
	Liquid	3	471		
	Liquid	4	518		
	Liquid	5	232		
ΔpilG ΔcyaB ΔfliC	Liquid	1	235		
	Liquid	2	921		
	Liquid	3	600		
ΔpilG ΔfliC	Liquid	1	155		
	Liquid	2	457		
	Liquid	3	510		
ΔpilH ΔcpdA ΔfliC	Liquid	1	109		
	Liquid	2	605		
	Liquid	3	478		
	Liquid	1	106		

Strain	Growth	Replicate	Counted cells		
	Liquid	2	927		
	Liquid	3	833		
ΔpilH ΔfliC	Liquid	1	187		
	Liquid	2	677		
	Liquid	3	568		
ΔpilTU ΔfliC	Liquid	1	572		
	Liquid	2	586		
	Liquid	3	764		
	Liquid	4	376		

Pili count (Supplementary Figure 4.1*D*)

Strain	Growth	Replicate	Counted cells	
ΔfliC	Liquid	1	33	
	Liquid	2	31	
	Liquid	3	21	
	Solid	1	8	
	Solid	2	11	
	Solid	3	35	
	Solid	4	47	
ΔcpdA ΔfliC	Liquid	1	10	
	Liquid	2	11	
	Liquid	3	22	
ΔpilH ΔfliC	Liquid	1	25	
	Liquid	2	20	
	Liquid	3	16	
ΔpilH ΔcyaB ΔfliC	Liquid	1	20	
	Liquid	2	14	
	Liquid	3	15	
	Liquid	4	49	
ΔcyaB ΔfliC	Liquid	1	28	
	Liquid	2	9	

	Liquid	3	49		
	Liquid	1	16		
ΔpilG ΔfliC	Liquid	2	15		
	Liquid	3	27		
	Liquid	1	12		
ΔpilG ΔcpdA ΔfliC	Liquid	2	16		
	Liquid	3	15		
	Liquid	4	36		

Pili assymetry (Supplementary Figure 4.3)

Strain	Replicates	Counted cells			
ΔfliC	pooled data	59			
ΔcpdA ΔfliC	pooled data	23			
ΔpilG ΔcpdA ΔfliC	pooled data	42			
ΔpilH ΔcyaB ΔfliC	pooled data	57			

Colocalization of FimX and PilG (Supplementary Figure 4.12*B*)

Analysis file: "Counting_Colocalization.xlsx"

Strain	Replicates	Imaging interval / Time on surface	Counted movies	Tracks (moving)	
1006 ΔfliC mNG-FimX mScI-PilG	1	3s interval-2h37	3	49	
	2	3s interval-2h37	3	59	
	3	10s interval-2h37	2	53	
1013 ΔfliC PilB-mNG mScI-PilG	1	5s interval-3h37	2	57	
	2	5s interval-3h37	2	45	
	3	10s interval-3h37	1	31	

Reversal delay time (Supplementary Figure 4.13)

Analysis script: "Reversal_Delay_Tau.m"

Analysis data file: "Count_Reversal_Delay_Tau.xlsx"					
Strain	Replicates	Imaging interval / Time on surface	Tracks (moving)		
463 ΔfliC mNG_FimX	pooled data	1 and 2 h	47		
923 ΔfliC mNG_PilG	pooled data	1 and 2 h	29		

Movie S4.1: Phase contrast image sequences of *P. aeruginosa* cells twitching forward and reversing. Videos corresponding to **Figure 4.1*B***. Scalebar, 2 µm.

Movie S4.2: Phase contrast image sequence showing *P. aeruginosa* Δ*cpdA* Δ*pilG* cells moving back and forth, without much net migration. Scalebar, 10 µm.

Movie S4.3: Phase contrast image sequence of reversal behaviors upon collisions. A WT *P. aeruginosa* cell collides with another cell, then reverses. A Δ*pilH* cell collides with another cell but doesn't reverse. Videos correspond to images in **Figure 4.2*B***. Scalebar, 2 µm.

Movie S4.4: Phase contrast image sequence of reversal behaviors upon collisions with other cells or non-biological obstacles (glass microfibers). WT *P. aeruginosa* cells reverse both after collision with other cells as well as after collisions with a glass microfiber. White triangles indicate collisions with another cell, black triangles indicate collisions with a fiber. Videos correspond to images in **Figure 4.2*D***. Scalebar, 2 µm.

Movie S4.5: Twitching *P. aeruginosa* WT, Δ*pilH* and Δ*cpdA* Δ*pilG* cells at high cell density. Phase contrast image sequence corresponding to **Figure 4.2*F***. Scalebar, 50 µm.

Movie S4.6: Colony edge expansion of twitching *P. aeruginosa* WT and Δ*pilH* cells. WT cells spread evenly and reverse upon collision with other cells. Due to their inability to reverse, Δ*pilH* cells form transient comet-shaped rafts and swirls. In conditions that don't allow single cell twitching, donut-shaped swirls have been reported for Δ*pilH*, that likely arrive from the inability to reverse as well (*13*). Phase contrast image sequence corresponding to **Supplementary Figure 4.2**. Scalebar, 50 µm.

Movie S4.7: Fluorescent localization of PilB-mNG, mNG-FimX, mNG-PilT and mNG-PilU in twitching cells. PilB-mNG, mNG-FimX localizes more prominently to the leading pole. Fluorescence microscopy image sequence corresponding to **Supplementary Figure 4.4**. The arrow in the first frame indicates the cell depicted in the corresponding figure. Playback speed, 20x. Scalebar, 10 µm.

Movie S4.8: Fluorescence microscopy image sequence of PilB-mNG and mNG-FimX during reversal. Videos correspond to **Supplementary Figure 4.6**. Playback speed, 20x. Scalebar, 2 µm.

Movie S4.9: Fluorescence microscopy image sequence corresponding to **Figure 4.4*A***. mNG-FimX oscillates between poles in a non-moving cell 10 min after touching the surface. Playback speed, 50x. Scalebar, 2 µm.

Movie S4.10: Fluorescence microscopy image sequence corresponding to **Figure 4.4*C***. In Δ*pilA*, mNG-FimX keeps oscillating between poles in a non-moving cell even 60 min after touching the surface. Playback speed, 50x. Scalebar, 2 µm.

Movie S4.11: Fluorescent localization of mNG-PilG and mNG-PilH in twitching cells. Image sequence corresponding to **Supplementary Figure 4.10*A***. mNG-PilG localizes more prominently to the leading pole. The arrow in the first frame indicates the cell depicted in the corresponding figure. Playback speed, 20x. Scalebar, 10 µm.

Movie S4.12: mNG-PilG fluorescence during a reversal. mNG-PilG localizes to the new leading pole. Fluorescence microscopy image sequence corresponding to **Supplementary Figure 4.10*B***. Playback speed, 20x. Scalebar, 5 µm

NB: Movies are located at the following link: https://www.pnas.org/content/118/30/e2101759118/tab-figures-data

Chapter 5.   From surface contact to Chp activation: exploring the molecular and biophysical mechanism of mechanosensing in *P. aeruginosa*

Contributions:

Mutagenesis screen and mutant characterization: Xavier Pierrat, Zainebe Al-Mayyah, Alessandra Vitale, Janet Van der Graaf and <u>Lorenzo Talà</u>
BACTH: Ramiro Patino, Xavier Pierrat
CryoEM: <u>Lorenzo Talà</u>, Yi-Wei Chang, Longsheng Lai, Sergei Nasarov, Xavier Pierrat
PaQa Measurements: <u>Lorenzo Talà</u>
TEM, iSCAT and fluorescence of TFP: <u>Lorenzo Talà</u>
Polarization: <u>Lorenzo Talà</u> and Marco Kühn

5.1 Introduction:

Bacteria sense their surrounding environment in order to detect and migrate towards nutrient sources or escape from predators or harmful substances. Microbial sensors often consists in two-component systems (TCS) wherein a sensor kinase transduces an external stimulus to a functional unit that stimulates a cellular response (*112*, *113*). The signals activating these systems remain largely unknown. External stimuli can either be chemical, such as nutrient sources, or physical such as temperature. Chemical cues activate TCS to steer motility or regulate second messenger levels to modulate various biological responses (*114*). Recent studies have also underlined the importance of physical cues in triggering physiological responses such as, sensing light directionality in phototaxis (*98*, *115*) or temperature variations to trigger virulence (*116*, *117*). Mechanical signals have recently been proposed as regulators of virulence, surface motility or biofilm formation by stimulating TCS (*68*, *118*).

Motility plays a crucial role in bacterial survival, allowing cells to escape from a hostile environment and migrate to new favorable niches. Prokaryotes and archaea developed many different motility strategies to navigate the many diverse habitats in which they live (*67*). However, motility mechanisms can be classified in two categories: swimming in a liquid environment and translation on solid substrates (*119*). Most swimming bacteria use particular TCS called chemotaxis systems to direct motility. The canonical Che chemotaxis systems has been extensively studied for its role in steering swimming motility in *E. coli* and other species upon sensing gradients of nutrients (*80*).

The main sensory protein of the Che system is a methyl-accepting chemotaxis protein (MCP) that

changes conformation upon binding to a ligand. The change in conformation of the MCP activates a

histidine kinase (HK) called CheA that in turn transfers a phosphoryl group to a response regulator

called CheY (RR). The phosphorylated response regulator diffuses through the cytoplasm and

interacts with the flagellar stator to reverse its direction of rotation. By this, the cells control the

duration of forward swimming phases (runs) and the frequency of directional changes (tumbles),

ultimately guiding the cells for example up the chemical gradient of nutrients (*14*) (**Figure 5.1A**). In

addition, two proteins, CheR (a methyltransferase) and CheB (a methylesterase) are responsible for

modulating the methylation state of the MCP in order to adapt its sensitivity depending on the

baseline concentration of ligand (*80*). This adaptation mechanism provides a "memory" to the Che

system that allows to measure temporal changes in ligand concentrations rather than absolute

values.
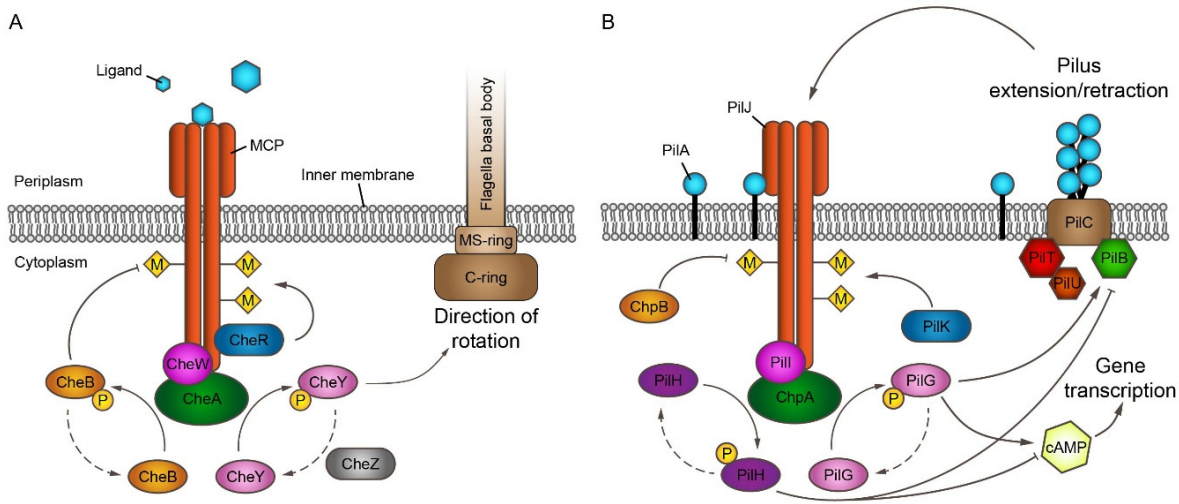
Figure 5.1: Comparison between the Che system of *E. coli* and the Chp system of *P. aeruginosa*

A) Simplified schematic of the Che system of *E. coli* depicting the interaction between the key players of the signaling pathway. Upon ligand binding the MCP activates the histidine kinase ChpA that phosphorylate the response regulator CheY. CheY-p diffuses to the flagellum rotor FliM and induces a CCW rotation. CheA also phosphorylates CheB, a methylesterase that in collaboration with the methyltransferase CheR is responsible for an adaptation mechanism that reset the MCP state. B) Similar schematic of the Chp system of *P. aeruginosa*. Upon binding of the putative activator PilA, PilJ activates ChpA that in turn phosphorylates two response regulators PilG and PilH with antagonistic effects on extension and regulation of gene transcription through cAMP production. A similar adaptation system as for *E. coli* is formed by the PilK methyltransferase and the ChpB methylesterase.

The opportunistic pathogen *Pseudomonas aeruginosa* can transition from a planktonic state to a surface associated state where cells move by extending and retracting its type IV pili (TFP), a process known as twitching (*17*, *22*, *41*). To direct surface motility, *P. aeruginosa* uses a chemotaxis-like TCS, called the Chp system, which is homologous to the Che system of *E. coli* (*40*). The Chp system comprises an MCP (PilJ) that activates a HK (ChpA) upon surface contact. In contrast to the Che system, the HK ChpA interacts with two RR (PilG and PilH) (*11*). The two RR work in an antagonistic manner to direct twitching motility during mechanotaxis (*40*). They also control virulence gene transcription by regulating the activity of the adenylate cyclase CyaB and the phosphodiesterase CpdA, which modulate cyclic adenosine monophosphate (cAMP) levels (*3*, *11*, *120*). The Chp system also has a methyltransferase (PilK) and a methylesterase (ChpB) which are homologous to the CheR and CheB proteins of the Che system (**Figure 5.1***B*). However, how PilK and ChpB regulate PilJ methylation, and ultimately twitching motility and surface response, remains unclear.

Surface sensing through the Chp system requires functional TFP as deletions in the major pilin gene *pilA* or the extension/retraction (*pilB*/*pilT*) motor genes respectively abolishe or reduce surface response (*3*). Chp activity was assessed through a reporter for cyclic-AMP-dependent surface response (*3*, *40*). This reporter is a fusion of the promoter sequence of the PaQa operon (type II secrection system) to YFP (yellow fluorescence) and includes mKate2 protein (red fluorescence) under the control of a constitutive promoter (*rpoD* promoter). By computing the ratio between the PaQa signal and the RFP background we can determine the Chp system activity of individual cells.
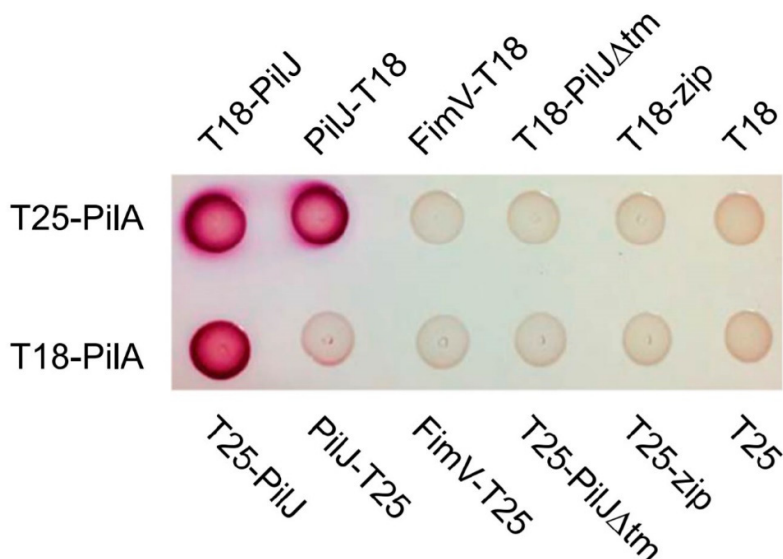
Figure 5.2: PilA-PilJ interaction in BACTH measurements.

Results of BACTH assay for PilA-PilJ interaction using colorimetry of β-galactosidase activity show a clear interaction between the two proteins. Adapted from Persat et *al. PNAS* 2015 (*3*).

The surface response is PilJ-dependent as a deletion mutant in *pilJ* is surface-blind (*3*) In addition, BACTH data shows that PilA can interact with PilJ (*3*) (**Figure 5.2**). However, BACTH has several limitations (*121*), namely the assay is performed in another host with different post-translational modifications that may lead to unnatural interactions. Nevertheless, this result suggests a hypothesis where the Chp system senses surface contact by interacting with PilA either as a monomer or in TFP (*3*). What does PilJ actually sense when TFP adhere on surfaces and pull the cell forward during twitching motility? Here we envision two non-exclusive mechanisms by which TFP may activate the Chp system in *P. aeruginosa*.

1) *TFP or PilA conformational changes*. Biophysical measurements show that TFP exert forces up to 100 pN during retraction (*53*, *54*). Under such tension TFP fibers stretch during which its conformation may change (*62*). The structure of the PilA protein predicts a melted region in its N-terminal alpha-helix from G14 to P22 which is conserved among many species (*122*). This region has been shown to participate in pilin packing during TFP assembly as well as providing flexibility to

the fiber (*15*). TFP initial structure is retrieved when no force is applied. This suggest that TFP undergo structural changes that are reversible, possibly through unfolding and refolding of the PilA N-terminus melted domain (*62*). We therefore hypothesize that tension-induced conformational changes during retraction activates PilJ. PilJ could either sense stretched TFP (**Figure 5.3A**) or stretched depolymerized PilA (**Figure 5.3C**).

2) *PilA monomer flux*. BACTH evidence shows that the pilin subunit PilA interacts with the MCP PilJ (*3*). As PilJ localizes to the poles of the bacteria (*123*) where TFP extension/retraction occur, we hypothesize that PilJ may be activated by binding PilA subunits to its periplasmic domain. Therefore, PilJ could act as a sensor for PilA concentration (**Figure 5.3B**). This hypothesis is analogous to a temporal ligand sensing mechanism stimulating the Che system. Recent evidence of local fluctuations of PilA at the TFP base during extension and retraction are consistent with this hypothesis (*124*).
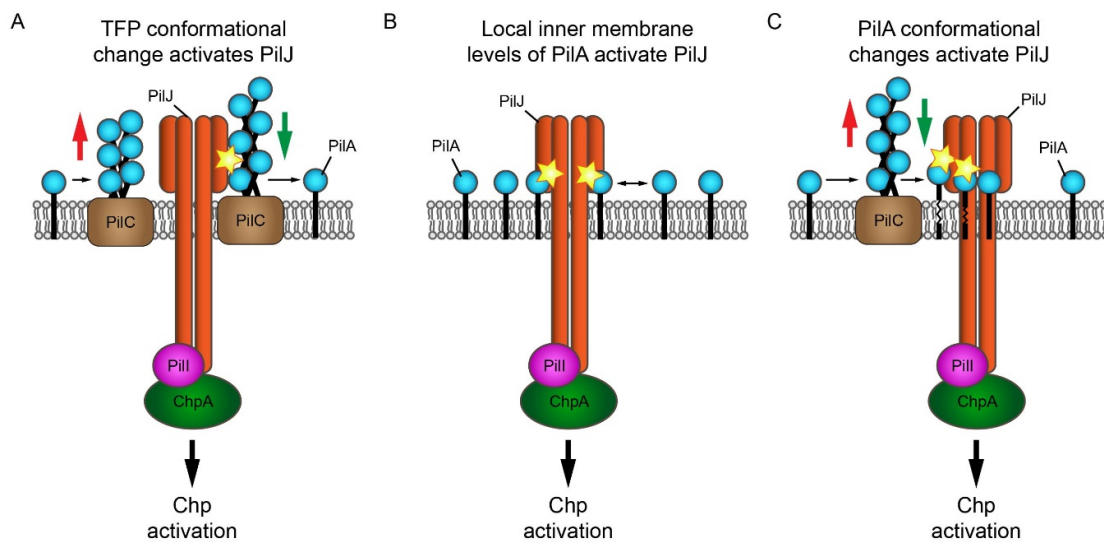
Figure 5.3: Putative mechanisms of mechanical signal transduction in the Chp system.

A) TFP stretching under tension during retraction of a bound pilus exposes new residues that can be sensed by PilJ. B) PilA binds and unbinds to PilJ with a certain affinity. PilA concentration changes are sensed by PilJ in order to regulate the activation of the Chp system. C) PilA melts a portion of its N-terminal α-helix between residues G14 and P22. Upon retraction of a bound pilus, the load on the TFP may induce melting of the pilin and reintegrated pilins may activate PilJ.

Finally, the mechanotransduction mechanism may also involve a combination of these models. Here, we combined genetic screens with biophysical measurements to test these two scenarios and ultimately tease out the surface sensing mechanism activating *P. aeruginosa* acute virulence. We first screen for gain of function mutations in *pilA* that result in increased activation of the transcriptional surface response in liquid. This screen identified a gain of function mutant that has TFP. We then perform biochemical, biophysical and structural characterization of this mutant which allowed us to improve our understanding of how TFP activates the Chp system.

5.2 Results

5.2.1 Screen for gain-of-function pilA mutants

To investigate the mechanism by which PilJ interacts with PilA to activate the Chp system, we performed a mutagenesis screen on the N-terminal alpha-helix of PilA to find potential gain-of-function (GoF) mutations. We reasoned that these GoF mutations may lock the Chp system in a conformation that activates PilJ, thereby providing valuable insights on the mechanism of activation. We restricted the mutagenesis screen to PilA residues F7 to R36 for the following reasons: 1) PilA is transcribed as a pre-pilin containing a membrane signal peptide from M1 to G6 that is cleaved by the peptidase PilD once the pilin is located into the inner membrane (*9*, *125*), 2) The globular domain of PilA is highly variable among *P. aeruginosa* strains that also possess a Chp system, compared to the more conserved N-terminal alpha helix domain (*126*). 3) Finally these residues reside in the inner core of the assembled TFP and are subject to conformational changes during assembly (*15*).

As a first step, we generated a library of *pilA* point mutants by error-prone PCR. This library was cloned into a low copy plasmid under expression of the native *pilA* promoter. We then transformed the *pilA** library in PAO1 Δ*pilA* background also containing the PaQa reporter (*3*, *40*). We then arrayed this library in glass bottom 96-well plates. We screened in total 960 mutants. The mutants were grown to exponential phase and were screened for PaQa YFP reporter intensity in liquid culture on a high content screening confocal spinning disc microscope (**Figure 5.4**).
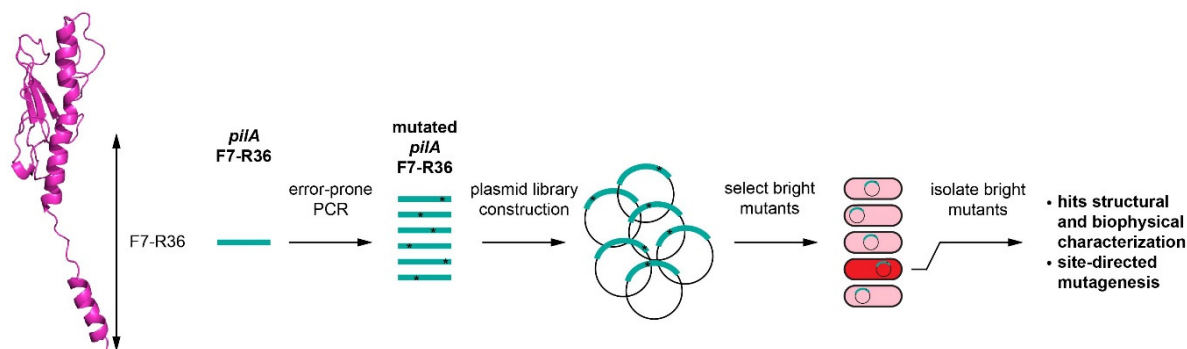
Figure 5.4: Schematic of the mutagenesis screen pipeline

A library of *pilA* random mutations in the residues F7 to R36 was generated through error-prone PCR. Cells containing the PaQa reporter were retransformed with the *pilA** library and then mutants were screened for elevated cAMP levels through high throughput fluorescence microscopy.

For each mutant in the screen, we computed the ratio between YFP and RFP fluorescence intensity. Cells that possessed elevated YFP/RFP ratio compared to WT *pilA* control were selected for subsequent characterization (**Figure 5.5***A*). Substitution of the threonine 8 by a valine (T8V) was the most frequent *pilA* GoF mutation. Therefore, we refined our screen by performing site-directed mutagenesis at T8 and included the following residues: F7 and L9 because they flank residue T8, E11 because it interacts with the T8 residue of adjacent pilins in the assembled TFP (*15*) (**Supplementary Figure 5.1)**. In addition, we further investigated P28 because it is crucial in melting of PilA during assembly (*122*) and Y30, N32, Y33 and R36 because they appeared to face the inner core of the assembled pilus in the published pilin structure of the *P. aeruginosa* PAK strain which shares a 100% identical sequence with PAO1 *pilA* for the first 44 residues (**Figure 5.5***B*). We performed this secondary screen by high throughput screening microscopy (see **Table 5-1** for details). For each targeted mutation we screened 96 mutants. We selected three T8 mutations (T8V, T8I and T8F) because they had elevated cAMP levels in liquid and retained an ability to twitch in the stab assay, indicating that functional pili fibers are assembled.
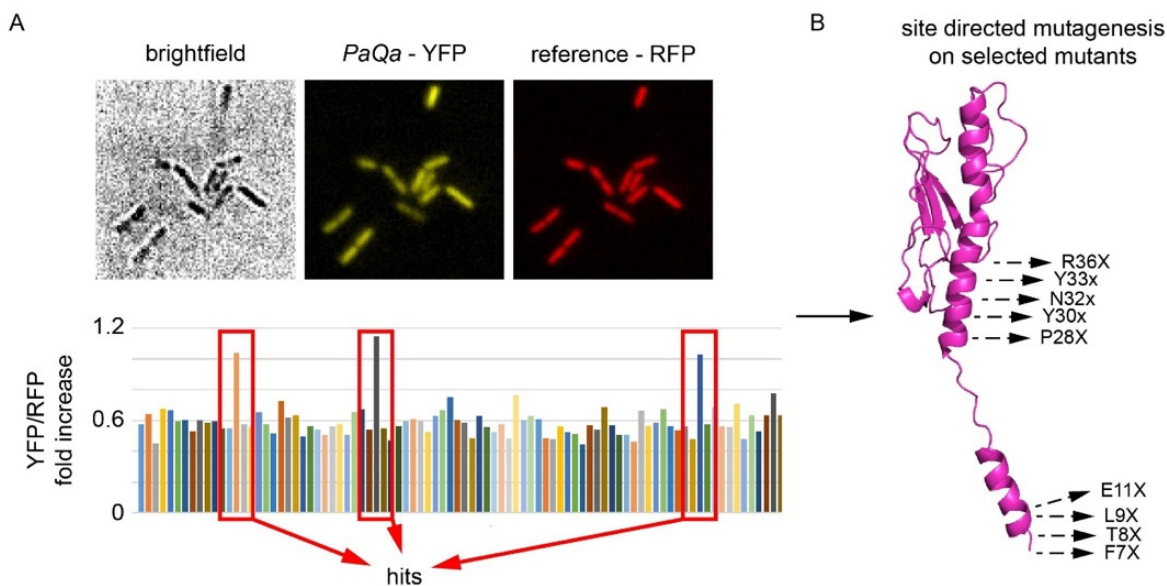
Figure 5.5: Mutagenesis screen results on activation of the Chp system and selection of specific residues for site-directed mutagenesis.

A) Cells were screened for high cAMP levels using high throughput fluorescence microscopy. One of the mutations that recurrently appeared on the screen was the mutation *pilA$_{T8V}$*. B) PilA structure model depicting the residues selected for site-directed mutagenesis.

PilA mutants have been selected based on their elevated cAMP levels in cells that were carrying a mutated *pilA* on a replicative plasmid. To validate their GoF phenotype, we induced the targeted *pilA* mutations at the native chromosomal locus. We then measured cAMP levels from exponential liquid cultures using the PaQa reporter. All three T8 mutations displayed higher levels of cAMP (**Figure 5.6**). Suggesting that residue T8 plays a role in the activation of PilJ, either by mimicking the effects of the signal input or by stimulating the interaction with PilJ.
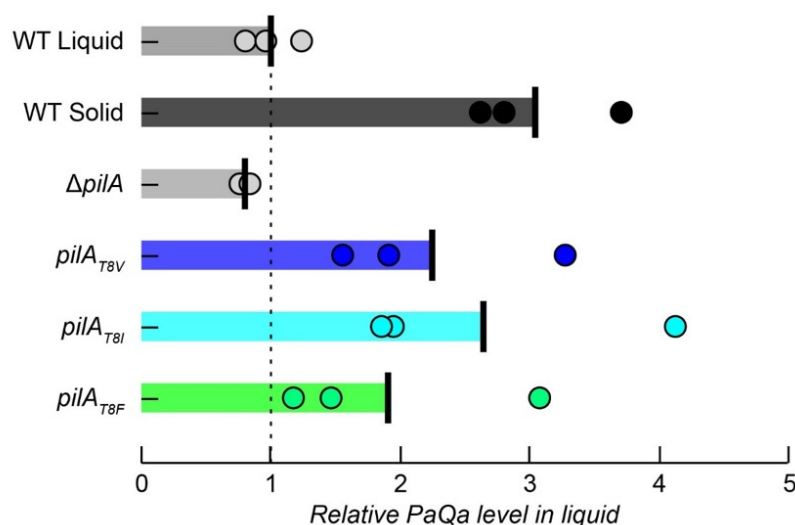
Figure 5.6: cAMP levels are elevated in T8 mutants.

YFP/RFP ratio normalized to the mean fluorescence ratio of the WT cells grown in liquid culture. All mutants measurements correspond to liquid-growth conditions, similar to WT liquid. The dotted vertical line is a reference point of the WT liquid mean. Colored circles are means of biological replicates. Colored bars and vertical black bars are means across biological replicates.

To confirm whether these mutants formed TFP, we first performed a phage-sensitivity experiment. We measured the decay of bacteria when infected with the lytic phage LUZ19 which uses TFP as an entry receptor (*47*). LUZ19 binds to extended TFP which it uses as means of infection through TFP retraction. Bacterial infection by Luz19 results in cell lysis leading to decrease optical density of liquid cultures. We confirmed that PAO1 Δ*pilA* is insensitive to LUZ19. *pilA*$_{T8V}$ had OD$_{600nm}$ decay curves largely similar to WT. The drop in OD was however slightly delayed by 20 min. *pilA*$_{T8I}$ and *pilA*$_{T8F}$ showed some slight decay but with a much longer delay (240 and 330 min respectively) suggesting that these mutants have a very low level of active TFP (**Figure 5.7A**).

To explore a potential relationship between piliation and *pilA* GoF activity, we quantified the proportion of piliated cells in each mutant using Interferometric scattering microscopy (iSCAT). We could surprisingly not observe any TFP in the *pilA*$_{T8}$ mutants, contradicting the phage sensitivity data. One limitation of iSCAT is that the signal generated by the strongly-scattering cell body "bleeds" around the cell, blocking the shorter filaments at the surface. We estimate that this effect masks TFP

within a range of 1 µm from the cell surface. We thus conclude that that these mutants must have TFP that are shorter than the ones of WT cells. This difference in TFP properties might in fact play a role in activating PilJ.

Our mutagenesis screen identified several *pilA* mutants in threonine 8 that had high cAMP levels in liquid culture. However, only *pilA_{T8V}* had active TFP with WT-level of phage sensitivity. Therefore, we focused the rest of our investigation of the mechanism of mechanosensation on the *pilA_{T8V}* GoF mutant.
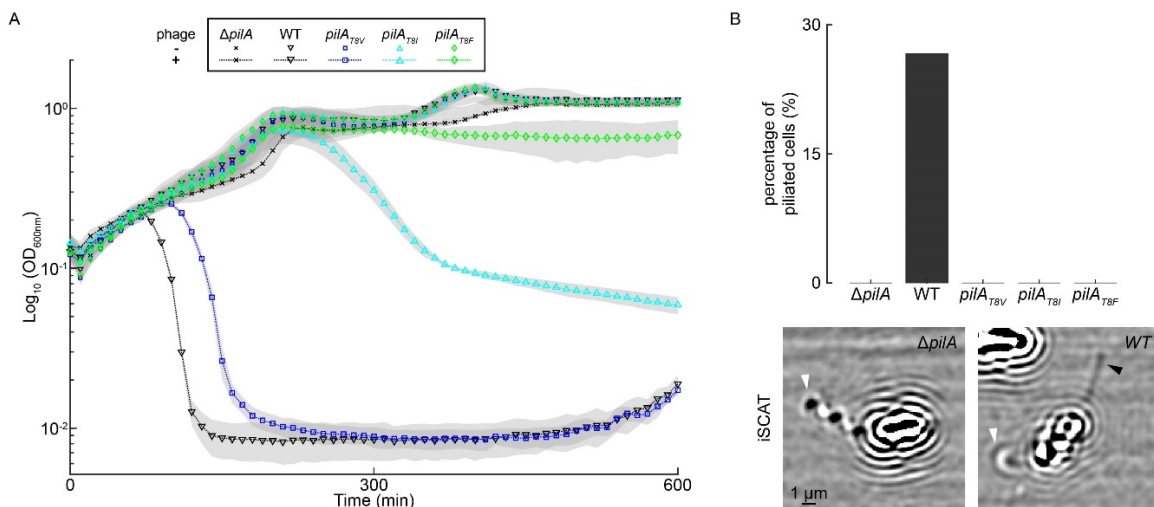
Figure 5.7: Phage sensitivity assay and iSCAT quantification of pili numbers.

A) Growth curves of all the pilA mutants measured at OD_{600} for 10 h grown with and without Luz19 phage. *pilA_{T8V}* show WT-like levels of Luz19 sensitivity whereas the other mutants show no or reduced sensitivity. B) iSCAT measurement of cell piliations. 26% of WT cells have at least one pilus whereas the other mutants displayed no pili in iSCAT. Bottom row: (left) iSCAT image of Δ*pilA* as an example of unpiliated but flagellated cells, (right) iSCAT image of WT as an example of piliated and flagellated cells. White arrow head: flagellum, Black arrow head: TFP. Number of cells considered per strain: Δ*pilA* = 29, WT = 30, *pilA_{T8V}* = 21, *pilA_{T8I}* = 27, *pilA_{T8F}* = 25.

5.2.2 *pilA*_{T8V} gain of function mutation is PilJ-dependent

We went on by further characterizing the mechanism by which *pilA_{T8V}* induced an increased level of cAMP in liquid culture. We first checked whether this sensitized state was due to an increased activation of the Chp system. To achieve this, we compared PaQa levels of *pilA_{T8V}* in WT and Δ*pilJ* backgrounds. *pilA_{T8V}* Δ*pilJ* abolished PaQa fluorescence, as did Δ*pilJ* in a WT *pilA* background (**Figure 5.8A**). To further test the contribution of T8V mutation in activating the Chp system, we

measured whether it would induce a change in the interaction between PilA and PilJ. We thus performed a BACTH assay and monitored β-galactosidase activity of $PilA_{T8V}$-PilJ and compared it with $PilA_{WT}$-PilJ interactions. $PilA_{T8V}$-PilJ interaction resulted in an increase in BACTH signal that was 2.3-fold higher than $PilA_{WT}$-PilJ. This suggests that the *pilA_{T8V}* mutation increases the affinity of the mutated pilin to PilJ (**Figure 8*B, C***). All in all, our data shows that $PilA_{T8V}$ over activation of the Chp system is mediated by PilJ, and that increasing PilA-PilJ interactions further stimulates the Chp response.
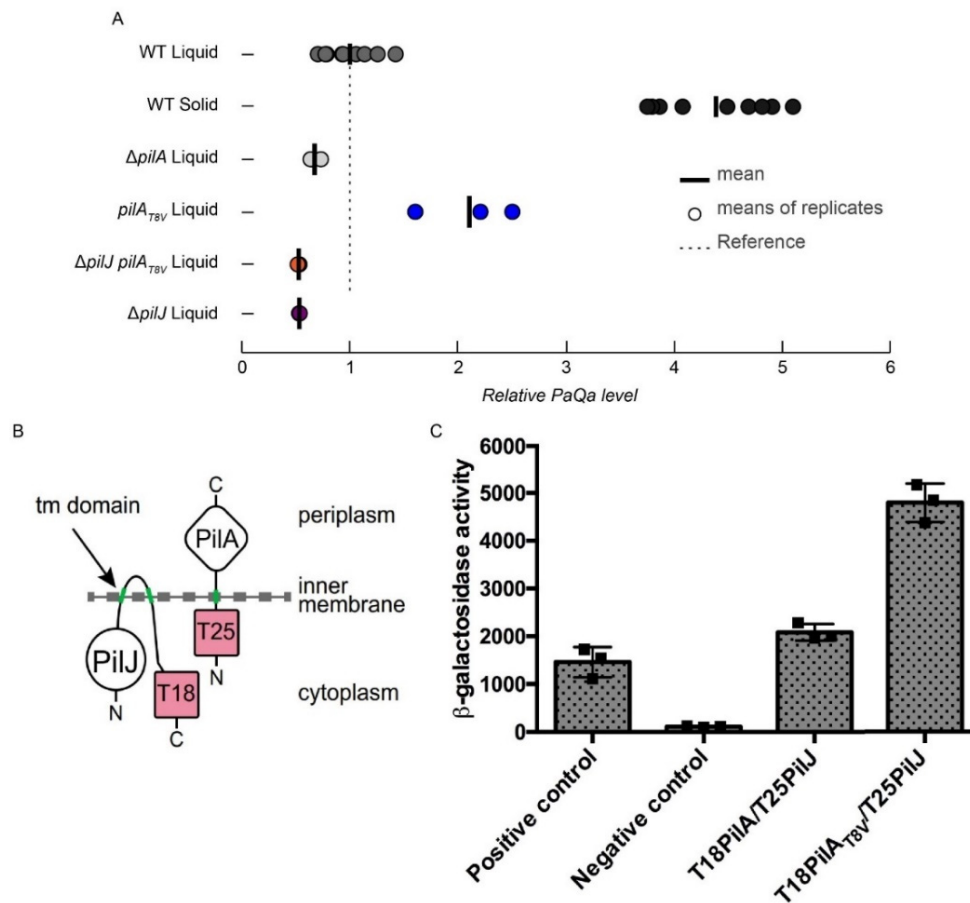
Figure 5.8: Chp activation through $PilA_{T8V}$ is PilJ-dependent

A) cAMP levels of both the *pilA_{T8V}* and *pilA_{T8V} ΔpilJ* mutants. As seen previously, the *pilA_{T8V}* mutant has a 2-fold increase of cAMP levels whereas the *pilA_{T8V} ΔpilJ* results in a 50% drop compared to the WT liquid data. This suggests that the cAMP response due to the *pilA_{T8V}* mutation is PilJ-dependent. Colored circles represent means of biological replicates, horizontal black bar represent means across biological replicates. B) Schematic of BACTH. The fragment T18 of an adenylate cyclase is fused to one interaction partner and the fragment T25 to the other interaction partner (here PilJ and PilA respectively). Modified from Persat et *al.* 2015 (*3*). C) BACTH readout shows a higher affinity of the mutated $PilA_{T8V}$ to PilJ compared to $PilA_{WT}$ performed by our collaborators at UCSF. Vertical black bars represent standard deviation across biological replicates.

5.2.3 pilA$_{T8V}$ perturbs mechanotaxis by increasing cell polarization

We then wondered whether the GoF mutation would change the ability of *P. aeruginosa* to mechanotax, that is to migrate persistently in one direction by sensing TFP attachment at one pole. We first explored this by quantifying single cell motility behaviors. Thus, we tracked displacement of bacteria sandwiched between glass and a 0.5% agarose hydrogel after growth at 37°C for 2h. Qualitatively, the behavior of *pilA$_{T8V}$* cells was similar to WT, which tend to migrate persistently forward while occasionally changing their direction of twitching (reversals) (*40*) (**Figure 5.9A, B**). Quantitatively computing cell trajectories showed that *pilA$_{T8V}$* twitched more slowly than WT (**Figure 5.9C**). In addition, we found that *pilA$_{T8V}$* had a much lower reversal frequency than WT (**Figure 5.9D**). In other words, *pilA$_{T8V}$* move more persistently in one direction compared to WT.
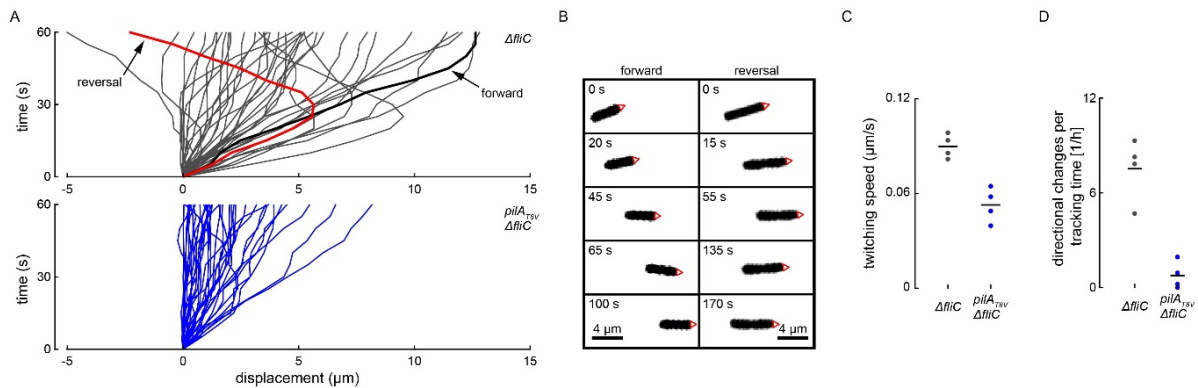
Figure 5.9: *pilA$_{T8V}$* reduces single-cell twitching motility

A) Displacement map for our WT *ΔfliC* and our mutant *pilA$_{T8V}$ ΔfliC*. In red, an example of a reversing cell, in black a trajectory for a cell moving in a constant forward direction. WT cells cover a greater distance and have more reversal events compared to the *pilA$_{T8V}$* mutant. B) Time-lapses of cells constantly twitching forward (left) or reverting their twitching direction (right). The red triangle represents the initial leading pole of the cell. C) Averaged twitching speed of WTcells is higher compared to *pilA$_{T8V}$* cells. D) Twitching reversals in WT are more frequent than *pilA$_{T8V}$* cells. To consider a reversal, a cell needs to travel in one direction for at least 2 consecutive frames before reverting its twitching direction for at least 2 consecutive frames. C) and D) Colored circles represent means of biological replicates, horizontal black bar represent means across biological replicates.

A lower reversal rate suggests an increase in polarization of the extension machinery during mechanotaxis (*40*). Therefore, we hypothesized that as *pilA*$_{T8V}$ GoF also activates PilJ in a localized, polar manner. This would result in a local positive feedback that strengthens twitching direction more strongly than in the WT PilA background. To verify this hypothesis, we generated a chromosomal fluorescent mNeonGreen fusion of the extension motor activator FimX (mNeonGreen_fimX) in the Δ*fliC* and the *pilA*$_{T8V}$ Δ*fliC* backgrounds. The FimX protein oscillates between both poles shortly after surface contact. However, the oscillations frequency slow down after 1 h of surface contact in a *pilA*-dependent manner (*40*). We therefore sought to measure the dynamic transitions of FimX between oscillations and polarization in *pilA*$_{T8V}$. Early on after surface contact (10 min), FimX fluorescent signal switched from one pole to the other in both *pilA*$_{T8V}$ and *pilA*$_{WT}$ as shown in **Figure 5.10A**. At this time, the frequencies of oscillations were similar between the WT and GoF strains (**Figure 5.10B**). After longer surface contact (60 min), when the cells have more time to sense the surface using their TFP, we observed a different response between *pilA*$_{T8V}$ and *pilA*$_{WT}$. *pilA*$_{T8V}$ cells had a largely lower pole switching frequency than WT. In other words, *pilA*$_{T8V}$ polarize more robustly after sensing surface contact. These results are consistent with the reduction in twitching reversal frequency observed in the GoF mutant. However, the fact that *pilA*$_{T8V}$ has similar oscillation frequency as WT is not consistent with a complete constitutive activation of the system in liquid. These results rather suggest that *pilA*$_{T8V}$ rather increases the sensitivity of the mechanosensing system to surface contact.
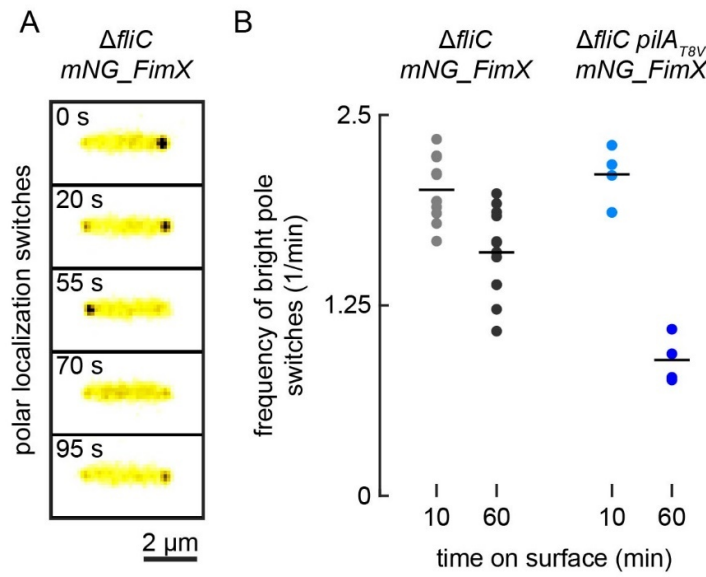
Figure 5.10: mNG_FimX oscillations after surface contact at early and late timepoints.

A) Time-lapse of two mNG_Fimx oscillation events in a WT cell. Similar events could be observed in the pilA$_{T8V}$ Δ*fliC* mutant. B) Surface contact dependent oscillations of WT and *pilA$_{T8V}$* Δ*fliC* cells. In both strains we can observe a reduction in oscillations after 60 min of surface growth showing that the cells have sensed the surface and started polarizing. However, the *pilA$_{T8V}$* Δ*fliC* mutant has a strong difference between late and early time points suggesting that the mutations provide a stronger sensitivity to the system. Colored circles represent means of biological replicates, horizontal black bar represent means across biological replicates.

Altogether our data shows that the mutation *pilA$_{T8V}$* activates of the Chp system which triggers both cAMP production and cell twitching polarization. However, how the PilA$_{T8V}$ pilin interacts with PilJ remains unclear. To decipher this, we explored how the effect of the *pilA$_{T8V}$* mutation could be explained by TFP/PilA conformational changes, or changes in pilin fluxes in the inner membrane.

5.2.4 Identifying TFP conformational changes of PilA GoF by cryo-EM

Surface attachment and retraction of TFP may cause a conformational in PilA or a change in its assembly. These changes may activate downstream Chp signaling events (*16*, *41*, *62*, *68*, *127*). In line with this hypothesis we speculate that the *pilA$_{T8V}$* mutation induce TFP conformational changes, so that TFP are in a permanent stretched state. PilA conformational changes would in principle lead to changes in TFP structure. We reasoned that if this hypothesis was valid, we would be able to measure such conformational changes using cryoEM.

We decided to further characterize their structure using cryo-EM 3D reconstruction. We purified TFP from the WT strain and the *pilA$_{T8V}$* mutant in the *pilT* deletion mutant background. Purified TFP were cryogenized and imaged on a Titan Kryos by Yi Wei Chang at the University of Pennsylvania. We performed the analysis of cryo-EM micrographs, which requires averaging of thousands of TFP segments in order to build 2D class-averages. From these 2D classes a 3D helical reconstruction model could then be generated and refined (*128*). In order to determine the final structure of assembled TFP we must then match the electron density map of our 3D model with a crystal structure of the pilin (*15*).

We performed all class averaging and 3D reconstruction using Relion. We were able to extract particles, create 2D classes and obtain a preliminary 3D structure for the WT TFP (**Figure 5.11**). The results of averages identified about 20 classes for WT and T8V mutant, from which we could extract structural features such as helical pitch. Working with 2D class averages as opposed to a single 3D helical reconstruction gives us a more probabilistic view of the conformations of the filaments. We found no coarse difference (less than 1%) between the mean helical pitch between the WT (40.37 Å) and the GoF mutant (40.74 Å). This result strongly suggests that PilA$_{T8V}$ TFP do not activate PilJ by conformational changes. We are however repeating these measurements to validate this observation and are refining the image analysis for 3D reconstruction in order to confirm the 3D structure of the TFP of our WT and our *pilA$_{T8V}$* mutant. This will allow us to get higher resolution on experiments and to improve our final 3D model of PilA_T8V TFP.
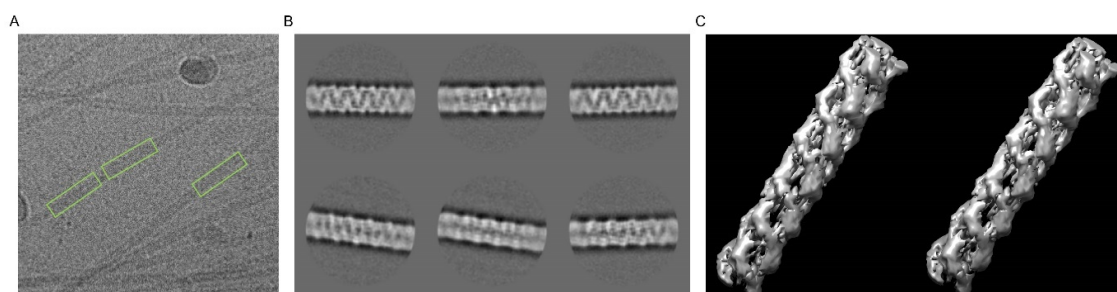
Figure 5.11: TFP 3D model using cryo-EM.

A) Example of cryo-EM micrographs and boxed particles along the TFP filament. B) Example of 2D classification of extracted particles form the micrographs in A). One needs to select the best-looking classes that contain the most abundant portion of extracted particles prior to perform a 3D reconstruction. C) Stereo view of the 3D structure obtained for WT TFP by helical reconstruction.

5.2.5 Changes in pilin flux in the inner membrane activates PilJ

Our preliminary cryo-EM data being inconsistent with large conformational changes driving PilJ activation, we turned towards our second hypothesis where asymmetric PilA fluxes towards PilJ during retraction stimulates surface sensing. To test this hypothesis, we first explored the role of extension and retraction in stimulating the GoF mutation phenotype. We generated mutants in both $pilA_{T8V}$ and the extension (Δ*pilB*) or retraction (Δ*pilT*) motors in which we transformed the PaQa reporter. A Δ*pilB* mutant in the $pilA_{T8V}$ background loses constitutive production of PaQa in liquid, (**Figure 5.12A**). On the other hand, $pilA_{T8V}$ Δ*pilT* had intermediate levels of PaQa reporter fluorescence (higher than $PilA_{WT}$ liquid culture but lower than $pilA_{T8V}$ (**Figure 5.12B**). These results prove that the GoF mutation requires the formation of TFP to stimulate PilJ. It also suggests that stimulation is improved by retraction, so that the temporal changes of the pilin concentration at the inner membrane play a crucial role in activation.
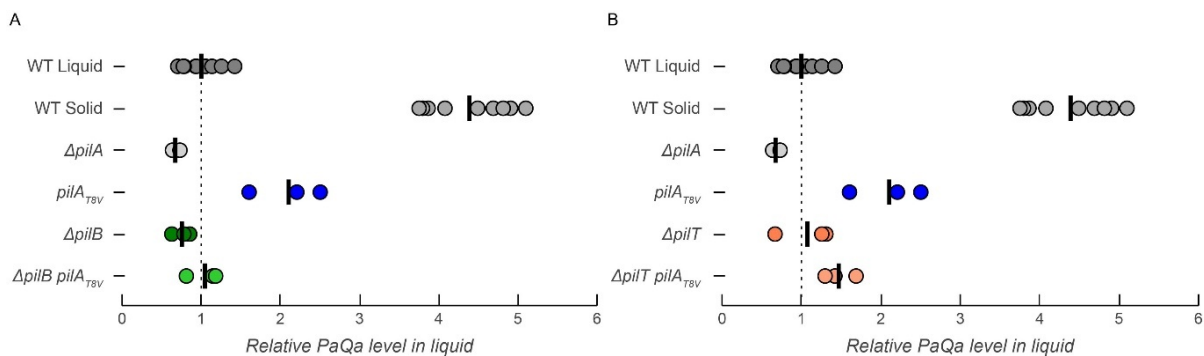
Figure 5.12: cAMP levels for $PilA_{WT}$ and $PilA_{T8V}$ in mutants lacking the extension or retraction motor.

A) Effect of the deletion of the extension motor PilB on cAMP levels in the WT and $pilA_{T8V}$ mutant TFP. cAMP levels drop in both strains. B) Similar graph than A) but for deletion of the retraction motor PilT. It is important to note that the Δ*pilT* $pilA_{T8V}$ mutant has a higher cAMP level compared to the WT grown in liquid. However, the levels do not quite reach the ones for the $pilA_{T8V}$ mutant. A) and B) Colored circles represent means of biological replicates, horizontal black bar represent means across biological replicates.

5.2.6 TFP of the pilA$_{T8V}$ gain of function mutant are shorter and have reduced extension and retraction speeds

To further refine the hypothesis that pilin flux changes stimulate PilJ, we sought to measure the changes of PilA turnover in the T8V GoF mutant. We could not initially observe the TFP of this mutant by iSCAT. We thus performed further characterization in hyperpiliated mutants such as deletion mutants in the retraction motor gene *pilT* or the response regulator gene *pilH* (*11*, *40*, *41*). We could observe long TFP in a plasmid-borne expression system for *pilA$_{T8V}$* in a Δ*fliC*Δ*pilA*Δ*pilT* triple deletion mutant. This confirmed that the TFP machinery can polymerize the mutated pilins into long filaments. We could also visualize active TFP in the chromosomal mutation of *pilA$_{T8V}$* in a Δ*fliC*Δ*pilH* background, confirming the ability of the retraction motor to depolymerize the mutated pilin as well (**Figure 5.13 iSCAT**). Altogether we found that longer pili can form more frequently in these hyperpiliated mutants (*40*).

In an attempt to quantify shorter filaments, we also imaged TFP by transmission electron microscopy (TEM). We imaged liquid grown WT and mutated *pilA$_{T8V}$* cells in a flagellum-less mutant Δ*fliC* (**Figure 5.13 TEM**). No TFP could be observed in *pilA$_{T8V}$* cells. In contrast, we counted 40% of piliated cells in the WT. This suggests that the TFP of *pilA$_{T8V}$* cells are too fragile and break during the negative staining protocol for TEM visualization. This is consistent with threonine 8 playing an important role in cohesion of assembled TFP (*15*).
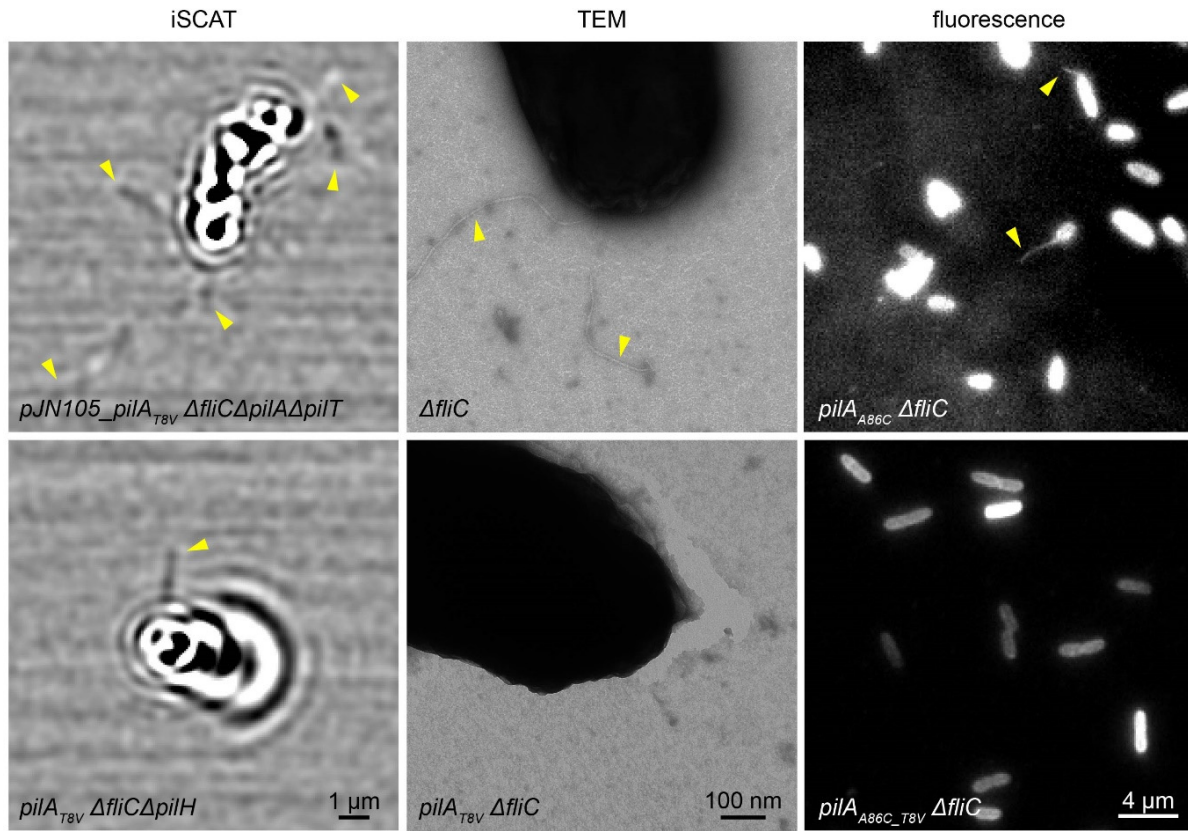
Figure 5.13: Observation of *pilA_{T8V}* TFP using three different microscopy techniques: iSCAT, transmission electron microscopy (TEM) and fluorescence

pilA_{T8V} TFP could not be observed in TEM or fluorescence microscopy but mutations in the retraction motor PilT or the response regulator PilH restored some levels of TFP visualization with iSCAT. iSCAT images of a Δ*fliC*Δ*pilA*Δ*pilT* triple deletion mutant containing a plasmid with the *pilA_{T8V}* gene under the control of its natural promoter showed many floppy TFP (yellow arrow head). Longer TFP in a *pilA_{T8V}* background could also be observed in a Δ*fliC*Δ*pilH* mutant.

As we could not detect *pilA_{T8V}* TFP with iSCAT or TEM, we decided to attempt another technique for TFP visualization. We leveraged a cysteine substitution mutant that allows for fluorescent labeling of TFP with a maleimide dye (*18*, *20*, *21*). To achieve this, we introduced an A86C mutation in the WT *pilA* or the *pilA_{T8V}* gene in a Δ*fliC* background. After labeling with Alexa Fluor 488 C_5 maleimide dye, we could observe extending and retracting TFP in the *pilA_{A86C}* mutant. However, we could not observe any TFP in the *pilA_{A86C_T8V}* *double* mutant (**Figure 5.13 fluorescence**). We therefore checked whether the *pilA_{A86C_T8V}* *and the pilA_{T8V}* mutants could still twitch in a twitching stab assay. The *pilA_{A86C}* mutant had a reduction in twitching zone of approximately 25% compared to the WT

pilA strain. However, the double mutant *pilA$_{A86C\_T8V}$* had a twitching zone reduction of 50% (**Supplementary figure 5.2**), consistent with the lack of TFP in the direct visualization.

Unable to detect *pilA$_{T8V}$* TFP in a WT background, we generated a chromosomal version of *pilA$_{A86C}$* and *pilA$_{A86C\_T8V}$* in a Δ*fliC*Δ*pilH* background as this background displayed long enough *pilA$_{T8V}$* TFP in iSCAT microscopy (**Figure 5.13 iSCAT**). Both of these mutants showed active TFP when labeled with a maleimide dye (**Figure 5.14*A***). Maximum intensity projections (MIP) of movie stacks underlined the differences in TFP dimensions and numbers between WT and *pilA$_{T8V}$*. MIP also allowed to show TFP polarization of Δ*pilH*Δ*fliC* cells (*40*) as well as pili length differences between *pilA$_{A86C}$* and *pilA$_{A86C\_T8V}$* (**Figure 5.14*A***). First, the *pilA$_{A86C\_T8V}$* mutant has shorter TFP compared to *pilA$_{A86C}$* in the Δ*fliC*Δ*pilH* background (**Figure 5.14*B***). This highlights a potential mechanism of activation wherein shorter TFP stimulate PilJ signaling. However, *pilA$_{A86C\_T8V}$* Δ*fliC*Δ*pilH* has same pili length distribution compared to *pilA$_{A86C}$* Δ*fliC*.

We then extracted kymographs of individual TFP in order to extract their extension and retraction speeds. We analyzed 10 TFP in each mutant. We saw a 2-fold increase of TFP extension and retraction speeds in *pilA$_{A86C}$* Δ*fliC*Δ*pilH* compared to *pilA$_{A86C}$* Δ*fliC*. On the other hand, the *pilA$_{A86C\_T8V}$* Δ*fliC*Δ*pilH* mutant had an 80% speed reduction compared to the *pilA$_{A86C}$* Δ*fliC*Δ*pilH* mutant and a 50% reduction compared to the *pilA$_{A86C}$* Δ*fliC* (**Figure 5.14*C***). This reduction in extension and retraction speeds may explain the lower twitching and phage sensitivity of *pilA$_{T8V}$*. Altogether, our data show that the T8V mutation has a strong effect on TFP assembly, affecting both their length and dynamics.
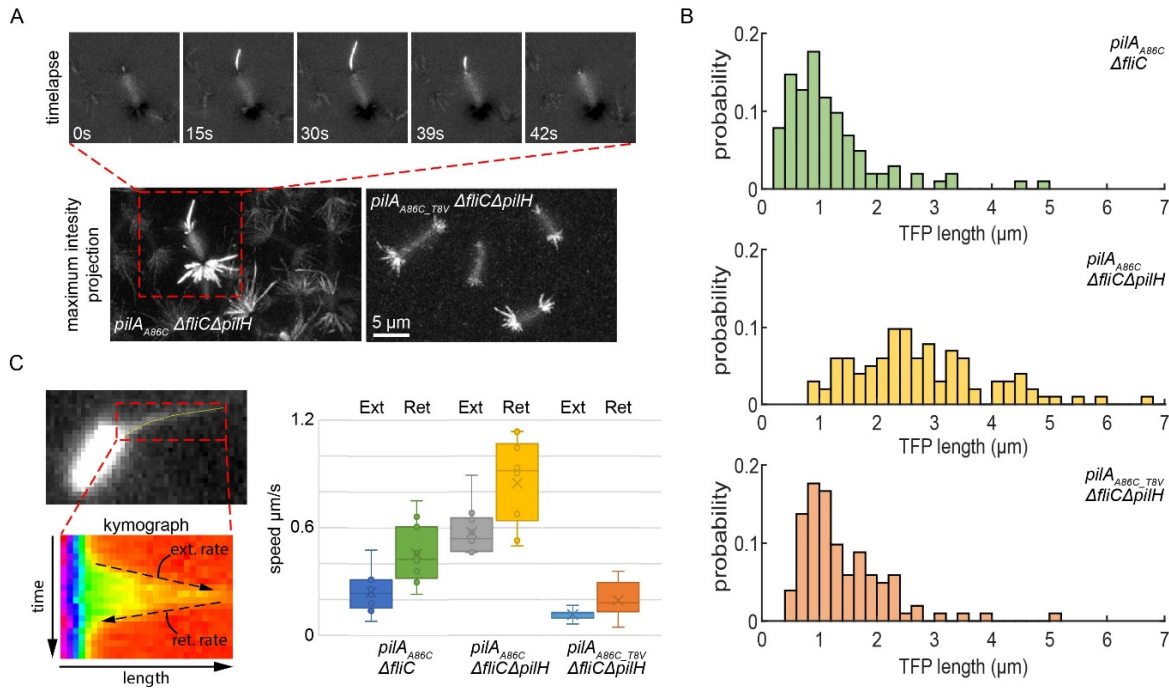
Figure 5.14: Visualization of TFP dynamics using fluorescence microscopy

A) Top row: time lapse visualization of an extension and retraction event of a TFP from *pilA_{A86C} ΔfliCΔpilH*. Bottom row: maximum intensity projection of the cell from the top row show the TFP space of both *pilA_{A86C}* and *pilA_{A86C_T8V} ΔfliCΔpilH*. B) TFP lengths distribution in the *pilA_{A86C}* labeled mutants of 102 TFP for each strain. TFP lengths distributions from *pilA_{A86C_T8V} ΔfliCΔpilH and pilA_{A86C} ΔfliC* are not statistically different. C) (left) kymograph used to extract the extension and retraction speeds of our mutants (right).

5.2.7 Depletion and enrichment of PilA at the TFP pole during extension and retraction.

We know that the Chp system is locally activated at the leading pole of twitching *P. aeruginosa* cells (*40*). PilJ is itself localized at both poles (*123*). During extension and retraction, PilA monomers freely diffuse in the membrane all around the cell. Therefore, if PilJ sensed steady state PilA levels once all monomers have diffused, cells wouldn't be able to polarize. We hypothesize that extension and retraction are sufficiently fast to respectively create a depletion or enrichment in pilins that would be erased by diffusion on a longer timescale. In other words, TFP assembly/disassembly is much faster than PilA diffusion. To test this hypothesis, we sought to measure pilin concentration on both poles during extension and retraction events. In **Figure 5.15**, we show a kymograph of a cell with an extending TFP. We can clearly see the cell body intensity dropping as soon as the pilus start extending until it reaches its apex. Conversely, we see an increase in fluorescence in the cell body

until the TFP is fully retracted some 50 s later. By looking at the fluorescent intensity of the piliated vs the unpiliated pole, we can observe that during TFP retraction the fluorescence intensity at the piliated pole increased faster (15 s ahead of time, **Figure 5.15 bottom row**) than the intensity at the unpiliated pole. We attribute this delay in a PilA flux imbalance between fast retraction and slow diffusion. As Chp activation results in recruitment of more extension motors to the sensing pole (*40*), this time delay could then recruit extension motors more rapidly at that pole, establishing a positive feedback which allows the cell to polarize.
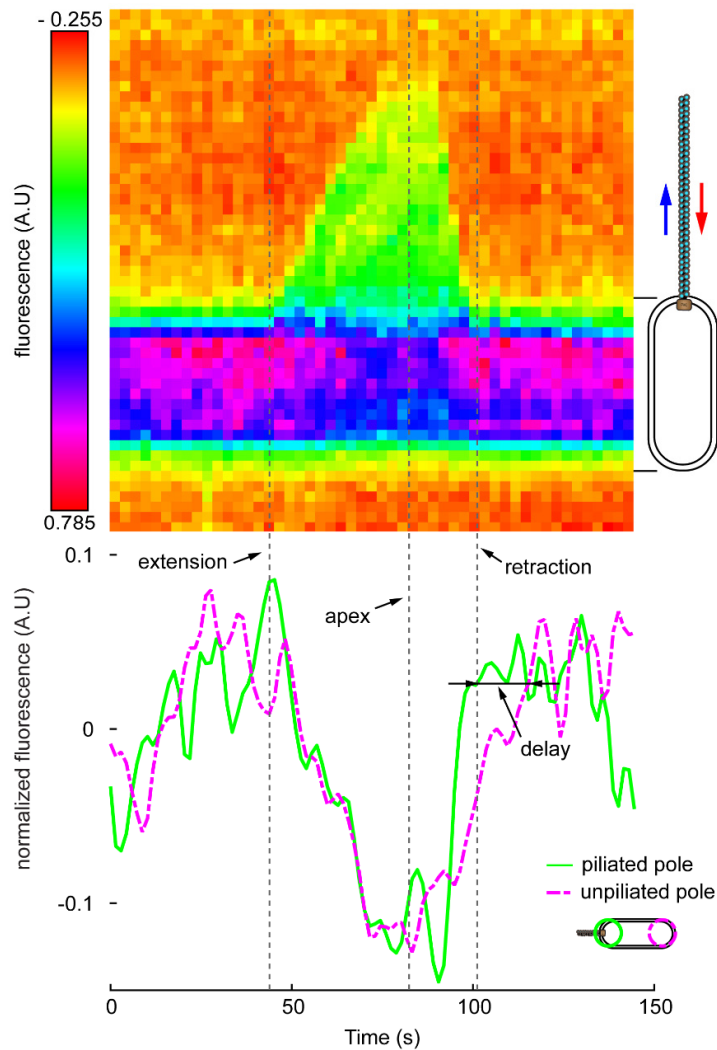
Figure 5.15: TFP extension induces cell body reduction in fluorescence signal as well as polar fluorescence asymmetry.

Top: Kymograph showing the fluorescence intensity changes along the cell body and TFP over time during extension (blue arrow) and retraction (red arrow). We can clearly see the inverse relationship between pilus extension and a resulting drop in fluorescence intensity of the cell body. Bottom: Normalized fluorescence intensity of the piliated (solid green line) and unpiliated (dashed magenta line) poles over time showing that the piliated pole increases faster compared to the unpiliated pole during retraction.

5.3 Discussion

We presented initial data helping construct a model for the mechanical stimulation of the Chp system through its MCP. We have identified a GoF mutation in the pilin gene ($pilA_{T8V}$) that over activate the Chp system and produces active TFP. However, the mutant seems to be less motile and more polarized compared to the WT. Furthermore, it produced shorter and slower TFP. We have shown that its ability to activate the Chp system is PilJ-dependent and that the mutated pilin interacts twice more with PilJ compared to the WT pilin. In order to make sense of the mechanisms of mechanosensation, we proposed two models.

Our first hypothesis relies on TFP conformational changes that could arise upon retraction or due to $pilA_{T8V}$ mutation that could activate the Chp system through its MCP PilJ. Our preliminary results on the PilA GoF mutant disprove this hypothesis, but does not rule it out entirely. We plan to analyze cryo-EM data to generate an accurate 3D model of our WT and $pilA_{T8V}$ TFP structures to better understand the possibility of a conformational change that could expose new residues to be sensed by PilJ. An ideal experiment would capture the conformational changes of TFP during retraction on surfaces while measuring the response of the Chp system. However, the hypothesis that PilJ reads out TFP conformation has one major limitation: by observation of the type IV pilus apparatus (*16*), we can envision that the cage formed by the structural proteins PilM, PilN, PilO and PilP would sterically preclude the Chp complex to reach the assembled TFP.

Our second hypothesis considers the pilin flux in the inner membrane of *P. aeruginosa* during TFP extension and retraction. This hypothesis is consistent with the loss of sensitivity of the *pilB* and *pilT* retraction mutants. PilJ shows a bipolar localization and therefore restricts Chp activation to the poles (*123*). We now know that PilA$_{T8V}$ interacts more strongly with PilJ compared to PilA$_{WT}$. In the pilin flux hypothesis, PilJ binds to free PilA subunits in the periplasm. During extension, the pilin levels in the membrane will decrease, therefore resulting in deactivating PilJ. Due to slow diffusion of pilins in the inner membrane (0.22 µm^2/s) (*124*) compared to the fast integration of pilins in the inner membrane during retraction (0.9 µm^2/s: example from the cell in **Figure 5.15**), a transient concentration gradient between the piliated and unpiliated poles would form which could be sensed by PilJ in a similar

manner as in chemotaxis systems (*124*). In **Figure 5.16**, a schematic representation of the pilin concentration profiles shows how the difference between the diffusion coefficient of pilins in the inner membrane and the rate of pilin disassembly from the TFP affect how pilins accumulate at the pole. Slower diffusion of pilin in the inner membrane compared to TFP retraction results in a pilin concentration overshoot. We showed that the piliated pole gets transiently more pilins compared to the lagging pole (**Figure 5.15**). Therefore, PilJ could be activated with a delay between poles, or be activated by the transient enrichment of pilins at the leading pole. In both hypotheses, PilJ differential activation between the two poles is consistent with our data about polarization of the cell upon surface contact.

The pilin flux hypothesis is reminiscent of the mechanism of signaling of the Che system. During chemotaxis, a swimming cell will encounter varying concentrations of nutrients. Small molecules will then diffuse and bind to the chemoreceptors at the inner membrane and activate the TCS. Similarly, PilJ could sense the variation of pilin concentration in the inner membrane during extension and retraction either by sensing a flux imbalance resulting in an overshoot in pilin concentration or by sensing concentration changes over time.

All in all, we provide new insights on the mechanisms of mechanotransduction in *P. aeruginosa* through the Pil-Chp system. However, we still have many unknown parameters that need further investigation. We hope to further confirm our findings as this mechanism could be a potential target to develop new treatment for multi-drug resistant bacteria.
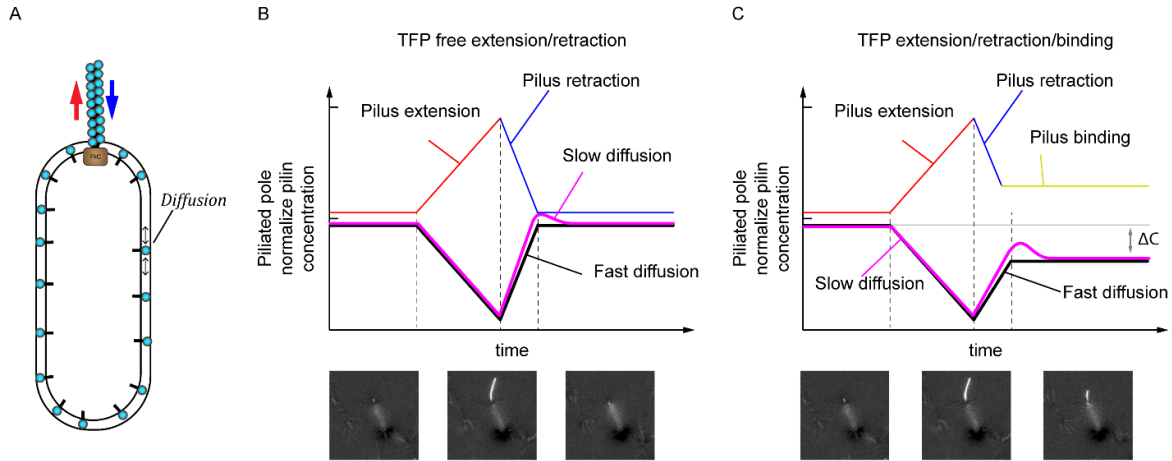
Figure 5.16: The difference in pilin concentration profiles at the piliated pole depends on the diffusion constant of the pilin in the inner membrane.

A) Schematic that represents a cell with an active TFP at one pole and pilins diffusing in the inner membrane. Extension and retraction are represented bythe blue and red arrows respectively. B) During a free extension of a TFP, the amount of pilin in the inner membrane of the cell will drop by the same number of pilins needed to assemble the nascent TFP. This results in a change in pilin concentration in the inner membrane of the cell. Depending on the diffusion coefficient of the pilins in the inner membrane, a different concentration pattern appears on the pole of the cell. If the diffusion coefficient D is fast (black line) compared to TFP extension (R_{ext}) and retraction (R_{ret}) rates, meaning $|D - R_{ex}|$ or $|D - R_{ret}| \approx 0$ the concentration changes at both poles are similar as there is a fast distribution of pilins throughout the cell. If the diffusion coefficient D is slow (magenta line) ($|D - R_{ex}|$ or $|D - R_{ret}| > 0$), we can clearly see differences in the concentration profiles as retraction induces an overshoot of pilin concentration at the piliated pole. Below are fluorescence timelaps of TFP extension and retraction. C) same as B) but when a pilus stays attached while retracting. On top of the overshoot of pilin concentration, there is a difference in concentration between the start of the extension and the end of pilus partial retraction. B) and C) Top curves correspond to the pilin incorporated in the growing TFP.

5.4 Methods

5.4.1 Bacterial strains and growth conditions

Strains and growth media were grown and prepared as described in (*40*). All strains used in this study are listed in **Table 5-2**. The *Pseudomonas aeruginosa* strain used was PAO1 strain ATCC 15692 (American Type Culture Collection). *Escherichia coli* strain DH5α was used for vector construction, *Escherichia coli* strain S17.1 was used for conjugation of vectors into *P. aeruginosa*. All bacterial strains were grown in LB medium (Carl Roth) at 37 °C with 290 rpm shaking. Regular solid LB media were prepared by adding 1.5 % (wt.vol^{-1}) agar (Fisher Bioreagents).

For surface association experiments cells were plated on pre-heated solid LB media containing 1 % agarose standard (Carl Roth) and incubated at 37 °C for 3 hours. For twitching motility assays semi-solid tryptone media were prepared by autoclaving (5 g.l^{-1} tryptone (Carl Roth), 2.5 g.l^{-1} NaCl (Fisher Bioreagents), 0.5 % (wt.vol^{-1}) agarose standard (Carl Roth)). For fluorescence visualization under correlative fluorescence and iSCAT cells were washed with PBS (BioConcept AG) and resuspended in M9 medium (VWR) containing 0.2 % of glucose.

5.4.2 Mutagenesis screen

For error-prone mutagenesis, GeneMorph II mutagenesis kit (Agilent) was used according to the manufacturer's protocol. We optimized the amount of template to have on average one nucleotide mutated per DNA fragment. For *pilA*(7-30) random mutagenesis, this consisted in 7 ng of pZA001 template. For other site directed random mutagenesis, NNK codons or their reverse complement MNN were introduced by PCR.

In both cases, the mutated fragment included overlaps for insertion into the corresponding PCR-linearized backbone using Gibson assembly (HiFi, NEB). The Gibson mixes were desalted using hydrophilic mixed cellulose esters (MCE) membrane dialysis discs, 0.025 µm pore (Merck) for 30 min on bi-distilled water. 4 µL of the dialyzed Gibson mix was added to 50 µL of competent *P. aeruginosa pilA*- PaQa and electroporated, rescued and selected on LB carb genta overnight at 37°C.

Colonies were inoculated in 96-well plates in appropriate antibiotics and grown overnight at 37°C. Overnight culture were diluted 1:200 in appropriate antibiotics and grown at 37°C for 4 to 5 hours. Late exponential cultures were further diluted 1:200 in PBS prior to high throughput imaging (PerkinElmer Operetta).

5.4.3 Strains and vector construction

Strains were generated as described in (*40*). Briefly, all strains used in this study, plasmids and corresponding oligonucleotides are listed in Table 5-2. Gene deletions and gene fusions were constructed by two-step allelic exchange (according to (*66*)) using the suicide vectors pEX18Amp or pEX18Gent. In-frame deletions were generated by combining approximately 500-bp fragments of the up- and downstream regions of the designated gene, leaving only a few codons (usually around six) and verified by colony PCR and sequencing. In-frame insertions were constructed in basically the same fashion. Insertion fragments with wild-type length (e.g. for complementation) were integrated into the corresponding deletion strain. Fluorophore genes were fused to the N- or C-termini of the desired gene separated by a GGGGG linker and introduced into the wild-type chromosome. Expression and integrity of fluorescent fusions were verified by Western blotting and functionality was tested by twitching motility assays (see corresponding methods). Plasmids were constructed using standard Gibson assembly protocols (*101*) and introduced into *P. aeruginosa* cells by conjugative mating with *E. coli* S17.1 as donor. For selection of *E. coli,* the following antibiotic concentrations were used: 100 µg/ml ampicillin, 10 µg.ml^{-1} gentamycin. For selection of *P. aeruginosa* the following antibiotic concentrations were used: 300 µg.ml^{-1} carbenicillin, 60 µg.ml^{-1} gentamycin.

5.4.4 Twitching motility stab assay

Twitching motility assays were performed as described in (*40*). Briefly, square plastic dishes (100x100x20 mm, Sarstedt) were filled with 50 ml of 0.5 % agarose tryptone medium and dried in a flow hood for 30 min. Single colonies grown overnight on LB agar at 37 °C were stabbed with a 10 µl pipette tip through the agarose hydrogel to the bottom of the dish without much force to prevent

separation of the hydrogel from the plastic. The plates were incubated at 37 °C overnight in a plastic

bag. The hydrogel was then scored around the edges with a 10 µl pipette tip and removed carefully.

Twitching motility was quantified by taking two measurements of the twitching zone diameters from

two to eight independent stabs. The twitching diameter of wild-type or Δ*fliC P. aeruginosa* was used

as reference.

5.4.5 Phage-sensitivity assay

Single colonies were grown in LB overnight. Overnight cultures were diluted in LB to OD_{600nm} 0.05

and grown for 2 hours until OD_{600nm} 0.5. Cultures were further diluted to matching ODs. Load in 96-

well plates with LB as blank. Add 4µl of Luz19 phage (10^6 PFU / ml) to 400 µl of cell culture and load

a multiplate reader with temperature control at 37°C to measure OD_{600nm} every 10 min for 10 hours.

5.4.6 Phase contrast and fluorescence microscopy

Microscopy parameters were set as in (*40*). Briefly, microscopy was performed on an inverted Nikon

TiE epifluorescence microscope controlled with NIS-Elements (version AR 5.02.03). For pure phase-

contrast microscopy a 40x Plan APO NA 0.9 phase contrast objective was used. For fluorescence

microscopy a 100x Plan APO NA 1.45 phase contrast oil objective and Semrock YFP-2427B or

TxRed-A-Basic-NTE filters were used as needed.

5.4.7 Fluorescence microscopy image processing

Image processing was performed as described in (*40*). Briefly, all fluorescent images were

background subtracted with ImageJ (version 1.53c). Snapshot images and movies were generated

with ImageJ and data were analyzed with custom scripts in Python (version 3.7.6 and 3.8.5) and

MATLAB (version R2019b and R2020a)

5.4.8 (iSCAT) fluorescence microscopy setup

Our iSCAT microscope setup was previously described in (*40, 41*).

5.4.9 Glass coverslip preparation

Glass coverslips were prepared as described in (*40*). Briefly, glass coverslips (Marienfeld, 22x40 mm No 1.5) were washed sequentially with distilled water, ethanol, distilled water, isopropanol, distilled water, ethanol, distilled water and excess water was dried with a stream of nitrogen. For visualization we deposited polydimethylsiloxane (PDMS) gaskets on the clean coverslips. PDMS gaskets were obtained using biopsy punches of 6 mm in diameter.

5.4.10 cAMP quantification using PaQa-YFP reporter

PaQa measurements were performed as described in (*40*). Briefly, single colonies were grown overnight in LB-carbenicillin, diluted to OD_{600} 0.05 and grown until mid-exponential phase. For surface-association growth, cells were grown for 3 h at 37 °C on LB 1 % agarose and then harvested in 1 ml LB by gentle scraping. 1 µl of culture was then loaded on a 1 % agarose-PBS pad and flipped onto a glass bottom dish (MatTek) prior to visualization. Several images in phase contrast, YFP and mKate2 channels were acquired. Images were binned 2x2 and fluorescence channels were background subtracted using a custom macro in ImageJ. Cells were segmented and the cell area and corresponding cell mean fluorescence were extracted using BacStalk (*102*). Median PaQa-YFP to mKate2 fluorescent intensity ratios were computed with a custom Python script for each biological replicate. Each median was then normalized to the mean of the WT biological replicates of liquid cultures.

5.4.11 iSCAT-based quantification of type IV pili number

iSCAT quantification of TFP number was performed as described in (*40*). Briefly, single colonies were inoculated in LB supplemented with appropriate antibiotics, grown overnight and diluted 1:500 or 1:1000 followed by a grow period of 2 h to obtain mid exponential phase cultures. Cells were diluted to OD_{600} 0.02 prior to visualization. Cells were loaded in 6 mm PDMS gaskets. Cells sticking to the surface were visualized with iSCAT and movies were recorded at 10 fps for either 2 min, 1 min or 30 s. To reveal the interferometric component of the signal, each frame was processed as

described in (*41*). Individual movies were manually analyzed by counting the total number of pili in each cell.

5.4.12 Single cell twitching behaviour without fluorescence

Single cell twitching was assessed as described in (*40*). Briefly, cells from an exponential culture grown in LB were diluted to an OD_{600} of 0.2 in tryptone medium. The agarose pads were prepared by autoclaving tryptone medium 0.5 % agarose, cooling down to 70 °C in the autoclave followed by cooling to 55 °C for 20 min in a water bath, pouring 28 ml into round petri dishes and letting dry for 30 min in a flow hood. Plates were then stored in a plastic bag at 4 °C for 1 day. A round pad was cut out and 1 μl of the diluted cell suspension was pipetted onto the upper side of the agarose pad (i.e. the side that was not in contact with the plastic dish bottom). We note that all of the following conditions were critical in order to reproducibly allow cells to twitch as single, isolated cells: The medium composition (see 5.4.1 Bacterial strains and growth conditions), autoclaving the agarose medium, cooling down and drying as specified above, the initial optical density of the droplet and pipetting on the upper side of the agarose pad. Then, without letting the droplet dry, the pad was flipped onto a microscope glass bottom dish (MatTek) and six droplets of PBS were added to the sides to prevent drying. The cells were incubated at 37 °C and imaged with phase contrast microscopy every hour at 0.2 frames per second for 5 min over 3 h.

The movies were processed with a custom ImageJ macro to ensure compatibility with the downstream analysis. If necessary, drift was also corrected using the *StackReg* plugin (version July 7, 2011; (*103*)) in that step. Cells were then segmented and tracked using BacStalk (version 1.8, (*102*)) to get the cell outline and position of the center of mass (CM) of each isolated bacterium for each frame. Subsequent analyses of the cell tracks were done with custom MATLAB scripts. For every analysis, cell tracks were categorized into moving and non-moving by using a speed threshold of 1 pixel per frame (here: 32.5 nm s^{-1}). The speed threshold was applied to the speed of each frame (converted from the displacement of the CM between the current and previous frame), setting the

speed to 0 if below the threshold. Cells were only considered moving when the speed was unequal to zero for at least three subsequent frames over the tracked time.

5.4.13   Spatiotemporal cumulative displacement maps

Cumulative displacement maps were generated as described in (*40*). Briefly, in order to analyze twitching displacement relative to the initial cell orientation, we defined a cell orientation unit vector $\vec{t}$ from the CM to the initial leading pole. The initial leading pole was determined by comparing the scalar products of the unit vectors from CM to poles A and B (arbitrary classification) to the normalized displacement vector $\vec{d}$ in the first frame with a speed above the speed threshold. The vectors $\vec{t}$ and $\vec{d}$ were then used to determine direction of the cell displacement δ relative to the initial leading pole, giving it a positive sign for forward (i.e. toward initial leading pole) and a negative sign for reverse (i.e. opposite to initial leading pole) movement. The spatiotemporal displacement maps were generated by cumulating the direction-corrected displacement as a function of time, for 200 tracks that were between 31 and 61 frames long.

5.4.14   Reversal frequency of isolated cells

Reversal frequencies of twitching cells were computed as described in (*40*). Briefly, to count the reversal frequency of twitching cells, the scalar product between the normalized displacement vector $\vec{d}$ and the cell orientation unit vector $\vec{t}$ was determined and rounded for each frame (starting from the first frame with a speed above the speed threshold). This resulted in a series of numbers that correspond to movement of the cell toward the initial leading pole (1), toward the initial lagging pole (-1) or no movement (0) at that timepoint. Timepoints corresponding to no movement were removed. Cells were considered moving in the same direction (relative to the initial leading pole) as long as the sign remained the same. A reversal was counted when the sign changed, however, only if at least two subsequent frames before and after the reversal had the same sign (this was done to correct for frequent sign changes when a cell was in a non-moving phase). The reversal frequency was calculated by dividing the sum of all considered reversals by the total tracked time over all cell tracks for each biological replicate.

5.4.15   Frequency of bright pole oscillations

Oscillations were computed as described in (*40*). Briefly, cells were grown and imaged in a heated chamber (37 °C) on the microscope at 0.2 frames per second for 3 min after 10 and 60 min. To count how often the brightest fluorescence signal of a fusion protein switched from one pole to the opposite pole, we measure the average fluorescence intensity of both poles over time. Then, a series of numbers (1 or -1) was generated that corresponds to a pole (arbitrary but same over the whole track) being the bright pole (1) or the dim pole (-1) for each frame. Similar to counting reversals, a bright pole switch was counted when the sign changed. Here, no additional filters were applied. The frequency of bright pole switches was calculated for each cell by dividing the sum of all bright pole switches by the tracked time.

5.4.16   Transmission electron microscopy

Single colonies were inoculated in LB supplemented with appropriate antibiotics, grown overnight and diluted 1:500 or 1:1000 followed by a grow period of 2 h to obtain mid exponential phase cultures. 100 μl of exponential phase cell culture were plated on 1% LB-agarose plates and left to dry before incubating for 3 hours at 37°C. Cells were harvested with 1 ml of LB. A drop of culture was placed on a parafilm film and a carbon coated grid was placed on the cell culture for 5 min. The grid was whashed 3 times in dH2O for 10 seconds, then placed on a drop of PFA 2% for 20 min. Dry PFA with whatman filter paper and place on Uranyl actetate for 30 s, dry excess with whatman paper and let dry 5 min. Data was acquired on a Tecnai Spirit electron microscope.

5.4.17   Fluorescence labeling of the type IV pili

Single colonies were inoculated in LB supplemented with appropriate antibiotics, grown overnight and diluted 1:500 or 1:1000 followed by a grow period of 2 h to obtain mid exponential phase cultures. 100 μl of exponential phase cell culture were plated on 1% LB-agarose plates and left to dry few minutes before incubating for 3 hours at 37°C. Cells were harvested with 1 ml of LB. Cells were centrifuged at 6000 rpm for 2 min. After discarding super natant, cells were gently resuspended in 100 μl of LB and 2 μl of Alexa Fluor 488 C5 mal dye was added and cells were inoculated in the

dark at 37°C for 30 min to 1 hour. Stained cells were incubated at 6000 rpm for 2 min, washed with 1 ml PBS twice and resuspended in 50 µl of LB prior to data acquisition.

5.4.18   Pili purification

Overnight cultures in appropriate growth medium were spread (50 µl) on 10 1.5% agar LB plates, dried for 30 minutes with half lid opened and incubated (lid facing up) for 24 hours at 30°C. Scrap the bacterial lawns off from the 10 plates with a big blue loop and resuspend in 8 ml chilled (4°C) Buffer 1 (150 mM ethanolamine (Sigma-Aldrich, 15014-1L), 1 mM Dithiothréitol (DTT, Fluorochem, 3483-12-3, M02712-25g), pH 10.5 (with 1M HCl)). Resuspend cells aggregate gently with a pipette. Shear pili from the cells by three cycles of 1 minute bursts of vigorous vortexing followed by 1 minute on ice. Remove cells by centrifugation (8000 x g, 30 min) at 4°C, three times (supernatant contains pili). Precipitate pili (7 ml) by the addition of 0.375 g ammonium sulfate (= 10% saturation). Dissolve ammonium sulfate by gently mixing by hand the tube and incubate tubes for 16 hours at 16° C. Collect pili by centrifugation 13 000 x g, 60 minutes, 4° C. Resuspend pellet in 7 ml solubilization buffer (20 mM ethanolamine (Sigma-Aldrich, 15014-1L), pH 10.5 (with 1M HCl)). Purify pili by precipitating a second time in ammonium sulfate to 10% saturation (in 7 ml) and incubate tubes 16 hours at 16° C. Collect pili by centrifugation 13 000 x g, 60 minutes, 4° C. Resuspend pellet in 500 µl solubilization buffer (that contains 1mM DTT to prevent disulphide bonds on TFP). Shortly centrifuge to remove unsoluble aggregate. Transfer supernatant (containing pili) to a new Eppendorf. Should yield 2 mg/ml in 500 µl

5.4.19   Transformation protocol for BTH101 cells for BACTH assay:

10 ng of the two plasmids carrying the T25 and T18 fusions are added to 100 µl of competent cells in an ice cold 1.5 ml tube and incubated on ice during 20 min. The cells are then heat shocked at 42 °C during 45 sec followed immediately by 1 min on ice. 400 µl of SOC media (room temp is fine) are added and cells are placed at 37 °C for recovery for 1 h. 100 µl of cells is spread on LB plates containing CARB, KAN, IPTG. Plates are incubated at 30 °C for 40 h.

5.4.20   Single-step ß-galactosidase assay (BACTH)

Inoculate transformed BTH101 colonies of interest in 300 µL of LB + 100 µg/ml carb + 50 µg/ml kan + 0.5mM IPTG (in a deep-well plate), and grow at 30°C with shaking overnight at 900 rpm. Make a 1:16 dilution for each well with cells according to your 96-well plate template. Transfer 80 µL of 1:16 dilution to each well of a flat-bottom microplate, according to your labelled 96-well plate template. For blank, 80 µL of sterile LB is used. Add 120 µL mix (36 mM BME (beta-mercaptoethanol), 166 µg/ml lysozyme[a] 1.1 mg/ml ONPG (ortho-nitrophenhyl- ß-galactoside, Sigma L3790-10X1ML), 6.7% PopCulture reagent) to each well that contains cells using a multichannel pipette. Reaction starts immediatly so proceed quickly. Place plate into the SpectraMax 340 PC plate reader. calculate the Miller Units using the following formula:

$$Miller\ Units = \frac{5000 * (\frac{OD_{420}}{time(\text{minutes})})}{OD_{600}} \qquad (6)$$

The slope is the (OD_{420}/time(sec)) variable in the equation. OD_{600} values are taken from the reading at time zero.

5.5 Supplementary Data
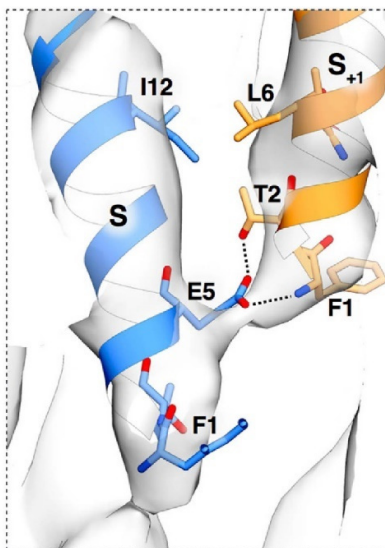
Supplementary Figure 5.1: Pilin-pilin interaction in the assembled TFP

Pili-pilin interaction is mediated through hydrogen bonds between residue T8 (T2) of pilin S_{+1} and residue E11 (E5) of pilin S in the assembled TFP. An electrostatic bond is also made between E11 of pilin S and F7 (F1) of pilin S_{+1}. Figure taken from Wang et *al. Structure* 2017 (*15*).
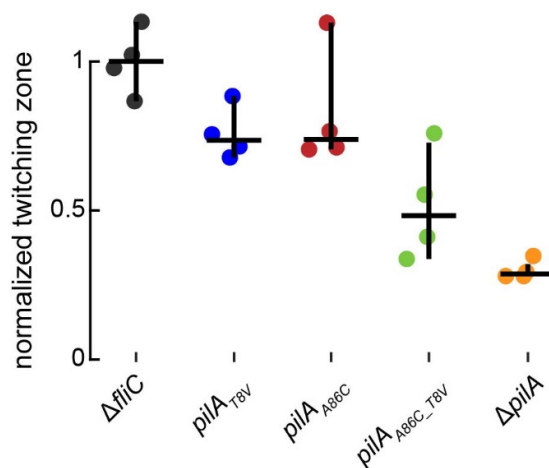
Supplementary Figure 5.2: Twitching stab assay quantification

Single colonie were stab inoculated at the bottom of a 0.5% agarose with Twitching Medium and then incubated at 37°C for 24 hours prior to measuring twitching zones. Colored circles represent means of biological replicates, horizontal black bar represent means across biological replicates and vertical black bar represent the mean bootstrap 95% and confidence interval.

Table 5-1 Site directed mutagenesis screen results

Groupe 1: similar virulence as WT, some level of twitching		
Mutation	*YFP/RFP ratio*	*Twitching*
PilA PAK	+	+
F7S	+	+
T8F	+	+
T8Y	+	+
T8L	+	+
G20C	+	+
A24G	+	+
Y30H/T	+	+
N32Q/L/N	+	+
Y33Q	+	+
R36E	+	+
K50H	+	+
R36N	+	+
Groupe 2: higher virulence than WT, no twitching		
Mutation	*YFP/RFP ratio*	*Twitching*
G6V	++	-
F7E	++	-
T8W	++	-
E11R	++	-
Groupe 3: higher virulence than WT, twitching		
Mutation	*YFP/RFP ratio*	*Twitching*
T8V	++	+
T8I	++	+
L22Q	++	+
Groupe 4: loss of virulence		
Mutation	*YFP/RFP ratio*	*Twitching*

PilA(1-36)	-	-
F7C/P	-	-
L9R	-	-
E11L	-	NA

Table 5-2 Strains and plasmids

Internal reference	Plasmid name(s)	Description **Construction by Gibson assembly unless stated otherwise:** - **Templates, primers used for PCR or enzymes for digestion**	Reference
62	pJN105	Broad-host-range expression vectors that carry the L-arabinose-inducible *E. coli* araBAD promoter and the araC regulator. Works in PAO1, with leaky basal expression. Genta[R]	Newmann and Fuqua, 1999 (*110*)
299	pEx18Ap	Suicide vector for two-step allelic exchange for S17-Pseudomonas mating. Amp[R]	Generous gift from Urs Jenal lab, Unibasel. Hoang et al, 1998 (*109*)
287	pZA001 pPilA – PilA WT	Wild type PAO1 PilA expression driven by the wild type promoter of pilA (500 bp upstream of the start codon) in the replicative plasmid pJN105, cloned in the MCS in opposite direction from the arabinose promoter. Genta[R]. Ligation of the following: - pJN105, XmaI + SacI - PAO1 gDNA, cata*cccggg*GCCACCTTCGATCACCTTAG + cata*gagctc*GTGTTGGCGGACCAGCTTTTC followed by XmaI + SacI	This study
NA	PilA random (7-30)	Error-prone mutagenesis of PilA from position 7 to 30 in pZA001 (pJN105). Genta[R] - pZA001, TCGGAAGGTGCTTCGG + GCCTTTTTGAGCTTTCATGAAT - pZA001 (7 nanograms, using the mutagenesis kit GeneMorph II [Agilent]), ATTCATGAAAGCTCAAAAAGGC + CCGAAGCACCTTCCGA	This study

NA	PilA T8X, plasmid based	Site directed saturation mutagenesis of PilA at position T8 in pZA001 (pJN105). Genta[R] - pZA001, TCGGAAGGTGCTTCGG + GCCTTTTTGAGCTTTCATGAAT - pZA001, CATGAAAGCTCAAAAAGGCTTTnnkTTGATCGAACTGATGATCG + TCGGAAGGTGCTTCGG	This study
libXP407	PilA R36X, plasmid based	Site directed saturation mutagenesis of PilA at position R36 in pZA001 (pJN105). Genta[R] - pZA001, GCCTTTTTGAGCTTTCATGAAT + TCGTTGCTGCTGCGTAACATttattatttccttcctctttctaca - pZA001, ATTCATGAAAGCTCAAAAAGGC + CCGAAGCACCTTCCGAmnnCGCAACATAGTTCTGATAC	This study
pXP486	PilA WT in pEx18Ap	Suicide vector for re-introducing *pilA* WT into *pilA*- PAO1 strain. Amp[R] - pEx18Ap, EcoRI + XbaI - PAO1 gDNA, atgaccatgattacgaattcGATGGCCAGGCCAAGC + gcctgcaggtcgactctagaCCGCAGCCAGCACTAC	This study
pXP487	PilA T8V in pEx18Ap	Suicide vector for introducing *pilA*(T8V) into *pilA*- PAO1 strain. Amp[R] - pEx18Ap, EcoRI + XbaI - PAO1 gDNA, atgaccatgattacgaattcGATGGCCAGGCCAAGC + AAAGCCTTTTTGAGCTTTCATGAATC - PAO1 gDNA, TGAAAGCTCAAAAAGGCTTTgtgTTGATCGAACTGATGATC + gcctgcaggtcgactctagaCCGCAGCCAGCACTAC	This study
pXP488	PilA T8I in pEx18Ap	Suicide vector for introducing *pilA*(T8I) into *pilA*- PAO1 strain. Amp[R] - pEx18Ap, EcoRI + XbaI - PAO1 gDNA, atgaccatgattacgaattcGATGGCCAGGCCAAGC + AAAGCCTTTTTGAGCTTTCATGAATC - PAO1 gDNA, TGAAAGCTCAAAAAGGCTTTatcTTGATCGAACTGATGATC+ gcctgcaggtcgactctagaCCGCAGCCAGCACTAC	This study

pXP489	PilA T8F in pEx18Ap	Suicide vector for introducing *pilA*(T8I) into *pilA*-PAO1 strain. Amp^R - pEx18Ap, EcoRI + XbaI - PAO1 gDNA, atgaccatgattacgaattcGATGGCCAGGCCAAGC + AAAGCCTTTTTGAGCTTTCATGAATC - PAO1 gDNA, TGAAAGCTCAAAAAGGCTTTttcTTGATCGAACTGATGATC+ gcctgcaggtcgactctagaCCGCAGCCAGCACTAC	This study
pXP490	PilA R36E in pEx18Ap	Suicide vector for introducing *pilA*(R36E) into *pilA*- PAO1 strain. Amp^R - pEx18Ap, EcoRI + XbaI - PAO1 gDNA, atgaccatgattacgaattcGATGGCCAGGCCAAGC + CGCAACATAGTTCTGATACTGGG - PAO1 gDNA, AGTATCAGAACTATGTTGCGgaaTCGGAAGGTGCTTCG+ gcctgcaggtcgactctagaCCGCAGCCAGCACTAC	This study
pXP491	PilA R36N in pEx18Ap	Suicide vector for introducing *pilA*(R36N) into *pilA*- PAO1 strain. Amp^R - pEx18Ap, EcoRI + XbaI - PAO1 gDNA, atgaccatgattacgaattcGATGGCCAGGCCAAGC + CGCAACATAGTTCTGATACTGGG - PAO1 gDNA, AGTATCAGAACTATGTTGCGaacTCGGAAGGTGCTTCG+ gcctgcaggtcgactctagaCCGCAGCCAGCACTAC	This study

Chapter 6. Conclusion

6.1 Achieved results

In this thesis I presented how I optimized iSCAT microscopy to live-cell imaging of TFP in *P. aeruginosa*. This involved a series of improvements over classical iSCAT, including reduction of phototoxicity induced by utilizing alternative laser sources. Selecting less energetic laser wavelength (638 nm for iSCAT and 850 nm for autofocus system) coupled with automated laser beam blocking allowed to image cells for extended period of time (minutes to hours). Overcoming these limitations has not only helped us understand *P. aeruginosa* TFP dynamics: we now have an imaging tool that allows us to visualize any nanometer-scale filament at the surface of any microbes.

By leveraging iSCAT, we could characterize TFP dynamics in live *P. aeruginosa* cells and readily test many of our hypotheses on TFP and mechanosensing. By visualizing many mutants, including those that lack either the extension motor (PilB) or the retraction motors (PilT and PilU) at high temporal resolution, we were able to highlight essential physical aspects of TFP dynamics (*41*). By measuring the dwell time of individual TFP, we discovered an active mechanism of adherence wherein adhesion is strengthened by retraction forces, in a similar manner as catch bonds. Furthermore, we found that TFP retract very rapidly (~100 ms) after their tips attach onto a surface. This time is in the same order of magnitude as the dwell time of random TFP attachment/detachment suggesting that there exists a reinforcement mechanism during retraction. Finally, we rarely saw TFP retraction without prior tip attachment. This suggests that the TFP tip attachment could trigger retraction. While we were able to observe it, the mechanisms of TFP tip sensing is unknown. iSCAT will constitute a powerful technique that will help identify the mechanisms of contact-induced TFP retraction.

We next investigated the coupling between TFP and the Chp system in *P. aeruginosa*. To achieve this, we sought to simultaneously measure in single cells TFP activity and the response of the Chp system. We could implement this with a new version of iSCAT which was coupled with fluorescence microscopy (*40*). First, we used iSCAT to count pili on each pole of the cells and compute the

polarization of TFP extension in several Chp mutants. We first visualized whether cells extend pili at one pole or on both poles. We found that the response regulator PilG was responsible to polarize TFP extension to one pole, in contrast the response regulator PilH was responsible to promote symmetrical distribution of TFP. We then correlated TFP distribution to the localization of the extension motor PilB and the two response regulators PilT and PilU using correlative iSCAT-fluorescence microscopy. We found that TFP asymmetrical distribution was mediated by the localization of the extension motor PilB. Finally, using single cell motility and response regulators localization we were able to show that the Chp system regulates the localization of the extension motor PilB and its activator FimX in order to polarize cells motility. Furthermore, we found that cell polarization depended on TFP activity as Δ*pilA* mutants could not polarize the localization of FimX over time. This underlines a direct positive feedback loop from the activated Chp system to TFP activity and biogenesis that steered twitching direction in a term we defined as mechanotaxis. We now have a much more detailed understanding of the coupling between TFP and the Chp system signaling activity. We established that there are multiple feedbacks between these two systems, both on the second timescale of extension and retraction and at the transcriptional timescale. Thus, TFP are both sense and respond to mechanosensing. This feedback loop makes however our investigations of mechanosensing more complex.

Finally, we explored the mechanisms of mechanosensation in *P. aeruginosa*. We first used a mutagenesis screen with the goal to identify gain-of-function mutants in *pilA*. We reasoned that such mutant would allow us to identify mutants mimicking force-induced conformation changes of TFP. We found that the *pilA$_{T8V}$* mutant interacted more with the Chp chemosensor PilJ compared to the WT pilin. We did not have data to support a mechanism where *pilA$_{T8V}$* induces a conformational change that is sensed by PilJ but our investigation suggests that PilJ senses a change in pilin concentration at the poles during extension and retraction of TFP. Due to the similarities of the Chp system with the Che system we hypothesized that PilJ could act as the MCPs of the Che system and sense transient concentrations of PilA in the inner membrane by either sensing short burst of

pilin influx during TFP retraction or by sensing temporal differences of pilin concentration between the poles.

All in all, we now have a better understanding on how *P. aeruginosa* senses surfaces and respond to this mechanical stimulus. TFP adhere to a surface, this changes the inner flux of pilins in the inner membrane which consequently activates the Chp system. The activated Chp system will simultaneously trigger cAMP production (on a timescale of minutes) and recruit more extension motors at the same pole. This results in another TFP extension and a positive feedback on Chp activation resulting in cell polarization and persistent forward twitching.

6.2 Future development

One of the main iSCAT limitations is that the cell body scatters a large amount of light and generates an interference pattern around the cell body that masks the signal of all TFP smaller than 1 μm. As described in Chapter 2.4, we tried to reduce the interference patterns of the cell body by using DMDs to locally dampen the illumination light intensity. Due to the short amount of time available to test this method, we encountered several technical limitations. First, we used a miniprojector and an HDMI cable to send our mask images on the DMDs. This has a major limitation as the drivers converting the video signal in DMDs actuator commands are using RGB signals and will sequentially execute DMDs positioning for the R, G, and B channels. The switch between channels could therefore be detrimental for the final image quality of iSCAT. Therefore, using a binary image with a mono channel governing DMDs on/off states will most probably yield better results. Second, we could then envision an automated cell body tracker that generates live masks in order to dampen the intensity on many cells at the same time during acquisition.

As mentioned in Chapter 5, our model for PilJ activation by pilin flux in the inner membrane still has many unknown variables which need further work. First, we want to generate accurate 3D models of our WT and T8V TFP in order to see if any subtle differences arise in their respective structure. Second, we want to further understand what mechanism PilJ uses to sense pilin flux, whether it is a

rush of concentration or a measure of past and present concentrations like in the Che system. Finally,

we want to develop a mathematical model to validate ours and confirm our experimental data.

References

1. L. Talà, "Characterization of Pseudomonas aeruginosa mechanosensing through label-free imaging of type IV pili" (Candidacy report (unpublished), EPFL, Lausanne, 2018), pp. 3–10.

2. R. E. W. Hancock, D. P. Speert, Antibiotic resistance in Pseudomonas aeruginosa: mechanisms and impact on treatment. *Drug Resistance Updates*. **3**, 247–255 (2000).

3. A. Persat, Y. F. Inclan, J. N. Engel, H. A. Stone, Z. Gitai, Type IV pili mechanochemically regulate virulence factors in *Pseudomonas aeruginosa*. *Proceedings of the National Academy of Sciences*. **112**, 7563–7568 (2015).

4. H. C. Berg, The Rotary Motor of Bacterial Flagella. *Annual Review of Biochemistry*. **72**, 19–54 (2003).

5. J. D. Schilling, M. A. Mulvey, S. J. Hultgren, Structure and Function of *Escherichia coli* Type 1 Pili: New Insightinto the Pathogenesis of Urinary Tract Infections. *The Journal of Infectious Diseases*. **183**, S36–S40 (2001).

6. K. A. Kline, S. Fälker, S. Dahlberg, S. Normark, B. Henriques-Normark, Bacterial Adhesins in Host-Microbe Interactions. *Cell Host & Microbe*. **5**, 580–592 (2009).

7. J. Henrichsen, Twitching Motility. *Annual Review of Microbiology*. **37**, 81–93 (1983).

8. J. S. Mattick, Type IV Pili and Twitching Motility. *Annual Review of Microbiology*. **56**, 289–314 (2002).

9. L. L. Burrows, *Pseudomonas aeruginosa* Twitching Motility: Type IV Pili in Action. *Annual Review of Microbiology*. **66**, 493–520 (2012).

10. J. W. Costerton, Z. Lewandowski, D. E. Caldwell, D. R. Korber, H. M. Lappin-Scott, Microbial biofilms. *Annu. Rev. Microbiol.* **49**, 711–745 (1995).

11. J. J. Bertrand, J. T. West, J. N. Engel, Genetic analysis of the regulation of type IV pilus function by the Chp chemosensory system of Pseudomonas aeruginosa. *Journal of bacteriology*. **192**, 994–1010 (2010).

12. C. B. Whitchurch, A. J. Leech, M. D. Young, D. Kennedy, J. L. Sargent, J. J. Bertrand, A. B. T. Semmler, A. S. Mellick, P. R. Martin, R. A. Alm, M. Hobbs, S. A. Beatson, B. Huang, L. Nguyen, J. C. Commolli, J. N. Engel, A. Darzins, J. S. Mattick, Characterization of a complex chemosensory signal transduction system which controls twitching motility in Pseudomonas aeruginosa. *Molecular Microbiology*. **52**, 873–893 (2004).

13. A. Darzins, Characterization of a Pseudomonas aeruginosa gene cluster involved in pilus biosynthesis and twitching motility: sequence similarity to the chemotaxis proteins of enterics and the gliding bacterium Myxococcus xanthus. *Molecular Microbiology*. **11**, 137–153 (1994).

14. G. H. Wadhams, J. P. Armitage, Making sense of it all: Bacterial chemotaxis. *Nature Reviews Molecular Cell Biology*. **5**, 1024–1037 (2004).

15. F. Wang, M. Coureuil, T. Osinski, X. Nassif, E. H. Egelman, L. Craig, Cryoelectron Microscopy Reconstructions of the Pseudomonas aeruginosa and Neisseria gonorrhoeae Type IV Pili at Sub-nanometer Resolution. *Structure/Folding and Design*. **25**, 1423-1435.e4 (2017).

16. Y.-W. Chang, L. A. Rettberg, A. Treuner-Lange, J. Iwasa, L. Søgaard-Andersen, G. J. Jensen, Architecture of the type IVa pilus machine. *Science*. **351**, aad2001 (2016).

17. J. M. Skerker, H. C. Berg, Direct observation of extension and retraction of type IV pili. *Proceedings of the National Academy of Sciences*. **98**, 6901–6904 (2001).

18. C. K. Ellison, J. Kan, R. S. Dillard, D. T. Kysela, A. Ducret, C. Berne, C. M. Hampton, Z. Ke, E. R. Wright, N. Biais, A. B. Dalia, Y. V. Brun, Obstruction of pilus retraction stimulates bacterial surface sensing. *Science*. **358**, 535–538 (2017).

19. C. K. Ellison, T. N. Dalia, A. Vidal Ceballos, J. C.-Y. Wang, N. Biais, Y. V. Brun, A. B. Dalia, Retraction of DNA-bound type IV competence pili initiates DNA uptake during natural transformation in Vibrio cholerae. *Nature Microbiology*. **3**, 773–780 (2018).

20. D. W. Adams, S. Stutzmann, C. Stoudmann, M. Blokesch, DNA-uptake pili of Vibrio cholerae are required for chitin colonization and capable of kin recognition via sequence-specific self-interaction. *Nat Microbiol*. **4**, 1545–1557 (2019).

21. M. D. Koch, C. Fei, N. S. Wingreen, J. W. Shaevitz, Z. Gitai, Competitive binding of independent extension and retraction motors explains the quantitative dynamics of type IV pili. *Proceedings of the National Academy of Sciences*. **118**, e2014926118 (2021).

22. B. Maier, G. C. L. Wong, How Bacteria Use Type IV Pili Machinery on Surfaces. *Trends in Microbiology*. **23**, 775–788 (2015).

23. Y. Brill-Karniely, F. Jin, G. C. L. Wong, D. Frenkel, J. Dobnikar, Emergence of complex behavior in pili-based motility in early stages of P. aeruginosa surface adaptation. *Scientific Reports*. **7**, 45467 (2017).

24. F. Jin, J. C. Conrad, M. L. Gibiansky, G. C. L. Wong, Bacteria use type-IV pili to slingshot on surfaces. *Proceedings of the National Academy of Sciences*. **108**, 12617–12622 (2011).

25. M. Clausen, M. Koomey, B. Maier, Dynamics of Type IV Pili Is Controlled by Switching Between Multiple States. *Biophysj*. **96**, 1169–1177.

26. Y. F. Dufrêne, Sticky microbes: forces in microbial cell adhesion. *Trends in Microbiology*. **23**, 376–382 (2015).

27. L. Priest, J. S. Peters, P. Kukura, Scattering-based Light Microscopy: From Metal Nanoparticles to Single Proteins. *Chem. Rev.* **121**, 11937–11970 (2021).

28. K. Lindfors, T. Kalkbrenner, P. Stoller, V. Sandoghdar, Detection and Spectroscopy of Gold Nanoparticles Using Supercontinuum White Light Confocal Microscopy. *Physical Review Letters*. **93**, 037401 (2004).

29. V. Jacobsen, P. Stoller, C. Brunner, V. Vogel, V. Sandoghdar, Interferometric optical detection and tracking of very small gold nanoparticles at a water-glass interface. *Optics express*. **14**, 405–14 (2006).

30. J. Ortega-Arroyo, P. Kukura, Interferometric scattering microscopy (iSCAT): new frontiers in ultrafast and ultrasensitive optical microscopy. *Physical Chemistry Chemical Physics*. **14**, 15625 (2012).

31. J. Ortega Arroyo, D. Cole, P. Kukura, Interferometric scattering microscopy and its combination with single-molecule fluorescence imaging. *Nature Protocols*. **11**, 617–633 (2016).

32. A. S. CURTIS, the Mechanism of Adhesion of Cells To Glass. a Study By Interference Reflection Microscopy. *The Journal of cell biology*. **20**, 199–215 (1964).

33. G. Young, P. Kukura, Interferometric Scattering Microscopy. *Annual Review of Physical Chemistry*. **70**, 301–322 (2019).

34. G. Young, N. Hundt, D. Cole, A. Fineberg, J. Andrecka, A. Tyler, A. Olerinyova, A. Ansari, E. G. Marklund, M. P. Collier, S. A. Chandler, O. Tkachenko, J. Allen, M. Crispin, N. Billington, Y. Takagi, J. R. Sellers, C. Eichmann, P. Selenko, L. Frey, R. Riek, M. R. Galpin, W. B. Struwe, J. L. P. Benesch, P. Kukura, Quantitative mass imaging of single biological macromolecules. *Science*. **360**, 423–427 (2018).

35. J. Andrecka, J. O. Arroyo, Y. Takagi, G. de Wit, A. Fineberg, L. MacKinnon, G. Young, J. R. Sellers, P. Kukura, Structural dynamics of myosin 5 during processive motion revealed by interferometric scattering microscopy. *eLife*. **2015** (2015), doi:10.7554/eLife.05413.

36. J. Ortega-Arroyo, A. J. Bissette, P. Kukura, S. P. Fletcher, Visualization of the spontaneous emergence of a complex, dynamic, and autocatalytic system. *PNAS*. **113**, 11122–11126 (2016).

37. J. Andrecka, J. Ortega Arroyo, K. Lewis, R. A. Cross, P. Kukura, Label-free Imaging of Microtubules with Sub-nm Precision Using Interferometric Scattering Microscopy. *Biophysical Journal*. **110**, 214–217 (2016).

38. P. Kukura, H. Ewers, C. Müller, A. Renn, A. Helenius, V. Sandoghdar, High-speed nanoscopic tracking of the position and orientation of a single virus. *Nature Methods*. **6**, 923–927 (2009).

39. J. Ortega Arroyo, J. Andrecka, K. M. Spillane, N. Billington, Y. Takagi, J. R. Sellers, P. Kukura, Label-free, all-optical detection, imaging, and tracking of a single protein. *Nano Letters*. **14**, 2065–2070 (2014).

40. M. J. Kühn, L. Talà, Y. F. Inclan, R. Patino, X. Pierrat, I. Vos, Z. Al-Mayyah, H. Macmillan, J. Negrete, J. N. Engel, A. Persat, Mechanotaxis directs *Pseudomonas aeruginosa* twitching motility. *Proc Natl Acad Sci USA*. **118** (2021), doi:10.1073/pnas.2101759118.

41. L. Talà, A. Fineberg, P. Kukura, A. Persat, Pseudomonas aeruginosa orchestrates twitching motility by sequential control of type IV pili movements. *Nature Microbiology*. **4**, 774–780 (2019).

42. J. Schindelin, I. Arganda-Carreras, E. Frise, V. Kaynig, M. Longair, T. Pietzsch, S. Preibisch, C. Rueden, S. Saalfeld, B. Schmid, J.-Y. Tinevez, D. J. White, V. Hartenstein, K. Eliceiri, P. Tomancak, A. Cardona, Fiji: an open-source platform for biological-image analysis. *Nature Methods*. **9**, 676–682 (2012).

43. C. L. Giltner, Y. Nguyen, L. L. Burrows, Type IV pilin proteins: versatile molecular modules. *Microbiology and molecular biology reviews : MMBR*. **76**, 740–72 (2012).

44. L. Turner, W. S. Ryu, H. C. Berg, Real-Time Imaging of Fluorescent Flagellar Filaments. *Journal of Bacteriology*. **182**, 2793–2801 (2000).

45. Y. Magariyama, S. Sugiyama, K. Muramoto, I. Kawagishi, Y. Imae, S. Kudo, Simultaneous measurement of bacterial flagellar rotation rate and swimming speed. *Biophys J*. **69**, 2154–2162 (1995).

46. M. Fujii, S. Shibata, S.-I. Aizawa, Polar, Peritrichous, and Lateral Flagella Belong to Three Distinguishable Flagellar Families. *Journal of Molecular Biology*. **379**, 273–283 (2008).

47. R. Lavigne, E. Lecoutere, J. Wagemans, W. Cenens, A. Aertsen, L. Schoofs, B. Landuyt, J. Paeshuyse, M. Scheer, M. Schobert, P.-J. Ceyssens, A multifaceted study of Pseudomonas aeruginosa shutdown by virulent podovirus LUZ19. *mBio*. **4**, e00061-00013 (2013).

48. J. M. Budzik, W. A. Rosche, A. Rietsch, G. A. O'Toole, Isolation and Characterization of a Generalized Transducing Phage for Pseudomonas aeruginosa Strains PAO1 and PA14. *Journal of Bacteriology*. **186**, 3270–3273 (2004).

49. M. L. Gibiansky, J. C. Conrad, F. Jin, V. D. Gordon, D. A. Motto, M. A. Mathewson, W. G. Stopka, D. C. Zelasko, J. D. Shrout, G. C. L. Wong, Bacteria Use Type IV Pili to Walk Upright and Detach from Surfaces. *Science*. **330**, 197–197 (2010).

50. T. R. D. Costa, C. Felisberto-Rodrigues, A. Meir, M. S. Prevost, A. Redzej, M. Trokter, G. Waksman, Secretion systems in Gram-negative bacteria: structural and mechanistic insights. *Nature Reviews Microbiology*. **13**, 343 (2015).

51. A. Persat, Bacterial mechanotransduction. *Current Opinion in Microbiology*. **36**, 1–6 (2017).

52.   A. J. Merz, M. So, M. P. Sheetz, Pilus retraction powers bacterial twitching motility. *Nature*. **407**, 98–102 (2000).

53.   B. Maier, L. Potter, M. So, H. S. Seifert, M. P. Sheetz, Single pilus motor forces exceed 100 pN. *PNAS*. **99**, 16012–16017 (2002).

54.   A. Beaussart, A. E. Baker, S. L. Kuchma, S. El-Kirat-Chatel, G. A. O'Toole, Y. F. Dufrêne, Nanoscale Adhesion Forces of Pseudomonas aeruginosa Type IV Pili. *ACS Nano*. **8**, 10723–10733 (2014).

55.   L. Ping, J. Birkenbeil, S. Monajembashi, Swimming behavior of the monotrichous bacterium Pseudomonas fluorescens SBW25. *FEMS Microbiology Ecology*. **86**, 36–44 (2013).

56.   M. Krishnan, N. Mojarad, P. Kukura, V. Sandoghdar, Geometry-induced electrostatic trapping of nanometric objects in a fluid. *Nature*. **467**, 692–695 (2010).

57.   C. B. Whitchurch, J. S. Mattick, Characterization of a gene, pilU, required for twitching motility but not phage sensitivity in Pseudomonas aeruginosa. *Molecular Microbiology*. **13**, 1079–1091 (1994).

58.   H.-S. M. Park, M. Wolfgang, M. Koomey, Modification of Type IV Pilus-Associated Epithelial Cell Adherence and Multicellular Behavior by the PilU Protein of Neisseria gonorrhoeae. *Infect Immun*. **70**, 3891–3903 (2002).

59.   S. L. Kuchma, N. J. Delalez, L. M. Filkins, E. A. Snavely, J. P. Armitage, G. A. O'Toole, Cyclic Di-GMP-Mediated Repression of Swarming Motility by Pseudomonas aeruginosa PA14 Requires the MotAB Stator. *J. Bacteriol.* **197**, 420–430 (2015).

60.   P. Chiang, M. Habash, L. L. Burrows, Disparate Subcellular Localization Patterns of Pseudomonas aeruginosa Type IV Pilus ATPases Involved in Twitching Motility. *J Bacteriol*. **187**, 829–839 (2005).

61.   W. E. Thomas, V. Vogel, E. Sokurenko, Biophysics of Catch Bonds. *Annual Review of Biophysics*. **37**, 399–416 (2008).

62.   N. Biais, D. L. Higashi, J. Brujic, M. So, M. P. Sheetz, Force-dependent polymorphism in type IV pili reveals hidden epitopes. *Proceedings of the National Academy of Sciences of the United States of America*. **107**, 11358–63 (2010).

63.   O. Kiehn, Decoding the organization of spinal circuits that control locomotion. *Nature Reviews Neuroscience*. **17**, 224–238 (2016).

64.   V. Dietz, Proprioception and locomotor disorders. *Nature Reviews Neuroscience*. **3**, 781–790 (2002).

65.   A. Persat, C. D. Nadell, M. K. Kim, F. Ingremeau, A. Siryaporn, K. Drescher, N. S. Wingreen, B. L. Bassler, Z. Gitai, H. A. Stone, The Mechanical World of Bacteria. *Cell*. **161**, 988–997 (2015).

66.   L. R. Hmelo, B. R. Borlee, H. Almblad, M. E. Love, T. E. Randall, B. S. Tseng, C. Lin, Y. Irie, K. M. Storek, J. J. Yang, R. J. Siehnel, P. L. Howell, P. K. Singh, T. Tolker-Nielsen, M. R. Parsek, H. P. Schweizer, J. J. Harrison, Precision-engineering the Pseudomonas aeruginosa genome with two-step allelic exchange. *Nature Protocols*. **10**, 1820–1841 (2015).

67.   K. F. Jarrell, M. J. McBride, The surprisingly diverse ways that prokaryotes move. *Nature Reviews Microbiology*. **6**, 466–476 (2008).

68.   Y. F. Dufrêne, A. Persat, Mechanomicrobiology: how bacteria sense and respond to forces. *Nature Reviews Microbiology*. **18**, 227–240 (2020).

69.   S. Bi, V. Sourjik, Stimulus sensing and signal processing in bacterial chemotaxis. *Current Opinion in Microbiology*. **45**, 22–29 (2018).

70.   P. J. M. Van Haastert, P. N. Devreotes, Chemotaxis: signalling the way forward. *Nature Reviews Molecular Cell Biology*. **5**, 626–634 (2004).

71.   A. M. Stock, V. L. Robinson, P. N. Goudreau, Two-Component Signal Transduction. *Annual Review of Biochemistry*. **69**, 183–215 (2000).

72.   M. A. Matilla, T. Krell, The effect of bacterial chemotaxis on host infection and pathogenicity. *FEMS Microbiology Reviews*. **42** (2018), doi:10.1093/femsre/fux052.

73.   S. L. Porter, G. H. Wadhams, J. P. Armitage, Rhodobacter sphaeroides: complexity in chemotactic signalling. *Trends in Microbiology*. **16**, 251–260 (2008).

74.   N. B. Fulcher, P. M. Holliday, E. Klem, M. J. Cann, M. C. Wolfgang, The Pseudomonas aeruginosa Chp chemosensory system regulates intracellular cAMP levels by modulating adenylate cyclase activity. *Molecular Microbiology*. **76**, 889–904 (2010).

75.   D. B. Kearns, J. Robinson, L. J. Shimkets, Pseudomonas aeruginosa Exhibits Directed Twitching Motility Up Phosphatidylethanolamine Gradients. *Journal of Bacteriology*. **183**, 763–767 (2001).

76.   D. H. Limoli, E. A. Warren, K. D. Yarrington, N. P. Donegan, A. L. Cheung, G. A. O'Toole, Interspecies interactions induce exploratory motility in Pseudomonas aeruginosa. *eLife*. **8**, e47365 (2019).

77.   N. M. Oliveira, K. R. Foster, W. M. Durham, Single-cell twitching chemotaxis in developing biofilms. *Proceedings of the National Academy of Sciences*. **113**, 6532–6537 (2016).

78.   L. M. Nolan, L. C. McCaughey, J. Merjane, L. Turnbull, C. B. Y. 2020 Whitchurch, ChpC controls twitching motility-mediated expansion of Pseudomonas aeruginosa biofilms in response to serum albumin, mucin and oligopeptides. *Microbiology*. **166**, 669–678 (2020).

79.   R. N. C. Buensuceso, M. Daniel-Ivad, S. L. N. Kilmury, T. L. Leighton, H. Harvey, P. L. Howell, L. L. Burrows, Cyclic AMP-Independent Control of Twitching Motility in Pseudomonas aeruginosa. *Journal of Bacteriology*. **199** (2017), doi:10.1128/JB.00188-17.

80.   H. C. Berg, *E. coli in Motion* (Springer New York, New York, NY, 2004; http://link.springer.com/10.1007/b97370), *Biological and Medical Physics, Biomedical Engineering*.

81.   S. Thutupalli, M. Sun, F. Bunyak, K. Palaniappan, J. W. Shaevitz, Directional reversals enable Myxococcus xanthus cells to produce collective one-dimensional streams during fruiting-body formation. *Journal of The Royal Society Interface*. **12**, 20150049 (2015).

82.   B. D. Blackhart, D. R. Zusman, "Frizzy" genes of Myxococcus xanthus are involved in control of frequency of reversal of gliding motility. *PNAS*. **82**, 8767–8770 (1985).

83.   O. J. Meacock, A. Doostmohammadi, K. R. Foster, J. M. Yeomans, W. M. Durham, Bacteria solve the problem of crowding by moving slowly. *Nature Physics*. **17**, 205–210 (2021).

84.   R. Jain, O. Sliusarenko, B. I. Kazmierczak, C. Jacobs-Wagner, C. Jones, D. Sanchez, Interaction of the cyclic-di-GMP binding protein FimX and the Type 4 pilus assembly ATPase promotes pilus assembly. *PLOS Pathogens*. **13**, e1006594 (2017).

85.   B. I. Kazmierczak, M. B. Lebron, T. S. Murray, Analysis of FimX, a phosphodiesterase that governs twitching motility in Pseudomonas aeruginosa. *Molecular Microbiology*. **60**, 1026–1043 (2006).

86.   C. Galicia, S. Lhospice, P. F. Varela, S. Trapani, W. Zhang, J. Navaza, J. Herrou, T. Mignot, J. Cherfils, MglA functions as a three-state GTPase to control movement reversals of Myxococcus xanthus. *Nature Communications*. **10**, 5300 (2019).

87.   M. Guzzo, S. M. Murray, E. Martineau, S. Lhospice, G. Baronian, L. My, Y. Zhang, L. Espinosa, R. Vincentelli, B. P. Bratton, J. W. Shaevitz, V. Molle, M. Howard, T. Mignot, A gated relaxation oscillator

mediated by FrzX controls morphogenetic movements in Myxococcus xanthus. *Nature Microbiology*. **3**, 948–959 (2018).

88.　O. Brandman, T. Meyer, Feedback Loops Shape Cellular Signals in Space and Time. *Science*. **322**, 390–395 (2008).

89.　Y. F. Inclan, A. Persat, A. Greninger, J. V. Dollen, J. Johnson, N. Krogan, Z. Gitai, J. N. Engel, A scaffold protein connects type IV pili with the Chp chemosensory system to mediate activation of virulence signaling in Pseudomonas aeruginosa. *Molecular Microbiology*. **101**, 590–605 (2016).

90.　A. Levchenko, P. A. Iglesias, Models of Eukaryotic Gradient Sensing: Application to Chemotaxis of Amoebae and Neutrophils. *Biophysical Journal*. **82**, 50–63 (2002).

91.　K. Son, J. S. Guasto, R. Stocker, Bacteria can exploit a flagellar buckling instability to change direction. *Nature Physics*. **9**, 494–498 (2013).

92.　I. Hug, S. Deshpande, K. S. Sprecher, T. Pfohl, U. Jenal, Second messenger–mediated tactile response by a bacterial rotary motor. *Science*. **358**, 531–534 (2017).

93.　J. E. Sanfilippo, A. Lorestani, M. D. Koch, B. P. Bratton, A. Siryaporn, H. A. Stone, Z. Gitai, Microfluidic-based transcriptomics reveal force-independent bacterial rheosensing. *Nat Microbiol*. **4**, 1274–1281 (2019).

94.　J. M. Kefauver, A. B. Ward, A. Patapoutian, Discoveries in structure and physiology of mechanically activated ion channels. *Nature*. **587**, 567–576 (2020).

95.　R. Sunyer, V. Conte, J. Escribano, A. Elosegui-Artola, A. Labernadie, L. Valon, D. Navajas, J. M. García-Aznar, J. J. Muñoz, P. Roca-Cusachs, X. Trepat, Collective cell durotaxis emerges from long-range intercellular force transmission. *Science*. **353**, 1157–1161 (2016).

96.　A. R. Houk, A. Jilkine, C. O. Mejean, R. Boltyanskiy, E. R. Dufresne, S. B. Angenent, S. J. Altschuler, L. F. Wu, O. D. Weiner, Membrane Tension Maintains Cell Polarity by Confining Signals to the Leading Edge during Neutrophil Migration. *Cell*. **148**, 175–188 (2012).

97.　H. C. Berg, E. M. Purcell, Physics of chemoreception. *Biophysical Journal*. **20**, 193–219 (1977).

98.　N. Schuergers, T. Lenn, R. Kampmann, M. V. Meissner, T. Esteves, M. Temerinac-Ott, J. G. Korvink, A. R. Lowe, C. W. Mullineaux, A. Wilde, Cyanobacteria use micro-optics to sense light direction. *eLife*. **5**, 1–16 (2016).

99.　N. Schuergers, C. W. Mullineaux, A. Wilde, Cyanobacteria in motion. *Curr Opin Plant Biol*. **37**, 109–115 (2017).

100.　S. L. Porter, G. H. Wadhams, J. P. Armitage, Signal processing in complex chemotaxis pathways. *Nature Reviews Microbiology*. **9**, 153–165 (2011).

101.　D. G. Gibson, L. Young, R.-Y. Chuang, J. C. Venter, C. A. Hutchison, H. O. Smith, Enzymatic assembly of DNA molecules up to several hundred kilobases. *Nature Methods*. **6**, 343–345 (2009).

102.　R. Hartmann, M. C. F. van Teeseling, M. Thanbichler, K. Drescher, BacStalk: A comprehensive and interactive image analysis software tool for bacterial cell biology. *Molecular Microbiology*. **114**, 140–150 (2020).

103.　P. Thévenaz, U. E. Ruttimann, M. Unser, A pyramid approach to subpixel registration based on intensity. *IEEE Trans Image Process*. **7**, 27–41 (1998).

104.　B. W. Holloway, A. F. Morgan, Genome organization in Pseudomonas. *Annu Rev Microbiol*. **40**, 79–105 (1986).

105. K. B. Barken, S. J. Pamp, L. Yang, M. Gjermansen, J. J. Bertrand, M. Klausen, M. Givskov, C. B. Whitchurch, J. N. Engel, T. Tolker-Nielsen, Roles of type IV pili, flagellum-mediated motility and extracellular DNA in the formation of mature multicellular structures in Pseudomonas aeruginosa biofilms. *Environmental Microbiology*. **10**, 2331–2343 (2008).

106. B.-J. Laventie, M. Sangermani, F. Estermann, P. Manfredi, R. Planes, I. Hug, T. Jaeger, E. Meunier, P. Broz, U. Jenal, A Surface-Induced Asymmetric Program Promotes Tissue Colonization by Pseudomonas aeruginosa. *Cell Host & Microbe*. **25**, 140-152.e6 (2019).

107. Y. F. Inclan, M. J. Huseby, J. N. Engel, FimL Regulates cAMP Synthesis in Pseudomonas aeruginosa. *PLoS ONE*. **6**, e15867 (2011).

108. H. P. Schweizer, T. T. Hoang, An improved system for gene replacement and xylE fusion analysis in Pseudomonas aeruginosa. *Gene*. **158**, 15–22 (1995).

109. T. T. Hoang, R. R. Karkhoff-Schweizer, A. J. Kutchma, H. P. Schweizer, A broad-host-range Flp-FRT recombination system for site-specific excision of chromosomally-located DNA sequences: application for isolation of unmarked Pseudomonas aeruginosa mutants. *Gene*. **212**, 77–86 (1998).

110. J. R. Newman, C. Fuqua, Broad-host-range expression vectors that carry the l-arabinose-inducible Escherichia coli araBAD promoter and the araC regulator. *Gene*. **227**, 197–203 (1999).

111. H. P. Schweizer, Escherichia-Pseudomonas shuttle vectors derived from pUC18/19. *Gene*. **97**, 109–112 (1991).

112. J. J. Falke, R. B. Bass, S. L. Butler, S. A. Chervitz, M. A. Danielson, THE TWO-COMPONENT SIGNALING PATHWAY OF BACTERIAL CHEMOTAXIS: A Molecular View of Signal Transduction by Receptors, Kinases, and Adaptation Enzymes. *Annual Review of Cell and Developmental Biology*. **13**, 457–512 (1997).

113. Á. Ortega, I. B. Zhulin, T. Krell, Sensory Repertoire of Bacterial Chemoreceptors. *Microbiology and Molecular Biology Reviews*. **81** (2017), doi:10.1128/MMBR.00033-17.

114. M. A. Matilla, D. Martín-Mora, J. A. Gavira, T. Krell, Pseudomonas aeruginosa as a Model To Study Chemosensory Pathway Signaling. *Microbiology and Molecular Biology Reviews*. **85** (2021), doi:10.1128/mmbr.00151-20.

115. Y. Yang, V. Lam, M. Adomako, R. Simkovsky, A. Jakob, N. C. Rockwell, S. E. Cohen, A. Taton, J. Wang, J. C. Lagarias, A. Wilde, D. R. Nobles, J. J. Brand, S. S. Golden, Phototaxis in a wild isolate of the cyanobacterium Synechococcus elongatus. *Proceedings of the National Academy of Sciences of the United States of America*. **115**, E12378–E12387 (2018).

116. S. Chakraborty, M. Li, C. Chatterjee, J. Sivaraman, K. Y. Leung, Y.-K. Mok, Temperature and Mg2+ Sensing by a Novel PhoP-PhoQ Two-component System for Regulation of Virulence in Edwardsiella tarda*. *Journal of Biological Chemistry*. **285**, 38876–38888 (2010).

117. R. S. Shapiro, L. E. Cowen, Thermal Control of Microbial Development and Virulence: Molecular Mechanisms of Microbial Temperature Sensing. *mBio*. **3** (2012), doi:10.1128/mBio.00238-12.

118. B.-J. Laventie, U. Jenal, Surface Sensing and Adaptation in Bacteria. *Annual Review of Microbiology*. **74**, 735–760 (2020).

119. N. Wadhwa, H. C. Berg, Bacterial motility: machinery and mechanisms. *Nat Rev Microbiol*, 1–13 (2021).

120. E. L. Fuchs, E. D. Brutinel, A. K. Jones, N. B. Fulcher, M. L. Urbanowski, T. L. Yahr, M. C. Wolfgang, The Pseudomonas aeruginosa Vfr Regulator Controls Global Virulence Factor Expression through Cyclic AMP-Dependent and -Independent Mechanisms. *Journal of Bacteriology*. **192**, 3553–3564 (2010).

121. J. Mehla, J. H. Caufield, N. Sakhawalkar, P. Uetz, in *Methods in Enzymology*, A. K. Shukla, Ed. (Academic Press, 2017; https://www.sciencedirect.com/science/article/pii/S0076687916303858), vol. 586 of *Proteomics in Biology, Part B*, pp. 333–358.

122. B. Bardiaux, G. C. de Amorim, A. Luna Rico, W. Zheng, I. Guilvout, C. Jollivet, M. Nilges, E. H. Egelman, N. Izadi-Pruneyre, O. Francetic, Structure and Assembly of the Enterohemorrhagic Escherichia coli Type 4 Pilus. *Structure*. **27**, 1082-1093.e5 (2019).

123. P. DeLange, T. Collins, G. Pierce, J. Robinson, PilJ localizes to cell poles and is required for type IV pilus extension in Pseudomonas aeruginosa. *Current microbiology*. **55**, 389–395 (2007).

124. M. D. Koch, E. Han, J. W. Shaevitz, Z. Gitai, "Pseudomonas aeruginosa differentiates substrate rigidity using retraction of type IV pili" (2021), p. 2021.08.26.457786, , doi:10.1101/2021.08.26.457786.

125. D. N. Nunn, S. Lory, Product of the Pseudomonas aeruginosa gene pilD is a prepilin leader peptidase. *Proceedings of the National Academy of Sciences*. **88**, 3281–3285 (1991).

126. C. Kiewitz, B. Tümmler, Sequence Diversity of Pseudomonas aeruginosa: Impact on Population Structure and Genome Evolution. *Journal of Bacteriology*. **182**, 3125–3135 (2000).

127. R. Ghosh, A. Kumar, A. Vaziri, Type-IV Pilus Deformation Can Explain Retraction Behavior. *PLoS ONE*. **9**, e114613 (2014).

128. S. He, S. H. W. Scheres, Helical reconstruction in RELION. *J Struct Biol*. **198**, 163–176 (2017).

Curriculum Vitae

LORENZO ANTON-LOUIS TALÀ

49, Rue du Lac | 74200 Thonon-les-Bains | France

+41 (0)76 439 41 00 | lorenzo.tala@alumni.epfl.ch

Date of Birth: 2 October 1986 | Nationality: Swiss, Italian | Gender: Male

EMPLOYMENT HISTORY

ÉCOLE POLYTECHNIQUE FÉDÉRALE DE LAUSANNE   **Lausanne, Switzerland**

Mar 17 – Present *Researcher as PHD student*

- Implement and adapt an interferometric scatting microscope (iSCAT) to study bacterial mechanosensation.

- Hardware integration and microscope software development

- Research project management

- Image processing and image analysis including machine-learning based methods

- Bacterial gene editing and cloning

- Work with P2 class bacteria

- Lab IT manager

- Student project tutoring

LAB OF GENETIC SKIN DISEASES, IMAGINE INSTITUTE, INSERM   **Paris, France**

Aug 16 – Dec 16 *Research Engineer*

- Study cancer development in genetics skin diseases

- Animal experimentation

- Cell culture

- Patient sample handling

- Molecular biology

Jul 15 – Sept 15 *Research Intern*

- Gene cloning for mouse model generation

SYSTEMS ASSEMBLING SA   **Boudry, Switzerland**

Oct 08 – Dec 08 *Electrical systems installer*

- Wiring of electrical cabinets, quality control, machining of electrical cabinet components.

THE CHURCH OF JESUS-CHRIST OF LATTER-DAY SAINTS   **Catania, Italy**

Jun 06 – Jul 08 *Volunteering missionary*

- Social service, teaching and assisting people in need

- Assuring the well-being of groups of 10 to 15 other missionaries.

ETA – SWATCH GROUP   Fontainemelon, Switzerland

Jan 06 – Jun 06 *Maintenance Electrician*

- Maintenance and breakdown service of plastic injection machines, production of watch components.

SWISS CIVIL PROTECTION   Neuchâtel, Switzerland

Mar 06 – Jul 16 *Sargent – Nuclear, Biological and Chemical Department*

- Assessing risk related to radioactive, biological, and chemical hazards

- Applying safety protocols for protection and decontamination

- Computing radioactivity exposure doses and take appropriate actions

EDUCATION

ECOLE POLYTECHNIQUE FEDERALE DE LAUSANNE   Lausanne, Switzerland

Mar 17 – Present *PHD in Bioengineering*

Sept 14 – Jul 16 *Master of Science MSC in Bioengineering*

Sept 10 – Jul 14 *Bachelor of Science BSC in Life Sciences and Technologies*

GYMNASE FRANCAIS DE BIENNE   Bienne, Switzerland

Aug 09 – Jul 10 *Complementary examination for federal Matura*

CENTRE PROFESSIONNEL DU LITTORAL NEUCHÂTELOIS   Neuchâtel, Switzerland

Aug 02 – Jul 05 *Technical Electrician Diploma*

PROFESSIONAL QUALIFICATIONS AND SKILLS

- Language skills: Italian (native), French (native), English (C2), Spanish (B1), German (A1)

- Digital skills: Office suite, Zoom, Social Media, Google suite

- Life Science: Microbiology and Molecular Biology techniques, light microscopy, Electron Microscopy, Biophysics Tissue Engineering, Live Cell Imaging, Animal Experiementation

- Engineering: Utility electronics repair programming: C C++ Java (J2EE), Optics programming language: Python, labview (Base), Image processing, proficient user of MATLAB Analytical skills

- Soft skills: Good listener and communicator, Multidiscipilnary work, Team-work oriented, Motivated

PUBLICATIONS

- Talà, L., Fineberg, A., Kukura, P. & Persat, A. *Pseudomonas aeruginosa* orchestrates twitching motility by sequential control of type IV pili movements. Nat. Microbiol. 1 (2019). doi:10.1038/s41564-019-0378-9

- Marco J. Kühn, Lorenzo Talà, Yuki Inclan, Ramiro Patino, Xavier Pierrat, Iscia Vos, Zainebe Al-Mayyah, Henriette MacMillan, Jose Negrete, Joanne N. Engel, Alexandre Persat, Mechanotaxis directs *Pseudomonas aeruginosa* twitching motility. Proceedings of the National Academy of Sciences, USA (2021) doi: https://doi.org/10.1101/2021.01.26.428277

CONFERENCES AND SEMINARS

- Revealing bacterial surface structures with Interferometric Scattering Microscopy (iSCAT)/ Talà, L., Fineberg, A., Kukura, P. & Persat, A. Accepted in ASM biofilm conference, Washington D.C. in 2018 as a poster presetation.

- Interferometric Scattering Microscopy reveals how *Pseudomonas aeruginosa* use type IV pili to twitch on surfaces/ Talà, L., Fineberg, A., Kukura, P. & Persat, A. Accepted in EMBO | EMBL Symposium: New Approaches and Concepts in Microbiology, Heidelberg, Germany. in 2019 as a poster presetation

- Combining fluorescence and interferometric scattering microscopy in live imaging of bacterial motility processes. Lorenzo Talà and Alex Persat. Accepted in Interferometric scattering microscopy workshop for a short talk (2020).

- Positive feedback between type IV pili activity and mechanosensation commits *P. aeruginosa* to surface associated behaviors. Marco J. Kühn, Lorenzo Talà, Yuki Inclan, Ramiro Patino, Xavier Pierrat, Iscia Vos, Zainebe Al-Mayyah, Henriette MacMillan, Jose Negrete, Joanne N. Engel, Alexandre Persat. Accepted in EMBO | EMBL Symposium: Life at the Periphery: Mechanobiology of the Cell Surface for a poster presentation (2021).

- Positive feedback between type IV pili activity and mechanosensation commits *P. aeruginosa* to surface associated behaviors. Marco J. Kühn, Lorenzo Talà, Yuki Inclan, Ramiro Patino, Xavier Pierrat, Iscia Vos, Zainebe Al-Mayyah, Henriette MacMillan, Jose Negrete, Joanne N. Engel, Alexandre Persat. Accepted in APS March meeting: DBIO for a short talk (2021).

INTERESTS

- Astronomy: I built my own telescope from scratch, I love to look at the stars and planets

- Music: I play the guitare, the bass and some piano

- Scouting: Since I was eight, I always enjoyed nature through campouts, hikes. I loved learning how to use a compass, make fire and especially respect nature.